Technische Universität München

Fakultät für Mathematik

Numerical methods and applications in nonlinear acoustics and seismology: Medical ultrasound and earthquake simulations

Markus Muhr

Vollständiger Abdruck der von der Fakultät für Mathematik der Technischen Universität München zur Erlangung des akademischen Grades eines

Doktors der Naturwissenschaften (Dr. rer. nat.)

genehmigten Dissertation.

Vorsitzender: Prof. Dr. Matthias Scherer

Prüfer der Dissertation:

1. Prof. Dr. Barbara Wohlmuth

2. Prof. Dr. Barbara Kaltenbacher

Die Dissertation wurde am 06.12.2021 bei der Technischen Universität München eingereicht und durch die Fakultät für Mathematik am 09.03.2022 angenommen.

It is the supreme art of the teacher to awaken joy in creative expression and knowledge.
Albert Einstein

—

If you can't explain it simply, you don't understand it well enough.
Albert Einstein

Zusammenfassung

Titel in deutscher Sprache:
Numerische Methoden und Anwendungen in nichtlinearer Akustik und Seismologie: Medizinische Ultraschall- und Erdbebensimulationen

Diese Arbeit beschäftigt sich mit verschiedenen Aspekten nichtlinearer akustischer und seismischer Wellen. In der mathematischen Modellierung von Ultraschallwellen hoher Intensität, wie sie in der medizinischen Therapie von Nierensteinen und Tumoren verwendet werden, sind die Westervelt- und Kuznetsov-Gleichung bekannte Modelle. Diese nichtlinearen partiellen Differentialgleichungen modellieren Effekte wie die Verzerrung von Wellen und die Ausbildung steiler Wellenfronten aufgrund physikalischer Gesetze bei starken Druckvariationen. Für ein solches Wellenmodell werden transparente Randbedingungen entwickelt, die es erlauben das numerische Simulationsgebiet künstlich zu begrenzen, ohne dass von diesen Grenzen ausgehende, unphysikalische Reflexionen die Lösung im Inneren des Gebietes beeinträchtigen. Des Weiteren betrachtet die Arbeit die Kopplung der akustischen Modelle mit einem Festkörpermodell zur Simulation von elasto-akustischen Problemen mit unterschiedlichen Materialien. Das resultierende, nichtlineare, gekoppelte System partieller Differentialgleichungen wird mittels der *discontinuous Galerkin spectral element method* diskretisiert und im Rahmen einer numerischen Fehleranalysis die Konvergenz des Verfahrens gezeigt. Numerische Beispiele stützen dabei jeweils die theoretischen Resultate und vermitteln mögliche Einsätze in anwendungsorientierten Szenarien. In Bezug auf die seismologische Anwendung der Arbeit wird ein numerisches Modell für die Simulation des Verhaltens eines Dammes während eines Erdbebens konstruiert. Die resultierende Simulation umfasst mehrere Längenskalen von der Quelle bis hin zur betrachteten Gebäudestruktur und enthält Modelle für die seismische Quelle und Wellenausbreitung sowie elasto-akustische Interaktion zwischen dem festen Boden und Damm sowie dem Wasser im Reservoir-See dahinter. Die Methoden werden auf ein reales Erdbeben aus dem Jahr 2020 mit echten Daten zur Modellierung und Validierung angewendet.

Abstract

This thesis deals with different aspects of nonlinear acoustic as well as seismic waves. For the mathematical modeling of high intensity ultrasound waves, as they are used in the medical treatment of kidney stones or tumors, the Westervelt and Kuznetsov equations are well known models. These nonlinear partial differential equations model effects such as the distortion of a wave field and the development of sharp wavefront-gradients due to physical laws valid for waves in the regime of high pressure variations. For such a wave model absorbing boundary conditions are developed, which allow the truncation of the computational domain without reflections reentering from these boundaries, impacting the solution in the interior. Furthermore, the coupling of the acoustic models with a solid model for the simulation of elasto-acoustic problems with different materials is considered. The resulting, nonlinear, coupled system of partial differential equations is then discretized using the *discontinuous Galerkin spectral element method* and convergence of the method is shown via a numerical error-analysis. Numerical examples always support the theoretical findings and show possible usages in applicational scenarios. Concerning the seismic application of the thesis, a numerical model for the simulation of the response of dam structures during earthquakes is constructed. The resulting simulation spans multiple length scales from source to site and contains seismic fault and propagation models as well as elasto-acoustic interaction between the solid ground and dam structure and the water of the reservoir lake behind. The methods are applied to a real seismic event from the year 2020 with actual data used for modeling and validation.

Acknowledgements

The completion of my doctoral studies definitely poses a milestone in my life. Looking back to the past five years, there is a lot to find. From the driving feeling to gain new knowledge and a deeper understanding, even if it is already late night, the frustration if some idea just won't work out and one starts to spin in circles, but also the excitement, once the last problem was fixed and everything works. Also beside pure science my time at the chair for numerical mathematics is full of impressions and memories. From occasions during my teaching activities, interesting courses, workshops or visits and time well spent with colleagues and friends. I would like to use these lines to thank all the people who shared with me those moments, who helped me in whatever way through drought-periods but also celebrated with me the successes. I am grateful to have all of you!

First and foremost my gratitude goes to Prof. Dr. Barbara Wohlmuth, who greatly supervised me during my whole thesis project. Always ready to give new ideas, a helpful hint or constructive critics, I have the feeling to have learned a lot from our discussions! I am also thankful for the funded position at the chair that allowed me to also develop and practice my skills in teaching, which I enjoyed a lot. In the same way I would like to thank my mentor Prof. Dr. Vanja Nikolić as a great source of advice and encouraging words in all scientific matters from my first day on at the chair. I really enjoyed our conversations and it is always a pleasure to work and travel with you. The same holds true for Dr. Ilario Mazzieri and Dr. Marco Stupazzini who always had an open ear for questions from Fortran to the hazard of seismic events, thank you for your patience and nice introduction to a new and interesting field of research. I would also like to thank Prof. Dr. Barbara Kaltenbacher for agreeing to review my thesis and Prof. Dr. Matthias Scherer for taking the chair of the examining committee.

Moreover my thanks also go to Dr. Daniel Drzisga, Dr. habil. Tobias Köppl and Dr. Linus Wunderlich. With your expertise you helped me more than once and I am thankful for the time you took, whenever I had a question, even if it lead beyond work. Especially concerning my teaching activities at the university I would like to thank my fellow tutors, exercise coordinators and colleagues (alphabetically) Gladys Gutiérrez, Dr. Laura Melas, Dr. Mario Parente, Prof. Dr. Laura Scarabosio, Andreas Wagner and Dr. Fabian Wagner for exchanging experiences, ideas and a lot of amusing moments. Working in a team with you was great! Special thank goes to Prof. Dr. Rainer Callies for your always good advice and council from teaching to formalities and more, it is appreciated a lot! And since university work contains more non-scientific parts than one would think, I would also like to thank Jenny Radeck and Silvia Toth-Pinter for all the help in these matters.

On evenings, weekends and vacations, especially when my head already started to smoke and needed a break from maths, I am very grateful to have a large amount of good and close friends. Having all of you for such a long time now is something extremely valuable to me. So, thank you Annika, Annkathrin, Babsi, Benny, Efdal, Ettore, Felix, Krissy, Malte, Markus[2], Marvin, Mel, Miriam, Nadine, Nora, Sandra, Schreiti, Simon, Steffi and Tim.

And finally, my sincere gratitude to my family for their continuous and unparalleled encouragement, help and support, thank you Karlheinz, Monika, Raphael, Rita and Sarah!

Markus Muhr
December 2021

List of contributed articles

This thesis is based on the following articles:

Core articles as principal author

[I]) Muhr, Markus, Vanja Nikolić, and Barbara Wohlmuth
Self-adaptive absorbing boundary conditions for quasilinear acoustic wave propagation.
Journal of Computational Physics 388 (2019): 279-299.
(see also article [224] in the bibliography)

[II]) Muhr, Markus, Vanja Nikolić, and Barbara Wohlmuth
A discontinuous Galerkin coupling for nonlinear elasto-acoustics
To appear in: *IMA Journal of Numerical Analysis* (2021), accepted on 26.10.2021
(see also article [225] in the bibliography)

Further articles

[III]) Mazzieri, Ilario, Markus Muhr, Marco Stupazzini, and Barbara Wohlmuth
Elasto-acoustic modelling and simulation for the seismic response of structures: The case of the Tahtalı dam in the 2020 İzmir earthquake
Submitted to: *Journal of Computational Physics* at 03.11.2021, currently under review
(see also arXiv version of the article [213] in the bibliography)

[IV]) Antonietti, Paola F., Ilario Mazzieri, Markus Muhr, Vanja Nikolić, and Barbara Wohlmuth
A high-order discontinuous Galerkin method for nonlinear sound waves.
Journal of Computational Physics 415 (2020): 109484.
(see also article [12] in the bibliography)

I, Markus Muhr, am the principal author of the articles [I] and [II].

List of further contributed articles

The following articles include further contributions by the author which are not part of this thesis. They are included for the sake of completeness only. Note that the author of this thesis does *not* claim to be the principal author of the following articles.

Further articles which are not part of this thesis

[V]) Muhr, Markus, Vanja Nikolić, Barbara Wohlmuth, and Linus Wunderlich
Isogeometric shape optimization for nonlinear ultrasound focusing.
Evolution Equations & Control Theory, Volume 8, pp. 163
(see also article [226] in the bibliography)

Contents

1. Introduction

Waves are an omnipresent phenomenon in various fields of science and engineering. Starting from gravitational waves with wavelengths up to cosmic scales, over seismic and water waves in the earth's crust and seas up to sound and finally electro-magnetic ones; waves come in all shapes and sizes, each with its own physical mechanisms. In this work I mainly focus on ultrasound-waves with frequencies in the kHz to MHz range traveling in acoustic media like water, air or human tissue with wavelengths within the μm to mm scale. For article [III] of the thesis, I will move to the regime of seismic waves, which is settled in the order of magnitude of Hz, however also on a much larger scale of several km.

I start by giving a short introduction into the fields of application motivating the individual articles of this thesis in Sec. 1.1. For sound wave, this will be a medical background considering ultrasound-based treatment methods for kidney stones or cancer, for the seismic wave part it will be the simulation of earthquakes and their effects on building structures. Then, in Sec. 1.2, I formulate the concrete problems coming from these fields of applications, that are tackled in this thesis. A mathematical background review stating the problems in a mathematical-abstract setting, summarizing existing literature and giving further details about important equations, results and theorems is given in Sec. 2. Similar Sec. 3 gives an overview over the numerical methods used in this thesis. Finally Sec. 4 summarizes the results of the individual articles being part of this thesis, relates them to the scientific questions asked in Sec. 1.2 and reflects on further possible research topics following or emerging from the articles of this thesis. All core-articles that are part of this thesis are included in appendix A, all further (non-core) articles in appendix B. References to these articles within the following sections are denoted by the roman numbers introduced in the contributed article list (with full bibliography information being linked therein), references to other works are denoted by arabic numbers as listed in the bibliography.

1.1. Applications and motivations for (nonlinear) waves

Ultrasound in medicine: The areas of application for natural and artificially generated waves are huge. For the later especially concerning ultrasound, which is defined as acoustic waves with frequencies above 20 kHz. The most prominent application concerning ultrasound lies within its publicly well-known diagnostic capabilities, sending ultrasound waves through the human body as an acoustic medium, then detecting the intensity of their reflections to compute an image of e.g. internal organs or a fetus. Typical pressure amplitudes for diagnostic ultrasound range from $0.1-4$ MPa [77, Sec. 12.2.2] leaving the human tissue unharmed. However, ultrasound may not only be used for diagnostic reasons, but also as a direct medical treatment method. An example for such a therapeutic application would be extracorporeal shockwave lithotripsy (ESWL) for the treatment of kidney stones [70]. As its name suggests, this method avoids a larger, open surgery to remove a stuck kidney stone by applying a short-pulsed ultrasound wave with a much higher pressure amplitude of up to 100 MPa [310, p. 852] at the kidney stone

from outside the body. This fractures the kidney stone into smaller debris that can pass out naturally [91]. Also the applications to certain types of cancer, making use of the heat generated by the high pressure amplitudes (ultrasound hyperthermia treatment), are summarized for example in [212, 317].

With such high pressure amplitudes, aiming is important to avoid or at least reduce damage dealt to tissue in the vicinity of the kidney stone [187]. Hence, a method of focusing the high-intensity ultrasound beam is needed. Similar to the focusing of light with an optical lens, acoustic lenses made e.g. of rubber can be used to achieve that goal [229], assigning to the resulting application the term high-intensity focused ultrasound (HIFU). Of course the specific shape of such a focusing lens is of crucial importance for its focusing capabilities. Finding an optimal lens-shape to aim for a given focal point [294] by means of isogeometric shape optimization [63, 109, 110, 186, 297] is the main topic of article [V] being the chronological first that I was involved in. Another focusing mechanism using a curved, vibrating transducer (array) directly aiming at the focal region without a lens is considered and simulated involving its elasto-acoustic interaction in [II].

Another point that comes with the high frequency and amplitude of HIFU applications is the process of wave-steepening. A sine-wave, assuming no damping and no wave-spread, for instance when propagation takes place in a confined channel, does not change its shape during propagation. HIFU waves in contrast are distorted over time resulting in sawtooth-like wave shapes eventually exhibiting shocks, even if they are driven by a smooth sine-wave excitation, see for example, [170, Fig. 5.37], [V, Fig. 2]. A reason for that behavior is the nonlinear pressure-density relation (4), that is otherwise often linearized with differences becoming evident only at higher amplitudes. The linear wave equation, while being an often used approximation within moderate amplitude regimes, does not capture such nonlinear effects, which is why nonlinear wave models such as the Westervelt (6) or Kuznetsov equation (7) are employed instead for increased accuracy.

A problem common to acoustic as well as the later mentioned elastic waves, being linear or nonlinear, once it comes to numerical simulation is the sensible truncation of the computational domain. Take for example a simulation of a certain part of the human body with direct application of an aforementioned HIFU beam as it is done in [II, V]. It is often not possible to simulate its complete surrounding such as the whole body or ambient room as a closed system due to computational constraints or the limitations of the model used. However, often this is also not necessary as influences from there can be neglected. Hence, the computational domain can be cut off at an artificial boundary to only incorporate the region of interest. For mathematical models based on partial differential equations (PDEs), such as the nonlinear wave equations in this thesis, this approach now yields the necessity to prescribe some boundary conditions on the newly introduced artificial boundaries. However, the first naive idea of homogeneous Dirichlet or Neumann conditions would result in reflections on a, physically non existent, wall traveling back into the truncated domain, spoiling the solution therein with unphysical data. Hence, just neglecting what lies outside the truncated domain is not enough, one

also has to make sure that wave components trying to leave the domain of interest can do so unhindered, i.e. in the ideal case without any reflections back into the interior. [I] deals with the derivation of such absorbing boundary conditions (ABCs) [119, 228] for the Westervelt equation (8) [275], that also adaptively detect and incorporate the angle of incidence [133, 274] the wave has at the artificial boundary. The resulting conditions drastically improve their quality compared to e.g. the most classical, linear ones by Engquist and Majda [95], especially at large, oblique incidence angles, being the main motivation for this ([I]), chronologically second, publication.

Seismological earthquake simulations: From the destruction of the ancient colossus of Rhodes, 226 BC [181], up to more recent, famous events such as the collapse of the CTV Building in Christchurch, New Zealand on the 22$^{\text{nd}}$ of February 2011 [247], earthquakes pose a serious threat to human civilizations all over the world, especially concerning their destructive effects in general [25], on buildings [173], and with special attention in this work, on dam structures [2, 185, 316]. It has therefore been of major interest since the antiquity to measure, understand and ultimately being able to predict earthquakes, the damages they might cause and to assess the risk that is posed to structures in specific areas of the world. Besides empirical methods such as ground motion measurements using seismographs or theoretical foundations of seismology [5] yielding seismic source and propagation models, the numerical simulation of earthquakes poses an additional mean to reach these goals.

Seismic waves are variations in the vectorial displacement field of the earth's body. As such, they behave a bit different to acoustic waves as they might not only contain a compression component, usually denoted by the term P-wave, but also a shear component, denoted by S-wave, with the two components typically traveling at different velocities [152, Chap. 2], also see Sec. 2.4. Nevertheless, the general structure of a wave equation is applicable here as well, resulting in a dynamic elasticity equation assuming that an elastic material law is employed. The consideration of also seismic waves in this thesis was ultimately motivated by the goal to conduct earthquake simulations such as finally done in [III] analyzing the effects of seismic scenarios on building structures [13, 180, 214, 215] like dams using realistic seismic source and topography data as well as real live measurement data to validate the simulations against. Considering a dam, it becomes obvious that if the water in the reservoir sea should not be neglected, an elasto-acoustic interface [7, 106] between the elastic domains, the dam and sub-soil layers, and the acoustic domain being the water is present. Also, due to stacked layers of different soil materials in the earth's crust as well as even more different materials used for human built structures, jumps in the material coefficients for such large scale simulations need to be considered. Such problems fitted well not only to the seismic setting, but also to the initially introduced medical application. Therefore the two articles [IV] and [II] being chronologically third and fourth were given priority to analyze the required methods also mathematically in depth on simpler examples that I was already familiar with.

First, in [IV] the emphasize is put on the application of a high-order discontinuous Galerkin (DG) method to the nonlinear acoustic problem. To keep the setting more general, polygonal shaped elements were assumed [15, 52]. The main result of the article is the proof of convergence for the applied method under h-refinement together with an a-priori error-bound in a suitable energy-norm. Besides some academic test-cases in 2D using MATLAB to show the convergence results also numerically, the article also contains two first, larger simulations in 3D using the high-performance code framework *SPEED* [14, 214, 283] paving the way for all subsequently following, more complex and application-driven 3D simulations in the remaining articles.

In [II] then the coupling of an acoustic (pressure-field) domain to an elastic (displacement-field) domain is studied. The motivating application comes again from medical ultrasound therapy using beam focusing. However, this time the alternative focusing mechanism using a piezoelectric transducer [170, Fig. 12.47] is employed instead of the lens mechanism. The elastic parts of that focusing mechanism are modeled using the equations of linear elasticity, while the acoustic wave guide is again modeled using the nonlinear acoustic equations of Westervelt and Kuznetsov. The elasto-acoustic interface in between is then equipped with suitable coupling conditions communicating the force exchange between the two models. Also the human tissue where the pressure focus is aimed to is modeled. In case of an acoustic model for the tissue also acoustic-acoustic interfaces between different materials and hence jumps in the material parameters appear. The article then generalizes the numerical DG scheme from [IV] in a hybrid way to capture all features mentioned. Again convergence of the resulting method is proven and error bounds are given together with numerical examples in academic as well as application inspired scenarios.

Finally my, for this thesis chronologically last, publication [III] accomplishes the original plan to perform realistic, large scale and real data driven earthquake simulations. Here the elasto-acoustic mathematical model is applied to the seismic scenario of an earthquake impacting a dam-structure analyzing the response of the dam in terms of e.g. maximal displacement and velocity being relevant for an engineering risk assessment. Using the magnitude 7 earthquake that took place on the 30^{th} of October 2020 in the Icarian Sea near Samos (Greece) [59] as a case study, the article analyses the threat the earthquake posed to the Tahtalı dam (Turkey) being approximately 30 km away from the hypocenter. The publication goes into details about geometry (topography) acquisition from satellite data [155], mesh generation, seismic sources, modeling the fault plane and its slip-process [103, 290], validation against real data and model comparisons. While in reality luckily no damage was caused to the dam, such simulations can for example be used in future work to not only recreate the actual situation, but also to conduct sensible variants of the event, ultimately yielding a seismic hazard analysis for the region of interest. This publication can be seen as the application of a general, numerical model to a specific case study with influences from seismology, using the methods derived and analyzed in the previous articles. It combines them together with a high-performance, parallel implementation, resulting in the largest simulations conducted for this thesis, as well as extensive data evaluation to obtain actual application-relevant results.

1.2. Scientific questions and problems

Coming from the motivational examples of Sec. 1.1, the following list contains the concrete scientific questions and problems that were asked before the work on the individual articles. The mathematical tools and methods used to answer these questions are described and embedded in a broader (literature) context in Sec. 2 and 3 and are elaborated in detail in the respective articles in the appendix.

Core articles as principal author

- Core article [I] in appendix A.1 as reference [224]:
  Self-adaptive absorbing boundary conditions for quasilinear acoustic wave propagation

  Derivations/Proofs: How can absorbing boundary conditions for the nonlinear Westervelt equation (in potential form) be derived, including the angle of incidence information?
  Methodological/algorithmic aspects: How can the angle of incidence be automatically detected/computed efficiently?
  Implementational aspects: How can the quality of the newly derived absorbing boundary conditions be tested and compared to others?
  Evidence aspects: How large is the influence of the angle of incidence? How large is the influence of the nonlinearity in the equation on the boundary conditions compared to the linear one?

- Core article [II] in appendix A.2 as reference [225]:
  A discontinuous Galerkin coupling for nonlinear elasto-acoustics

  Modeling aspects: How can a transducer based excitation ESWL scenario be modeled using elastic and acoustic components? How to formulate coupling conditions on the elasto-acoustic interfaces? How does an elastic tissue model differ from an acoustic one?
  Derivations/Proofs: Does the higher-order hybrid DG spectral element method converge, when applied to the nonlinear acoustic problem, coupled to an elastic one? What is the order of convergence? How are nonlinearities, damping in the acoustic equation and jumping material coefficients treated especially?
  Implementational aspects: How can the resulting coupled model/method be implemented and error-rates tested in the high-performance software *SPEED* for larger 3D coupled simulations?

Further articles

- Article [III] in appendix B.1 as reference [213]:
  Elasto-acoustic modelling and simulation for the seismic response of structures: The case of the Tahtalı dam in the 2020 İzmir earthquake

  Modeling aspects: How can the seismic ground-dam-water configuration be described as a mathematical model using real data? What kind of seismic source models are applicable?
  Methodological/algorithmic aspects: How can the complex geometry of ground-dam and water be meshed efficiently, especially concerning multiple length scales? How can real data such as topography information be included into the setup?
  Implementational aspects: How can the implementation be made efficient enough to solve the given problem in reasonable times?
  Evidence/application aspects: With which other seismological models/data can the results be compared? What are physically relevant quantities of interest and which values do they attain?

- Article [IV] in appendix B.2 as reference [12]:
  A high-order discontinuous Galerkin method for nonlinear sound waves

  Derivations/Proofs: Does the higher order DG spectral element method, based on polygonal elements, converge for the nonlinear Westervelt equation? What is the order of convergence?
  Implementational aspects: How can a nonlinear acoustic solver be implemented in the high-performance software *SPEED*? Can it solve physically motivated 3D problems?

Further articles which are not part of this thesis

- Article [V] as reference [226]:
  Isogeometric shape optimization for nonlinear ultrasound focusing

  Modeling aspects: How can the focus capability of an acoustic focusing lens be modeled, resp. judged? How can the full problem of finding a lens shape with optimal focusing be formulated in the context of shape optimization? In what sense is an optimal lens shape optimal?
  Derivations/Proofs: How does the shape derivative read when using the nonlinear Westervelt equation as the acoustic model? How does the adjoint equation read?
  Methodological/algorithmic aspects: How can the shapes of acoustic focusing lenses be represented on a computer in a way that is easily accessible to shape optimization? How can the involved equations be solved efficiently, the shape derivative computed and the geometry be updated/improved?
  Implementational aspects: How can the implementation be verified?

2. Mathematical problem formulations

In this section mathematical background information about the models, equations and concepts considered in the articles of this thesis are summarized. Important properties and results are stated and accompanied by further literature references. The content provided in this section forms the basis to formulate the problems introduced in Sec. 1 in a mathematical precise way, as (systems of) PDEs with suitable boundary conditions, making them accessible to the numerical methods that are provided in Sec. 3.
In Sec. 2.1 the nonlinear wave models such as the Westervelt or Kuznetsov equation are described from a modeling and analysis perspective. Sec. 2.2 then states some main results and tools from the development of absorbing boundary conditions for waves. A short glimpse at the competing method of perfectly matched layers (PMLs) is given. Sec. 2.3 provides a short introduction to linear elasticity stating key quantities and equations, while Sec. 2.4 then focuses more on the seismological point of view such as seismic source models. Finally Sec. 2.5 highlights some general mathematical tools used in some of the proofs of the articles of this thesis.

2.1. Equations of nonlinear acoustics

Derivation of acoustic model equations: The Westervelt (6) and Kuznetsov equation (7), that will be the main models for the acoustic part of this thesis, are by far not the only nonlinear acoustic models that exist. Starting from the *compressible* Navier-Stokes equations (1)-(2), a whole sequence of nonlinear wave equations can be derived, depending on the degree of simplifications resp. assumptions, where the Westervelt equation can be seen as one of the simpler second order in time representatives.

Compressible Navier Stokes system with entropy and state equation
The starting point for the derivation of nonlinear wave equations

$$\dot{\rho} + \nabla \cdot (\rho \underline{\boldsymbol{v}}) = 0 \tag{1}$$

$$\rho \left(\dot{\underline{\boldsymbol{v}}} + \nabla \underline{\boldsymbol{v}} \cdot \underline{\boldsymbol{v}} \right) = -\nabla p + \nabla \cdot \left[\eta \left(\nabla \underline{\boldsymbol{v}} + \nabla \underline{\boldsymbol{v}}^{\top} \right) + \left(\eta_B - \frac{2\eta}{3} \right) (\nabla \cdot \underline{\boldsymbol{v}}) \cdot \mathbf{1} \right] \tag{2}$$

$$\rho T \left(\dot{s} + \underline{\boldsymbol{v}} \cdot \nabla s \right) = \lambda \Delta T + \eta (\nabla \cdot \underline{\boldsymbol{v}})^2 + \frac{\eta}{2} \left(\nabla \underline{\boldsymbol{v}} + \nabla \underline{\boldsymbol{v}}^{\top} - \frac{2}{3} (\nabla \cdot \underline{\boldsymbol{v}}) \cdot \mathbf{1} \right)^2 \tag{3}$$

$$p' = \rho_0 c_0^2 \left(\frac{\rho'}{\rho_0} + \frac{B}{2!\, A} \left(\frac{\rho'}{\rho_0} \right)^2 + \frac{C}{3!\, A} \left(\frac{\rho'}{\rho_0} \right)^3 + \dots \right) \tag{4}$$

(1) *mass conservation,* ***(2)*** *momentum conservation, with density ρ, pressure p and velocity $\underline{\boldsymbol{v}}$. η is the dynamic viscosity, η_B the bulk viscosity,* ***(3)*** *entropy equation with entropy s, temperature T, heat conductivity λ [275],* ***(4)*** *Taylor expansion of equation of state [130].*

Detailed examples of such derivations can be found in [74, 131, 170, 275, 224], with typical steps involving a decomposition of the field variables into background and perturbation component such as $\rho = \rho_0 + \rho'$, the assumption of vanishing rotation $\nabla \times \underline{\boldsymbol{v}} = 0$ and the simplifying, repeated insertion of the linear wave equation $\ddot{p} - c^2 \Delta p = 0$ and the linearized Euler equation $\dot{\underline{\boldsymbol{v}}} = -\frac{1}{\rho_0} \nabla p$.

The **coefficient of nonlinearity** B/A that distinguishes the nonlinear models (6)-(9) from a linear wave equation enters the derivation via the pressure-density relation $p = p(\rho)$, see (4), that is used as an equation of state. In the most simplest case, only considering *first order* terms, the approximation $p' = c_0^2 \rho'$ would be used with $c_0^2 = \kappa \frac{p_0}{\rho_0}$ being the undisturbed background flow's speed of sound computed via the heat capacity ratio κ. This leads to the linear wave equation. Employing the Taylor-like expansion (4) up to *second order*, the nonlinearity enters, where under constant entropy the parameter B/A can be interpreted as $B/A = 2\rho_0 c_0 \left(\partial c / \partial p\right)|_{p=p_0}$ [131, §2.2], [259, §8.3]. This not only explains the origin of the parameter B/A within the wave equations but also sheds light on the wave distortion process that can be observed in nonlinear wave propagation, cf. Fig. 2 in [V]. The larger B/A becomes, the larger the sensitivity of c with respect to p becomes, changing the local speed of sound within the wave field more drastically, eventually distorting the waveform [130]. Vividly explained, high pressure parts of the wave travel faster than low pressure parts, leading to a steepening of the wavefronts.

In order to account for **dissipative losses in thermoviscous media** an entropy-equation such as (3) is considered [74, 275] to derive an expression for the *diffusivity of sound parameter* b [204] within (6),(7) reading $b = \frac{1}{\rho_0}\left(\frac{4\eta}{3} + \eta_B\right) + \frac{\kappa}{\rho_0}\left(\frac{1}{c_V} - \frac{1}{c_P}\right)$, with c_P and c_V being specific heat capacities of the propagation medium. In combination with $\Delta \dot{p}$, b enters as a weak damping parameter depending on the medium of propagation. Finally, suppressing the sub- and superscripts indicating background and perturbation values, equations (6) and (7) follow [199, 303]. An approach to incorporate the (transport of) heat generated in this process by considering a coupled system of the nonlinear wave and a heat equation is made in [277], also see [127, 257]

Noting, that besides pressure, the Kuznetsov equation (7) still contains the particle velocity $\underline{\boldsymbol{v}}$ as an additional unknown, the acoustic potential ψ can be introduced to solve that issue. It relates pressure and velocity via:

$$\textbf{(Acoustic potential)} \qquad p = \rho \dot{\psi}, \qquad\qquad v = -\nabla \psi \tag{5}$$

Insertion into the pressure form equations (6) and (7) then yields the respective potential forms (8) and (9) with ψ being the only unknown in both cases.

Nonlinear acoustic equations, pressure and potential forms

The main models for the nonlinear acoustic parts of this thesis

Pressure forms:

$$\textbf{(Westervelt eq.)} \qquad \ddot{p} - c^2\Delta p - b\Delta\dot{p} = \frac{(2+B/A)}{\rho c^2}(p\ddot{p} + \dot{p}^2) \tag{6}$$

$$\textbf{(Kuznetsov eq.)} \qquad \ddot{p} - c^2\Delta p - b\Delta\dot{p} = \frac{B/A}{\rho c^2}(p\ddot{p} + \dot{p}^2) - \rho_0\partial_t^2(\underline{\boldsymbol{v}}\cdot\underline{\boldsymbol{v}}) \tag{7}$$

Potential forms:

$$\textbf{(Westervelt eq.)} \qquad \ddot{\dot{\psi}} - c^2\Delta\psi - b\Delta\dot{\psi} = \frac{2+B/A}{c^2}\dot{\psi}\ddot{\psi} \tag{8}$$

$$\textbf{(Kuznetsov eq.)} \qquad \ddot{\dot{\psi}} - c^2\Delta\psi - b\Delta\dot{\psi} = \frac{B/A}{c^2}\dot{\psi}\ddot{\psi} + 2\nabla\psi\cdot\nabla\dot{\psi} \tag{9}$$

Differences between the two models resp. in their derivation are the fact that for the Westervelt equation it is sufficient to use the linearized Euler equation instead of the fully nonlinear momentum conservation (2) and the assumption that the Lagrangian density $\mathcal{L} := \frac{1}{2}\rho_0|\underline{\boldsymbol{v}}|^2 - \frac{p^2}{2\rho_0 c^2}$ vanishes, which can be interpreted as "[...] the pressure/density and velocity are in phase." [65, Sec. 3.3, p. 480]. Via the acoustic potential this assumption, for simplicity in 1D, translates to $|\partial_x\psi| = |\frac{1}{c}\dot{\psi}|$, which is true for linear plane waves and a good approximation for mild deviations from them, but loses its validity the more cummulative nonlinear effects such as the wave steepening start to dominate, leading to e.g. different shock formation times [64, 65], making the Kuznetsov equation the more physically accurate one for the price of a more challenging mathematical and numerical treatment.

Honorable mentions of **further nonlinear acoustic models** are the closely related Blackstock equation [41, 108], being even more *general* than Kuznetsov's equation, and on the other side the more *simple* Burgers' equation $\dot{p} + (c + bp)\,\partial_x p = d\partial_x^2 p$ [74], which can be seen as a further simplification of Westervelt's equation in 1D [131]. Some more advanced models are the Khokhlov-Zabolotskaya-Kuznetsov-equation [260] that incorporates directivity effects in sound-beams or the third order in time Jordan-Moore-Gibson-Thompson equation [159, 165] incorporating the heat flux according to the Maxwell-Cattaneo law $\tau\dot{\underline{\boldsymbol{q}}} + \underline{\boldsymbol{q}} = -K\nabla T$ instead of Fourier's law [251] eventually avoiding infinite (thermal) propagation speeds, resulting in an additional term of the form $\tau\dddot{\psi}$, where τ is a relaxation time parameter. For a broader overview [168] lists several acoustic models in a clear, hierarchical structure giving an overview over how they are connected, while [160] gives a review of the historical development of nonlinear acoustic models.

Well posedness results: For both, the Westervelt and Kuznetsov equation well posedness results, mainly by Kaltenbacher and Lasiecka, exist [68, 161, 162, 163, 164, 167, 279]. Even though they are most often restricted to smooth domains and specific types of boundary conditions, which are conditions that are not always guaranteed in the further

applications, the computations within their proofs can shed light on certain aspects of the model. As an example Westervelt's equation in pressure form (6) could be rewritten as $(1-2kp)\ddot{p} - c^2\Delta p - b\Delta\dot{p} = 2k\dot{p}^2$ where $2k := \frac{2+B/A}{\rho c^2} > 0$ is another coefficient for the nonlinear term. The assumption $(1-2kp) > 0$ used in the analysis to preserver the character of the equation for example is directly linked to the smallness of data requirement, i.e. that p does not become too large to prevent the model from degeneracy. A few of those results are summarized in the following. If not stated differently it is assumed that $\Omega \subset \mathbb{R}^d, d \in \{1,2,3\}$ is open, bounded with C^2 boundary and the respective equations are always considered with initial data $(p(0), \dot{p}(0)) = (p_0, p_1)$. Furthermore the following energy functional are a key ingredient for the respective statements:

Definition 2.1 (Energy functionals)**.** *Define the following energy functionals, where* $|\cdot|_0$ *stands for the standard* $L^2(\Omega)$*-norm.*

$$E_{p,0}(t) = \frac{1}{2}\left(|\dot{p}(t)|_0^2 + |\nabla p(t)|_0^2\right), \qquad E_{p,1}(t) = \frac{1}{2}\left(|\ddot{p}(t)|_0^2 + |\nabla\dot{p}(t)|_0^2 + |\Delta p(t)|_0^2\right)$$

The well-posedness results for classical boundary conditions (Dirichlet and Neumann) with finite time horizon from [162, 163, 164] for both model equations can then be summarized as follows.

Theorem 2.1.1 (Local well posedness)**.**
Consider Westervelt's/Kuznetsov's equation in pressure form (6)/(7) together with either

a) Dirichlet data $p = g$ *on* $\partial\Omega$ *[163, 164] or*

b) Neumann data $\partial_n p = g$ *on* $\partial\Omega$ *[162]*

each being compatible with the initial data at $t = 0$*, then for any* $T > 0$*, there exist* $\rho_e > 0, \rho_g > 0$ *such that with the following smallness of data assumption*

$$E_{p,0}(0) + E_{p,1}(0) \leq \rho_e, \qquad g \in X^{*)}, \|g\|_X^2 \leq \rho_g$$

there exists a unique weak solution with $p \in C([0,T]; H^2(\Omega)) \cap C^1([0,T]; H^1(\Omega)) \cap C^2([0,T]; L^2(\Omega)), \quad \ddot{p} \in L^2((0,T); H^1(\Omega))$.

[*)] The space X *contains further requirements on the boundary data* g *depending on case a) or b), for details see the individual references.*

Let $M > 0$, then under additional smallness and regularity assumptions on the given data and some further modifications in the Neumann case [162], these well posedness results can also be extended to be global in time, resulting in global existence of a solution and energy bounds such as $E_{p,0}(t) + E_{p,1}(t) \leq M$ for all $t > 0$.

In [166, 217, 219] similar well posedness results are given also for the potential form equation. Also in the presence of certain absorbing boundary conditions (cf. Sec. 2.2),

existence and uniqueness results are available for the nonlinear acoustic models. In [68] an optimal boundary control problem using (6) or (7) in combination with an inhomogeneous Dirichlet excitation signal $\partial_n p = g$ on $\Gamma \subset \partial\Omega$ is considered. On the remaining boundary $\partial\Omega\backslash\Gamma$ zero order, linear, absorbing boundary conditions (10) are prescribed. Well posedness of the resulting initial boundary value problem is proven in up to three dimensions. In [167, 279] well posedness of the Westervelt equation also together with the higher order, nonlinear, absorbing boundary conditions derived in [275] is shown.

2.2. Absorbing boundary conditions

The need for boundary conditions that behave *transparent* is immanent to many different PDE-based (wave) models, from shallow water waves [230] over the Schrödinger equation [197] to the acoustic case considered here but also to geophysics/seismology [9, 57] where such conditions are applied to the elastic wave equation, also see [II, III] of this thesis. Considering only a finite spatial domain $\Omega \subset \mathbb{R}^d$ with waves being induced in the interior, it is only a matter of (simulation-) time until these waves reach the artificial truncation-boundaries. The goal is now to prescribe ABCs on said boundaries that let waves coming *from the interior* of the domain pass, but annihilate unphysical reflections traveling *back into* the domain as good as possible. Also for parabolic problems such as the heat and convection-diffusion equation [129, 284, 308] similar problems occur and similar techniques are used to derive corresponding ABCs.

Classical results: The situation can be understood best in 1D considering $\Omega = (-\infty, 0)$, where the artificial truncation boundary lies at $x = 0$. Thinking of the derivation of d'Alemberts formula [269, Sec. 2.3], the linear wave equation $\ddot{u} - c^2\Delta u = 0$ can be rewritten as $(\partial_t - c\partial_x)(\partial_t + c\partial_x)\, u = 0$, with the two factors corresponding to wave components $u_\pm(t, x) := a_\pm e^{i(kx \pm \omega t)}$ traveling to the left (+, hence back into Ω), resp. right (−, hence out of Ω) [183]. Using $c = \omega/k$, it directly follows that $(\partial_t - c\partial_x)u_+ = 0$ is fulfilled by reentering waves and $(\partial_t + c\partial_x)u_- = 0$ by the ones leaving Ω but *not* vice-versa. This makes $\partial_t u + c\partial_x u = 0 \Leftrightarrow \partial_x u + \frac{1}{c}\partial_t u = 0$ the first candidate for an ABC. The problem becomes more involved in higher dimensions, where one assumes Ω to be the negative half-space in the first spatial, i.e. x, direction. In [95, 228] the situation is described in 2D but instead of the operator splitting, a general solution to the wave equation is directly represented in Fourier-space. Again by distinguishing in- and outward moving waves, the following, perfectly absorbing, condition is derived, still in Fourier-space.

$$\partial_x \hat{u} + i\frac{\omega}{c}\sqrt{1 - \frac{c^2k^2}{\omega^2}}\hat{u} = 0$$

Here $\hat{u}(\omega, x, k)$ is the Fourier-transform of $u(t, x, y)$ w.r.t. the t and y coordinates. Expressing that condition in physical space requires the application of the inverse Fourier-transform. However, due to the square-root function not being a polynomial, nor even rational, the result would not be a classical, but a pseudo differential operator (PSDO) (cf. next paragraph, (15)) one could prescribe on the boundary. Such, even though math-

ematically perfectly absorbing, conditions are called *non local* as they involve information from the whole space-time domain in order to perform the Fourier-transformation, which requires large effort from a computational complexity perspective.

The original idea of Engquist and Majda (EM) [95] was then to replace the problematic **square root function** $f(x) = \sqrt{1-x}$ by means of its **Taylor resp. Padé approximation** of a certain order around $k = 0$. For those the inverse Fourier-transformation then again yields classical partial differential operators (PDOs). The two most prominent of their approximations together with the respectively resulting boundary conditions read:

Engquist-Majda ABCs of 0^{th} and 1^{st} order:
The order relates to the order of the Taylor-approximation used for the square root function.

0^{th} order:

$$\sqrt{1-\frac{c^2k^2}{\omega^2}} \approx 1 \Longrightarrow \mathcal{F}^{-1}\left(\partial_x \hat{u} + i\frac{\omega}{c}\hat{u}\right) \qquad \Longrightarrow \partial_x u + \frac{1}{c}\partial_t u = 0 \tag{10}$$

1^{st} order:

$$\sqrt{1-\frac{c^2k^2}{\omega^2}} \approx 1 - \frac{1}{2}\frac{c^2k^2}{\omega^2} \Longrightarrow \mathcal{F}^{-1}\left(\partial_x \hat{u} + i\frac{\omega}{c}\hat{u} - \frac{1}{2}i\frac{ck^2}{\omega}\hat{u}\right) \overset{\cdot i\omega/c}{\Longrightarrow} \frac{1}{c}\partial_{tx}u + \frac{1}{c^2}\partial_t^2 u - \frac{1}{2}\partial_y^2 u = 0 \tag{11}$$

Here $\mathcal{F}^{-1}$ denotes the inverse Fourier-transformation. In a general oriented setting the y-derivative has to be replaced by the tangential-, the x-derivative by the normal-derivative. Due to their simple structure and straight forward implementation the conditions (10) are among the most renown ones and are often simply denoted as EM conditions (of 0^{th} order) where the order corresponds to the order of the Taylor-approximation of the square root function.

A measure for the quality of these ABCs is also discussed in [95, 254], where the amplitude A_r of the spurious reflection of a plane wave hitting the absorbing boundary under the angle of incidence α, i.e. w.r.t. its normal, is compared to the incident wave's amplitude A_i. The ratio $|R| = |A_r/A_i|$, called the **reflection coefficient**, would be zero in case of perfect absorption. However, for the just stated conditions the expression $|R| = |A_r/A_i| = \left|\frac{\cos\alpha - 1}{\cos\alpha + 1}\right|^{\sigma}$ was derived with $\sigma = 1$ for (10) and $\sigma = 2$ for (11). Even more, [183] uses a more general, geometric setting to show that, up to a scaling, the n^{th} order EM conditions differential operator can be written as the $(n+1)$-st power of the 0^{th} order corresponding differential operator. Indeed (11) can be written as $\frac{1}{2}(\partial_x + \frac{1}{c}\partial_t)^2 u$ and the corresponding reflection coefficients share that property in the sense that for the n^{th} order conditions, $\sigma = n + 1$ in the above formula.

This shows that while all those conditions yield good results for small angles of incidence α, their reflection coefficients also tend to 1 when α gets close to 90°, i.e. full reflection at glancing. The reason is that k, corresponding to the tangential direction of the boundary in Fourier-space, grows with the angle of incidence deteriorating the

Taylor-approximations in (10) and (11). This already suggests that an angle dependent variant of the conditions might yield some improvement.

In [197, 308] very similar ideas and computations are employed to derive ABCs also for the heat- and Schrödinger equation, showing a broad applicability of the approach. Before continuing with details about angle dependent conditions, [112, 119] give reviews about the development of ABCs from foundations, even before EM's seminal work [95], over the incorporation of incidence angles by Higdon [133], see (12) up to the development of ABCs for elastic waves (cf. Sec. 2.3) and the competing technology of PMLs, for which a short overview is given at the end of this section.

Angle dependency: The idea to consider a plane wave traveling in x (resp. normal) direction towards a boundary was generalized by Higdon in [133], where he considers the plane wave field $u(t,x,y) = f(x\cos(\alpha)+y\sin(\alpha)+t)$ defined on $\Omega = \{(x,y) \in \mathbb{R}^2, x > 0\}$, i.e. with the absorbing boundary on the left hand side in contrast to before, for some function f. This plane wave hits the artificial boundary at $x = 0$ exactly with an angle of incidence of α fulfilling the modified version of (10) reading $\cos(\alpha)\partial_t u - \partial_x u = 0$. This condition guarantees perfect absorption in case that the angle of incidence is exactly α. Similar to the $(n+1)$-st power of 0^{th} order conditions, see [183] from before, he then generalizes that approach to conditions of order p, taking into account different possible angles α_i.

$$\prod_{i=1}^{p}(\cos(\alpha_i)\partial_t u - \partial_x u) = 0, \qquad |\alpha_i| < \frac{\pi}{2} \ \forall i = 1, ..., p \tag{12}$$

The condition is perfectly absorbing, if the wave's angle of incidence matches any of the angles $\alpha_i, i = 1, \dots, p$, which have to be chosen in advance. In detail the reflection coefficient of these conditions turns out to be $|R| = \prod_{i=1}^{p} \left|\frac{\cos\alpha_i - \cos\alpha}{\cos\alpha_i + \cos\alpha}\right|$. Further notes on Higdon's conditions also regarding its discretization using finite differences can be found in [134].

The advantage of the conditions (12) to be **perfectly absorbing for a predefined set of angles** α_i requires some knowledge about the specific situation. Provided the wave field is known approximately a sensible choice of angles α_i can be made to balance accuracy and computational complexity. However, it would be advantageous to determine the local angle of incidence adaptively, especially in case of non-timeharmonic wave fields. Such an approach was studied by Shevchenko and Wohlmuth [274] in 2D, where the local wave propagation direction is computed using a localized Fourier-transformation of the wave field to determine the spatial main frequencies. From the propagation direction the local angle of incidence α follows readily, resulting in ABCs having the form $\partial_n u - \frac{1}{c}\cos(\alpha)\partial_t u = 0$ but with α varying in space (and time).

So far, all mentioned ABCs have been developed for the linear (undamped) wave equation. Application of these conditions to nonlinear wave models such as (6)-(9) is possible as well, especially in the regime of mild nonlinearity. However, with increasing parameters of nonlinearity and in more complex domains, conditions specialized for the nonlinear equations outperform them as it is shown in [I]. In the following some tools and references concerning the derivation of ABCs for the nonlinear acoustic models are given.

ABCs for nonlinear equations: Pursuing the idea to derive ABCs for the nonlinear wave equations (6)-(9), the act of splitting the associated PDO is not as straight forward as in the linear case. Shevchenko and Kaltenbacher [275, 276] used pseudo-differential techniques to derive nonlinear analoga of the conditions (10) and (11) up to order 1 (2D), resp. 2 (1D) for the Westervelt equation in pressure form (6). [285] uses the same approach for another, general nonlinear wave equation. Elements from pseudo-differential calculus also form the basis for the derivation of the nonlinear ABCs in [I], where they are combined with an angle-of-incidence detection algorithm in order to well approximate α and incorporate angle dependency as in (12). The final result therein reads:

$$c\partial_n\psi + \frac{b}{c}\partial_{nt}^2\psi = -\sqrt{1 - M\partial_t\psi}\ \partial_t\psi\cos(\alpha_h) \tag{13}$$

Here M is a constant depending on the parameter of nonlinearity $(2 + B/A)/c^2$ of (8), vanishing together with it, as well as the used linearization strategy. Hence, in the absence of nonlinearities and damping ($b = 0$) the conditions fall back to the linear, angle dependent conditions (12) where α_h is assumed to be the precise or at least a good approximation to the angle of incidence with details on how to obtain such an approximation being given in [I, Sec. 5]. For an orthogonal impingement the conditions then even reduce to the classical ones (10). In that sense they can really be seen as an extension by combination of the previous ideas.

Pseudo differential calculus: The concept of PSDOs can be understood best, if one first tries to express a regular, linear PDO in terms of pseudo-differential calculus and then generalizes. Following the definition in [306, Chap. 6], (14) defines a classical linear PDO over $\mathbb{R}^d$ and its corresponding symbol being, for fixed $\underline{\boldsymbol{x}}$, a polynomial in the components of $\underline{\boldsymbol{\delta}} = (\delta_1, \ldots, \delta_d)^\top$. (15) then poses a, compared to the classical application of P to a function ϕ, quite complicated method to evaluate $P(\underline{\boldsymbol{x}}, D)\phi$. It consist of first applying the Fourier-transformation to ϕ, then multiplying the resulting $\hat{\phi}$, in Fourier-space, with the symbol of the PDO and then an inverse Fourier-transformation back to physical space. This way of evaluation becomes interesting once one allows also expressions for $p(\underline{\boldsymbol{x}}, \underline{\boldsymbol{\delta}})$ that are non-polynomial in $\underline{\boldsymbol{\delta}}$ and hence would not result in a classical PDO in physical space. This then renders (15) the *definition* of what is called a PSDO.

The theory of PSDOs is rich, details can be found in the works of Hörmander [144] and Kohn and Nirenberg [188] or [145, 306] also defining the proper symbol-spaces S^m and (Schwartz-)function-spaces from and to which PSDOs map [306, Def. 6.1, Prop. 6.7].

(Pseudo) differential operators and their symbols

Definition of a classical, linear PDO, its symbol and the connection between the two, [306, (6.1)-(6.4)]

$$\textbf{(PDO)}\ P(\underline{\boldsymbol{x}}, D) = \sum_{|\alpha|\leq m} a_\alpha(\underline{\boldsymbol{x}}) D^\alpha, \qquad \textbf{(symbol)}\ p(\underline{\boldsymbol{x}}, \underline{\boldsymbol{\delta}}) = \sum_{|\alpha|\leq m} a_\alpha(\underline{\boldsymbol{x}}) \underline{\boldsymbol{\delta}}^\alpha \tag{14}$$

$$\textbf{(Connection)}\ (P(\underline{\boldsymbol{x}}, D)\phi)(\underline{\boldsymbol{x}}) = (2\pi)^{-d/2} \int_{\mathbb{R}^d} e^{i\underline{\boldsymbol{x}}\cdot\underline{\boldsymbol{\delta}}} p(\underline{\boldsymbol{x}}, \underline{\boldsymbol{\delta}}) [\mathcal{F}(\phi)](\underline{\boldsymbol{\delta}})\ \mathrm{d}\underline{\boldsymbol{\delta}} \tag{15}$$

Since PSDOs only serve as a tool for the splitting of the wave operator to derive ABCs in this work, only the following definitions and theorems are introduced, which are also used in [I].

First, the definition of an **asymptotic expansion of a symbol** falls back one step from the very *general* definition by stating a way of approximation, again with *special* functions. If $p(x, \delta)$ is a polynomial of degree m in δ, as in (14), it can be written (exactly) as a sum of monomials $p_j(x, \delta) = a_{m-j}(x)\delta^{m-j}$, which are homogeneous of degree $m - j$, $j = 0, 1, 2, \ldots, m$ respectively. The asymptotic expansion of a symbol makes use of that idea by approximating a general symbol $a \in S^m$ via a sum of (homogeneous) functions a_j according to the following definition.

Definition 2.2 (Asymptotic expansion of symbols, [306, Def. 6.9])**.** *Given a symbol $a \in S^m$ and a strictly decreasing sequence $(m_j)_{j=0}^\infty$ diverging to $-\infty$, starting with $m_0 = m$. If there are symbols $a_j \in S^{m_j}$ with $a - \sum_{j=0}^{N-1} a_j \in S^{m_N}$ for all $N \in \mathbb{N}$, then the series $\sum_{j=0}^\infty a_j$ is called asymptotic expansion of the symbol a, denoted by $a \sim \sum_{j=0}^\infty a_j$.*

In [234, (5.5)] Nirenberg then restricts his considerations to the class of symbols where the expansion terms are homogeneous of degree $m - j$ each.

With these definitions at hand, **factorization results** such as in [20] or in detail [234, Lem. 1], are employed in [129, Thm. 3.1, (3.10)], [275, (51)], [285, (3.2)] and in the same way in [I, (14)] to the (linearized) PDO $\mathcal{P}$ of the equation considered. One then arrives at the following decomposition of $\mathcal{P}$.

$$\mathcal{P} = -(\partial_x - \mathcal{A})(\partial_x - \mathcal{B}) + \mathcal{R}, \tag{16}$$

where $\mathcal{A}, \mathcal{B}, \mathcal{R}$ are pseudo-differential operators and one of them, i.e. the term $\partial_x - \mathcal{A}$, will eventually yield the desired ABC. In order to determine $\mathcal{A}$ and $\mathcal{B}$, their respective asymptotic expansions are inserted into (16). In the subsequent formal multiplication of $\mathcal{A} \cdot \mathcal{B}$ in (16), resp. their symbols $a \cdot b$, an expression for the product of two asymptotic expansions is required. It can be found in [145, Thm. 18.18], [306, Thm. 8.1]. Ultimately the (symbol of) $\mathcal{A}$ is then approximated by considering only a finite portion of its asymptotic expansion a. Its coefficients a_j can be determined up to the desired order via an ordering by their degree of homogeneity and a **coefficient comparison** with the left hand side of (16) being (the symbol of) $\mathcal{P}$.

Angle-adaptive ABCs for Westervelt's equation - Contribution of [I]: In this article absorbing boundary conditions for the potential form of the Westervelt equation (8) are derived using methods from pseudo differential calculus. First, they form an extension to the classical EM conditions taking into account the nonlinear term similar to [275]. However, additionally the angle of incidence is considered in the derivation. In contrast to the approach of [133], where a predefined set of angles with optimal absorption properties is chosen, in [I] the angle of incidence is adaptively *computed* and then directly inserted into the respective boundary condition formula. An efficient algorithm for the computation of the angle of incidence is stated with further method parameters for fine tuning. Different linearization strategies for the nonlinear part of the equation are compared, where one specific variant outperforms the others by far. The conditions are tested and compared in 2D and 3D application relevant scenarios dealing with ultrasound.

Perfectly matched layers: A different approach to the artificial boundary problem is summarized under the term of PMLs. Originally introduced by Berenger [36] for the electrodynamic Maxwell equations, their basic idea consists of a highly damping "sponge"-layer encasing the truncated computational domain Ω at all artificial boundaries. Within that layer, waves are damped to non-critical amplitudes such that their reflections coming from the very outer (outside of the encasing layer) boundaries can be neglected. On those very outer boundaries classical boundary conditions such as Dirichlet can be used then. The mathematically challenging part in the derivation of PMLs however is not the mere introduction of an additional damping parameter σ, which is then just chosen wide enough. On the interface between Ω and the PML, hence before damping to negligible amplitude, reflections can originate if the impedance difference between the two materials is not zero. Hence the PML's material has to fulfill an **impedance-matching condition** with the interior material in addition to its damping property. In one dimension this can be achieved by extending from real to complex material parameters and choosing for example $\rho_{\text{pml}} = \rho(1 - i\sigma)$ and $c_{\text{pml}} = \frac{c}{1-i\sigma}$ [170, (5.139)]. This results in a match with the interior material's impedance $Z_{\text{pml}} = \rho_{\text{pml}} c_{\text{pml}} = \rho c = Z$ as well as a damping of the wave by the factor $e^{-\sigma x}$ with x being the depth of the wavefront within the PML. In two and three dimensions again the angle of incidence plays a role, which is resolved by splitting even scalar fields such as pressure into *artificial* spatial components treating each of them with their own damping parameters according to the one dimensional result. A further strategy to increase the damping provided within the PML while retaining the matched impedance at the interior-PML interface is to apply the impedance-matching condition to determine the damping coefficients at the interface and then smoothly increase them towards the outer boundary [36]. For a PML layer of width L this results in a decrease of the outgoing wave's amplitude by $\sim e^{-2\int_0^L \sigma(x)\,\mathrm{d}x}$ until it reenters Ω. Specifically for the acoustic case derivations can be found in [170] and in combination with the Helmholtz equation also in [228] employing an analytical continuation of the plane wave solution and a coordinate transformation, also see [61, 158, 252]. An application of PMLs to a nonlinear wave equations is discussed in [16].

2.3. Elastic solid model

The equations of linear elasticity form the second mathematical model that is part of this thesis. [II] studies the interplay of the elastic wave-equation when coupled to the acoustic models from before and gives convergence results for the numerical solution of the resulting coupled system. [III] then considers the problem in an applied case-study from seismology where additional model components such as special source mechanisms are added. A background about those additional factors directly relating to the seismic modeling is given in Sec. 2.4, while here in Sec. 2.3 general foundations of linear elasticity theory are presented.

Derivations from continuum mechanics: The equations of **static (linear) elasticity** can be derived from continuum mechanical considerations [90] such as the conservation of mass and (angular) momentum in combination with a constitutive material law describing the material internal stress-reaction to deformation. Employing a displacement base approach, the base variable is the displacement vector field $\underline{\boldsymbol{u}}$ from which the strain-tensor $E = \frac{1}{2}\left(\nabla\underline{\boldsymbol{u}} + \nabla\underline{\boldsymbol{u}}^\top + \nabla\underline{\boldsymbol{u}} \cdot \nabla\underline{\boldsymbol{u}}^\top\right)$ and the linearized strain-tensor $\varepsilon = \frac{1}{2}\left(\nabla\underline{\boldsymbol{u}} + \nabla\underline{\boldsymbol{u}}^\top\right)$, neglecting the geometric nonlinearity $\nabla\underline{\boldsymbol{u}} \cdot \nabla\underline{\boldsymbol{u}}^\top$ are formed, where this *geometric linearization* is valid for relatively small displacements. So far, all involved quantities are valid for arbitrary materials as they only contain given deformations. The question arises, what internal stresses, i.e. forces per infinitesimal area, are created in a specific material subjected to deformations. It was Cauchy who proved in 1822 [22, 278] that the answer can be given in terms of a symmetric stress-tensor σ allowing to compute internal forces acting over virtual cut-surfaces via $F = \int_\Gamma \sigma \cdot \underline{\boldsymbol{n}}\, \mathrm{d}S$. It remains to specify the relation between strain ε and stress σ. Here the choice of a linear relation in the form of Hook's law $\sigma = \mathcal{C} : \varepsilon$ with the fourth order material tensor $\mathcal{C}$ results in *linear elasticity theory*. Symmetry considerations depending on the internal structure of the material in use reduce the amount of free parameters within $\mathcal{C}$ [72]. While organic materials such as wood or bones might for example be modeled by an orthotropic material law [143, 265] respecting some e.g. fiber-orientation, isotropic materials, without any preferred direction, state the most simplest case. By the Rivlin-Ericksen theorem [67, Thm. 3.6-1, 3.8–1] for such an isotropic material tensor only two free parameters are left, ultimately leading to the *linear, homogeneous, isotropic material law* $\sigma(\underline{\boldsymbol{u}}) = 2\mu\varepsilon(\underline{\boldsymbol{u}}) + \lambda(\nabla \cdot \underline{\boldsymbol{u}})I$, where the parameters λ and μ are called Lamé-parameters. Returning to the continuum mechanical conservation laws, the state equation (17) is derived, where $\underline{\boldsymbol{f}}$ denotes some external (volumetric) force and suitable boundary conditions have to be prescribed. This could be Dirichlet conditions in case of a fixed/prescribed displacement $\underline{\boldsymbol{u}} = \underline{\boldsymbol{g}}$, homogeneous Neumann conditions $\sigma\underline{\boldsymbol{n}} = 0$ in case of free surfaces, elasto-acoustic coupling conditions (cf. Sec. 3.3) or absorbing boundary conditions specifically tailored for elastic waves (see below).

Elasticity equations:
Equations used for the modeling of solids, e.g. the transducer and tissue parts in [II] or the earth's soil layers in [III].

$$\textbf{(Static)} \qquad -\nabla \cdot \sigma = \underline{\boldsymbol{f}} \tag{17}$$

$$\textbf{(Dynamic)} \qquad \rho\underline{\ddot{\boldsymbol{u}}} - \nabla \cdot \sigma = \underline{\boldsymbol{f}} \tag{18}$$

$$\textbf{(Dynamic with damping)} \qquad \rho\underline{\ddot{\boldsymbol{u}}} + 2\rho\zeta\underline{\dot{\boldsymbol{u}}} + \rho\zeta^2\underline{\boldsymbol{u}} - \nabla \cdot \sigma = \underline{\boldsymbol{f}} \tag{19}$$

Seismic (moment) sources can be incorporated via $\underline{\boldsymbol{f}}$ or directly by a modification of σ. ρ denotes the materials density, ζ is damping parameter.

In order to move from a static to a **dynamic model**, Newton's second law $\underline{\boldsymbol{F}} = m\underline{\ddot{\boldsymbol{u}}}$ can be employed to arrive at the elastic, second order in time, wave equation (18) which then of course needs to be supported by suitable initial conditions.

To incorporate **damping or attenuation** in the equation additional damping terms scaling with a damping parameter ζ, as used in [202] and the articles of this thesis, allow to specify frequency independent attenuation e.g. in each soil layer of the earth's crust as in [III]. The parameter ζ is related to the materials quality factor $Q = 2\pi\frac{E}{\Delta E}$ [9, 286] expressing the relative energy decay of a wave per wavelength. The damping approach can also be related to the PML technique mentioned in Sec. 2.2 damping the whole wave-field with a defined attenuation factor [55, 194], however, in contrast to the outer PML-layer, extended to the whole interior region. It is furthermore advantageous from a computational perspective as in the semi-discrete form of the equation it only introduces scalar multiples of the mass matrix being diagonal in the spectral element method, see Sec. 3.1. Hence, almost no additional numerical effort has to be invested. Another famous method to introduce damping would be by means of Rayleigh-damping [206]. The resulting model equation (19) states a relatively simple model that, considering all the uncertainties involved in real seismic applications such as the distribution of soil materials or fault parameters, is still often used due to its computational advantages. The model can be extended in various directions e.g. by means of different constitutive laws involving not only elastic but also plastic models [113, 184, 200, 236], or by means of visco-elastic/hysteresis based attenuation models [42, 83, 205] such as the Maxwell- or Kelvin-Voigt-model introducing certain degrees of nonlinearity into the equation.

ABCs for elastic waves: The dynamic elasticity equation (19) is a vector-valued wave equation. As such, the same requirements on absorbing boundary conditions to cope with artificially truncated domains as in the acoustic case arise. Results very similar to [95] in the acoustic case can be found also by Engquist and Majda for the elastic case in [94]. Also very similar to the acoustic case Higdon generalizes the angle dependent conditions from [133] to the elastic case in [135, 136]. [120] supports such conditions with further numerical experiments in the finite element setting. A common idea in the derivation of ABCs for elastic waves is the splitting of the displacement wave field into two components being normal and tangential, resp. pressure- and shear-waves, each

propagating with its own velocity c_n, resp. c_t. To each of them e.g. the simplest 0^{th}-order EM conditions (10) can then be applied with the respective value of c [207]. A short derivation of these two wave components which is of special relevance for seismic applications is given in Sec. 2.4. Finally, as in [9, 57, 216] the articles of this thesis use the absorbing boundary conditions proposed by Stacey [280], who combined the individual terms for normal and tangential wave-components in order to find correction terms that improve the order to the ABCs w.r.t. to the incidence angle without requiring higher order derivatives.

2.4. Seismic modeling

There is a number of special properties and additional methodology to linear elasticity that becomes especially useful in certain areas of application. For the seismology part, I will highlight two of them. First will be the decomposition of the dynamical elasticity equation into its pressure- and shear wave components, which already played some important role in the derivation of ABCs for elastic wave propagation. Second, there will be shortly summarize the seismic source mechanisms that were used e.g. in [III].

P- and S-waves, elasticity revisited: In contrast to pure, longitudinal pressure (P)-waves as they occur in acoustic media like water or air, the elastodynamic wave equation (18) (for this section the additional damping terms of (19) and the external force $\underline{\boldsymbol{f}}$ will be dropped) allows for a second propagation mechanism being transversal shear (S)-waves. The two wave components propagate with different, material dependent velocities that are denoted by c_P and c_S. The distinction of these two wave types is important as for example in case of an earthquake their wave speeds can differ by a factor of 1.5 - 2, see for example [288] with P-waves arriving prior to S-waves. Derivations of that splitting can be found in [272], or [152, Chap. 2], where equation (18), with the linear, homogeneous, isotropic material law for $\sigma(\underline{\boldsymbol{u}})$ inserted, is transformed using vector identities to obtain:

$$\rho\ddot{\underline{\boldsymbol{u}}} - (\lambda + 2\mu)\nabla(\nabla \cdot \underline{\boldsymbol{u}}) + \mu\nabla \times (\nabla \times \underline{\boldsymbol{u}}) = \underline{\mathbf{0}} \tag{20}$$

assuming potentials $(\Phi_\circ, \Phi_\times)$ for a Helmholtz-decomposition of $\underline{\boldsymbol{u}} = \underline{\boldsymbol{u}}_\circ + \underline{\boldsymbol{u}}_\times$ into a rotation free component $\underline{\boldsymbol{u}}_\circ = \nabla\Phi_\circ$ and a divergence free component $\underline{\boldsymbol{u}}_\times = \nabla \times \Phi_\times$ one can see (20) as the superposition of the two independent potential-waves:

$$\ddot{\Phi}_\circ - \frac{\lambda + 2\mu}{\rho}\Delta\Phi_\circ = \underline{\mathbf{0}}, \qquad \ddot{\Phi}_\times - \frac{\mu}{\rho}\Delta\Phi_\times = \underline{\mathbf{0}} \tag{21}$$

the first traveling with $c_P = \sqrt{\frac{\lambda+2\mu}{\rho}}$, the second with $c_S = \sqrt{\frac{\mu}{\rho}}$. Often seismological soil material datasets contain these speeds instead of other material parameters, where the larger one of the two, c_P, is also used e.g. for the computation of the Courant-Friedrichs-Lewy (CFL)-number within a simulation.

Seismic source mechanism: With the dynamic elasticity equation (19) describing the *propagation* of seismic waves, it remains the question how to model the *source/origin* of such waves, resp. an earthquake. For a general, first understanding of earthquake sources [291, Chap. 1] summarizes underlying physical mechanism taking place at a *seismic fault*, i.e. a (two-dimensional) crack in the solid earth's body where the body parts on either side of it slide parallel to each other due to a sudden release of accumulated stress. A seismic fault can be approximated by a e.g. rectangular fault-plane of area A with orientation being defined via the azimuth-angle ϕ w.r.t. north and the dip-angle δ w.r.t. a horizontal plane. Distributed over the fault plane one then defines the **slip vector field** $\underline{\boldsymbol{s}}$. It describes how far each material point on the fault plane has moved compared to its (former) counter part on the other side of the fault. A measure for the intensity of an earthquake is given by the overall seismic moment $M_0 = \mu \underline{\hat{\boldsymbol{s}}} A$ [4, 5], where $\underline{\hat{\boldsymbol{s}}}$ is the mean slip and μ the shear modulus of the material. From M_0 also the publicly well recognized (moment magnitude) scale value $M_W = 2/3 \log_{10}(M_0) - 10.7$, associated with the severity of an earthquake, can be computed [5, 171].

For the mathematical modeling of the fault one generally distinguishes [264] on the one hand side dynamic rupture models resolving the rupture-process [75, 244, 293] and the resulting slip involving e.g. friction models. On the other hand side, there are kinematic rupture models, where these data are already given, e.g. by measurement data and/or other models, and only the wave propagation into the rest of the domain during the predefined rupture process is numerically computed. In [III] the later approach is employed to recreate a realistic earthquake relying on the broad range of fault data obtained from [290]. In detail that data is used in the source models described in [103] especially with the **seismic-source-tensor**/stress-glut model [24],[291, Chap. 5]. The idea of the model is to incorporate the non-elastic stress contributions, e.g. induced by the slip vector-field $\underline{\boldsymbol{s}}$ on the fault-plane with normal $\underline{\boldsymbol{n}}$ into a seismic moment tensor $\boldsymbol{m} = (m_{ij}(\underline{\boldsymbol{x}}, t))_{i,j=1}^{3}$ depending on the spatial location $\underline{\boldsymbol{x}}$ and time.

$$\textbf{(Seismic moment tensor)} \qquad \boldsymbol{m}(\underline{\boldsymbol{x}}, t) = m_0(\underline{\boldsymbol{x}}) \cdot m^{(t)}(t) \cdot \left[(\underline{\boldsymbol{s}} \otimes \underline{\boldsymbol{n}}) + (\underline{\boldsymbol{s}} \otimes \underline{\boldsymbol{n}})^{\top} \right],$$

where m_0 scales with the magnitude of the earthquake and $m^{(t)}(t)$ is the moment release function associated with the time-evolution of the rupture process. The seismic moment tensor, resp. its equivalent body force $\underline{\boldsymbol{f}} = -\nabla \cdot \boldsymbol{m}$ [103], models the stresses that are induced in the surrounding material by the non-elastic slip caused by the rupture process. These are then used to startle a wave propagation from the fault plane into the rest of the computational domain eventually attaining a displacement field that is again in equilibrium with the the overall stress being the sum of elastic and non-elastic/prescribed stresses.

For specific earthquakes, fault-plane data such as the moment-distribution $m_0(\underline{\boldsymbol{x}})$ or the slip-vector field $\underline{\boldsymbol{s}}$ [290] can be obtained by seismic wave-form inversion techniques [132, 156] relying on actual measurement data such as they are provided by [1] for the region of Turkey considered in [III]. The situation is more complex if one tries to simulate alternative, however still realistic scenarios that have not (yet) happened. This is done for example in the seismic risk assessment [13], also see Sec. 3.4 of a region by means

of physics based simulations, where several possible scenarios with different parameter distributions are simulated. In order to conduct such *random* simulations with sensible parameters, correlations between fault parameters have been analyzed e.g. in [73, 264] from which reasonable choices of parameters can be deducted.

2.5. Further mathematical tools

In this section I will briefly state a small selection of mathematical tools/theorems that are mainly used in the proofs of the articles constituting this thesis.

Young's ε inequality Young's ε inequality is a variant of the standard Young inequality involving a parameter ε. By choosing ε either very large or very small, it allows to control *one* of the terms on the right hand side.

Lemma 2.2.1 (Young's ε inequality [105, App. A])**.**
Let $a, b \in \mathbb{R}$ and $\varepsilon \in \mathbb{R}_{>0}$, then there holds:

$$ab \leq \frac{a^2}{2\varepsilon} + \frac{\varepsilon b^2}{2} \tag{22}$$

This becomes relevant in situations where one wants to absorb e.g. the a^2 term on the right by some additional term Ca^2 on the left, where $C > 0$ is an unknown constant. In order to avoid rendering the left hand side negative, one has to choose ε large enough such that $\frac{1}{2\varepsilon} < C$. Then the term can be brought to the left hand side easily. Of course the choice of a large ε increases the b^2 term on the right hand side, which again emphasizes why only *one* term can be controlled by that approach. This fact, in combination with the common saying "*You have to rob Peter to pay Paul*" also yields the name *Peter-Paul inequality* to (22) [84].

Gronwall's lemma For the lemma of Gronwall a lot of different versions exist. Their common purpose is that they allow to derive from an implicit estimate $\varphi(t) \leq F(t, \varphi)$ of some quantity φ an explicit estimate $\varphi(t) \leq C(t)$, where F typically involves integration and C grows with time. The lemma is employed, e.g., in stability estimates for time dependent problems.

Lemma 2.2.2 (Gronwall's lemma [250, Lem. 2.2])**.**
Let $a, b \in \mathbb{R}, b > a$ and $A, B, \varphi : [a, b] \to \mathbb{R}$ where $A \in L^1(a, b)$ is non-negative, B and φ are continuous and B is non-decreasing. Then the implicit estimate

$$\varphi(t) \leq B(t) + \int_a^t A(\tau)\varphi(\tau)\ \mathrm{d}\tau, \qquad \forall t \in [a, b],$$

implies the explicit estimate

$$\varphi(t) \leq B(t) \exp\left(\int_a^t A(\tau)\ \mathrm{d}\tau\right), \qquad \forall t \in [a, b].$$

Banach's fixed point theorem Banach's fixed point theorem plays an important role in proofs dealing with *nonlinear* equations as for example the a priori error estimate in [II, IV], where it guarantees the existence of a solution to a nonlinear problem, also see for example [232, 240]. The typical procedure therein first assumes a linearized version of the nonlinear problem around a reference solution. If for example u would be the exact solution of the (nonlinear) PDE, one might choose a finite element function w_h that is, in some energy-norm $\|\cdot\|_E$, "close to u", i.e. $\|u - w_h\|_E \lesssim h^r$ for some $r > 0$, as such a reference solution. With $u_h^{(w_h)}$ being the solution of the resulting *linear* problem one finds an estimate like $\|u - u_h^{(w_h)}\|_E \lesssim h^r + \|f(u) - f(w_h)\|$. Here the later term $\|f(u) - f(w_h)\|$ contains differences from the nonlinear terms f resulting from the use of the exact solution u vs. the use of the linearization w_h. This estimate however also still depends on w_h. In order to get rid of w_h one carefully defines a **mapping $\mathcal{S}$ that maps the reference solution w_h onto $u_h^{(w_h)}$**. A fixed point of such a mapping would then constitute a finite element function z_h with $\|u - z_h\|_E = \|u - \mathcal{S}(z_h)\|_E \lesssim h^r + \|f(u) - f(z_h)\|$. From here it becomes visible that the last term involving the nonlinear terms f must be bounded somehow by Ch^r in order to carry over the error-estimate from the linear to the nonlinear model as well as to show contractivity of the mapping $\mathcal{S}$ as it is needed in Banach's fixed point theorem 2.2.1 that guarantees existence of such a fixed point.

Theorem 2.2.1 (Banach's fixed point theorem [302, Ch. IV.7])**.**
Let (X, d) be a complete metric space and let $M \subset X$ be non-empty and closed. If a mapping $\mathcal{S} : X \to X$ fulfills:

- ***Self-mapping property:*** $\mathcal{S}(M) \subset M$
- ***Contractivity:*** $d(\mathcal{S}(x), \mathcal{S}(y)) \leq L \cdot d(x, y), \qquad \forall x, y \in M \text{ with } L < 1$

*then **M contains exactly one fixed-point** x^* of $\mathcal{S}$, i.e. $\mathcal{S}(x^*) = x^*$. Furthermore the sequence $x_{n+1} := \mathcal{S}(x_n)$ with $x_0 \in M$ being arbitrary converges to x^* with:*

$$d(x_n, x^*) \leq \frac{L^n}{1 - L} d(x_1, x_0)$$

While existence of such a fixed point can then directly be guaranteed by means of Banach's fixed point theorem, the challenging task to be done is the proper definition of the set M and the mapping $\mathcal{S}$ and to proof the prerequisites necessary for the application of the fixed-point theorem, being the self-mapping property and contractivity. Such remaining estimates on the nonlinear terms $\|f(u) - f(w_h)\|$ now rely on inverse- (Lem. 3.2.1) and interpolation-estimates (Lem. 3.2.3) from classical finite element, resp. DG literature.

3. Numerical methods

Having introduced the mathematical models for acoustics and elasticity as well as some theoretical foundations for the applied methods, this section focuses on the numerical methods used to solve the resulting (systems of) PDEs.

For the spatial discretization there will be summarized results, references and tools about discontinuous Galerkin methods in Sec. 3.1, especially in connection with the spectral (element) method. Since all involved models are time-dependent, Sec. 3.2 contains an overview over Newmark-type time integration schemes that were used in this thesis with special attention to the numerical damping of higher modes. In Sec. 3.3 the elasto acoustic coupling employed in [II, III] will be discussed. Sec. 3.4 gives an overview over different applications and the internal structure of the high-performance software-framework *SPEED* that was mainly used for this thesis.

3.1. Discontinuous Galerkin spectral element method

The method used for spatial discretization in articles [II, III, IV] is the discontinuous Galerkin spectral element method (DGSEM) as discussed in [14, 214], applied to the model equations of elasticity [9, 13] and acoustics, where examples for the linear wave equation are given in [8]. The method is a combination of the classical spectral element method (SEM) [54, 53, 273] using polynomials associated with Gauss-Legendre-Lobatto (GLL) quadrature nodes on hexahedral elements as finite element basis functions and a DG approach [81, 255], in detail the symmetric interior penalty Galerkin method (SIPG) [17, 304], that allows jumps across element faces. To some extend the faces, where the DG paradigm is applied and where a conforming approach is used instead, can be chosen by the user. While it is possible to treat every element face as a DG-face, resulting in a classical, full DG scheme, the idea of DGSEM is to partition Ω into subdomains $\Omega_i, i = 1, \dots, N$, each meshed and treated in a conforming way using spectral elements, while the DG approach is only applied at the subdomain-interfaces. This hybrid approach combines advantages from both continuous and discontinuous discretizations such as the lower number of degrees of freedom in the conforming and the flexibility in meshing and local h- and p-refinement of the non-conforming approach. It further becomes especially useful in situations where a complex geometry consisting out of different materials, possibly spanning multiple length scales or having varying accuracy requirements, is considered. Prime examples for applications of DG, SEM and DGSEM can be found in seismology and the simulation of earthquakes [60, 88, 100, 193, 191, 214, 216, 305], where such methods offer an attractive alternative to e.g. finite difference schemes [195, 220, 221] and classical finite element approaches [37, Sec. 2]. In the rest of this section first some background information and definitions for the DG parts of the method are introduced working with an arbitrary elementwise polynomial basis. Second, important inequalities such as trace-, inverse- and error-estimates are summarized. Finally a short review on SEM is given, from which a specific elementwise basis and numerical quadrature rule is employed to constitute the final DGSEM scheme.

Historical development of DG-methods: Following the introductory article [116, part I, article 5] and [18, 69], the DG method can be traced back to Reed and Hill [253], with a numerical analysis of [157, 201], considering a first order, hyperbolic transport equation arising from nuclear physics. In (one of) their formulations, the weak form of the equation was already discretized using independent, elementwise degrees of freedom (DOFs) allowing for discontinuities in between. Applications also to elliptic and parabolic problems, especially involving the SIPG method, which is also applied to the second order spatial derivative part in this work, then followed [17, 26, 304]. Further developments related to DG methods include the weak incorporation of Dirichlet boundary conditions [235], a posteriori error-estimators [56, 99, 175] or shock-capturing methods and slope limiters [146, 198, 289] also known from finite volume methods. Also see [19] for a broader overview over different DG techniques.

By now DG methods have been applied to many different problems. From the aforementioned seismic applications, over waves [78, 126, 147, 227], especially also nonlinear acoustic ones [182, 287], mostly via their conservative system formulation, the shallow water equation [3] up to fluid-mechanics [118] and turbulence [31] and magneto-hydrodynamics [300].

Meshing: For the rest of this section the Westervelt equation (8) will serve as a model problem in order to formulate fundamental parts of the method. The basis of a DG (or general finite element) discretization of e.g. the model problem is formed by meshing the domain Ω, i.e. forming a non-overlapping subdivision $\mathcal{T} = \{\tau_k\}_{k=1}^N, \overline{\Omega} = \bigcup_{k=1}^N \overline{\tau_k}$, where the τ_k s can be simplices, quadrilaterals in 2D resp. hexahedra in 3D, or even general polyhedra. In contrast to a conforming mesh, hanging nodes are allowed in a DG setting. As in classical finite elements, h_τ stands for the diameter of the element τ and by $h := \max_{\tau\in\mathcal{T}} h_\tau$ one denotes the maximal element diameter present in the mesh. Further classical terms such as shape-regularity, i.e. the existence of a constant $\kappa > 0$ such that $\kappa h_\tau \leq \rho_\tau$, $\forall \tau \in \mathcal{T}$, ρ_τ being the radius of the largest inscribed ball within τ, are defined for simplicial, but also general meshes for example in [81]. It sets in relation the element diameter h_τ with the area resp. volume of the element and hence avoids degeneracy. For anisotropic elements that are e.g. very thin in only one direction [114, 115], for prismatic elements [51] or for even more general polyhedral elements, that are of interest recently, [15, 50, 52, IV] state similar conditions and results. In [II] the DG approach is only applied on subdomain interfaces, as introduced in [14]. There further mesh assumptions dealing with the comparability of the subdomain meshes are formulated.

For the rest of this chapter $\mathcal{E}$ will denote the set of all element edges (2D) resp. faces (3D) that are part of the DG approach. In case of the subdomain wise DG interface coupling, it will only contain the interface- and boundary-faces, in the full DG approach, it will contain all faces. With each face $e \in \mathcal{E}$ one associates the face normal $\underline{\boldsymbol{n}}_e$ being either the outward normal of the element on the left side of e, denoted by $\underline{\boldsymbol{n}}^+$ or the outward normal of the element on the right side of e denoted by $\underline{\boldsymbol{n}}^-$, where the choice of "left and right" is arbitrary but fixed for each face. With the face normal at hand one

then defines the mean- and jump-values of a scalar quantity ψ as:

$$\textbf{(Mean- and jump-values)} \qquad \{\!\{\psi\}\!\} = \frac{1}{2}(\psi^+ + \psi^-), \qquad [\![\psi]\!] = (\psi^+ - \psi^-)\underline{\boldsymbol{n}}_e,$$

where again ψ^+ and ψ^- stand for the values of ψ on the left resp. right hand side of the face, where on Dirichlet boundary faces the boundary value is taken instead of the "outer" evaluation. For vectorial or even tensorial quantities similar definitions can be found in [7, 9].

Variational formulation: With the non-conforming mesh $\mathcal{T}_h$ also comes a broken definition of the space $H^n(\mathcal{T}_h)$ as well as the finite element ansatz space V_h, where the index h denotes the dependency on a particular mesh with mesh-size h e.g. from a family of successively refined meshes. For the later, $\mathbb{P}^p(\tau)$ denotes the space of polynomials up to order p over the element τ and $\mathbb{Q}^p(\tau)$ the space of polynomials up to order p *per dimension* over τ, which can be set up via a tensor product.

Definition 3.1 (Broken spaces)**.** *Let $n, p \geq 1$ and $\mathbb{S}^p(\tau)$ be either $\mathbb{P}^p(\tau)$ or $\mathbb{Q}^p(\tau)$, then the broken space H^n and finite element ansatz space V_h in a full DG setting are defined as:*

$$H^n(\mathcal{T}_h) := \{\psi \in L^2(\Omega) \mid \psi|_\tau \in H^n(\tau)\ \forall \tau \in \mathcal{T}_h\}$$
$$V_h := \{\psi \in L^2(\Omega) \mid \psi|_\tau \in \mathbb{S}^p(\tau)\ \forall \tau \in \mathcal{T}_h\}$$

Again, in a subdomain-wise conforming approach with DG faces only at the interfaces, the spaces are defined differently as subdomain-wise H^1 instead of only L^2 [14, II].

Returning to the Westervelt equation (8) as a model-problem, its variational form using the SIPG is stated in the following as an example. To that extend, the DG paradigm will be employed over the whole domain, i.e. assume every element as a material subdomain and hence all element faces are assumed to be DG interfaces. For simplicity of exposition the damping factor is chosen to be $b = 0$ with homogeneous Dirichlet conditions assumed on all of $\partial\Omega$ and $f \in L^2(\Omega)$ as a right hand side force term.

Definition 3.2 (Bilinear forms and penalty)**.** *The following bilinear forms are defined, where the gradient has to be understood in a broken, elementwise, sense:*

- ***Interior bilinear form:*** $a_h : V_h \times V_h \to \mathbb{R}, a_h(\psi_h, \phi_h) := (c^2 \nabla\psi_h, \nabla\phi_h)_\Omega$
- ***Consistency term:*** $b_h : V_h \times V_h \to \mathbb{R}, b_h(\psi_h, \phi_h) := \sum_{e\in\mathcal{E}_h} \langle \{\!\{c^2\nabla\psi_h\}\!\}, [\![\phi_h]\!] \rangle_e$
- ***Symmetry term:*** $s_h : V_h \times V_h \to \mathbb{R}, s_h(\psi_h, \phi_h) := \sum_{e\in\mathcal{E}_h} \langle \{\!\{c^2\nabla\phi_h\}\!\}, [\![\psi_h]\!] \rangle_e$
- ***Penalty term:*** $p_h : V_h \times V_h \to \mathbb{R}, p_h(\psi_h, \phi_h) := \sum_{e\in\mathcal{E}_h} \langle \chi [\![\psi_h]\!], [\![\phi_h]\!] \rangle_e$

where the penalty parameter χ on the face $e \in \mathcal{E}$ is defined as $\chi|_e := \sigma \max_{\tau\in\{\tau^+,\tau^-\}} \frac{c^2p^2}{h_\tau}$ with τ^+ and τ^- being the elements left and right of the face e and σ is constant to be chosen appropriately (large).

With these definitions and $2k = \frac{2+B/A}{c^2}$ being a more compact notation for the nonlinear coefficient, the semi-discrete variational form then reads:

(Semi-discrete variational form)
Find $\psi_h \in V_h$ such that for almost all $t \in (0,T)$ and for all $\phi_h \in V_h$ there holds:

$$(\ddot{\psi}_h, \phi_h)_\Omega + a_h(\psi_h, \phi_h) - b_h(\psi_h, \phi_h) - s_h(\psi_h, \phi_h) + p_h(\psi_h, \phi_h) = \int_\Omega 2k\dot{\psi}_h\ddot{\psi}_h\phi_h \, \mathrm{d}x + (f, \phi_h)_\Omega \tag{23}$$

with initial conditions $(\psi_h(0), \dot{\psi}_h(0)) = (\psi_{0,h}, \psi_{1,h}) \in V_h \times V_h$.

Inequalities and estimates: Inverse inequalities and trace estimates are some of the main tools for the error analysis of DG methods. The main purpose of trace estimates lies in relating norms on element faces, e.g. stemming from the above introduced consistency, symmetry or penalty terms of the weak form with norms on the interior of the element, in order to arrive at a specific norm for the final error-estimate. Inverse estimates on the other hand estimate higher order Sobolev-norms of finite element functions/polynomials against lower order ones. In the following the notation $x \lesssim y$ is used standing for $x \leq Cy$ with some constant $C > 0$.

Lemma 3.2.1 (Trace and inverse estimates [81, Lem. 1.44, 1.46], [268, Thm. 4.76])**.**
Let $\tau \in \mathcal{T}_h$ and $\psi_h \in \mathbb{S}^p(\tau)$, then there holds:

Trace estimate: *i)* $\|\psi_h\|_{L^2(\partial\tau)} \lesssim \frac{1}{h_\tau^{1/2}} \|\psi_h\|_{L^2(\tau)}$,

Inverse estimates: *ii)* $|\psi_h|_{H^1(\tau)} \lesssim \frac{1}{h_\tau} \|\psi_h\|_{L^2(\tau)}$, *iii)* $\|\psi_h\|_{L^\infty(\tau)} \lesssim \frac{1}{h^{d/2}} \|\psi_h\|_{L^2(\tau)}$

where d is the spatial dimension of Ω.

Details as well as precise values for the constants - at least for simplicial elements - of the trace inequality are considered in [301], while for more general, polygonal shaped elements a variant can be found in [52].

For interpolation estimates as in Lem. 3.2.3, but using for example the DG norm (24), the trace of a non-polynomial function ψ, resp. its interpolation error $\psi - \Pi^p\psi$ has to be estimated on element faces as well. Therefore the following continuous trace estimate can be employed. Such trace inequalities are not only restricted to DG methods but can also be found for example in isogeometric analysis [102].

Lemma 3.2.2 (Continuous trace estimate [81, Lem. 1.49]). *Let $\mathcal{T}_h$ be a shape regular mesh, $\tau \in \mathcal{T}_h, e$ be a face of τ and $\psi \in H^1(\mathcal{T}_h)$, then there holds:*

$$\begin{aligned}\|\psi\|^2_{L^2(e)} &\lesssim \left(|\psi|_{H^1(\tau)} + h_\tau^{-1}\|\psi\|_{L^2(\tau)}\right)\|\psi\|_{L^2(\tau)} \\ &\lesssim h_\tau|\psi|^2_{H^1(\tau)} + h_\tau^{-1}\|\psi\|^2_{L^2(\tau)}\end{aligned}$$

Interpolation-estimates: Following the typical structure of finite element a priori error estimates a decomposition of the error $\|\psi - \psi_h\|$ of exact solution ψ and finite element solution ψ_h into an interpolation part $\|\psi - \Pi^p\psi\|$ and an approximation part $\|\Pi^p\psi - \psi_h\|$ is employed. Here Π^p is a suitable interpolation operator from $H^1(\mathcal{T}_h)$ to V_h which, in the full DG setting, can be employed element-wise. In order to control the interpolation part of the error the following interpolation estimates are needed, which can also be found in [II, Lem. 4.4] and [IV, Lem. 2].

Lemma 3.2.3 (Interpolation estimate [45, Thm. 4.4.4, 4.6.11, Cor. 4.4.7]). *Let $\mathcal{T}_h$ be a shape regular mesh, $\tau \in \mathcal{T}_h$ and $\psi \in H^n(\tau)$. Then there exists an interpolation operator $\Pi^p : H^n(\tau) \to \mathbb{S}^p(\tau)$ such that with $m := \min\{n, p+1\}$ there holds:*

$\boldsymbol{L^2}$**-estimate:**	*i)*	$\|\psi - \Pi^p\psi\|_{L^2(\tau)} \lesssim h_\tau^m\|\psi\|_{H^n(\tau)}$,	$n \geq 0$,
$\boldsymbol{H^1}$**-estimate:**	*ii)*	$\|\psi - \Pi^p\psi\|_{H^1(\tau)} \lesssim h_\tau^{m-1}\|\psi\|_{H^n(\tau)}$,	$n \geq 1$,
$\boldsymbol{L^\infty}$**-estimate:**	*iii)*	$\|\psi - \Pi^p\psi\|_{L^\infty(\tau)} \lesssim h_\tau^{m-d/2}\|\psi\|_{H^n(\tau)}$,	$n > d/2$.

The aforementioned interpolation estimate on element faces can be found for example in [81, Lem. 1.59] and again [52] states similar results in the general polygonal case. Finally [45, Lem. 4.4.1] also states a stability estimate for $\|\Pi^p\psi\|_{W^{k,p}(\tau)}$, which is then used in [II, Lem. 4.5].

Finite element error-estimates: Having available the semi-discrete form (23) of the model problem as well as the estimates and inequalities from above, a priori error-estimates can be derived. In the elliptic case of e.g. Poisson's equation, the strategy consist of showing continuity and coercivity [81] of the bilinear form $a_h(\psi_h, \phi_h) - b_h(\psi_h, \phi_h) - s_h(\psi_h, \phi_h) + p_h(\psi_h, \phi_h)$ from above w.r.t. the DG-norms:

$$\begin{aligned}\|\varphi\|^2_{\mathrm{DG}} &:= \sum_{\tau\in\mathcal{T}} |\varphi|^2_{H^1(\tau)} + \sum_{e\in\mathcal{E}} \|\sqrt{\chi}\,[\![\varphi]\!]\,\|^2_{L^2(e)} \\ |||\varphi|||^2_{\mathrm{DG}} &:= \|\varphi\|^2_{\mathrm{DG}} + \sum_{e\in\mathcal{E}} h_e\|\,\{\!\{\nabla\varphi\cdot\underline{\boldsymbol{n}}_e\}\!\}\,\|^2_{L^2(e)}\end{aligned} \tag{24}$$

For coercivity to hold true, it is required that the penalty parameter σ within the definition of χ is large enough [17, 116]. Lower bounds on σ to be actually large enough can be found in [96]. The elliptic case then proceeds by estimating the individual norm

contributions to the interpolation error-terms on the right hand side of

$$\|\psi - \psi_h\|_{\mathrm{DG}} \lesssim \inf_{\phi_h \in V_h} |||\psi - \phi_h|||_{\mathrm{DG}} \leq |||\psi - \Pi^p \psi|||_{\mathrm{DG}}$$

by means of the interpolation estimates of Lem. 3.2.3 as well as their trace-equivalents by means of Lem. 3.2.2. Finally one arrives at

$$\|\psi - \psi_h\|_{\mathrm{DG}} \lesssim h^{m-1} \|\psi\|_{H^n(\mathcal{T}_h)}, \qquad m = \min\{n, p+1\},$$

provided $\psi \in H^n(\Omega)$.

For **time dependent problems**, the approach is similar, e.g. for parabolic equations like the heat-equation [17, 256], or the (linear) scalar wave-equation [126] or elastic wave equation [15]. In order to account for the time evolution of the problem, the norm (24) used for the error-estimate is extended for example by $\|\dot{\varphi}\|^2_{L^2(\Omega)}$ to form a, now time dependent, energy-norm

$$\|\psi(t)\|^2_E := \|\dot{\psi}(t)\|^2_{L^2(\Omega)} + \|\psi(t)\|^2_{\mathrm{DG}} + \int_0^t \|\ddot{\psi}(s)\|^2_{L^2(\Omega)} \, \mathrm{d}s,$$

where the last term appears additionally in case of the Westervelt and Kuznetsov equation, see [II, (4.1)]. In that energy norm then stability- and later also error-estimates are derived, typically by testing the weak form, resp. the error equation, i.e. the difference of the variational forms with the exact and numerical solutions being inserted, with a suitable test function. Here partial integration in time and the lemma of Gronwall Lem. 2.2.2 play an important role to obtain estimates that are explicit in the energy (energy/stability-estimate) or the error (error-estimate).

Numerical analysis of nonlinear (elasto-) acoustics - Contribution of [II] and [IV]: Here the novel contribution of [II] and [IV] lies in the incorporation of the nonlinear term $\int_\Omega 2k\dot{\psi}_h\ddot{\psi}_h\phi_h \, \mathrm{d}x$, resp. its equivalent in case of the Kuznetsov equation (9) even involving gradients $\sum_{\tau\in\mathcal{T}} \int_\tau 2k'\nabla\psi_h\nabla\dot{\psi}_h\phi_h \, \mathrm{d}x$, of the variational form. The error-analysis is first conducted for a linearization around a reference solution, where the nonlinear terms, evaluated at this reference solution, are treated as additional force contributions to the right hand side. By doing so, the linear version can be analyzed with standard methods and results from literature, while the problematic nonlinear part is dealt with separately. The method of choice to extend the error-estimate to the nonlinear regime is by means of Banach's fixed point theorem (Thm. 2.2.1) and the procedure described in Sec. 2.5. The result shows that the method converges with the same order of h in the nonlinear case as in the linear one, for both Westervelt and Kuznetsov type nonlinearities, resp. a combination of both. The result holds true for elasto-acoustic interfaces in the same way as for acoustic-acoustic interfaces between subdomains of different materials.

Spectral (element) method: Even though there is of course a connection, one has to distinguish between (globally) spectral methods and spectral *element* methods SEM. The first one is mainly attributed to Orszag during the 1970's, where he used truncated series of orthogonal polynomials [237] or Fourier-series [238], i.e. globally smooth, mutual orthogonal basis functions - hence the name spectral - to represent the solution of a PDE, see also the details in the more recent text books [53, 54, 123, 273]. Originally restricted to rectangular domain shapes the method was soon extended to more general shaped domains via mappings and by coupling multiple patches [239], both being principles also used for finite element meshes. Eventually it was a logical step to combine the flexibility of finite elements concerning general domain shapes with the spectral methods advantages such as spectral convergence [54, Sec. 5.1, 5.4] as it can also be found in the very similar [80, Sec. 2.3.2, 2.4] higher-order p-FEM e.g. in [23], [268, Cor. 3.12]. With the finite element space V_h being defined in Def. 3.1, resp. its analogue for conforming finite elements, it still remains to choose an (elementwise, polynomial) basis $\{\psi_j\}_{j=1}^{p+1}$ spanning that space. A sensible choice for this basis now poses the connection to the original spectral methods, see also [312] for a detailed review of the development of the method.

In classical, conforming finite elements, Lagrange-polynomials associated with (equidistant) Lagrange interpolation nodes on each element can be chosen. Stitched together across element boundaries they yield globally continuous basisfunctions with local supports. Applying a numerical quadrature rule with sufficiently high degree of exactness to assemble mass- and stiffness matrices results in their well known sparse structure. These are properties one wishes to pass on to the spectral basis to be chosen. Starting in one dimension, a well known family of orthogonal polynomials are the Legendre polynomials $\mathcal{L}_n \in \mathbb{P}^n([-1,1]), n = 0, 1, 2, \ldots, p+1$. Their roots $(x_i)_{i=1}^n$ are known to be the Gauss-Legendre quadrature nodes yielding the highest possible degree of exactness, $2n-1$ resp. $2p+1$ for $n = p+1$, for the associated quadrature rule. However, since the nodes x_i lie strictly in the interior of $[-1,1]$, continuity across element boundaries can not be enforced, posing a problem if the DG approach is not employed between all elements but a partly conforming approach is used, see [II]. In that case the boundary points $x = -1$ and $x = 1$ are supposed to be interpolation nodes as well and a **modified (nodal) basis, based on the GLL nodes** being the roots of $(1-x^2)\mathcal{L}'_{n-1}$, is used. The associated quadrature formula yields a reduced degree of exactness of $2n-3$, resp. again $2p-1$ for $n = p+1$ [54] but the chosen basis has the desired properties from above. The resulting method is called (a version of) the nodal SEM [80, 292]. On quadrilateral/hexahedral elements a simple tensor product approach is used to obtain the GLL-grid also in more dimensions while for simplicial elements different approaches are analyzed in [243].

An important trait of the just created method, where quadrature and interpolation nodes coincide, is the fact that by choosing the Gauss-Lobatto quadrature for the numerical integration of the mass matrix, one automatically obtains a **diagonal, lumped mass matrix** with much less computational quadrature effort than with standard elements thanks to the interpolatory property of the interpolation polynomials. It has

to be noted though that due to the aforementioned reduced order of exactness of the Gauss-Lobatto-quadrature, a variational crime is committed by the numerical integration of each mass-matrix entry comprising the reference-element integral of $\hat{\psi}_h\hat{\varphi}_h$ being of degree $2p$ plus the Jacobian determinant of the element mapping. The effect on the convergence order can be analyzed using the first lemma of Strang [98, Lem. 2.27], where the order of the quadrature error enters. For parallelpiped-shaped elements the quadrature formula is still "good enough" and no order reduction is inferred, while for generally shaped elements a dependency on the dimension d enters with an order reduction for $d \geq 3$ [89, Thm 3.6., Rem. 3.3. and 3.4.], also see [210]. However, the underintegration is performed on purpose [60, Sec. 5.1] as such a diagonal mass matrix goes hand in hand with explicit time integration schemes such as the leap-frog or explicit Newmark scheme [313, 314].

Even though the invention of the SEM is now mainly associated with Maday and Patera [312, Ch. 7.3], an earlier applications of the SEM, even though not yet called like that, to a reservoir simulation can be found by Young [311]. Later applications to the acoustic waves [270, 313, 314] as well as seismic waves [190, 191, 192, 193, 222, 248], where the SEM is one of the most commonly used methods, followed. While in [II] the error analysis for the DGSEM method is only conducted w.r.t. an h-refinement assuming fixed values of p, the degree-dependency is resolved e.g. in [245] for a diffusion-problem or in [7, 10] for elastic and acoustic waves.

3.2. Newmark-type methods for time integration

After spatial discretization of any of the acoustic models (6),(8),(9) one arrives at a system of ordinary differential equations (ODEs) of the structure:

$$M\underline{\ddot{\boldsymbol{u}}} + C\underline{\dot{\boldsymbol{u}}} + K\underline{\boldsymbol{u}} + \mathcal{T}(\underline{\boldsymbol{u}}, \underline{\dot{\boldsymbol{u}}}, \underline{\ddot{\boldsymbol{u}}}) = \underline{\boldsymbol{b}} \tag{25}$$

where M, C and K are mass, damping and stiffness matrices, $\underline{\boldsymbol{b}}$ is a right hand side vector of possible external forces or Neumann data that might vary over time and space and $\mathcal{T}$ summarizes all nonlinearities present in the respective equation, see for example the model problem (23). The precise shape of $\mathcal{T}$ depends on the equation in use consisting out of up to two of the third order tensors $\mathcal{T}_1[\underline{\boldsymbol{u}}, \underline{\ddot{\boldsymbol{u}}}, \cdot], \mathcal{T}_2[\underline{\dot{\boldsymbol{u}}}, \underline{\dot{\boldsymbol{u}}}, \cdot], \mathcal{T}_3[\underline{\dot{\boldsymbol{u}}}, \underline{\ddot{\boldsymbol{u}}}, \cdot], \mathcal{T}_4[\underline{\boldsymbol{u}}, \underline{\dot{\boldsymbol{u}}}, \cdot]$ each, see for example [170, p. 165 f.], [IV, (7.1)], [V, p. 181], or even further nonlinearities entering through nonlinear ABCs such as in [I, (33)]. Dirichlet data are incorporated either via a lifting, see [I, (33)], or in a weak sense, see [IV, (7.1)], also on the right hand side. For brevity, homogeneous Dirichlet data are assumed in this section and without further notation the system (25) is considered only for interior, non-Dirichlet DOFs. Initial conditions are given for $\underline{\boldsymbol{u}}$ and $\underline{\dot{\boldsymbol{u}}}$ as usual.

In order to integrate (25) through time, different options are available. One common approach is to transform the second order in time system (25) into a first order system, e.g. by introducing the new variable $\underline{\boldsymbol{v}} := \underline{\dot{\boldsymbol{u}}}$. For first order systems a long list of time

integration methods can then be used ranging from classical Runge-Kutta methods [125, 295], over linear multistep methods [30, 174] up to symplectic methods [208, 263] making use of the Hamiltonian structure of the resulting first order system. Especially when it comes to nonlinear systems mixed methods consisting of implicit and explicit (IMEX) time stepping schemes are advantageous combining the stability of implicit methods for the linear parts and the fast evaluation of explicit ones e.g. for the evaluation of the nonlinear part [138]. Another class of methods are exponential integrators. They employ a linearization of the nonlinear equation producing a nonlinear remainder term on the right hand side. The resulting ODE system with inhomogeneity is transformed into an integral equation by means of the variation of constant principle. The resulting integral involving a matrix exponential is then solved numerically by a quadrature rule. A review of such methods can be found in [139]. Considering spatially high-order approximations with error rates $\mathcal{O}(h^p), p \geq 5$, classical Runge-Kutta methods aiming at the same order for the temporal error $\mathcal{O}(\tau^p), p \geq 5$ suffer from the Butcher-barriers resulting in a continuously growing effort to compute the necessary amount of stages to reach the respective order. Here the arbitrary derivative (ADER) methods are settled. With them the solution is expanded into a (temporal) Taylor-series around the current time-step. Then the higher-order time derivatives are expressed via spatial derivatives such that upon evaluation of the Taylor-series at the new timestep the high spatial order of the method carries over to the temporal error [178, 266]. Even though acoustic, elastic as well as further wave-type equations have distinct features and differences, they follow the same general structure. Hence, a common framework for acoustic, elastic and electromagnetic waves being discretized using the DG method in space with subsequent application of different time integration methods can be found in [140].

Alternative approaches that solve the time-dependent equations not in a separate spatio-temporal way exist as well. As an example methods that involve a combined space-time discretization are discussed in [11]. Here the time interval is divided into sub-intervals over which spatial discretization is done independently with a coupling across sub-intervals by means of DG interfaces and jump-terms. For such a space-time method also see [82].

Finally, the approach that is also used in the articles of this thesis is a predictor-corrector scheme of Newmark type with nonlinear extensions directly operating on the second order equation as proposed in [141, 170]. Generalizations to cope with Gibbs-like high frequency overshoots at steep wave-fronts typical in nonlinear acoustics are discussed as well in terms of the so called Generalized-α schemes [66].

Derivation of the Newmark scheme: The original method of Newmark [231], formulated in displacement $\underline{\boldsymbol{u}}$, velocity $\underline{\boldsymbol{v}} = \dot{\underline{\boldsymbol{u}}}$ and acceleration $\underline{\boldsymbol{a}} = \ddot{\underline{\boldsymbol{u}}}$, can be derived by **approximating $\underline{\boldsymbol{a}}$ in between timesteps** t^n and t^{n+1} either as mean-value of the respective value $\underline{\boldsymbol{a}}^n$ and $\underline{\boldsymbol{a}}^{n+1}$, their linear interpolation or for example a centered step function. Each of these choices leads to a different parameter value β in the resulting scheme below. In any case, $\underline{\boldsymbol{a}}^{n+1}$ is treated as an unknown, while all values are assumed to be known at the old timestep t^n. The value of $\underline{\boldsymbol{v}}^{n+1}$ is then obtained

via a **numerical integration of $\underline{\boldsymbol{a}}$**, where the parameter γ enters as a weighting factor for the quadrature weights. The quadrature is repeated to obtain $\underline{\boldsymbol{u}}^{n+1}$ from the numerical integration of $\underline{\boldsymbol{v}}$ where the second parameter β enters. One obtains the relations (26), (27), where $\underline{\boldsymbol{a}}^{n+1}$ is still unknown. To compute it, the original ODE (25) is evaluated at the new timestep t^{n+1} with the predicted values $\underline{\boldsymbol{u}}_{\text{pred}}$ and $\underline{\boldsymbol{v}}_{\text{pred}}$ being inserted. This yields the (nonlinear) system (28) that remains to be solved for example via a fixed-point iteration using $\underline{\boldsymbol{a}}^n$ and the predictions for $\underline{\boldsymbol{u}}$ and $\underline{\boldsymbol{v}}$ as initial values. One then iterates, with iteration index κ, the solution of the linear system $M^*\underline{\boldsymbol{a}}^{n+1,\kappa+1} = \underline{\boldsymbol{b}}^{n+1} - \mathcal{T}(\underline{\boldsymbol{u}}^{n+1,\kappa}, \underline{\boldsymbol{v}}^{n+1,\kappa}, \underline{\boldsymbol{a}}^{n+1,\kappa}) - C\underline{\boldsymbol{v}}_{\text{pred}} - K\underline{\boldsymbol{u}}_{\text{pred}}$ and the correction steps in (26),(27) until a sufficient termination criterion is met before advancing to the next time step. M^* is called the effective mass matrix. Details about the algorithm can be found in [141] as well as, for its generalized-α form, in [V, Alg. 1] and [IV, Sec. 7.1].

Newmark-relations

Predictor Corrector scheme with initial predictions for $\underline{\boldsymbol{u}}$, $\underline{\boldsymbol{v}}$, then alternating solution of the linear system and correction using its solution $\underline{\boldsymbol{a}}^{n+1}$. γ and β are the Newmark methods parameters with classical choices $\gamma = \frac{1}{2}$, $\beta = \frac{1}{4}$.

Prediction and Correction equations

$$\underline{\boldsymbol{v}}^{n+1} = \underline{\boldsymbol{v}}^n + \Delta t(1-\gamma)\underline{\boldsymbol{a}}^n + \Delta t\gamma\underline{\boldsymbol{a}}^{n+1} \qquad =: \underline{\boldsymbol{v}}_{\text{pred}} + \Delta t\gamma\underline{\boldsymbol{a}}^{n+1} \tag{26}$$

$$\underline{\boldsymbol{u}}^{n+1} = \underline{\boldsymbol{u}}^n + \Delta t\underline{\boldsymbol{v}}^n + \frac{\Delta t^2}{2}(1-2\beta)\underline{\boldsymbol{a}}^n + \frac{\Delta t^2}{2}2\beta\underline{\boldsymbol{a}}^{n+1} =: \underline{\boldsymbol{u}}_{\text{pred}} + \frac{\Delta t^2}{2}2\beta\underline{\boldsymbol{a}}^{n+1} \tag{27}$$

Algebraic system

$$M^*\underline{\boldsymbol{a}}^{n+1} + C\underline{\boldsymbol{v}}_{\text{pred}} + K\underline{\boldsymbol{u}}_{\text{pred}} = \underline{\boldsymbol{b}}^{n+1} - \mathcal{T}(\underline{\boldsymbol{u}}^{n+1}, \underline{\boldsymbol{v}}^{n+1}, \underline{\boldsymbol{a}}^{n+1}) \tag{28}$$

The matrix M^* is given by $M^* = M + \gamma\Delta tC + \beta\Delta t^2K$

For the special choice of parameters $\gamma = \frac{1}{2}$ and $\beta = 0$ the method becomes the Störmer-Verlet, resp. Leapfrog method (with full timestep size) [128, Ch. I.1.4]. In that sense, the Newmark algorithm is a generalization of those methods which, for $\beta > 0$ adds an implicit component also to the $\underline{\boldsymbol{u}}$-update (27). It should be noted that also *explicit* versions of the Newmark-scheme exist as in [121] or [148, 149], where the ODE is evaluated at the new (unknown) timestep t^{n+1} only for the acceleration $\underline{\boldsymbol{a}}^{n+1}$ while for $\underline{\boldsymbol{u}}$ and $\underline{\boldsymbol{v}}$ the predicted values are inserted. This results in an algorithm where instead of the effective mass matrix M^* only the original mass matrix M appears in the algebraic system to be solved. Especially for spectral elements, see Sec. 3.1, where M is diagonal this yields a fast, explicit algorithm, however, in the general case of $C \neq 0$ with only a first order convergence [148] compared to the, see below, order $p = 2$ of the implicit, "original" Newmark-method. In [211, 314] further versions of the Newmark scheme are discussed and compared in the context of acoustic waves, in [315] for elastic ones.

Consistency and stability: The presence of the parameters γ and β in the Newmark scheme yield the questions, for which values of them is the resulting scheme stable and convergent with which order? In the linear case the question has been addressed in [124] by means of a modal decomposition and in [62, 121] by deriving a recursion relation for the Newmark scheme, i.e. formulating it as a linear two-step method, then using stability criteria from the theory of such. As a result, one obtains the following general conditions [149].

Consistency: If $\gamma = \frac{1}{2}$, the method is consistent of order $p = 2$, otherwise at least of order $p = 1$. In the absence of damping, i.e. $C = 0$ in (25), the additional choice of $\beta = \frac{1}{12}$ then even leads to order $p = 4$ consistency [121].

Stability: If $\gamma \geq \frac{1}{2}$, hence especially in the second order case, stability is unconditional, provided $\beta \geq \frac{\gamma}{2}$, as it is the case for the classical choice of parameters. For values $\beta < \frac{\gamma}{2}$ conditional stability is given, restricting the time stepsize w.r.t. the maximal present frequency of the oscillation, again see [149].

An increase of the parameter γ beyond the value of $\frac{1}{2}$ introduces artificial damping to the system. Especially in the context of nonlinear waves such behavior is favored since the additional damping helps to cope with the aforementioned high-frequency overshoots. For a given value of $\gamma > \frac{1}{2}$ the choice of $\beta = \frac{1}{4}(\gamma + \frac{1}{2})^2$ yields an optimal damping behavior [148]. However, recalling the above consistency condition on γ the higher-mode damping comes for the price of a reduction to an order $p = 1$ method. In addition, damping is not only confined to the high frequency range but also affects the remaining spectrum ultimately preventing oscillations. A method that allows to apply the additional damping ideally only on those high frequency components while not, or at least less, affects the low frequency band, would be the searched for remedy. Generalized-α methods as employed in the articles of this thesis accomplish exactly that.

Generalized-α-schemes: The need for a method with the just mentioned damping, accuracy but also stability properties led to the development of a multitude of methods very similar to the Newmark method e.g. the Hilber-Hughes-Taylor HHT-α [137] or Wood-Bossak-Zienkiewicz WBZ-α method [307]. The idea of these two consists of evaluating the ODE (25) at the new timestep $t^{(n+1)}$ as in the Newmark method, but instead of $\underline{\boldsymbol{u}}^{(n+1)}$ a linear combination of $(1+\alpha)\underline{\boldsymbol{u}}^{(n+1)} - \alpha\underline{\boldsymbol{u}}^{(n)}$ (HHT-α) and similar with $\underline{\ddot{\boldsymbol{u}}}$ (WBZ-α) is used, shifting the purely implicit equation a bit more to the explicit side. Chung and Hulbert [66] then combined these two methods into a mathematical framework with two additional parameters α_m and α_f consituting the generalized-α method. Indeed for specific choices of α_m and α_f the Newmark method or any of the other two mentioned schemes can be recovered. The derived scheme is consistent of second order for $\gamma = \frac{1}{2} - \alpha_m + \alpha_f$ and unconditionally stable for $\alpha_m \leq \alpha_f \leq \frac{1}{2}, \beta \geq \frac{1}{4} + \frac{1}{2}(\alpha_f - \alpha_m)$. This allows to increase γ beyond $\frac{1}{2}$ without losing second order accuracy as it was the case with the standard Newmark scheme. Further more in [66] it is also shown that the parameters α_f and α_m can be expressed by one single free parameter $\rho_\infty \in [0, 1]$, which represents the **numerical high-frequency damping** of the method with no numerical damping at all ($\rho_\infty = 1$) vs. immediate annihilation in only one timestep ($\rho_\infty = 0$).

The algorithm parameters and conditions are compared between the generalized-α and its predecessor methods in [97, Tab. 1-3], where the high-frequency damping capability of the method as well as its consistency order have also been analyzed for certain nonlinearities, see also [43].

Generalized-α methods have already been applied to (nonlinear) wave problems e.g. in solid mechanics [44, 85, 150] and nonlinear (vibro) acoustics [258, 298] e.g. in aircraft simulations [271]. There are also versions of the method extended to first order systems by employing the idea of linear combinations between new and old timesteps in a similar way with order and stability conditions also carrying over from second to first order [154]. Exemplary applications are in fluid-mechanics [154] or to phase-field models [122]. Just recently also a 3$^{\text{rd}}$ order version of the method was derived in [33], with even higher order versions for different types of equations following [32, 34, 35]. The precise way how the generalized-α method is used to resolve the steep wave fronts of the nonlinear acoustic models in this thesis can be found in [IV, Sec. 7.2], [V, Alg. 1].

3.3. Elasto-acoustic coupling

In the simulation of complex (mechanical) systems different materials, each with its own physics and modeling-equations, interact with each other. Formerly individual fields such as displacement, pressure or temperature now exhibit dependencies, which need to be captured by appropriate coupling mechanisms. One distinguishes between the coupling of variables once on the same domain Ω, such as acoustic potential and temperature in [257, 277] or a flow equation such as the Navier-Stokes system and a convection-diffusion concentration/heat equation in fluid mechanics [79, 172, 223] influencing each other on the whole volume of Ω; and second the coupling of different (material) regions over an interface, as it is classically done for example in fluid-structure interaction [107, 261]. Also for the coupling of an elastic to an acoustic material the later, interface-based approach is commonly used as the materials are usually separated. In the presented examples the elastic materials are a solid ultrasound excitator, a portion of human tissue, the earth's ground or a building structure, while the acoustic material is most often a fluid such as water or air. In the elastic and acoustic linear case the problem is treated for example in [7, 106] with further, more elaborated simulation results in [8], where the key concept to transport information from one material domain to the other is an exchange via interface conditions. The conditions are chosen in such a way that **continuity of (particle) velocity and normal stresses** is given across the interface. In that sense the interface conditions avoid the penetration of one material into the other and hence keep the interface intact. Making use of the definition of the acoustic potential ψ (5) relating it to pressure p and particle velocity v, these conditions, without damping, read:

$$\textbf{(Interface conditions)} \qquad \sigma(\underline{\boldsymbol{u}}) \cdot \underline{\boldsymbol{n}} = -\rho\dot{\psi}\underline{\boldsymbol{n}}, \qquad \nabla\psi \cdot \underline{\boldsymbol{n}} = -\dot{\underline{\boldsymbol{u}}} \cdot \underline{\boldsymbol{n}}$$

where the first one can be identified as a Neumann-condition on the solid displacement field $\underline{\boldsymbol{u}}$ for equation (19), the second one in reverse is a Neumann-condition for the acous-

tic wave equation in ψ. While the interface conditions can be kept the same also in the presence of the nonlinear terms of e.g. Westervelt's or Kuznetsov's equation, for the incorporation of the additional damping term $b\Delta\dot{\psi}$, see (8), (9), the conditions have been extended in [II]. Similar interface conditions that have been extended even more to also incorporate nonlinear contributions can be found in [298] with the presented conditions as a linear approximation.

For the solution process of the coupled system with its mutually dependent coupling conditions, a staggered time integration approach is well suited. Time integration schemes of the Newmark family for the acoustic part discussed in Sec. 3.2 are of predictor-corrector type. Combining them also with such a scheme for the elastic part, as for example the leapfrog scheme allows for a sequential solution process where the interface conditions for the first variable can be evaluated from the predicted values of the other allowing for an explicit time integration approach. Wrapping the solution process into an outer fixed point iteration loop as well as local time-stepping for only one of the two variables [277, III] are further options, easy to realize. Noting, that *SPEED* already contained routines dealing with e.g. interface quadratures coming from the coupling of elastic-elastic interfaces between non-matching grids [14, 214], the incorporation of the elasto-acoustic interface via boundary-conditions is straight forward for non-matching interfaces as well. Alternative approaches using Lagrange-multipliers for the interface coupling can be found in [106, 203].

Transducer-Fluid-Tissue simulation - Contribution of [II] part 2: From a modeling and applicational point of view the simulations conducted in [II] are of interest as they contain the whole propagation process of a focused ultrasound wave. Starting with the curved transducer mechanical impulses are applied to excite an elastic wave. Then the first elasto-acoustic interface transmits that wave into an ultrasound wave-guide where it propagates according to the nonlinear acoustic models showing the typical effects such as wave-steepening. Finally the wave enters a portion of human tissue for which different, elastic and acoustic models are used. In that way, the conducted numerical examples pose a further step in the simulation of medical ESWL, as it was one of the first motivations for this thesis.

3.4. Seismic simulations in *SPEED*

The software framework *SPEED* is mainly developed at the MOX laboratory for Modeling and Scientific Computing at Politecnico di Milano in Italy, with strong influence from the older software *GeoELSE* [282, 283]. The acronym *SPEED* stands for ***SP****ectral* ***E****lements in* ***E****lastodynamics with* ***D****iscontinuous Galerkin*, which shows its original scope being in the simulation of (purely) elastic problems by means of the DGSEM approach [14]. This of course changed over time with *SPEED* now being able to handle also the nonlinear acoustic equations discussed in this thesis [IV] and coupled elasto-acoustic problems [7, II].

Features and application scenarios: The main area of application for *SPEED* lies for sure in the simulation of seismological scenarios. Studies conducted so far encompass ground-only cases, however with a complex sub-soil layer structure, e.g. in the Netherlands [242], in combination with a seismic risk assessment in China [13] or a topography-including case in Italy [101]. However, also ground-structure interactions were considered for example in [180, 209, 214, 216] for China, New Zealand and again Italy. Also for a different region of Turkey than in [III] a study was already conducted with it [153]. In that sense, the case study of the Tahtalı dam in [III] queues up in a long range of other scenarios on which validation of the *SPEED* code was repeatedly performed. It brings together the new elasto-acoustic coupling features by considering the full 3D interaction of the dam with the reservoir-lake behind it, the dam as a more complex fully resolved building structure as well as its embedding into a real topography. Making use of the rich set of available real-life data in the presented scenario makes the article [III] a good showcase of *SPEED*'s capabilities in terms of **large, complex simulations involving real data**. The DG approach is utilized in [III] to great extend in a full source-to-site simulation including the seismic fault model from Sec. 2.3 on a kilometer scale as well as the, comparably much smaller scaled, dam. The multiscale nature of the problem is resolved by locally refined sub-meshes (h- and p-variability) that are coupled using DG interfaces as in [216, II, IV].

The output data of the simulation are of importance from a seismological and engineering perspective especially concerning *peak values* of displacement, velocity and acceleration [58, 92, 309]. Those values, presented e.g. in peak-ground maps such as in [III], are crucial for the assessment of seismic risks. Other quantities of interest might be the deformation, (maximum) displacement or frequency and spectral responses spectra (of a building) or stress and elastic pressure values, all being extractable from the numerical simulations [104]. Building structures for example might be designed to resist ground motions up to a certain percentage of the earth's acceleration $g \approx 9.81 \frac{\mathrm{m}}{\mathrm{s}^2}$ before taking damage or even collapsing [13, 93]. Often, the buildings themselves are simulated using single- or multi-degree of freedom spring and damper models [93, 196], but also finite difference and finite element models are used [180, 215], especially for large, non-filigree buildings such as dams [176, 299], also under consideration of the dam-reservoir interaction [6, 117].

Seismic dam simulation - Contribution of [III]: The case study performed in [III] provides a detailed numerical study of the considered seismic event. The large scale simulation containing the actual seismic fault, modeled with the equations from Sec. 2.4, as well as the analyzed building structure does not depend on additional assumptions on the wave excitation such as a single backtraced seismogram measurement which, however, is also used for a comparison. The whole simulation workflow is contained in one large, coupled multi-scale model, incorporating specific site effects such as the material properties of soil layers, topographic information, the dam geometry as well as the influence of the reservoir lake. The simulation is validated by comparison of the numerical data with actual seismogram readings at several locations, see [III, Fig. 8]. Altogether,

the simulation capabilities created and shown in this work offer a robust, accurate and computationally efficient numerical model for the assessment of the seismic response of dam structures, involving various physical aspects. Due to its mathematical generality, in the future, it can also be employed at different locations for different scenarios.

Based on the simulation results such as peak values of quantities of interest and statistical consideration concerning the probabilities of occurrence of certain (magnitude) events [142, 262], it is also of interest to conduct projections of other possible scenarios that might happen. This ultimately leads to the field of seismic hazard analysis [71, 153, 281, 296], which also poses a possible further field of research after completion of this thesis.

Internal, (parallel) structure of SPEED: The core of *SPEED* is written in (procedural) FORTRAN and designed for parallelization using MPI (OpenMPI [111]) from top to bottom. *SPEED* follows a domain decomposition approach by dividing the mesh input using METIS [177] among the specified number of MPI ranks by partitioning the element-based graph using an edge-cut minimization, which allows to keep the communication volume between the different ranks low. The mesh itself can be generated by an arbitrary third party software such as for example Cubit [40] with standard export capabilities to e.g. EXODUS files, which are then suitably converted. In order to use the tensor-product structure of spectral elements in *SPEED*, hexahedral elements are required. The creation of such hexahedral meshes can be challenging for complex geometries such as in [III]. It can be suitably achieved by a semi-automatic pave-and-sweep approach [38, 39, 218] with details for the presented case being given in [III].

All steps involved in time integration, from the initial assembly of matrices, setup of initial conditions, prediction, correction, evaluation of boundary conditions up to the diagonal solver (e.g. in case of a diagonal matrix to be inverted) are executed on each rank in parallel with the necessary information exchange across the rank's mesh-portion's boundaries in between. For solver tasks that go beyond a diagonal-divide, e.g. for non-diagonal matrices as they appear in the Newmark-method once the matrix to be inverted also contains the stiffness matrix, an interface to PETSc [27, 28, 29] is available in order to use the huge variety of (iterative) solvers provided by it.

Independently from the domain decomposition, *SPEED* allows to define material subdomains also called *blocks*. Of course a natural choice for such blocks are indeed different material components like soil layers of different mechanical properties or different fluid regions. However, this structure can also be exploited to facilitate locally h- and/or p-refined grids as the meshes of these sub-blocks do not have to coincide at their interfaces thanks to the discontinuous Galerkin approach [14, 214]. Finally the graphical output of *SPEED* can conveniently be based on those material blocks as well by generating VTK [267] files with the desired data for each of the blocks individually, which can then be read and displayed using Paraview [21] also individually allowing to "switch on and off" individual material components of the solution for inspection.

SPEED is by far not the only high performance computing (HPC)-oriented software used for seismic simulations. While *SPEED* has historically grown mainly from physical and engineering applications such as different source and soil models and coupling (now also elasto-acoustic) methods, the software package EDGE incorporates techniques such as *fused simulations* running multiple inputs at the same time [47, 49]. The realization of such is not only interesting from a computer science point of view but yields also a desired feature for the aforementioned seismic risk analysis where multiple scenarios with different sources need to be computed. EDGE as also SeisSol [46, 48] uses an ADER-DG method for time integration, also see the paper series [86, 87, 178, 179, 249]. In seismic simulations also the finite difference method is still widely used, e.g. in the SW4- (Seismic Waves, 4th order) [215, 246] or FLAC3D-code [241]. In the light of advances in graphics processing unit (GPU) computing, [76, 189] consider the seismic wave problem with GPU-bases implementations using finite differences resp. spectral elements. Finally [151] gives a review over the development of different methods, problems and applications.

4. Summary of results and outlook

The articles contributed deal with different topics of nonlinear acoustics and seismology ranging from a heuristic, methodological side in the derivation of the ABCs in [I], over the numerical analysis of its model equations in [II, IV] up to an application, coupled with optimization methods in [V] and an extensive, real-data driven computational model and simulation case-study in [III]. The articles contain novel contributions in these fields but also open new research questions and possibilities for future work. Closing the circle to the originally asked scientific questions from Sec. 1.2 a short summary of results and outlook to further questions will be given.

Beginning with [I] the ABCs derived therein for the Westervelt equation outperform classical conditions by far, depending on the linearization strategy used in the derivation. Taking into account the angle of incidence is also of great importance for the quality of the conditions. Therefore the introduced adaptive algorithm for the angle computation provides an efficient, easy to use and implement option, where no a-priori knowledge about possible angles is necessary. Future work on absorbing boundary conditions might involve their derivation for even higher orders, see e.g. [275], also for different model equations, as well as their efficient implementation considering the higher order derivatives that come with them. Similar, the derivation of the shortly mentioned PMLs for more advanced nonlinear acoustics models is as well of interest in order to effectively truncate computational domains.

In [IV] the purely acoustic problem, then in [II], with similar methods, the coupled elasto-acoustic problem was discretized using the DGSEM approach. The model considers interfaces between elastic and acoustic materials as well as acoustic-acoustic interfaces with jumps in the acoustic material parameters. This allows for multi-material simulations such as the medically interesting, elaborated model example of an elastic ultrasound transducer, an acoustic wave-guide and a portion of human tissue, where for the later one different material models were compared. Using a linearization around a

reference solution and a fixed-point argument, it was proven that the method converges with the same order as in the linear case also for nonlinear acoustic models of Westervelt and Kuznetsov type in the presence of elasto-acoustic and acoustic-acoustic interfaces between different materials. Numerous, also computationally more intensive, numerical experiments were performed to show the theoretically derived error-rates and to place the considered model into the applicational context. That context being medical ESWL therapy also links the works with [V], where the shape optimization of such an acoustic focusing device was conducted, increasing precision of an acoustic focusing lens. Due to the need for high resolution approximations a lot of attention can be payed to the respective simulations with lens or transducer focusing as well as different model equations in the future, also from a computational perspective applying methods from high performance computing. Also a further development of combined models and simulations for example a thermo-(elasto)-acoustic one considering the effect of heat generated by the focused ultrasound e.g. on tissue or a tumor might contribute to patient-specific treatment [127, 257]. From a mathematical perspective the field of nonlinear acoustic models yields a variety of possible works concerning well-posedness but also numerical analysis of e.g. the higher (than two) order models [165, 169, 233].

Finally [III] brought the elasto-acoustic framework and implementation into the field of seismology. It combines the DGSEM method with source models for earthquakes and ultimately constitutes a multi-scale numerical model for the simulation of the seismic response of dam-structures during earthquakes. The simulations conducted use real data for the computational model as well as measurements from an actual seismic even for validation. The work can be summarized as a realistic simulation case study yielding a better understanding and additional evidence for the considered seismic event as well as constituting a general numerical tool for seismic analyses with possible usage in various other events and locations in the future. With such simulation capabilities at hand, further studies could implement more advanced sediment or solid models involving e.g. plastic deformations into the source to site setting, the use of a dynamic rupture model or lead into the (see Sec. 3.4) direction of physics based seismic hazard analyses encompassing statistical data and methods.

Acronyms

ABC absorbing boundary condition . . . 3

ADER arbitrary derivative . . . 31

CFL Courant-Friedrichs-Lewy . . . 19

DG discontinuous Galerkin . . . 4

DGSEM discontinuous Galerkin spectral element method . . . 23

DOF degree of freedom . . . 24

EM Engquist and Majda . . . 12

ESWL extracorporeal shockwave lithotripsy . . . 1

GLL Gauss-Legendre-Lobatto . . . 23

GPU graphics processing unit . . . 38

HIFU high-intensity focused ultrasound . . . 2

HPC high performance computing . . . 38

IMEX implicit and explicit . . . 31

ODE ordinary differential equation . . . 30

PDE partial differential equation . . . 2

PDO partial differential operator . . . 12

PML perfectly matched layer . . . 7

PSDO pseudo differential operator . . . 11

SEM spectral element method . . . 23

SIPG symmetric interior penalty Galerkin method . . . 23

Bibliography

[1] AFAD, Seismographic measurement station records. Weblink: https://tadas.afad.gov.tr/event-detail/11995, Retrieval date 01.06.2021.

[2] H. Agurto-Detzel, M. Bianchi, M. Assumpção, M. Schimmel, B. Collaço, C. Ciardelli, J. R. Barbosa, and J. Calhau. "The tailings dam failure of 5 November 2015 in SE Brazil and its preceding seismic sequence". Geophysical Research Letters 43.10 (2016), pp. 4929–4936. DOI: 10.1002/2016GL069257.

[3] V. Aizinger and C. Dawson. "A discontinuous Galerkin method for two-dimensional flow and transport in shallow water". Advances in Water Resources 25.1 (2002), pp. 67–84. DOI: 10.1016/S0309-1708(01)00019-7.

[4] K. Aki. "Generation and Propagation of G Waves from the Niigata Earthquake of June 16, 1964.: Part 2. Estimation of earthquake moment, released energy, and stress-strain drop from the G wave spectrum". Bulletin of the Earthquake Research Institute, University of Tokyo 44.1 (1966), pp. 73–88. DOI: 10.15083/0000033586.

[5] K. Aki and P. G. Richards. Quantitative seismology. University Science Books, 2002. ISBN: 9781891389634.

[6] M. Akköse, S. Adanur, A. Bayraktar, and A. A. Dumanoğlu. "Elasto-plastic earthquake response of arch dams including fluid–structure interaction by the Lagrangian approach". Applied Mathematical Modelling 32.11 (2008), pp. 2396–2412. DOI: 10.1016/j.apm.2007.09.014.

[7] P. F. Antonietti, F. Bonaldi, and I. Mazzieri. "A high-order discontinuous Galerkin approach to the elasto-acoustic problem". Computer Methods in Applied Mechanics and Engineering 358 (2020), p. 112634. DOI: 10.1016/j.cma.2019.112634.

[8] P. F. Antonietti, F. Bonaldi, and I. Mazzieri. "Simulation of three-dimensional elastoacoustic wave propagation based on a discontinuous Galerkin spectral element method". International Journal for Numerical Methods in Engineering 121.10 (2020), pp. 2206–2226. DOI: 10.1002/nme.6305.

[9] P. F. Antonietti, A. Ferroni, I. Mazzieri, R. Paolucci, A. Quarteroni, C. Smerzini, and M. Stupazzini. "Numerical modeling of seismic waves by discontinuous spectral element methods". ESAIM: Proceedings and Surveys 61 (2018), pp. 1–37. DOI: 10.1051/proc/201861001.

[10] P. F. Antonietti, A. Ferroni, I. Mazzieri, and A. Quarteroni. "hp-version discontinuous Galerkin approximations of the elastodynamics equation". Spectral and High Order Methods for Partial Differential Equations ICOSAHOM 2016. Springer, 2017, pp. 3–19. ISBN: 9783319658704. DOI: 10.1007/978-3-319-65870-4_1.

[11] P. F. Antonietti, I. Mazzieri, and F. Migliorini. "A discontinuous Galerkin time integration scheme for second order differential equations with applications to seismic wave propagation problems" (2021). https://mox.polimi.it/publication-results/?id=934&tipo=add_qmox.

[12] P. F. Antonietti, I. Mazzieri, M. Muhr, V. Nikolić, and B. Wohlmuth. "A high-order discontinuous Galerkin method for nonlinear sound waves". Journal of Computational Physics 415 (2020), p. 109484. DOI: 10.1016/j.jcp.2020.109484.

[13] P. F. Antonietti, I. Mazzieri, L. Melas, R. Paolucci, A. Quarteroni, C. Smerzini, and M. Stupazzini. "Three-dimensional physics-based earthquake ground motion simulations for seismic risk assessment in densely populated urban areas". Mathematics In Engineering 3.2 (2021). DOI: 10.3934/mine.2021012.

[14] P. F. Antonietti, I. Mazzieri, A. Quarteroni, and F. Rapetti. "Non-conforming high order approximations of the elastodynamics equation". Computer Methods in Applied Mechanics and Engineering 209 (2012), pp. 212–238. DOI: 10.1016/j.cma.2011.11.004.

[15] P. Antonietti and I. Mazzieri. "High-order discontinuous Galerkin methods for the elastodynamics equation on polygonal and polyhedral meshes". Computer Methods in Applied Mechanics and Engineering 342 (2018), pp. 414–437. DOI: 10.1016/j.cma.2018.08.012.

[16] D. Appelö and G. Kreiss. "Application of a perfectly matched layer to the nonlinear wave equation". Wave Motion 44.7-8 (2007), pp. 531–548. DOI: 10.1016/j.wavemoti.2007.01.004.

[17] D. N. Arnold. "An interior penalty finite element method with discontinuous elements". SIAM Journal on Numerical Analysis 19.4 (1982), pp. 742–760. DOI: 10.1137/0719052.

[18] D. N. Arnold, F. Brezzi, B. Cockburn, and D. Marini. "Discontinuous Galerkin methods for elliptic problems". Discontinuous Galerkin Methods. Springer, 2000, pp. 89–101. ISBN: 9783642597213. DOI: 10.1007/978-3-642-59721-3_5.

[19] D. N. Arnold, F. Brezzi, B. Cockburn, and L. D. Marini. "Unified analysis of discontinuous Galerkin methods for elliptic problems". SIAM Journal on Numerical Analysis 39.5 (2002), pp. 1749–1779. DOI: 10.1137/S0036142901384162.

[20] R. A. Artino and J. Barros–Neto. "The Factorization of Hypoelliptic Pseudodifferential Operators". Indiana University Mathematics Journal 42.4 (1993), pp. 1101–1120. DOI: 10.1512/iumj.1993.42.42051.

[21] U. Ayachit. The paraview guide: a parallel visualization application. Kitware, Inc., 2015. ISBN: 9781930934306.

[22] E. Azadi. "Cauchy Tetrahedron Argument and the Proofs of the Existence of Stress Tensor, a Comprehensive Review, Challenges, and Improvements" (2017). arXiv: 1706.08518 [physics.hist-ph].

[23] I. Babuska, B. A. Szabo, and I. N. Katz. "The p-version of the finite element method". SIAM Journal on Numerical Analysis 18.3 (1981), pp. 515–545. DOI: 10.1137/0718033.

[24] G. Backus and M. Mulcahy. "Moment tensors and other phenomenological descriptions of seismic sources—I. Continuous displacements". Geophysical Journal International 46.2 (1976), pp. 341–361. DOI: 10.1111/j.1365-246X.1976.tb04162.x.

[25] J. Badal, M. Vazquez-Prada, and Á. González. "Preliminary quantitative assessment of earthquake casualties and damages". Natural Hazards 34.3 (2005), pp. 353–374. DOI: 10.1007/s11069-004-3656-6.

[26] G. A. Baker. "Finite element methods for elliptic equations using nonconforming elements". Mathematics of Computation 31.137 (1977), pp. 45–59. DOI: 10.1090/S0025-5718-1977-0431742-5.

[27] S. Balay, W. D. Gropp, L. C. McInnes, and B. F. Smith. "Efficient Management of Parallelism in Object Oriented Numerical Software Libraries". Modern Software Tools in Scientific Computing. Ed. by E. Arge, A. M. Bruaset, and H. P. Langtangen. Birkhäuser Boston, 1997, pp. 163–202. DOI: 10.1007/978-1-4612-1986-6_8.

[28] S. Balay et al. PETSc Users Manual. Tech. rep. ANL-95/11 - Revision 3.15. Argonne National Laboratory, 2021.

[29] S. Balay et al. PETSc Web page. https://www.mcs.anl.gov/petsc. 2021.

[30] L. Banjai and D. Peterseim. "Parallel multistep methods for linear evolution problems". IMA Journal of Numerical Analysis 32.3 (2012), pp. 1217–1240. DOI: 10.1093/imanum/drq040.

[31] F. Bassi, A. Crivellini, S. Rebay, and M. Savini. "Discontinuous Galerkin solution of the Reynolds-averaged Navier–Stokes and k–ω turbulence model equations". Computers & Fluids 34.4-5 (2005), pp. 507–540. DOI: 10.1016/j.compfluid.2003.08.004.

[32] P. Behnoudfar, Q. Deng, and V. M. Calo. "Higher-order generalized-α methods for hyperbolic problems". Computer Methods in Applied Mechanics and Engineering 378 (2021), p. 113725. DOI: 10.1016/j.cma.2021.113725.

[33] P. Behnoudfar, Q. Deng, and V. M. Calo. "High-order generalized-alpha method". Applications in Engineering Science 4 (2020), p. 100021. ISSN: 2666-4968. DOI: 10.1016/j.apples.2020.100021.

[34] P. Behnoudfar, Q. Deng, and V. M. Calo. "Higher-order generalized-α methods for parabolic problems" (2021). arXiv: 2102.05910 [math.NA].

[35] P. Behnoudfar, G. Loli, A. Reali, G. Sangalli, and V. M. Calo. "Explicit high-order generalized-α methods for isogeometric analysis of structural dynamics" (2021). arXiv: 2102.11536 [math.NA].

[36] J.-P. Berenger. "A perfectly matched layer for the absorption of electromagnetic waves". Journal of computational physics 114.2 (1994), pp. 185–200. DOI: 10.1006/jcph.1994.1159.

[37] J. Bielak, O. Ghattas, and E. Kim. "Parallel octree-based finite element method for large-scale earthquake ground motion simulation". Computer Modeling in Engineering and Sciences 10.2 (2005), p. 99. DOI: 10.3970/cmes.2005.010.099.

[38] T. D. Blacker and M. B. Stephenson. "Paving: A new approach to automated quadrilateral mesh generation". International journal for numerical methods in engineering 32.4 (1991), pp. 811–847. DOI: 10.1002/nme.1620320410.

[39] T. D. Blacker, M. B. Stephenson, and S. Canann. "Analysis automation with paving: a new quadrilateral meshing technique". Advances in engineering software and workstations 13.5-6 (1991), pp. 332–337. DOI: 10.1016/0961-3552(91)90037-5.

[40] T. D. Blacker et al. "CUBIT Geometry and Mesh Generation Toolkit 15.2 User Documentation" (May 2016). DOI: 10.2172/1457612. URL: https://www.osti.gov/biblio/1457612.

[41] D. T. Blackstock. Approximate equations governing finite-amplitude sound in thermoviscous fluids. Tech. rep. General Dynamics/Electronics Rochester NY, 1963. URL: https://apps.dtic.mil/sti/citations/AD0415442.

[42] T. Bohlen, M. R. Fernandez, J. Ernesti, C. Rheinbay, A. Rieder, and C. Wieners. "Visco-acoustic full waveform inversion: From a DG forward solver to a Newton-CG inverse solver". Computers & Mathematics with Applications 100 (2021), pp. 126–140. DOI: 10.1016/j.camwa.2021.09.001.

[43] A. Bonelli, O. Bursi, S. Erlicher, and L. Vulcan. "Analyses of the generalized-α method for linear and non-linear forced excited systems". Structural Dynamics-EURODYN. Vol. 2. 2002, pp. 1523–1528. URL: http://citeseerx.ist.psu.edu/viewdoc/download?doi=10.1.1.573.5832&rep=rep1&type=pdf.

[44] A. L. Braun and A. M. Awruch. "Geometrically non-linear analysis in elastodynamics using the eight-node finite element with one-point quadrature and the generalized-α method". Latin american journal of solids and structures 5.1 (2008), pp. 17–45. URL: http://hdl.handle.net/10183/205098.

[45] S. C. Brenner and L. R. Scott. The Mathematical Theory of Finite Element Methods. Vol. 3. Springer, 2010. ISBN: 9781441926111.

[46] A. Breuer, A. Heinecke, and M. Bader. "Petascale local time stepping for the ADER-DG finite element method". 2016 IEEE international parallel and distributed processing symposium (IPDPS). IEEE. 2016, pp. 854–863. DOI: 10.1109/IPDPS.2016.109.

[47] A. Breuer, A. Heinecke, and Y. Cui. "EDGE: Extreme scale fused seismic simulations with the discontinuous Galerkin method". International Supercomputing Conference. Springer. 2017, pp. 41–60. ISBN: 9783319586670. DOI: 10.1007/978-3-319-58667-0_3.

[48] A. Breuer, A. Heinecke, S. Rettenberger, M. Bader, A.-A. Gabriel, and C. Pelties. "Sustained petascale performance of seismic simulations with SeisSol on SuperMUC". International Supercomputing Conference. Springer. 2014, pp. 1–18. ISBN: 9783319075181. DOI: 10.1007/978-3-319-07518-1_1.

[49] A. N. Breuer. "High Performance Earthquake Simulations". https://mediatum.ub.tum.de/doc/1276756. PhD thesis. Technische Universität München, 2015.

[50] A. Cangiani, Z. Dong, and E. Georgoulis. "hp-version discontinuous Galerkin methods on essentially arbitrarily-shaped elements". Mathematics of Computation (2021). DOI: 10.1090/mcom/3667. URL: https://www.ams.org/journals/mcom/0000-000-00/S0025-5718-2021-03667-4/.

[51] A. Cangiani, Z. Dong, and E. H. Georgoulis. "hp-version space-time discontinuous Galerkin methods for parabolic problems on prismatic meshes". SIAM Journal on Scientific Computing 39.4 (2017), A1251–A1279. DOI: 10.1137/16M1073285.

[52] A. Cangiani, E. H. Georgoulis, and P. Houston. "hp-version discontinuous Galerkin methods on polygonal and polyhedral meshes". Mathematical Models and Methods in Applied Sciences 24.10 (2014), pp. 2009–2041. DOI: 10.1142/S0218202514500146.

[53] C. Canuto, M. Y. Hussaini, A. Quarteroni, and T. A. Zang. Spectral Methods: Evolution to Complex Geometries and Applications to Fluid Dynamics. Springer Science & Business Media, 2007. ISBN: 9783540307280. DOI: 10.1007/978-3-540-30728-0.

[54] C. Canuto, M. Y. Hussaini, A. Quarteroni, and T. A. Zang. Spectral Methods: Fundamentals in Single Domains. Springer Science & Business Media, 2007. ISBN: 9783540307259. DOI: 10.1007/978-3-540-30726-6.

[55] J. M. Carcione and D. Kosloff. “Representation of matched-layer kernels with viscoelastic mechanical models”. International Journal of Numerical Analysis and Modeling 10.1 (2013), pp. 221–232. URL: http://www.math.ualberta.ca/ijnam/Volume-10-2013/No-1-13/2013-01-11.pdf.

[56] C. Carstensen, T. Gudi, and M. Jensen. “A unifying theory of a posteriori error control for discontinuous Galerkin FEM”. Numerische Mathematik 112.3 (2009), pp. 363–379. DOI: 10.1007/s00211-009-0223-9.

[57] F. Casadei, E. Gabellini, G. Fotia, F. Maggio, and A. Quarteroni. “A mortar spectral/finite element method for complex 2D and 3D elastodynamic problems”. Computer methods in applied mechanics and engineering 191.45 (2002), pp. 5119–5148. DOI: 10.1016/S0045-7825(02)00294-3.

[58] P. Castaldo, B. Palazzo, T. Ferrentino, and G. Petrone. “Influence of the strength reduction factor on the seismic reliability of structures with FPS considering intermediate PGA/PGV ratios”. Composites Part B: Engineering 115 (2017), pp. 308–315. DOI: 10.1016/j.compositesb.2016.09.072.

[59] K. Çetin, G. Mylonakis, A. Sextos, J. Stewart, and T. Irmak. Seismological and Engineering Effects of the M 7.0 Samos Island (Aegean Sea) Earthquake. Tech. rep. 2020. DOI: 10.18118/G6H088.

[60] E. Chaljub, D. Komatitsch, J.-P. Vilotte, Y. Capdeville, B. Valette, and G. Festa. “Spectral-element analysis in seismology”. Advances in Geophysics 48 (2007), pp. 365–419. DOI: 10.1016/S0065-2687(06)48007-9.

[61] W. C. Chew and W. H. Weedon. “A 3D perfectly matched medium from modified Maxwell’s equations with stretched coordinates”. Microwave and optical technology letters 7.13 (1994), pp. 599–604. DOI: 10.1002/mop.4650071304.

[62] F. Chiba and T. Kako. “On the Stability of Newmark’s β method”. 数理解析研究所講究録 1040 (1998). Kyoto University. http://hdl.handle.net/2433/62040, pp. 39–44.

[63] S. Cho and S.-H. Ha. “Isogeometric shape design optimization: exact geometry and enhanced sensitivity”. Structural and Multidisciplinary Optimization 38.1 (2009), p. 53. DOI: 10.1007/s00158-008-0266-z.

[64] I. Christov, C. Christov, and P. Jordan. “Cumulative nonlinear effects in acoustic wave propagation”. Computer Modeling in Engineering and Sciences 17.1 (2007), p. 47. DOI: 10.3970/cmes.2007.017.047.

[65] I. Christov, C. Christov, and P. Jordan. “Modeling weakly nonlinear acoustic wave propagation”. Quarterly Journal of Mechanics and Applied Mathematics 60.4 (2007), pp. 473–495. DOI: 10.1093/qjmam/hbm017.

[66] J. Chung and G. M. Hulbert. “A Time Integration Algorithm for Structural Dynamics With Improved Numerical Dissipation: The Generalized-α Method”. Journal of Applied Mechanics 60.2 (June 1993), pp. 371–375. ISSN: 0021-8936. DOI: 10.1115/1.2900803.

[67] P. G. Ciarlet. Mathematical Elasticity: Volume I: three-dimensional elasticity. Studies in Mathematics and Its Applications. North-Holland, Apr. 1988. ISBN: 9780444702593.

[68] C. Clason, B. Kaltenbacher, and S. Veljović. “Boundary optimal control of the Westervelt and the Kuznetsov equations”. Journal of mathematical analysis and applications 356.2 (2009), pp. 738–751. DOI: 10.1016/j.jmaa.2009.03.043.

[69] B. Cockburn, G. E. Karniadakis, and C.-W. Shu. "The development of discontinuous Galerkin methods". Discontinuous Galerkin Methods. Springer, 2000, pp. 3–50. ISBN: 9783642597213. DOI: 10.1007/978-3-642-59721-3_1.

[70] A. Coleman and J. Saunders. "A review of the physical properties and biological effects of the high amplitude acoustic fields used in extracorporeal lithotripsy". Ultrasonics 31.2 (1993), pp. 75–89. DOI: 10.1016/0041-624X(93)90037-Z.

[71] C. A. Cornell. "Engineering seismic risk analysis". Bulletin of the seismological society of America 58.5 (1968), pp. 1583–1606. DOI: 10.1785/BSSA0580051583.

[72] S. C. Cowin and M. M. Mehrabadi. "Anisotropic Symmetries of Linear Elasticity". Applied Mechanics Reviews 48.5 (May 1995), pp. 247–285. ISSN: 0003-6900. DOI: 10.1115/1.3005102.

[73] J. G. Crempien and R. J. Archuleta. "UCSB method for simulation of broadband ground motion from kinematic earthquake sources". Seismological Research Letters 86.1 (2015), pp. 61–67. DOI: 10.1785/0220140103.

[74] D. G. Crighton. "Model equations of nonlinear acoustics". Annual Review of Fluid Mechanics 11.1 (1979), pp. 11–33. DOI: 10.1146/annurev.fl.11.010179.000303.

[75] V. Cruz-Atienza and J. Virieux. "Dynamic rupture simulation of non-planar faults with a finite-difference approach". Geophysical Journal International 158.3 (2004), pp. 939–954. DOI: 10.1111/j.1365-246X.2004.02291.x.

[76] Y. Cui et al. "Physics-based seismic hazard analysis on petascale heterogeneous supercomputers". SC'13: Proceedings of the International Conference on High Performance Computing, Networking, Storage and Analysis. IEEE. 2013, pp. 1–12. DOI: 10.1145/2503210.2503300.

[77] D. R. Dance, S. Christofides, A. D. A. Maidment, I. D. McLean, and K. H. Ng. Diagnostic radiology physics: A handbook for teachers and students. Endorsed by: American Association of Physicists in Medicine, Asia-Oceania Federation of Organizations for Medical Physics, European Federation of Organisations for Medical Physics. Sept. 2014. ISBN: 9789201310101.

[78] J. D. De Basabe, M. K. Sen, and M. F. Wheeler. "The interior penalty discontinuous Galerkin method for elastic wave propagation: grid dispersion". Geophysical Journal International 175.1 (2008), pp. 83–93. DOI: 10.1111/j.1365-246X.2008.03915.x.

[79] J. Deteix, A. Jendoubi, and D. Yakoubi. "A Coupled Prediction Scheme for Solving the Navier–Stokes and Convection-Diffusion Equations". SIAM Journal on Numerical Analysis 52.5 (2014), pp. 2415–2439. DOI: 10.1137/130942516.

[80] M. O. Deville, P. F. Fischer, and E. H. Mund. High-order Methods for Incompressible Fluid Flow. Vol. 9. Cambridge University Press, 2002. ISBN: 9780521453097.

[81] D. A. Di Pietro and A. Ern. Mathematical Aspects of Discontinuous Galerkin Methods. Vol. 69. Springer Science & Business Media, 2011. ISBN: 9783642229794. DOI: 10.1007/978-3-642-22980-0.

[82] W. Dörfler, S. Findeisen, C. Wieners, and D. Ziegler. "Parallel adaptive discontinuous Galerkin discretizations in space and time for linear elastic and acoustic waves". Space-Time Methods. Applications to Partial Differential Equations 25 (2019), pp. 61–88. DOI: 10.1515/9783110548488-002.

[83] W. Dörfler, C. Wieners, and D. Ziegler. “Space-Time Discontinuous Galerkin Methods for Linear Hyperbolic Systems and the Application to the Forward Problem in Seismic Imaging”. International Conference on Finite Volumes for Complex Applications. Springer. 2020, pp. 477–485. ISBN: 978-3-030-43651-3. DOI: 10.1007/978-3-030-43651-3_44.

[84] Dr Chris Tisdell. The Peter Paul Inequality. 17.05.2013. [Video] YouTube. URL: https://www.youtube.com/watch?v=C_bjbjTzHP4.

[85] D. Drzisga, B. Keith, and B. Wohlmuth. “The surrogate matrix methodology: Accelerating isogeometric analysis of waves”. Computer Methods in Applied Mechanics and Engineering 372 (2020), p. 113322. DOI: 10.1016/j.cma.2020.113322.

[86] M. Dumbser and M. Käser. “An arbitrary high-order discontinuous Galerkin method for elastic waves on unstructured meshes—II. The three-dimensional isotropic case”. Geophysical Journal International 167.1 (2006), pp. 319–336. DOI: 10.1111/j.1365-246X.2006.03120.x.

[87] M. Dumbser, M. Käser, and E. F. Toro. “An arbitrary high-order Discontinuous Galerkin method for elastic waves on unstructured meshes-V. Local time stepping and p-adaptivity”. Geophysical Journal International 171.2 (2007), pp. 695–717. DOI: 10.1111/j.1365-246X.2007.03427.x.

[88] K. Duru, L. Rannabauer, A.-A. Gabriel, and H. Igel. “A new discontinuous Galerkin spectral element method for elastic waves with physically motivated numerical fluxes”. Journal of Scientific Computing 88.51 (2021). DOI: 10.1007/s10915-021-01565-1.

[89] M. Duruflé, P. Grob, and P. Joly. “Influence of Gauss and Gauss-Lobatto quadrature rules on the accuracy of a quadrilateral finite element method in the time domain”. Numerical Methods for Partial Differential Equations 25.3 (2009), pp. 526–551. DOI: 10.1002/num.20353.

[90] C. Eck, H. Garcke, and P. Knabner. Mathematical Modeling. Springer, 2017. ISBN: 9783319551609. DOI: 10.1007/978-3-319-55161-6.

[91] W. Eisenmenger. “The mechanisms of stone fragmentation in ESWL”. Ultrasound in medicine & biology 27.5 (2001), pp. 683–693. DOI: 10.1016/s0301-5629(01)00345-3.

[92] A. Elenas and K. Meskouris. “Correlation study between seismic acceleration parameters and damage indices of structures”. Engineering Structures 23.6 (2001), pp. 698–704. DOI: 10.1016/S0141-0296(00)00074-2.

[93] A. Elghazouli. Seismic design of buildings to Eurocode 8. CRC Press, 2016. ISBN: 9781498751605.

[94] B. Engquist and A. Majda. “Radiation boundary conditions for acoustic and elastic wave calculations”. Communications on Pure and Applied Mathematics 32 (1979), pp. 313–357. DOI: 10.1002/cpa.3160320303.

[95] B. Engquist and A. Majda. “Absorbing boundary conditions for numerical simulation of waves”. Proceedings of the National Academy of Sciences 74.5 (1977), pp. 1765–1766. DOI: 10.1073/pnas.74.5.1765.

[96] Y. Epshteyn and B. Rivière. “Estimation of penalty parameters for symmetric interior penalty Galerkin methods”. Journal of Computational and Applied Mathematics 206.2 (2007), pp. 843–872. DOI: 10.1016/j.cam.2006.08.029.

[97] S. Erlicher, L. Bonaventura, and O. S. Bursi. "The analysis of the generalized-α method for non-linear dynamic problems". Computational mechanics 28.2 (2002), pp. 83–104. DOI: 10.1007/s00466-001-0273-z.

[98] A. Ern and J.-L. Guermond. Theory and Practice of Finite Elements. Vol. 159. Springer Science & Business Media, 2013. ISBN: 9780387205748. DOI: 10.1007/978-1-4757-4355-5.

[99] A. Ern and A. F. Stephansen. "A posteriori energy-norm error estimates for advection-diffusion equations approximated by weighted interior penalty methods". Journal of Computational Mathematics 26.4 (2008), pp. 488–510. URL: https://www.jstor.org/stable/43693458.

[100] V. Étienne, E. Chaljub, J. Virieux, and N. Glinsky. "An hp-adaptive discontinuous Galerkin finite-element method for 3-D elastic wave modelling". Geophysical Journal International 183.2 (2010), pp. 941–962. DOI: 10.1111/j.1365-246X.2010.04764.x.

[101] L. Evangelista et al. "Physics-based seismic input for engineering applications: a case study in the Aterno river valley, Central Italy". Bulletin of Earthquake Engineering 15.7 (2017), pp. 2645–2671. DOI: 10.1007/s10518-017-0089-7.

[102] J. A. Evans and T. J. Hughes. "Explicit trace inequalities for isogeometric analysis and parametric hexahedral finite elements". Numerische Mathematik 123.2 (2013), pp. 259–290. DOI: 10.1007/s00211-012-0484-6.

[103] E. Faccioli, F. Maggio, R. Paolucci, and A. Quarteroni. "2D and 3D elastic wave propagation by a pseudo-spectral domain decomposition method". Journal of Seismology 1.3 (1997), pp. 237–251. DOI: 10.1023/A:1009758820546.

[104] G. Fernandez Lorenzo, M. P. Santisi d'Avila, A. Deschamps, E. Bertrand, E. Mercerat, L. Foundotos, and F. Courboulex. "Numerical and Empirical Simulation of Linear Elastic Seismic Response of a Building: The Case of Nice Prefecture (Southeastern France)". Earthquake Spectra 34 (Sept. 2017). DOI: 10.1193/042216EQS064M.

[105] G. Fibich. The Nonlinear Schrödinger Equation. Springer, 2015. ISBN: 9783319127477. DOI: 10.1007/978-3-319-12748-4.

[106] B. Flemisch, M. Kaltenbacher, and B. I. Wohlmuth. "Elasto–acoustic and acoustic–acoustic coupling on non-matching grids". International Journal for Numerical Methods in Engineering 67.13 (2006), pp. 1791–1810. DOI: 10.1002/nme.1669.

[107] S. Frei, T. Richter, and T. Wick. "Eulerian techniques for fluid-structure interactions: Part I–Modeling and simulation". Numerical Mathematics and Advanced Applications-ENUMATH 2013. Springer, 2015, pp. 745–753. ISBN: 9783319107059. DOI: 10.1007/978-3-319-10705-9_74.

[108] M. Fritz, V. Nikolić, and B. Wohlmuth. "Well-posedness and numerical treatment of the Blackstock equation in nonlinear acoustics". Mathematical Models and Methods in Applied Sciences 28.13 (2018), pp. 2557–2597. DOI: 10.1142/S0218202518500550.

[109] D. Fußeder and B. Simeon. "Algorithmic aspects of isogeometric shape optimization". Isogeometric Analysis and Applications 2014. Springer, 2015, pp. 183–207. ISBN: 9783319233154. DOI: 10.1007/978-3-319-23315-4_8.

[110] D. Fußeder, B. Simeon, and A.-V. Vuong. "Fundamental aspects of shape optimization in the context of isogeometric analysis". Computer Methods in Applied Mechanics and Engineering 286 (2015), pp. 313–331. DOI: 10.1016/j.cma.2014.12.028.

[111] E. Gabriel et al. "Open MPI: Goals, Concept, and Design of a Next Generation MPI Implementation". Proceedings, 11th European PVM/MPI Users' Group Meeting. Budapest, Hungary, Sept. 2004, pp. 97–104. DOI: 10.1007/978-3-540-30218-6_19.

[112] Y. Gao, H. Song, J. Zhang, and Z. Yao. "Comparison of artificial absorbing boundaries for acoustic wave equation modelling". Exploration Geophysics 48.1 (2017), pp. 76–93. DOI: 10.1071/EG15068.

[113] F. Gatti. "Analyse physics-based de scénarios sismiques «de la faille au site»: prédiction de mouvement sismique fort pour l'étude de vulnérabilité sismique de structures critiques." PhD thesis. Université Paris-Saclay; Politecnico di Milano, 2017. URL: https://tel.archives-ouvertes.fr/tel-01626230.

[114] E. H. Georgoulis. "hp-version interior penalty discontinuous Galerkin finite element methods on anisotropic meshes". Int. J. Numer. Anal. Model 3.1 (2006), pp. 52–79. URL: http://www.math.ualberta.ca/ijnam/Volume-3-2006/No-1-06/2006-01-03.pdf.

[115] E. H. Georgoulis, E. Hall, and P. Houston. "Discontinuous Galerkin methods for advection-diffusion-reaction problems on anisotropically refined meshes". SIAM Journal on Scientific Computing 30.1 (2008), pp. 246–271. DOI: 10.1137/060672352.

[116] E. H. Georgoulis, A. Iske, and J. Levesley. Approximation Algorithms for Complex Systems. Springer, 2011. ISBN: 9783642266652. DOI: 10.1007/978-3-642-16876-5.

[117] M. Ghaemian and A. Ghobarah. "Nonlinear seismic response of concrete gravity dams with dam–reservoir interaction". Engineering Structures 21.4 (1999), pp. 306–315. DOI: 10.1016/S0141-0296(97)00208-3.

[118] V. Girault, B. Rivière, and M. Wheeler. "A discontinuous Galerkin method with nonoverlapping domain decomposition for the Stokes and Navier-Stokes problems". Mathematics of computation 74.249 (2005), pp. 53–84. DOI: 10.1090/S0025-5718-04-01652-7.

[119] D. Givoli. "Non-reflecting boundary conditions". Journal of Computational Physics 94.1 (1991), pp. 1–29. DOI: 10.1016/0021-9991(91)90135-8.

[120] D. Givoli and J. B. Keller. "Non-reflecting boundary conditions for elastic waves". Wave motion 12.3 (1990), pp. 261–279. DOI: 10.1016/0165-2125(90)90043-4.

[121] I. Gladwell and R. Thomas. "Stability properties of the Newmark, Houbolt and Wilson θ methods". International Journal for Numerical and Analytical Methods in Geomechanics 4.2 (1980), pp. 143–158. DOI: 10.1002/nag.1610040205.

[122] H. Gómez, V. M. Calo, Y. Bazilevs, and T. J. Hughes. "Isogeometric analysis of the Cahn–Hilliard phase-field model". Computer Methods in Applied Mechanics and Engineering 197.49-50 (2008), pp. 4333–4352. DOI: 10.1016/j.cma.2008.05.003.

[123] D. Gottlieb and S. A. Orszag. Numerical analysis of spectral methods: theory and applications. SIAM, 1977. ISBN: 9780898710236. DOI: 10.1137/1.9781611970425.

[124] G. L. Goudreau and R. L. Taylor. "Evaluation of numerical integration methods in elastodynamics". Computer Methods in Applied Mechanics and Engineering 2.1 (1973), pp. 69–97. DOI: 10.1016/0045-7825(73)90023-6.

[125] M. J. Grote, M. Mehlin, and T. Mitkova. “Runge–Kutta-Based Explicit Local Time-Stepping Methods for Wave Propagation”. SIAM Journal on Scientific Computing 37.2 (2015), A747–A775. DOI: 10.1137/140958293.

[126] M. J. Grote, A. Schneebeli, and D. Schötzau. “Discontinuous Galerkin Finite Element Method for the Wave Equation”. SIAM Journal on Numerical Analysis 44.6 (2006), pp. 2408–2431. DOI: 10.1137/05063194X.

[127] P. Gupta and A. Srivastava. “Numerical analysis of thermal response of tissues subjected to high intensity focused ultrasound”. International Journal of Hyperthermia 35.1 (2018), pp. 419–434. DOI: 10.1080/02656736.2018.1506166.

[128] E. Hairer, C. Lubich, and G. Wanner. Geometric Numerical Integration: Structure-Preserving Algorithms for Ordinary Differential Equations. 2nd ed. Springer, 2010. ISBN: 9783642051579.

[129] L. Halpern and J. Rauch. “Absorbing boundary conditions for diffusion equations”. Numerische Mathematik 71.2 (1995), pp. 185–224. DOI: 10.1007/s002110050141.

[130] M. F. Hamilton and D. T. Blackstock. “On the coefficient of nonlinearity β in nonlinear acoustics”. The Journal of the Acoustical Society of America 83.1 (1988), pp. 74–77. DOI: 10.1121/1.396187.

[131] M. F. Hamilton, D. T. Blackstock, et al. Nonlinear Acoustics. Vol. 237. Academic press San Diego, 1998. ISBN: 9780123218605.

[132] S. H. Hartzell and T. H. Heaton. “Inversion of strong ground motion and teleseismic waveform data for the fault rupture history of the 1979 Imperial Valley, California, earthquake”. Bulletin of the Seismological Society of America 73.6A (1983), pp. 1553–1583. DOI: 10.1785/BSSA07306A1553.

[133] R. L. Higdon. “Absorbing boundary conditions for difference approximations to the multidimensional wave equation”. Mathematics of Computation 47.176 (1986), pp. 437–459. DOI: 10.1090/S0025-5718-1986-0856696-4.

[134] R. L. Higdon. “Numerical absorbing boundary conditions for the wave equation”. Mathematics of Computation 49.179 (1987), pp. 65–90. DOI: 10.1090/S0025-5718-1987-0890254-1.

[135] R. L. Higdon. “Absorbing boundary conditions for elastic waves”. Geophysics 56.2 (1991), pp. 231–241. DOI: 10.1190/1.1443035.

[136] R. L. Higdon. “Absorbing boundary conditions for acoustic and elastic waves in stratified media”. Journal of Computational Physics 101.2 (1992), pp. 386–418. DOI: 10.1016/0021-9991(92)90016-R.

[137] H. M. Hilber, T. J. Hughes, and R. L. Taylor. “Improved numerical dissipation for time integration algorithms in structural dynamics”. Earthquake Engineering & Structural Dynamics 5.3 (1977), pp. 283–292. DOI: 10.1002/eqe.4290050306.

[138] M. Hochbruck and J. Leibold. “An implicit–explicit time discretization scheme for second-order semilinear wave equations with application to dynamic boundary conditions”. Numerische Mathematik 147.4 (2021), pp. 869–899. DOI: 10.1007/s00211-021-01184-w.

[139] M. Hochbruck and A. Ostermann. “Exponential integrators”. Acta Numerica 19.May (2010), pp. 209–286. DOI: 10.1017/S0962492910000048.

[140] M. Hochbruck, T. Pažur, A. Schulz, E. Thawinan, and C. Wieners. “Efficient time integration for discontinuous Galerkin approximations of linear wave equations”. ZAMM-Journal of Applied Mathematics and Mechanics/Zeitschrift für Angewandte Mathematik und Mechanik 95.3 (2015), pp. 237–259. DOI: 10.1002/zamm.201300306.

[141] J. Hoffelner, H. Landes, M. Kaltenbacher, and R. Lerch. “Finite element simulation of nonlinear wave propagation in thermoviscous fluids including dissipation”. IEEE transactions on ultrasonics, ferroelectrics, and frequency control 48.3 (2001), pp. 779–786. DOI: 10.1109/58.920712.

[142] J. R. Holliday, W. R. Graves, J. B. Rundle, and D. L. Turcotte. “Computing earthquake probabilities on global scales”. Pure and Applied Geophysics 173.3 (2016), pp. 739–748. DOI: 10.1007/s00024-014-0951-3.

[143] T. Horger, B. Wohlmuth, and L. Wunderlich. “Reduced basis isogeometric mortar approximations for eigenvalue problems in vibroacoustics”. Model reduction of parametrized systems. Springer, 2017, pp. 91–106. ISBN: 9783319587868. DOI: 10.1007/978-3-319-58786-8_6.

[144] L. Hörmander. “Pseudo-differential operators”. Communications on Pure and Applied Mathematics 18.3 (1965), pp. 501–517. DOI: 10.1002/cpa.3160180307.

[145] L. Hörmander. The Analysis of Linear Partial Differential Operators III: Pseudo-Differential Operators. Springer Science & Business Media, 2007. ISBN: 9783540499374. DOI: 10.1007/978-3-540-49938-1_3.

[146] H. Hoteit, P. Ackerer, R. Mosé, J. Erhel, and B. Philippe. “New two-dimensional slope limiters for discontinuous Galerkin methods on arbitrary meshes”. International Journal for Numerical Methods in Engineering 61.14 (2004), pp. 2566–2593. DOI: 10.1002/nme.1172.

[147] F. Q. Hu, M. Y. Hussaini, and P. Rasetarinera. “An analysis of the discontinuous Galerkin method for wave propagation problems”. Journal of Computational Physics 151.2 (1999), pp. 921–946. DOI: 10.1006/jcph.1999.6227.

[148] T. J. Hughes and W. Liu. “Implicit-explicit finite elements in transient analysis: stability theory”. Journal of Applied Mechanics 45.2 (1978). DOI: 10.1115/1.3424304.

[149] T. J. Hughes. The Finite Element Method: Linear Static and Dynamic Finite Element Analysis. Dover Publications Inc., 2000. ISBN: 9780486411811.

[150] G. M. Hulbert and I. Jang. “Automatic time step control algorithms for structural dynamics”. Computer Methods in Applied Mechanics and Engineering 126.1-2 (1995), pp. 155–178. DOI: 10.1016/0045-7825(95)00791-X.

[151] H. Igel, M. Käser, and M. Stupazzini. “Seismic Wave Propagation in Media with Complex Geometries, Simulation of”. Extreme Environmental Events: Complexity in Forecasting and Early Warning. Ed. by R. A. Meyers. New York, NY: Springer New York, 2011, pp. 765–787. ISBN: 9781441976956. DOI: 10.1007/978-1-4419-7695-6_41.

[152] L. T. Ikelle and L. Amundsen. Introduction to Petroleum Seismology. Society of Exploration Geophysicists, 2005. ISBN: 9781560801290.

[153] M. Infantino, I. Mazzieri, A. G. Özcebe, R. Paolucci, and M. Stupazzini. "3D physics-based numerical simulations of ground motion in Istanbul from earthquakes along the Marmara segment of the North Anatolian Fault". Bulletin of the Seismological Society of America 110.5 (2020), pp. 2559–2576. DOI: 10.1785/0120190235.

[154] K. E. Jansen, C. H. Whiting, and G. M. Hulbert. "A generalized-α method for integrating the filtered Navier–Stokes equations with a stabilized finite element method". Computer Methods in Applied Mechanics and Engineering 190.3-4 (2000), pp. 305–319. DOI: 10.1016/S0045-7825(00)00203-6.

[155] A. Jarvis, H. Reuter, A. Nelson, and E. Guevara. "Hole-filled seamless SRTM data V4". International Centre for Tropical Agriculture (CIAT) (2008). https://srtm.csi.cgiar.org.

[156] C. Ji, D. J. Wald, and D. V. Helmberger. "Source description of the 1999 Hector Mine, California, earthquake, part I: Wavelet domain inversion theory and resolution analysis". Bulletin of the Seismological Society of America 92.4 (2002), pp. 1192–1207. DOI: 10.1785/0120000916.

[157] C. Johnson and J. Pitkäranta. "An analysis of the discontinuous Galerkin method for a scalar hyperbolic equation". Mathematics of Computation 46.173 (1986), pp. 1–26. DOI: 10.1090/S0025-5718-1986-0815828-4.

[158] S. G. Johnson. "Notes on Perfectly Matched Layers (PMLs)" (2021). arXiv: 2108.05348 [cs.CE].

[159] P. M. Jordan. "Second-sound phenomena in inviscid, thermally relaxing gases". Discrete & Continuous Dynamical Systems - B 19.7 (2014), pp. 2189–2205. DOI: 10.3934/dcdsb.2014.19.2189.

[160] P. Jordan. "A survey of weakly-nonlinear acoustic models: 1910–2009". Mechanics Research Communications 73 (2016), pp. 127–139. DOI: 10.1016/j.mechrescom.2016.02.014.

[161] B. Kaltenbacher and I. Lasiecka. "Global existence and exponential decay rates for the Westervelt equation". Discrete & Continuous Dynamical Systems - S 2.3 (2009), pp. 503–523. DOI: 10.3934/dcdss.2009.2.503.

[162] B. Kaltenbacher and I. Lasiecka. "Well-posedness of the Westervelt and the Kuznetsov equation with nonhomogeneous Neumann boundary conditions". Conference Publications. Vol. 2011. Special. American Institute of Mathematical Sciences. 2011, pp. 763–773. DOI: 10.3934/proc.2011.2011.763.

[163] B. Kaltenbacher and I. Lasiecka. "An analysis of nonhomogeneous Kuznetsov's equation: Local and global well-posedness; exponential decay". Mathematische Nachrichten 285.2-3 (2012), pp. 295–321. DOI: 10.1002/mana.201000007.

[164] B. Kaltenbacher, I. Lasiecka, and S. Veljović. "Well-posedness and exponential decay for the Westervelt equation with inhomogeneous Dirichlet boundary data". Parabolic problems. Springer, 2011, pp. 357–387. DOI: 10.1007/978-3-0348-0075-4_19.

[165] B. Kaltenbacher and V. Nikolić. "The Jordan–Moore–Gibson–Thompson Equation: Well-posedness with quadratic gradient nonlinearity and singular limit for vanishing relaxation time". Mathematical Models and Methods in Applied Sciences 29.13 (2019), pp. 2523–2556. DOI: 10.1142/S0218202519500532.

[166] B. Kaltenbacher and V. Nikolić. "Parabolic approximation of quasilinear wave equations with applications in nonlinear acoustics" (2021). arXiv: 2011.07360 [math.AP].

[167] B. Kaltenbacher and I. Shevchenko. "Well-posedness of the Westervelt equation with higher order absorbing boundary conditions". Journal of Mathematical Analysis and Applications 479.2 (2019), pp. 1595–1617. DOI: 10.1016/j.jmaa.2019.07.014.

[168] B. Kaltenbacher and M. Thalhammer. "Fundamental models in nonlinear acoustics part I. Analytical comparison". Mathematical Models and Methods in Applied Sciences 28.12 (2018), pp. 2403–2455. DOI: 10.1142/S0218202518500525.

[169] B. Kaltenbacher and M. Thalhammer. "Convergence of implicit Runge–Kutta time discretization methods for fundamental models in nonlinear acoustics". J. Appl. Numer. Optim 3.2 (2021), pp. 361–401. DOI: 10.23952/jano.3.2021.2.08.

[170] M. Kaltenbacher. Numerical Simulation of Mechatronic Sensors and Actuators. Vol. 2. Springer, 2007. ISBN: 9783540713593. DOI: 10.1007/978-3-540-71360-9.

[171] H. Kanamori. "The energy release in great earthquakes". Journal of Geophysical Research 82.20 (1977), pp. 2981–2987. DOI: 10.1029/JB082i020p02981.

[172] P.-H. Kao and R.-J. Yang. "Simulating oscillatory flows in Rayleigh–Benard convection using the lattice Boltzmann method". International Journal of Heat and Mass Transfer 50.17-18 (2007), pp. 3315–3328. DOI: 10.1016/j.ijheatmasstransfer.2007.01.035.

[173] H. Kaplan, H. Bilgin, S. Yilmaz, H. Binici, and A. Öztas. "Structural damages of L'Aquila (Italy) earthquake". Natural Hazards and Earth System Sciences 10.3 (2010), pp. 499–507. DOI: 10.5194/nhess-10-499-2010.

[174] S. Karaa. "Approximate factorization for a viscous wave equation". Computing 89.3-4 (2010), pp. 199–215. DOI: 10.1007/s00607-010-0102-3.

[175] O. A. Karakashian and F. Pascal. "A Posteriori Error Estimates for a Discontinuous Galerkin Approximation of Second-Order Elliptic Problems". SIAM Journal on Numerical Analysis 41.6 (2003), pp. 2374–2399. DOI: 10.1137/S0036142902405217.

[176] M. E. Kartal, M. Çavuşli, and M. Geniş. "3D nonlinear analysis of Atatürk clay core Rockfill dam considering settlement monitoring". International Journal of Geomechanics 19.5 (2019), p. 04019034. DOI: 10.1061/(ASCE)GM.1943-5622.0001412.

[177] G. Karypis and V. Kumar. "A fast and high quality multilevel scheme for partitioning irregular graphs". SIAM Journal on Scientific Computing 20.1 (1998), pp. 359–392. DOI: 10.1137/S1064827595287997.

[178] M. Käser and M. Dumbser. "An arbitrary high-order discontinuous Galerkin method for elastic waves on unstructured meshes—I. The two-dimensional isotropic case with external source terms". Geophysical Journal International 166.2 (2006), pp. 855–877. DOI: 10.1111/j.1365-246X.2006.03051.x.

[179] M. Käser, M. Dumbser, J. De La Puente, and H. Igel. "An arbitrary high-order discontinuous Galerkin method for elastic waves on unstructured meshes—III. Viscoelastic attenuation". Geophysical Journal International 168.1 (2007), pp. 224–242. DOI: 10.1111/j.1365-246X.2006.03193.x.

[180] B. Kato and G. Wang. "Regional seismic responses of shallow basins incorporating site-city interaction analyses on high-rise building clusters". Earthquake Engineering & Structural Dynamics 50.1 (2020), pp. 214–236. DOI: 10.1002/eqe.3363.

[181] R. B. Kebric. "The Colossus of Rhodes: Its Height and Pedestal". Athens Journal of Humanities and Arts 6.4 (2019), pp. 259–298. DOI: 10.30958/ajha.6-4-1.

[182] J. F. Kelly, S. Marras, X. Zhao, and R. J. McGough. "Linear and nonlinear ultrasound simulations using the discontinuous Galerkin method". The Journal of the Acoustical Society of America 143.4 (2018), pp. 2438–2448. DOI: 10.1121/1.5032196.

[183] R. G. Keys. "Absorbing boundary conditions for acoustic media". Geophysics 50.6 (1985), pp. 892–902. DOI: 10.1190/1.1441969.

[184] A. Khoei, A. Azami, and S. Haeri. "Implementation of plasticity based models in dynamic analysis of earth and rockfill dams: A comparison of Pastor–Zienkiewicz and cap models". Computers and Geotechnics 31.5 (2004), pp. 384–409. DOI: 10.1016/j.compgeo.2004.04.003.

[185] A. Khouei, M. Anahid, M. Zarinfar, M. Ashouri, and A. Pak. "A large plasticity deformation of unsaturated soil for 3D dynamic analysis of lower san-fernando dam". Asian Journal of Civil Engineering (Building and Housing) 12.1 (2011).

[186] J. Kiendl, R. Schmidt, R. Wüchner, and K.-U. Bletzinger. "Isogeometric shape optimization of shells using semi-analytical sensitivity analysis and sensitivity weighting". Computer Methods in Applied Mechanics and Engineering 274 (2014), pp. 148–167. DOI: 10.1016/j.cma.2014.02.001.

[187] H. Koga, K. Matsuoka, S. Noda, and T. Yamashita. "Cumulative Renal Damage in Oogs by Repeated Treatment with Extracorporeal Shock Waves". International journal of urology 3.2 (1996), pp. 134–140. DOI: 10.1111/j.1442-2042.1996.tb00498.x.

[188] J. J. Kohn and L. Nirenberg. "An Algebra of Pseudo-Differential Operators". Communications on Pure and Applied Mathematics 18.1-2 (1965), pp. 269–305. DOI: 10.1002/cpa.3160180121.

[189] D. Komatitsch, D. Göddeke, G. Erlebacher, and D. Michéa. "Modeling the propagation of elastic waves using spectral elements on a cluster of 192 GPUs". Computer Science-Research and Development 25.1 (2010), pp. 75–82. DOI: 10.1007/s00450-010-0109-1.

[190] D. Komatitsch and J. Tromp. "Introduction to the spectral element method for three-dimensional seismic wave propagation". Geophysical Journal International 139.3 (1999), pp. 806–822. DOI: 10.1046/j.1365-246x.1999.00967.x.

[191] D. Komatitsch and J. Tromp. "Spectral-element simulations of global seismic wave propagation—I. Validation". Geophysical Journal International 149.2 (2002), pp. 390–412. DOI: 10.1046/j.1365-246X.2002.01653.x.

[192] D. Komatitsch and J. Tromp. "Spectral-element simulations of global seismic wave propagation—II. Three-dimensional models, oceans, rotation and self-gravitation". Geophysical Journal International 150.1 (2002), pp. 303–318. DOI: 10.1046/j.1365-246X.2002.01716.x.

[193] D. Komatitsch and J.-P. Vilotte. "The spectral element method: an efficient tool to simulate the seismic response of 2D and 3D geological structures". Bulletin of the seismological society of America 88.2 (1998), pp. 368–392. DOI: 10.1785/BSSA0880020368.

[194] R. Kosloff and D. Kosloff. “Absorbing boundaries for wave propagation problems”. Journal of Computational Physics 63.2 (1986), pp. 363–376. DOI: 10.1016/0021-9991(86)90199-3.

[195] J. E. Kozdon, E. M. Dunham, and J. Nordström. “Simulation of dynamic earthquake ruptures in complex geometries using high-order finite difference methods”. Journal of Scientific Computing 55.1 (2013), pp. 92–124. DOI: 10.1007/s10915-012-9624-5.

[196] H. Kuramoto, M. Teshigawara, T. Okuzono, N. Koshika, M. Takayama, and T. Hori. “Predicting the earthquake response of buildings using equivalent single degree of freedom system”. Proceedings of Twentieth World Conference on Earthquake Engineering. 2000. URL: https://www.iitk.ac.in/nicee/wcee/article/1039.pdf.

[197] J.-P. Kuska. “Absorbing boundary conditions for the Schrödinger equation on finite intervals”. Physical Review B 46.8 (1992), p. 5000. DOI: 10.1103/PhysRevB.46.5000.

[198] D. Kuzmin. “A vertex-based hierarchical slope limiter for p-adaptive discontinuous Galerkin methods”. Journal of Computational and Applied Mathematics 233.12 (2010), pp. 3077–3085. DOI: 10.1016/j.cam.2009.05.028.

[199] V. Kuznetsov. “ Уравнения нелинейной акустики”. Акустический журнал 16.4 (1970). Рубрика: 05.02 http://www.akzh.ru/pdf/1970_4_548-553.pdf, pp. 548–553.

[200] J. Lee and G. L. Fenves. “A plastic-damage concrete model for earthquake analysis of dams”. Earthquake Engineering & Structural Dynamics 27.9 (1998), pp. 937–956. DOI: 10.1002/(SICI)1096-9845(199809)27:9<937::AID-EQE764>3.0.CO;2-5.

[201] P. Lesaint and P.-A. Raviart. “On a Finite Element Method for Solving the Neutron Transport Equation”. Publications mathématiques et informatique de Rennes S4 (1974), pp. 1–40. URL: http://www.numdam.org/item/PSMIR_1974___S4_A8_0/.

[202] S. Li, M. Brun, I. Djeran-Maigre, and S. Kuznetsov. “Hybrid asynchronous absorbing layers based on Kosloff damping for seismic wave propagation in unbounded domains”. Computers and Geotechnics 109 (2019), pp. 69–81. DOI: 10.1016/j.compgeo.2019.01.019.

[203] Z. C. Li. “Lagrange Multipliers and Other Coupling Techniques”. Combined Methods for Elliptic Equations with Singularities, Interfaces and Infinities. Vol. 444. Boston, MA: Springer US, 1998, pp. 209–224. DOI: 10.1007/978-1-4613-3338-8_6.

[204] M. J. Lighthill. “Viscosity effects in sound waves of finite amplitude”. Surveys in mechanics 250–351 (1956).

[205] H.-P. Liu, D. L. Anderson, and H. Kanamori. “Velocity dispersion due to anelasticity; implications for seismology and mantle composition”. Geophysical Journal International 47.1 (1976), pp. 41–58. DOI: 10.1111/j.1365-246X.1976.tb01261.x.

[206] M. Liu and D. G. Gorman. “Formulation of Rayleigh damping and its extensions”. Computers & Structures 57.2 (1995), pp. 277–285. DOI: 10.1016/0045-7949(94)00611-6.

[207] L. Long and J. Liow. “A transparent boundary for finite-difference wave simulation”. Geophysics 55.2 (1990), pp. 201–208. DOI: 10.1190/1.1442827.

[208] X. Lu and R. Schmid. “A symplectic algorithm for wave equations”. Mathematics and Computers in Simulation 43.1 (1997), pp. 29–38. DOI: 10.1016/S0378-4754(96)00052-3.

[209] X. Lu, Y. Tian, G. Wang, and D. Huang. "A numerical coupling scheme for nonlinear time history analysis of buildings on a regional scale considering site-city interaction effects". Earthquake Engineering & Structural Dynamics 47.13 (2018), pp. 2708–2725. DOI: 10.1002/eqe.3108.

[210] Y. Maday and E. M. Rønquist. "Optimal error analysis of spectral methods with emphasis on non-constant coefficients and deformed geometries". Computer Methods in Applied Mechanics and Engineering 80.1-3 (1990), pp. 91–115. DOI: 10.1016/0045-7825(90)90016-F.

[211] F. Maggio and A. Quarteroni. "Acoustic wave simulation by spectral methods". East-West Journal of Numerical Mathematics 2.2 (1994), pp. 129–150.

[212] E. Maloney and J. H. Hwang. "Emerging HIFU applications in cancer therapy". International Journal of Hyperthermia 31.3 (2015), pp. 302–309. DOI: 10.3109/02656736.2014.969789.

[213] I. Mazzieri, M. Muhr, M. Stupazzini, and B. Wohlmuth. Elasto-acoustic modelling and simulation for the seismic response of structures: The case of the Tahtalı dam in the 2020 İzmir earthquake. Submitted to Journal of Computational Physics at 03.11.2021, currently under review. 2021. arXiv: 2110.15875 [math.NA].

[214] I. Mazzieri, M. Stupazzini, R. Guidotti, and C. Smerzini. "SPEED: SPectral Elements in Elastodynamics with Discontinuous Galerkin: A non-conforming approach for 3D multi-scale problems". International Journal for Numerical Methods in Engineering 95.12 (2013), pp. 991–1010. DOI: 10.1002/nme.4532.

[215] D. McCallen et al. "EQSIM—A multidisciplinary framework for fault-to-structure earthquake simulations on exascale computers part I: Computational models and workflow". Earthquake Spectra 37.2 (2021), pp. 707–735. DOI: 10.1177/8755293020970982.

[216] L. Melas. "Three-dimensional physics-based numerical simulations of earthquake ground motion for advanced seismic risk assessment". http://hdl.handle.net/10589/177110. PhD thesis. Politecnico di Milano, Feb. 2021.

[217] M. Meliani and V. Nikolić. "Shape sensitivity analysis for general optimization problems in nonlinear acoustics" (2021). arXiv: 2108.08652 [math.OC].

[218] L. Mingwu, S. E. Benzley, G. Sjaardema, and T. Tautges. "A multiple source and target sweeping method for generating all hexahedral finite element meshes". Proceedings, 5th International Meshing Roundtable. Vol. 96. 1996, pp. 217–225.

[219] K. Mizohata and S. Ukai. "The global existence of small amplitude solutions to the nonlinear acoustic wave equation". Journal of Mathematics of Kyoto University 33.2 (1993), pp. 505–522. DOI: 10.1215/kjm/1250519270.

[220] P. Moczo, J. Kristek, and M. Gális. The finite-difference modelling of earthquake motions: Waves and ruptures. Cambridge University Press, 2014. ISBN: 9781139236911. DOI: 10.1017/CBO9781139236911.

[221] P. Moczo, J. O. Robertsson, and L. Eisner. "The finite-difference time-domain method for modeling of seismic wave propagation". Advances in Geophysics 48 (2007), pp. 421–516. DOI: 10.1016/S0065-2687(06)48008-0.

[222] S. Mönkölä. “On the accuracy and efficiency of transient spectral element models for seismic wave problems”. Advances in Mathematical Physics 2016 (2016). DOI: 10.1155/2016/9431583.

[223] M. N. J. Moore. “Riemann-Hilbert Problems for the Shapes Formed by Bodies Dissolving, Melting, and Eroding in Fluid Flows”. Communications on Pure and Applied Mathematics 70.9 (2017), pp. 1810–1831. DOI: 10.1002/cpa.21689.

[224] M. Muhr, V. Nikolić, and B. Wohlmuth. “Self-adaptive absorbing boundary conditions for quasilinear acoustic wave propagation”. Journal of Computational Physics 388 (2019), pp. 279–299. DOI: 10.1016/j.jcp.2019.03.025.

[225] M. Muhr, V. Nikolić, and B. Wohlmuth. “A discontinuous Galerkin coupling for nonlinear elasto-acoustics” (2021). To appear in: IMA Journal of Numerical Analysis, accepted on 26.10.2021. DOI: 10.1093/imanum/drab089. NON final arXiv preprint: 2102.04311 (math.NA). URL: https://arxiv.org/abs/2102.04311.

[226] M. Muhr, V. Nikolić, B. Wohlmuth, and L. Wunderlich. “Isogeometric shape optimization for nonlinear ultrasound focusing”. Evolution Equations & Control Theory 8 (2019), pp. 163–202. DOI: 10.3934/eect.2019010.

[227] F. Müller, D. Schötzau, and C. Schwab. “Discontinuous Galerkin methods for acoustic wave propagation in polygons”. Journal of Scientific Computing 77.3 (2018), pp. 1909–1935. DOI: 10.1007/s10915-018-0706-x.

[228] F. Nataf. “Absorbing boundary conditions and perfectly matched layers in wave propagation problems”. Direct and Inverse Problems in Wave Propagation and Applications. Ed. by I. Graham, U. Langer, J. Melenk, and M. Sini. De Gruyter, 2013, pp. 219–232. DOI: 10.1515/9783110282283.219.

[229] A. Neisius et al. “Improving the lens design and performance of a contemporary electromagnetic shock wave lithotripter”. Proceedings of the National Academy of Sciences 111.13 (2014), E1167–E1175. DOI: 10.1073/pnas.1319203111.

[230] B. Neta, V. van Joolen, J. R. Dea, and D. Givoli. “Application of high-order Higdon non-reflecting boundary conditions to linear shallow water models”. Communications in Numerical Methods in Engineering 24.11 (2008), pp. 1459–1466. DOI: 10.1002/cnm.1044.

[231] N. M. Newmark. “A Method of Computation for Structural Dynamics”. Journal of the Engineering Mechanics Division 85.3 (1959), pp. 67–94. DOI: 10.1061/JMCEA3.0000098.

[232] V. Nikolić and B. Wohlmuth. “A Priori Error Estimates for the Finite Element Approximation of Westervelt’s Quasi-linear Acoustic Wave Equation”. SIAM Journal on Numerical Analysis 57.4 (2019), pp. 1897–1918. DOI: 10.1137/19M1240873.

[233] V. Nikolić and B. Said-Houari. “Mathematical analysis of memory effects and thermal relaxation in nonlinear sound waves on unbounded domains”. Journal of Differential Equations 273 (2021), pp. 172–218. DOI: 10.1016/j.jde.2020.11.047.

[234] L. Nirenberg. Lectures on Linear Partial Differential Equations. Vol. 17. American Mathematical Soc., 1973. ISBN: 9780821816677.

[235] J. Nitsche. "Über ein Variationsprinzip zur Lösung von Dirichlet-Problemen bei Verwendung von Teilräumen, die keinen Randbedingungen unterworfen sind". Abhandlungen aus dem mathematischen Seminar der Universität Hamburg. Vol. 36. 1. Springer. 1971, pp. 9–15. DOI: 10.1007/BF02995904.

[236] O. Omidi and V. Lotfi. "Earthquake response of concrete arch dams: a plastic–damage approach". Earthquake engineering & structural dynamics 42.14 (2013), pp. 2129–2149. DOI: 10.1002/eqe.2317.

[237] S. A. Orszag. "Accurate solution of the Orr–Sommerfeld stability equation". Journal of Fluid Mechanics 50.4 (1971), pp. 689–703. DOI: 10.1017/S0022112071002842.

[238] S. A. Orszag. "Numerical simulation of incompressible flows within simple boundaries. I. Galerkin (spectral) representations". Studies in applied mathematics 50.4 (1971), pp. 293–327. DOI: 10.1002/sapm1971504293.

[239] S. A. Orszag. "Spectral methods for problems in complex geometries". Vol. 37. 1. 1980, pp. 70–92. DOI: 10.1016/0021-9991(80)90005-4.

[240] C. Ortner and E. Süli. "Discontinuous Galerkin finite element approximation of nonlinear second-order elliptic and hyperbolic systems". SIAM Journal on Numerical Analysis 45.4 (2007), pp. 1370–1397. DOI: 10.1137/06067119X.

[241] B. Paap, D. Kraaijpoel, B. Wassing, and J.-D. Van Wees. "Simulation of induced seismic ground motions using coupled geomechanical and seismic wave propagation models". Geophysical Journal International 220.2 (2020), pp. 1284–1299. DOI: 10.1093/gji/ggz506.

[242] R. Paolucci, I. Mazzieri, G. Piunno, C. Smerzini, M. Vanini, and A. Özcebe. "Earthquake ground motion modeling of induced seismicity in the Groningen gas field". Earthquake Engineering & Structural Dynamics 50.1 (2021), pp. 135–154. DOI: 10.1002/eqe.3367.

[243] R. Pasquetti and F. Rapetti. "Spectral element methods on unstructured meshes: which interpolation points?" Numerical Algorithms 55.2-3 (2010), pp. 349–366. DOI: 10.1007/s11075-010-9390-0.

[244] C. Pelties, J. De la Puente, J.-P. Ampuero, G. B. Brietzke, and M. Käser. "Three-dimensional dynamic rupture simulation with a high-order discontinuous Galerkin method on unstructured tetrahedral meshes". Journal of Geophysical Research: Solid Earth 117.B2 (2012). DOI: 10.1029/2011JB008857.

[245] I. Perugia and D. Schötzau. "An hp-analysis of the local discontinuous Galerkin method for diffusion problems". Journal of Scientific Computing 17.1 (2002), pp. 561–571. DOI: 10.1023/A:1015118613130.

[246] A. Pitarka, A. Akinci, P. De Gori, and M. Buttinelli. "Deterministic 3D Ground-Motion Simulations (0–5 Hz) and Surface Topography Effects of the 30 October 2016 Mw 6.5 Norcia, Italy, Earthquake". Bulletin of the Seismological Society of America (Sept. 2021). ISSN: 0037-1106. DOI: 10.1785/0120210133.

[247] A. Pomonis, E. So, and J. Cousins. "Assessment of fatalities from the Christchurch New Zealand Earthquake of February 22nd, 2011". Seismological Society of America, 2011 Annual Meeting, April. 2011, pp. 13–15. DOI: 10.13140/RG.2.1.2191.3687.

[248] E. Priolo, J. M. Carcione, and G. Seriani. "Numerical simulation of interface waves by high-order spectral modeling techniques". The Journal of the Acoustical Society of America 95.2 (1994), pp. 681–693. DOI: 10.1121/1.408428.

[249] J. de la Puente, M. Käser, M. Dumbser, and H. Igel. "An arbitrary high-order discontinuous Galerkin method for elastic waves on unstructured meshes-IV. Anisotropy". Geophysical Journal International 169.3 (2007), pp. 1210–1228. DOI: 10.1111/j.1365-246X.2007.03381.x.

[250] A. Quarteroni. Numerical models for differential problems. Vol. 3. Springer, 2017. ISBN: 9783319493169. DOI: 10.1007/978-3-319-49316-9.

[251] R. Racke. "Heat conduction in elastic systems: Fourier versus Cattaneo". http://hdl.handle.net/2263/55905. 11-th International Conference on Heat Transfer, Fluid Mechanics and Thermodynamics. 2015.

[252] C. M. Rappaport. "Perfectly matched absorbing boundary conditions based on anisotropic lossy mapping of space". IEEE Microwave and Guided Wave Letters 5.3 (1995), pp. 90–92. DOI: 10.1109/75.366463.

[253] W. H. Reed and T. R. Hill. Triangular mesh methods for the neutron transport equation. Tech. rep. https://digital.library.unt.edu/ark:/67531/metadc1036080/. Los Alamos Scientific Lab., N. Mex.(USA), 1973.

[254] A. C. Reynolds. "Boundary conditions for the numerical solution of wave propagation problems". Geophysics 43.6 (1978), pp. 1099–1110. DOI: 10.1190/1.1440881.

[255] B. Rivière. Discontinuous Galerkin Methods for Solving Elliptic and Parabolic Equations: Theory and Implementation. SIAM, 2008. ISBN: 9780898716566. DOI: 10.1137/1.9780898717440.

[256] B. Rivière and M. F. Wheeler. "A discontinuous Galerkin Method Applied to Nonlinear Parabolic Equations". Discontinuous Galerkin Methods. Springer, 2000, pp. 231–244. DOI: 10.1007/978-3-642-59721-3_17.

[257] R. Roohi, S. Baroumand, R. Hosseinie, and G. Ahmadi. "Numerical simulation of HIFU with dual transducers: The implementation of dual-phase lag bioheat and non-linear Westervelt equations". International Communications in Heat and Mass Transfer 120 (2021), p. 105002. DOI: 10.1016/j.icheatmasstransfer.2020.105002.

[258] M. R. Ross, T. Walsh, J. W. Rouse, D. G. Tipton, E. Stasiunas, J. Freymiller, and M. Lawry. "Simulating the Response of External Stores on Aircraft Using Linear and Nonlinear Vibroacoustics". 54th AIAA/ASME/ASCE/AHS/ASC Structures, Structural Dynamics, and Materials Conference. 2013, p. 1557. DOI: 10.2514/6.2013-1557.

[259] T. D. Rossing. Springer Handbook of Acoustics. Vol. 1. Springer, 2007. ISBN: 9780387336336. DOI: 10.1007/978-0-387-30425-0.

[260] A. Rozanova-Pierrat. "On the derivation of the Khokhlov-Zabolotskaya-Kuznetsov (KZK) equation and validation of the KZK-approximation for viscous and non-viscous thermoelastic media". Communications in Mathematical Sciences 7.3 (2009), pp. 679–718. DOI: 10.4310/CMS.2009.v7.n3.a9.

[261] S. Rugonyi and K.-J. Bathe. "On finite element analysis of fluid flows fully coupled with structural interactions". CMES - Computer Modeling in Engineering and Sciences 2.2 (2001), pp. 195–212. DOI: 10.3970/cmes.2001.002.195.

[262] J. B. Rundle, J. R. Holliday, W. R. Graves, D. L. Turcotte, K. F. Tiampo, and W. Klein. "Probabilities for large events in driven threshold systems". Physical Review E 86.2 (2012), p. 021106. DOI: 10.1103/PhysRevE.86.021106.

[263] M. A. Sánchez, C. Ciuca, N. C. Nguyen, J. Peraire, and B. Cockburn. "Symplectic Hamiltonian HDG methods for wave propagation phenomena". Journal of Computational Physics 350 (2017), pp. 951–973. DOI: 10.1016/j.jcp.2017.09.010.

[264] J. Schmedes, R. J. Archuleta, and D. Lavallée. "A kinematic rupture model generator incorporating spatial interdependency of earthquake source parameters". Geophysical Journal International 192.3 (2013), pp. 1116–1131. DOI: 10.1093/gji/ggs021.

[265] R. Schneider, G. Faust, U. Hindenlang, and P. Helwig. "Inhomogeneous, orthotropic material model for the cortical structure of long bones modelled on the basis of clinical CT or density data". Computer Methods in Applied Mechanics and Engineering 198.27-29 (2009), pp. 2167–2174. DOI: 10.1016/j.cma.2009.02.010.

[266] S. Schoeder, M. Kronbichler, and W. A. Wall. "Arbitrary high-order explicit hybridizable discontinuous Galerkin methods for the acoustic wave equation". Journal of Scientific Computing 76.2 (2018), pp. 969–1006. DOI: 10.1007/s10915-018-0649-2.

[267] W. Schroeder, K. Martin, and B. Lorensen. The visualization toolkit. 4th ed. Kitware, 2006. ISBN: 9781930934191.

[268] C. Schwab. p-and hp-finite element methods: Theory and applications in solid and fluid mechanics. Oxford University Press, 1998. ISBN: 9780198503903.

[269] B. Schweizer. Partielle Differentialgleichungen. Springer, 2013. ISBN: 9783642406386. DOI: 10.1007/978-3-642-40638-6.

[270] G. Seriani and E. Priolo. "Spectral element method for acoustic wave simulation in heterogeneous media". Finite Elements in Analysis and Design 16.3-4 (1994), pp. 337–348. DOI: 10.1016/0168-874X(94)90076-0.

[271] C. Shearer and C. Cesnik. "Modified generalized alpha method for integrating governing equations of very flexible aircraft". 47th AIAA/ASME/ASCE/AHS/ASC Structures, Structural Dynamics, and Materials Conference 14th AIAA/ASME/AHS Adaptive Structures Conference 7th. 2006, p. 1747. DOI: 10.2514/6.2006-1747.

[272] P. M. Shearer. Introduction to Seismology. Cambridge university press, 2019. ISBN: 9781316877111. DOI: 10.1017/9781316877111.

[273] J. Shen, T. Tang, and L.-L. Wang. Spectral methods: algorithms, analysis and applications. Vol. 41. Springer Science & Business Media, 2011. ISBN: 9783540710417. DOI: 10.1007/978-3-540-71041-7.

[274] I. Shevchenko and B. Wohlmuth. "Self-adapting absorbing boundary conditions for the wave equation". Wave motion 49.4 (2012), pp. 461–473. DOI: 10.1016/j.wavemoti.2011.12.007.

[275] I. Shevchenko and B. Kaltenbacher. "Absorbing boundary conditions for nonlinear acoustics: The Westervelt equation". Journal of Computational Physics 302 (2015), pp. 200–221. DOI: 10.1016/j.jcp.2015.08.051.

[276] I. Shevchenko and B. Kaltenbacher. “Absorbing boundary conditions for the Westervelt equation”. Conference Publications. Vol. 2015. special. American Institute of Mathematical Sciences. 2015, pp. 1000–1008. DOI: 10.3934/proc.2015.1000.

[277] I. Shevchenko, M. Kaltenbacher, and B. Wohlmuth. “A multi-time stepping integration method for the ultrasound heating problem”. ZAMM-Journal of Applied Mathematics and Mechanics/Zeitschrift für Angewandte Mathematik und Mechanik 92.11-12 (2012), pp. 869–881. DOI: 10.1002/zamm.201200023.

[278] M. Šilhavý. “On Cauchy’s stress theorem”. Atti della Accademia Nazionale dei Lincei. Classe di Scienze Fisiche, Matematiche e Naturali. Rendiconti Lincei. Matematica e Applicazioni 1.3 (1990). https://eudml.org/doc/244201, pp. 259–263.

[279] G. Simonett and M. Wilke. “Well-posedness and longtime behavior for the Westervelt equation with absorbing boundary conditions of order zero”. Journal of Evolution Equations 17.1 (2017), pp. 551–571. DOI: 10.1007/s00028-016-0361-3.

[280] R. Stacey. “Improved transparent boundary formulations for the elastic-wave equation”. Bulletin of the Seismological Society of America 78.6 (1988), pp. 2089–2097. DOI: 10.1785/BSSA0780062089.

[281] M. Stupazzini, M. Infantino, A. Allmann, M. Kaeser, R. Paolucci, M. Mazzieri, and C. Smerzini. “PSHAe (Probabilistic Seismic Hazard Assessment Enhanced): the case of Istanbul”. Proceedings of the 16th World Conference on Earthquake Engineering (16WCEE2017), Santiago, Chile. Paper No. 1631, http://hdl.handle.net/11311/1061419. 2017.

[282] M. Stupazzini. “A Spectral Element Approach for 3D Dynamic Soil-Structure Interaction Problems”. PhD thesis. Politecnico di Milano, Apr. 2004.

[283] M. Stupazzini, R. Paolucci, and H. Igel. “Near-fault earthquake ground-motion simulation in the Grenoble valley by a high-performance spectral element code”. Bulletin of the Seismological Society of America 99.1 (2009), pp. 286–301. DOI: 10.1785/0120080274.

[284] J. Szeftel. “Absorbing boundary conditions for reaction–diffusion equations”. IMA Journal of Applied Mathematics 68.2 (2003), pp. 167–184. DOI: 10.1093/imamat/68.2.167.

[285] J. Szeftel. “A nonlinear approach to absorbing boundary conditions for the semilinear wave equation”. Mathematics of Computation 75.254 (2006), pp. 565–594. DOI: 10.1090/S0025-5718-06-01820-5.

[286] R. Tonn. “The Determination of the seismic quality factor Q from VSP data: A comparison of different computational methods”. Geophysical Prospecting 39.1 (1991), pp. 1–27. DOI: 10.1111/j.1365-2478.1991.tb00298.x.

[287] B. Tripathi. “Discontinuous Galerkin method for propagation of acoustical shock waves in complex geometry”. 2015PA066344. PhD thesis. Université Pierre et Marie Curie-Paris VI, 2015. URL: http://www.theses.fr/2015PA066344/document.

[288] A. Tryggvason, S. T. Rögnvaldsson, and O. G. Flóvenz. “Three-dimensional imaging of the P-and S-wave velocity structure and earthquake locations beneath Southwest Iceland”. Geophysical Journal International 151.3 (2002), pp. 848–866. DOI: 10.1046/j.1365-246X.2002.01812.x.

[289] S. Tu, S. Aliabadi, et al. “A slope limiting procedure in discontinuous Galerkin finite element method for gasdynamics applications”. International Journal of Numerical Analysis and Modeling 2.2 (2005), pp. 163–178. URL: http://www.math.ualberta.ca/ijnam/Volume-2-2005/No-2-05/2005-02-03.pdf.

[290] U.S. Geological Survey, 2021, Earthquake Event page. Weblink: https://earthquake.usgs.gov/earthquakes/eventpage/us7000c7y0/finite-fault, accessed May 26, 2021.

[291] A. Udías, R. Madariaga, and E. Buforn. Source Mechanisms of Earthquakes: Theory and Practice. Cambridge University Press, 2014. ISBN: 9781139628792. DOI: 10.1017/CBO9781139628792.

[292] F. Van de Vosse and P. Minev. “Spectral Elements Methods: Theory and Applications”. EUT report. W, Dept. of Mechanical Engineering (1996).

[293] I. Van Zelst, S. Wollherr, A.-A. Gabriel, E. H. Madden, and Y. van Dinther. “Modeling megathrust earthquakes across scales: One-way coupling from geodynamics and seismic cycles to dynamic rupture”. Journal of Geophysical Research: Solid Earth 124.11 (2019), pp. 11414–11446. DOI: 10.1029/2019JB017539.

[294] S. Veljović. Shape Optimization and Optimal Boundary Control for High Intensity Focused Ultrasound (HIFU). Shaker, 2010. ISBN: 9783832290672.

[295] J. G. Verwer. “Runge–Kutta methods and viscous wave equations”. Numerische Mathematik 112.3 (2009), pp. 485–507. DOI: 10.1007/s00211-009-0211-0.

[296] M. Villani, E. Faccioli, M. Ordaz, and M. Stupazzini. “High-resolution seismic hazard analysis in a complex geological configuration: the case of the Sulmona Basin in Central Italy”. Earthquake Spectra 30.4 (2014), pp. 1801–1824. DOI: 10.1193/1112911EQS288M.

[297] W. A. Wall, M. A. Frenzel, and C. Cyron. “Isogeometric structural shape optimization”. Computer methods in applied mechanics and engineering 197.33-40 (2008), pp. 2976–2988. DOI: 10.1016/j.cma.2008.01.025.

[298] T. Walsh and M. Torres. “Finite element methods for nonlinear acoustics in fluids”. Journal of Computational Acoustics 15.03 (2007), pp. 353–375. DOI: 10.1142/S0218396X0700338X.

[299] G. Wang, Y. Wang, W. Lu, M. Yu, and C. Wang. “Deterministic 3D seismic damage analysis of Guandi concrete gravity dam: A case study”. Engineering Structures 148 (2017), pp. 263–276. DOI: 10.1016/j.engstruct.2017.06.060.

[300] T. Warburton and G. E. Karniadakis. “A discontinuous Galerkin method for the viscous MHD equations”. Journal of Computational Physics 152.2 (1999), pp. 608–641. DOI: 10.1006/jcph.1999.6248.

[301] T. Warburton and J. S. Hesthaven. “On the constants in hp-finite element trace inverse inequalities”. Computer Methods in Applied Mechanics and Engineering 192.25 (2003), pp. 2765–2773. DOI: 10.1016/S0045-7825(03)00294-9.

[302] D. Werner. Funktionalanalysis. Springer, 2006. ISBN: 9783642210167. DOI: 10.1007/978-3-642-21017-4.

[303] P. J. Westervelt. “Parametric acoustic array”. The Journal of the Acoustical Society of America 35.4 (1963), pp. 535–537. DOI: 10.1121/1.1918525.

[304] M. F. Wheeler. “An Elliptic Collocation-Finite Element Method with Interior Penalties”. SIAM Journal on Numerical Analysis 15.1 (1978), pp. 152–161. DOI: 10.1137/0715010.

[305] L. C. Wilcox, G. Stadler, C. Burstedde, and O. Ghattas. “A high-order discontinuous Galerkin method for wave propagation through coupled elastic–acoustic media”. Journal of Computational Physics 229.24 (2010), pp. 9373–9396. DOI: 10.1016/j.jcp.2010.09.008.

[306] M. Wong. An Introduction to Pseudo-Differential Operators. 2014. DOI: 10.1142/9074.

[307] W. Wood, M. Bossak, and O. Zienkiewicz. “An alpha modification of Newmark’s method”. International Journal for Numerical Methods in Engineering 15.10 (1980), pp. 1562–1566. DOI: 10.1002/nme.1620151011.

[308] X. Wu and J. Zhang. “High-order local absorbing boundary conditions for heat equation in unbounded domains”. Journal of Computational Mathematics 29.1 (2011), pp. 74–90. DOI: 10.4208/jcm.1004-m3195.

[309] D. Xin, J. E. Daniell, and F. Wenzel. “State of the art of fragility analysis for major building types in China with implications for intensity-PGA relationships”. Natural Hazards and Earth System Sciences Discussions (2018), pp. 1–34. DOI: 10.5194/nhess-2018-254.

[310] S. Yoshizawa, T. Ikeda, A. Ito, R. Ota, S. Takagi, and Y. Matsumoto. “High intensity focused ultrasound lithotripsy with cavitating microbubbles”. Medical & biological engineering & computing 47.8 (2009), pp. 851–860. DOI: 10.1007/s11517-009-0471-y.

[311] L. C. Young. “A finite-element method for reservoir simulation”. Society of Petroleum Engineers Journal 21.01 (1981), pp. 115–128. DOI: 10.2118/7413-PA.

[312] L. C. Young. “Orthogonal collocation revisited”. Computer Methods in Applied Mechanics and Engineering 345 (2019), pp. 1033–1076. DOI: 10.1016/j.cma.2018.10.019.

[313] E. Zampieri and L. F. Pavarino. “An explicit second order spectral element method for acoustic waves”. Advances in Computational Mathematics 25.4 (2006), pp. 381–401. DOI: 10.1007/s10444-004-7626-z.

[314] E. Zampieri and L. F. Pavarino. “Approximation of acoustic waves by explicit Newmark’s schemes and spectral element methods”. Journal of computational and applied mathematics 185.2 (2006), pp. 308–325. DOI: 10.1016/j.cam.2005.03.013.

[315] E. Zampieri and A. Tagliani. “Numerical approximation of elastic waves equations by implicit spectral methods”. Computer methods in applied mechanics and engineering 144.1-2 (1997), pp. 33–50. DOI: 10.1016/S0045-7825(96)01167-X.

[316] J.-M. Zhang, Z. Yang, X. Gao, and J. Zhang. “Geotechnical aspects and seismic damage of the 156-m-high Zipingpu concrete-faced rockfill dam following the Ms 8.0 Wenchuan earthquake”. Soil Dynamics and Earthquake Engineering 76 (2015), pp. 145–156. DOI: 10.1016/j.soildyn.2015.03.014.

[317] L. Zhu, M. B. Altman, A. Laszlo, W. Straube, I. Zoberi, D. E. Hallahan, and H. Chen. “Ultrasound hyperthermia technology for radiosensitization”. Ultrasound in medicine & biology 45.5 (2019), pp. 1025–1043. DOI: 10.1016/j.ultrasmedbio.2018.12.007.

A. Core Articles

A.1. Self-adaptive absorbing boundary conditions for quasilinear acoustic wave propagation

Self-adaptive absorbing boundary conditions for quasilinear acoustic wave propagation

Markus Muhr, Vanja Nikolić and Barbara Wohlmuth

One of the first appearances of absorbing boundary conditions dates back to Engquist and Majda [95] who derived them for the linear wave equation. In more than one spatial dimension the quality of these conditions drastically depends on the angle of incidence of the wave at a given boundary part. Higdon [133] generalized the conditions to incorporate a whole set of angles for which the conditions work well, however, these angles need to be known a priori. Compared to the linear equation, Shevchenko and Kaltenbacher [275, 276] derived an extension taking into account the additional nonlinear terms of the nonlinear Westervelt equation in pressure form. In this article we combine ideas of both the angle incorporation side and the extensions to the nonlinear regime to develop absorbing boundary conditions for the Westervelt equation in potential form. Inspired by [274] the conditions contain an adaptive component that lets them automatically detect the angle of incidence and incorporates it to improve their quality.

Our derivation relies on a linearization of the considered PDE around a reference solution. Expressing the resulting equation in frequency space via a Fourier-transform lets us use methods from pseudo-differential calculus to factorize the partial differential wave operator into two parts, one being associated with a wave traveling towards the boundary the other with a wave traveling away from it. These operators are given in terms of asymptotic expansions allowing to determine their coefficients by solving an algebraic system. Also identifying the angle of incidence from the dispersion relation, transformation back to physical space and reinsertion of the (nonlinear) solution in place of the reference solution then finally yields angle dependent absorbing boundary conditions that also incorporate the nonlinear terms. For the adaptive computation of the angle of incidence we rely on the Poynting vector $P(\psi) = -\partial_t \psi \nabla \psi$ that can directly be computed from the wave field. Parameters to steer the sensitivity of the detection algorithm are introduced.

After the introduction, Sec. 2 gives a brief summary of the derivation and the different components of the Westervelt equation. Sec. 3 contains the mathematical main result. It discusses the aforementioned linearization, operator splitting and asymptotic expansion, where Subsec. 3.2.2 adds a short energy argument to also incorporate additional damping into the conditions. Sec. 4 then discusses the numerical treatment using finite elements and the generalized-α method for time integration, while Sec. 5 explains the angle detection algorithm in detail. Finally Sec. 6 contains a multitude of numerical experiments in 2D and 3D that show the capability of the derived conditions.

I was significantly involved in finding the ideas and carrying out the scientific work presented in this article including the write-up (in Sec. 3.2 only Subsec. 3.2.1). Furthermore I was solely in charge of the numerical part of the article, i.e. algorithm design, realization of the implementation and the creation of the figures.

Permission to include:

Muhr, Markus, Vanja Nikolić, and Barbara Wohlmuth
Self-adaptive absorbing boundary conditions for quasilinear acoustic wave propagation.
Journal of Computational Physics 388 (2019): 279-299.

Copyright

Describes the rights related to the publication and distribution of research. It governs how authors (as well as their employers or funders), publishers and the wider general public can use, publish and distribute articles or books.

Journal author rights Government employees Elsevier's rights Protecting author rights Open access

Journal author rights

In order for Elsevier to publish and disseminate research articles, we need publishing rights. This is determined by a publishing agreement between the author and Elsevier. This agreement deals with the transfer or license of the copyright to Elsevier and authors retain significant rights to use and share their own published articles. Elsevier supports the need for authors to share, disseminate and maximize the impact of their research and these rights, in Elsevier proprietary journals* are defined below:

For subscription articles	For open access articles
Authors transfer copyright to the publisher as part of a journal publishing agreement, but have the right to: • Share their article for Personal Use, Internal Institutional Use and Scholarly Sharing purposes, with a DOI link to the version of record on ScienceDirect (and with the Creative Commons CC-BY-NC- ND license for author manuscript versions) • Retain patent, trademark and other intellectual property rights (including research data). • Proper attribution and credit for the published work.	Authors sign an exclusive license agreement, where authors have copyright but license exclusive rights in their article to the publisher**. In this case authors have the right to: • Share their article in the same ways permitted to third parties under the relevant user license (together with Personal Use rights) so long as it contains a CrossMark logo, the end user license, and a DOI link to the version of record on ScienceDirect. • Retain patent, trademark and other intellectual property rights (including research data). • Proper attribution and credit for the published work.

***Please note that society or third party owned journals may have different publishing agreements. Please see the journal's guide for authors for journal specific copyright information.**

****This includes the right for the publisher to make and authorize commercial use, please see "Rights granted to Elsevier" for more details.**

Help and Support

- Download a sample publishing agreement for subscription articles in ↓ English and ↓ French.
- Download a sample publishing agreement for open access articles for authors choosing a ↓ commercial user license and ↓ non-commercial user license.
- For authors who wish to self-archive see our sharing guidelines
- See our author pages for further details about how to promote your article.
- For use of Elsevier material not defined below please see our permissions page or visit the Permissions Support Center ↗ .

Government employees

Elsevier has specific publishing agreements with certain government and inter-governmental organizations for their employee authors. These agreements enable authors to retain substantially the same rights as detailed in the "Author Rights section" but are specifically tailored for employees from the relevant organizations, including:

- World Bank
- World Health Organization
- For US government employees, works created within the scope of their employment are considered to be public domain and Elsevier's publishing agreements do not require a transfer or license of rights for such works.
- In the UK and certain commonwealth countries, a work created by a government employee is copyrightable but the government may own the copyright (Crown copyright). Click here for information about UK government employees publishing open access

Rights granted to Elsevier

For both subscription and open access articles, published in proprietary titles, Elsevier is granted the following rights:

- The exclusive right to publish and distribute an article, and to grant rights to others, including for commercial purposes.
- For open access articles, Elsevier will apply the relevant third party user license where Elsevier publishes the article on its online platforms.
- The right to provide the article in all forms and media so the article can be used on the latest technology even after publication.
- The authority to enforce the rights in the article, on behalf of an author, against third parties, for example in the case of plagiarism or copyright infringement.

Protecting author rights

Copyright aims to protect the specific way the article has been written to describe an experiment and the results. Elsevier is committed to its authors to protect and defend their work and their reputation and takes allegations of infringement, plagiarism, ethic disputes and fraud very seriously.

If an author becomes aware of a possible plagiarism, fraud or infringement we recommend contacting their Elsevier publishing contact who can then liaise with our in-house legal department. Note that certain open access user licenses may permit quite broad re-use that might otherwise be counted as copyright infringement. For details about how to seek permission to use an article see our permission page.

Open access

How copyright works with open access licenses

For Elsevier proprietary journals the following steps apply:

1. Authors sign a publishing agreement where they will have copyright but grant broad publishing and distribution rights to the publisher, including the right to publish the article on Elsevier's online platforms.
2. The author chooses an end user license under which readers can use and share the article.
3. The publisher makes the article available online with the author's choice of end user license.

Quick definitions

Personal use

Authors can use their articles, in full or in part, for a wide range of scholarly, non-commercial purposes as outlined below:

- Use by an author in the author's classroom teaching (including distribution of copies, paper or electronic)
- Distribution of copies (including through e-mail) to known research colleagues for their personal use (but not for Commercial Use)
- Inclusion in a thesis or dissertation (provided that this is not to be published commercially)
- Use in a subsequent compilation of the author's works
- Extending the Article to book-length form
- Preparation of other derivative works (but not for Commercial Use)
- Otherwise using or re-using portions or excerpts in other works

These rights apply for all Elsevier authors who publish their article as either a subscription article or an open access article. In all cases we require that all Elsevier authors always include a full acknowledgement and, if appropriate, a link to the final published version hosted on Science Direct.

Commercial use

This is defined as the use or posting of articles:

- **For commercial gain without a formal agreement with the publisher.**
  - For example by associating advertising with the full-text of the article, by providing hosting services to other repositories or to other organizations (including where an otherwise non-commercial site or repository provides a service to other organizations or agencies), or charging fees for document delivery or access
- **To substitute for the services provided directly by the journal.**
  - For example article aggregation, systematic distribution of articles via e-mail lists or share buttons, posting, indexing, or linking for promotional/marketing activities, by commercial companies for use by customers and intended target audiences of such companies (e.g. pharmaceutical companies and healthcare professionals/physician-prescribers).

If you would like information on how to obtain permission for such uses click here or if you would like to make commercial use of the article please visit the Permissions Support Center ↗ .

Internal institutional use

- Use by the author's institution for classroom teaching at the institution and for internal training purposes (including distribution of copies, paper or electronic, and use in coursepacks and courseware programs, but not in Massive Open Online Courses)
- Inclusion of the Article in applications for grant funding
- For authors employed by companies, the use by that company for internal training purposes

The above pages are copies from the webpage
https://www.elsevier.com/about/policies/copyright
Date: 03.12.2019

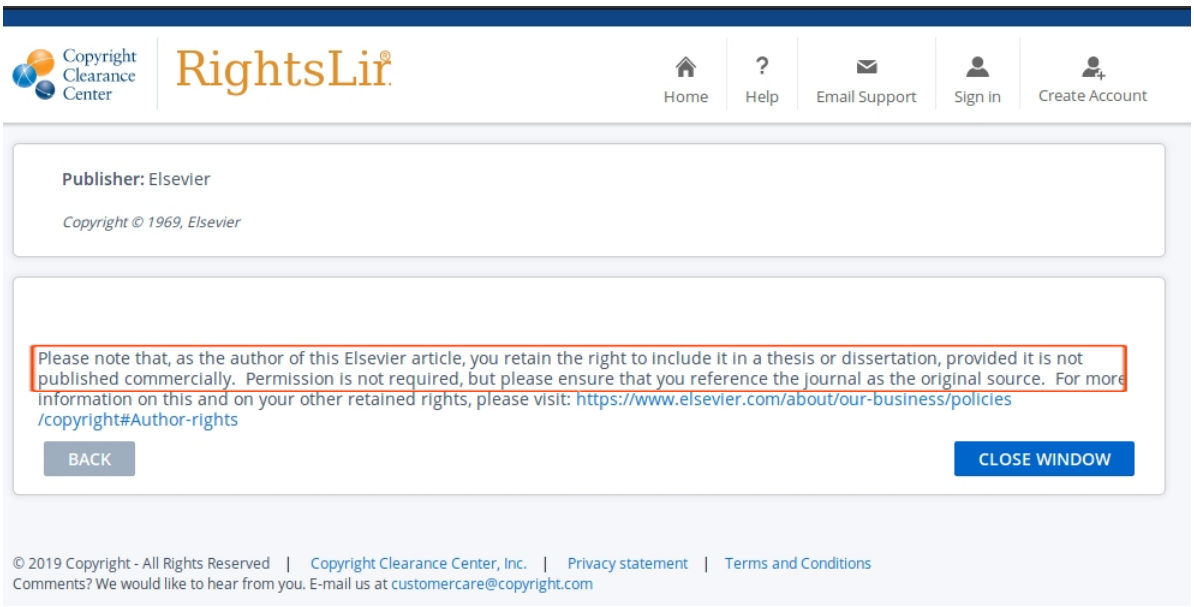

The above pages are copies from the webpage
https://s100.copyright.com/AppDispatchServlet#formTop
with input data:
https://s100.copyright.com/AppDispatchServlet?translating=No&rlPaymentProfileId=0&passThroughTarget=aboutyourwork-select&isMyAccount=false&convertibleP=%3C%25%3Dconvertible%25%3E&orderCurrencyCode=EUR&currentTargetPage=quickprice&myaccountlogin=true&publication=0021-9991&circulationRange=15&insideApp=true&defaultBillingType=Credit+Card&isCancelPressed=false&currentFooterPage=%2FApp%2FIncludes%2FFooter.jsp&publicationID=12613&popBackPage=&doCalc=true&jsonScriptName=&TermsAndConditions=&subPublisherID=-5555&buttonClicked=continue&currentBodyPage=%2FApp%2FQuickPrice.jsp&orderBeanReset=false&format=both+print+and+electronic&ignoreErrors=false&typeOfUseID=54&authorIndicator=Yes&linkClicked=unknown&timeStamp=1575450429212&offerIDValue=542&portionUsed=full+article&publisherID=70&install=&publisherName=ELS&loggedIn=false&orderThreadID=-5144448019828798206&rightID=1&grantDenyCheckIgnoreErrors=false&previousTargetPage=quickprice&requestToken=LAEVZ6C5oUFgz7PlJkJ7PAzz&currentTargetPageID=6134707&targetPage=inflowlogin&currentHeaderPage=%2FApp%2FIncludes%2FHeader.jsp&
Date: 09.12.2019

Journal of Computational Physics 388 (2019) 279–299

Contents lists available at ScienceDirect

Journal of Computational Physics

www.elsevier.com/locate/jcp

Self-adaptive absorbing boundary conditions for quasilinear acoustic wave propagation

Markus Muhr *, Vanja Nikolić, Barbara Wohlmuth

Technical University of Munich, Department of Mathematics, Chair of Numerical Mathematics, Boltzmannstraße 3, 85748 Garching, Germany

ARTICLE INFO

Article history:
Received 30 November 2018
Received in revised form 18 March 2019
Accepted 18 March 2019
Available online 21 March 2019

Keywords:
Absorbing conditions
Nonlinear acoustics
Westervelt's equation

ABSTRACT

We propose a self-adaptive absorbing technique for quasilinear ultrasound waves in two- and three-dimensional computational domains. As a model for the nonlinear ultrasound propagation in thermoviscous fluids, we employ Westervelt's wave equation solved for the acoustic velocity potential. The angle of incidence of the wave is computed based on the information provided by the wave-field gradient which is readily available in the finite element framework. The absorbing boundary conditions are then updated with the angle values in real time. Numerical experiments illustrate the accuracy and efficiency of the proposed method.

1. Introduction

Accurate simulation of nonlinear ultrasound offers a path to a better quality of many procedures in industry and medicine, from non-destructive detection of material damages [1–3] to non-invasive treatments of medical disorders [4–8]. When studying such procedures, there is always a region of interest: a kidney stone that will be disintegrated or a propagating fatigue crack in a component of an aircraft. The large physical space then often has to be truncated for numerical simulations. To accurately simulate ultrasound, we have to avoid spurious reflections of the wave at the boundary of the truncated domain.

Absorbing boundary conditions provide a simple and effective way of dealing with unwanted reflections. They were introduced by B. Engquist and E. Majda in their seminal work [9]. Since then many approaches have been developed for the non-reflecting boundary conditions; we refer the reader to the review papers [10,11] and the references given therein. In spite of such comprehensive research in this area, only a small portion of the results focus on nonlinear models.

A class of semilinear wave equations and nonlinear Schrödinger equations was investigated in [12,13]. Results for nonlinear hyperbolic systems of the form $u_t + A(u)u_x = 0$ were obtained in [14]. An approach based on the operator splitting method was used in [15] to derive absorbing conditions for a semilinear wave equation of the form $u_{tt} - a^2\Delta u = f(u)$. In [16,17], nonlinear ultrasound propagation was investigated in this context for the first time, and absorbing conditions were developed for the Westervelt equation in the pressure form.

Another commonly used approach for avoiding spurious reflections is the Perfectly Matched Layer (PML) technique. Developed by J.-P. Bérenger in [18], this method introduces an artificial absorbing layer around the computational domain. Linear acoustic wave equations have been extensively studied in this context; see, for example, [19–23].

* Corresponding author.
E-mail addresses: muhr@ma.tum.de (M. Muhr), vanja.nikolic@ma.tum.de (V. Nikolić), wohlmuth@ma.tum.de (B. Wohlmuth).

https://doi.org/10.1016/j.jcp.2019.03.025
0021-9991/

The main downside of absorbing conditions is that they are sensitive to the angle of incidence of the wave. As a rule of thumb, they perform bad if the range of incidence angles is large. The information on the incidence angles can be included in the conditions to tackle this issue; we refer to the work in [24–26]. However, these angles are not a priori known in a realistic computational setting. The idea behind the self-adaptive technique is to compute the local wave vector and then update the absorbing conditions with the angle information *in real time*. This approach was applied in [27] to the Schrödinger-type equations, where the wave number was computed via the Gabor transform. In [28], the linear wave equation was investigated in this context. It was proposed to divide the absorbing boundary into segments and compute the local incidence angle by employing the Fourier transformation only in the vicinity of the boundary. The self-adaptive approach to absorption can also be found in earlier works on acoustic scattering [29,30].

The goal of our work is to develop an efficient self-adaptive absorbing technique for nonlinear ultrasound propagation. As a model equation, we employ a classical quasilinear acoustic model - Westervelt's equation. We first extend the results from [16,17] by considering the potential form of Westervelt's equation and the non-zero angle of incidence θ. In addition, we derive the absorbing conditions for two- and three-dimensional computational domains. The derivation relies on choosing an appropriate linearization of the equation around a reference solution. The absorbing conditions are then formally derived for this linearization, after which we bring back the nonlinear term.

To obtain the angle θ in practice, we develop a self-adaptive method that locally computes the incidence angle and updates the absorbing conditions on the fly. Unlike the self-adaptive approach taken in [28], we base the local angle computation on the gradient of the wave field. Computation of the local propagation direction in isotropic media based on the information provided by the wave-field gradient has been studied in [31–36]. This approach is particularly suitable for our finite-element framework since the gradient information is already available at every time step in our simulations. The use of the field gradient information in the absorbing conditions has been already investigated for the Helmholtz equation in [37]. There it was proposed to replace the normal derivatives that appear in the absorbing conditions by the derivatives in the direction of the wave propagation. In the linear regime, our approach can be understood as an extension of the gradient method in [37] for a time-dependent wave model.

We organize the rest of the paper as follows. We begin in Section 2 by introducing the model and setting the problem. Section 3 contains the derivation of absorbing conditions for a given angle of incidence of the wave. In Section 4, we present the numerical scheme for solving the initial-boundary value problem for the Westervelt equation. Section 5 describes the computation of the local incidence angle via the information provided by the wave-field gradient. Finally, in Section 6, we present numerical experiments which illustrate the accuracy of the proposed adaptive boundary conditions.

2. Modeling and problem setting

The weakly nonlinear models in thermoviscous acoustics that are commonly used are obtained as an approximation of the compressible Navier-Stokes system. We here briefly reflect upon the derivation, which will give us a better understanding of the often-employed Westervelt equation. Mathematically rigorous justification of the classical acoustic models can be found in [38]. For a detailed insight into the acoustic field theory, we refer to [39–41].

Propagation of waves can be described by the time, the density $\bar{\varrho}$, the pressure $\bar{u}$ and the velocity $\bar{\mathbf{v}}$, decomposed into their ambient value and the acoustic perturbation

$$\begin{aligned}\bar{\varrho} &= \varrho_0 + \varrho,\\ \bar{u} &= u_0 + u,\\ \bar{\mathbf{v}} &= \mathbf{v}_0 + \mathbf{v};\end{aligned}$$

see [41]. We call ϱ the acoustic density, u the acoustic pressure, and $\mathbf{v}$ the acoustic particle velocity. The equations governing the wave propagation are then given by

- the equation of momentum conservation

$$(\varrho_0 + \varrho)\mathbf{v}_t + \frac{\varrho_0}{2}\nabla(\mathbf{v}\cdot\mathbf{v}) + \nabla u = \left(\frac{4\nu_V}{3} + \eta_V\right)\Delta\mathbf{v},$$

- the equation of mass conservation

$$\varrho_t + \varrho_0\nabla\cdot\mathbf{v} = -\varrho\nabla\cdot\mathbf{v} - \mathbf{v}\cdot\nabla\varrho,$$

- the pressure-density relation

$$\varrho = \frac{1}{c^2}u - \frac{1}{\varrho_0 c^4}\frac{B}{2A}u^2 - \frac{\kappa}{\varrho_0 c^4}\left(\frac{1}{c_\Omega} - \frac{1}{c_u}\right)u_t.$$

Above, η_V denotes the bulk viscosity and ν_V the shear viscosity. The constant κ stands for the adiabatic exponent, c_u and c_Ω denote the specific heat capacitance at constant pressure and constant volume, respectively. The parameter of nonlinearity B/A is an indicator of the nonlinearity of the medium. Finally, c denotes the speed of sound in the fluid.

This system of equations is approximated by one model, whereby every term of order two and higher in the acoustic Mach number is neglected. This approach results in

$$\begin{cases} \frac{1}{c^2}u_{tt} - \Delta u - \dfrac{b}{c^2}\Delta u_t = \dfrac{1}{\varrho_0 c^4}\dfrac{B}{2A}u_{tt} + \dfrac{\varrho_0}{c^2}\dfrac{\partial^2}{\partial t^2}(\mathbf{v}\cdot\mathbf{v}), \\ \varrho_0 \mathbf{v}_t = -\nabla u, \end{cases} \tag{1}$$

where the so-called sound diffusivity b is given by

$$b = \frac{1}{\varrho_0}\left(\frac{4\nu_V}{3} + \eta_V\right) + \frac{\kappa}{\varrho_0}\left(\frac{1}{c_V} - \frac{1}{c_u}\right).$$

The acoustic velocity potential ψ is then introduced to obtain a scalar equation; it is related to the acoustic pressure by

$$u \approx \varrho_0 \psi_t, \tag{2}$$

and to the acoustic particle velocity by

$$\mathbf{v} = -\nabla\psi. \tag{3}$$

By expressing (1) in terms of ψ, integrating with respect to time and taking the resulting constant of integration to be zero, we arrive at the Kuznetsov equation

$$\frac{1}{c^2}\psi_{tt} - \Delta\psi - \frac{b}{c^2}\Delta\psi_t = \frac{B/A}{c^4}\psi_t\psi_{tt} + \frac{2}{c^2}\nabla\psi\cdot\nabla\psi_t; \tag{4}$$

cf. [42]. If the cumulative nonlinear effects dominate the local ones in the sense of

$$\frac{2}{c^2}\nabla\psi\cdot\nabla\psi_t \approx \frac{2}{c^4}\psi_t\psi_{tt}, \tag{5}$$

a simplification of (4), known as the Westervelt equation [43], is obtained

$$\frac{1}{c^2}\psi_{tt} - \Delta\psi - \delta\Delta\psi_t = \frac{k}{c^2}\psi_t\psi_{tt}. \tag{6}$$

Above we have introduced the notation

$$\delta = \frac{b}{c^2},\ k = \frac{1}{c^2}(B/A + 2). \tag{7}$$

After numerically solving (6), the pressure field can be obtained in a post-processing step via the relation (2). We mention as well that the Westervelt equation in the pressure form is given by

$$\frac{1}{c^2}u_{tt} - \Delta u - \delta\Delta u_t = \frac{k}{\varrho c^2}(uu_{tt} + u_t^2). \tag{8}$$

Equation (8) can be obtained from (1) by employing the approximation (5) which in terms of the velocity and pressure reads as

$$\varrho_0(\mathbf{v}\cdot\mathbf{v})_t \approx \frac{1}{\varrho_0 c^2}(u^2)_t.$$

3. Absorbing conditions for the Westervelt equation

We consider the Westervelt equation (6) on a three-dimensional spatial domain $\Omega = \{(x, y, z) : x < 0,\ y, z \in \mathbb{R}\}$. We restrict ourselves in the problem description to the case of positive constant coefficients c, b, and k.

3.1. Linearization of the Westervelt equation

Following the approach from [16] where equation (8) was considered, we derive absorbing conditions for the Westervelt equation in the potential form (6) by first transforming it into a linear equation, deriving the non-reflecting conditions for this linear model, and then "plugging" back in the nonlinear term.

It is clear that the linearization of the equation plays a crucial role in deriving the absorbing conditions. A possible linearization of the Westervelt equation around a reference solution ψ^{ref} is given by

$$\frac{1}{c^2}\psi_{tt} - \Delta\psi - \delta\Delta\psi_t = \frac{k}{c^2}\beta(x, y, z, t)\,\psi_{tt}, \tag{9}$$

where $\beta = \psi_t^{\text{ref}}$. We note that, unlike in the derivation of the Westervelt equation in Section 2, here we do not split ψ into a background and oscillatory part, instead we assume ψ^{ref} to be a solution of the equation. This linearization is analogous to the one employed in [16] for the equation in the pressure formulation (8).

We propose an alternative linearization. Note that the right-hand side of the Westervelt equation (6) can be rewritten as $\frac{1}{2}\frac{k}{c^2}(\psi_t^2)_t$. We linearize the term ψ_t^2 as $\psi_t^{\text{ref}}\psi_t$ and study the following equation

$$\frac{1}{c^2}\psi_{tt} - \Delta\psi - \delta\Delta\psi_t = \frac{1}{2}\frac{k}{c^2}(\beta(x,y,z,t)\psi_t)_t, \tag{10}$$

where again $\beta = \psi_t^{\text{ref}}$. The absorbing boundary conditions based on linearizations (9) and (10) are numerically compared in Section 6.

We first derive absorbing conditions for the linear equation (10) and a given angle of incidence. After obtaining the conditions for such a model, the coefficient β is set back to ψ_t to obtain nonlinear conditions.

We remark that the linearization via Taylor expansion around a reference solution ψ^{ref} is not considered here since it would introduce the term $\psi_t^{\text{ref}}\psi_{tt}^{\text{ref}}$ into the linearized equation; we refer to a similar discussion in [16].

3.2. Derivation of absorbing conditions for the angle of incidence θ

We study here the derivation of the absorbing conditions for the linearization (10); equation (9) can be treated analogously. To derive the conditions, we could use the frozen coefficient approach which first transforms the variable coefficient equation into its constant-coefficient counterpart by "freezing" its coefficients at a given point before employing the Fourier transform in the (y,z,t) coordinates; cf. [9, Section 1]. Although the main focus of the present work is the derivation of the zero-order (adaptive) absorbing conditions, we still follow the approach based on the pseudo-differential calculus since it allows to arrive at a general system for determining the correcting terms beyond order zero in the absorbing conditions; see system (19) below.

We first rewrite the linearized equation (10) in the operator form as

$$\mathcal{P}u = 0, \tag{11}$$

where the operator $\mathcal{P}$ is given by

$$\mathcal{P} = \left(\frac{1}{c^2} - \frac{1}{2}\frac{k}{c^2}\beta(x,y,z,t)\right)\partial_t^2 - \partial_x^2 - \partial_y^2 - \partial_z^2 - \delta\partial_x^2\partial_t - \delta\partial_y^2\partial_t - \delta\partial_z^2\partial_t - \frac{1}{2}\frac{k}{c^2}\beta_t(x,y,z,t)\partial_t. \tag{12}$$

At this point we also introduce

$$\begin{aligned}\alpha_0(x,y,z,t) &= \sqrt{\frac{1}{c^2} - \frac{1}{2}\frac{k}{c^2}\beta(x,y,z,t)},\\ \alpha_1(x,y,z,t) &= \frac{1}{2}\frac{k}{c^2}\beta_t(x,y,z,t).\end{aligned} \tag{13}$$

Note that the well-posedness results for the Westervelt equation rely on the fact that the factor $\frac{1}{c^2}(1-k\psi_t)$ next to the second time derivative remains positive; see [44–46]. Therefore, it is reasonable to assume that the term under the square root in (13) is positive for sufficiently small data. We note that we proceed heuristically since the rigorous justification of the derivations given below would also require C^∞ regularity of α_0 and α_1 which is not proven here.

Absorbing boundary conditions for (11) will be derived by employing the pseudo-differential calculus and factorization of the operator $\mathcal{P}$ according to L. Nirenberg's procedure [47, Chapter II]. We briefly summarize the procedure here for the convenience of the reader. A detailed account on the pseudo-differential operators can be found in [48,47,49].

Definition 1. [49,50] Let the set $\mathcal{S}^m$, where $m \in \mathbb{R}$, be defined as the set of all functions $q(t,\tau) \in C^\infty(\mathbb{R}^d \times \mathbb{R}^d)$ such that for any two multi-indices k and l, there is a positive constant C_{kl} depending only on k and l, such that

$$|\partial_t^k \partial_\tau^l q(t,\tau)| \le C_{kl}(1+|\tau|)^{m-|l|}, \quad t,\tau \in \mathbb{R}^d.$$

$\mathcal{S}^m$ is called the space of symbols of order m. We set $S^{-\infty} = \cap_{m\in\mathbb{R}}\mathcal{S}^m$.

Definition 2. [49, Definition 5.2] Let q be a symbol. The pseudo-differential operator $\mathcal{Q}$ associated to q is defined by

$$(\mathcal{Q}\varphi)(t) = (2\pi)^{-d/2}\int_{\mathbb{R}^d} e^{it\cdot\tau}\, q(t,\tau)\,\mathcal{F}\varphi(\tau)\,d\tau,$$

where φ is a function from the Schwartz space, and $\mathcal{F}$ denotes the Fourier transform.

3.2.1. Propagation without losses

Following the approach in [16], we first derive the absorbing conditions with the assumption that $\delta = 0$. This assumption facilitates the derivation of the conditions based on the pseudo-differential factorization. The δ-term will be included as a post-processing step based on energy arguments.

The derivation of the conditions relies on the fact that the operator $\mathcal{P}$ can be factorized into the form

$$\mathcal{P} = -\left(\partial_x - \mathcal{A}\left(x, y, z, t, \partial_y, \partial_z, \partial_t\right)\right)\left(\partial_x - \mathcal{B}\left(x, y, z, t, \partial_y, \partial_z, \partial_t\right)\right) + \mathcal{R}\left(x, y, z, t, \partial_y, \partial_z, \partial_t\right); \tag{14}$$

see [47, Lemma 1]. In (14), the operators $\mathcal{A}$ and $\mathcal{B}$ are pseudo-differential operators with the symbols $a(x, y, z, t, \eta, \zeta, \tau)$ and $b(x, y, z, t, \eta, \zeta, \tau)$, respectively, from the space $\mathcal{S}^1$. The conditions on $\mathcal{A}$ that we will develop will have the effect of associating $\mathcal{A}$ with waves that travel out of the computational domain. The pseudo-differential operator $\mathcal{R}$ is a smoothing operator with the full symbol $r(x, y, z, t, \eta, \zeta, \tau)$ that belongs to $\mathcal{S}^{-\infty}$.

The symbols a and b formally admit asymptotic expansions

$$a(x, y, z, t, \eta, \zeta, \tau) \sim \sum_{j\geq 0} a_{1-j}(x, y, z, t, \eta, \zeta, \tau),$$
$$b(x, y, z, t, \eta, \zeta, \tau) \sim \sum_{j\geq 0} b_{1-j}(x, y, z, t, \eta, \zeta, \tau),$$

where a_{1-j} and b_{1-j} denote homogeneous functions of degree $1-j$ with respect to τ; see [49, Theorem 5.10]. We note that the symbol $a(x, y, z, t, \eta, \zeta, \tau)b(x, y, z, t, \eta, \zeta, \tau)$ of the product of $\mathcal{A}$ and $\mathcal{B}$ has an asymptotic expansion as well

$$a(x, y, z, t, \eta, \zeta, \tau)b(x, y, z, t, \eta, \zeta, \tau) \sim \sum_{\substack{j\geq 0,\\ k+l+n=j,\\ k,l,n\geq 0}} \frac{(-1)^n}{n!}\partial_\tau^n a_{1-l}(x, y, z, t, \eta, \zeta, \tau)\partial_t^n b_{1-k}(x, y, z, t, \eta, \zeta, \tau);$$

see [49, Theorem 7.1].

According to [51, Theorems 1 and 2], absorbing boundary conditions on the boundary $x = 0$ are given in the form

$$\left(\partial_x - \mathcal{A}\left(x, y, z, t, \partial_y, \partial_z, \partial_t\right)\right)\psi\Big|_{x=0} = 0.$$

Since the symbol a of $\mathcal{A}$ has an infinite expansion, in numerical simulations this expansion is truncated after a certain number of terms. Absorbing conditions of order $k \in \mathbb{N}_0$ are then on the symbolic level given by

$$\left(\partial_x - \sum_{j=0}^{k} a_{1-j}(0, y, z, t, \eta, \zeta, \tau)\right)\psi\Big|_{x=0} = 0. \tag{15}$$

The higher-order absorbing conditions, although numerically more accurate, are also significantly more involved when it comes to implementation. We will compute the absorbing conditions of order zero for the given angle of incidence θ. Combined with the proposed self-adaptive technique, this approach allows to improve the accuracy of zero-order conditions, yet keeps them easy to implement.

We recall how the operator $\mathcal{P}$ was defined in (12), set $\delta = 0$, and then develop factorization (14) to obtain

$$\begin{aligned} &\alpha_0^2\,\partial_t^2 - \partial_x^2 - \partial_y^2 - \partial_z^2 - \alpha_1\partial_t \\ &= -\partial_x^2 + (\mathcal{A}+\mathcal{B})\partial_x + \mathcal{B}_x - \mathcal{A}\mathcal{B} + \mathcal{R}. \end{aligned} \tag{16}$$

By employing the asymptotic expansion of the symbols a, b, and ab, equation (16) reduces on the symbolic level to

$$\begin{aligned} &\alpha_0^2(i\tau)^2 - (i\eta)^2 - (i\zeta)^2 - \alpha_1(i\tau) \\ &\cong \sum_{j\geq 0}(a_{1-j} + b_{1-j})\partial_x + \sum_{j\geq 0}\partial_x b_{1-j} - \sum_{\substack{j\geq 0,\\ k+l+n=j,\\ k,l,n\geq 0}} \frac{(-1)^n}{n!}\partial_\tau^n a_{1-l}\partial_t^n b_{1-k}. \end{aligned} \tag{17}$$

Above, we have denoted the dual variables to t, y, and z by τ, η, and ζ, with the correspondence $\partial_t \leftrightarrow i\tau$, $\partial_y \leftrightarrow i\eta$, and $\partial_z \leftrightarrow i\zeta$. Following the notation in [9], $\cong$ stands for "within a smooth error" because we have dropped $\mathcal{R}$. We note that the operator R can only be controlled in terms of its smoothness. However, its action on the solution is expected to be negligible for high frequencies that are present in ultrasound waves.

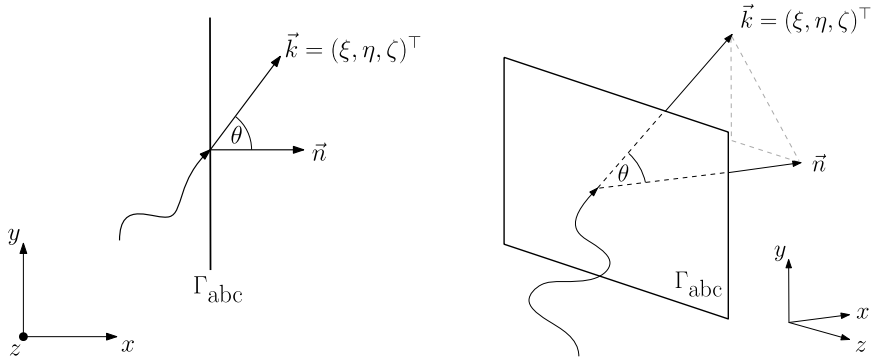

Fig. 1. Illustration of the interplay between the wave vector $\vec{k}$, outward normal vector $\vec{n}$, and the angle of incidence θ.

To determine a_1 and b_1, we equate the symbols with the same degree of homogeneity with respect to τ and get the system

$$\begin{cases} a_1 + b_1 = 0 \\ a_1 b_1 = -(\alpha_0^2 (i\tau)^2 - (i\eta)^2 - (i\zeta)^2), \end{cases} \tag{18}$$

assuming that $\alpha_0^2 \tau^2 \cong \eta^2 + \zeta^2$. The system that determines the coefficients $\{a_{1-j}, b_{1-j}\}_{j\geq 1}$ is then given by

$$\begin{cases} a_{1-j} + b_{1-j} = 0, \qquad j \geq 1, \\ -\alpha_1 (i\tau)\delta_{j1} = - \displaystyle\sum_{\substack{j\geq 1, \\ k+l+n=j, \\ k,l,n\geq 0}} \frac{(-1)^n}{n!} \partial_\tau^n a_{1-l} \partial_t^n b_{1-k} + \partial_x b_{1-j}, \end{cases} \tag{19}$$

where δ denotes the Kronecker delta. From (18), we find that

$$a_1 = -\sqrt{\alpha_0^2 (i\tau)^2 - (i\eta)^2 - (i\zeta)^2}$$

and

$$b_1 = \sqrt{\alpha_0^2 (i\tau)^2 - (i\eta)^2 - (i\zeta)^2}.$$

Note that the sign of a_1 determines the propagation direction of the wave. To obtain the absorbing conditions for the given angle of incidence, we freeze the coefficient β in (12) by assuming that it is constant in space and time. The dispersion relation for (10) when β is constant is as follows

$$\alpha_0^2 (i\tau)^2 - (i\xi)^2 - (i\eta)^2 - (i\zeta)^2 = 0. \tag{20}$$

The wave vector is given by (ξ, η, ζ). If we denote by $\theta \in [0°, 90°]$ the angle between the incident wave and the outer normal to the boundary, we have for $\tau > 0$

$$\sin\theta = \frac{\sqrt{\eta^2 + \zeta^2}}{\sqrt{\xi^2 + \eta^2 + \zeta^2}} = \frac{\sqrt{\eta^2 + \zeta^2}}{\alpha_0 \tau};$$

see Fig. 1.

Therefore, we can express a_1 as

$$a_1 = -\alpha_0 (i\tau) \sqrt{1 - \frac{\eta^2 + \zeta^2}{\alpha_0^2 \tau^2}} = -\alpha_0 (i\tau) \cos\theta.$$

According to (15), the absorbing conditions of order zero are then given by

$$\frac{\partial \psi}{\partial n} = -\alpha_0 \, \psi_t \cos\theta. \tag{21}$$

We mention that for a variable coefficient problem with jumps outside the computational domain, it is not possible to build an exact ABC based on local computations. After returning to $\beta = \psi_t$ and $\alpha_0 = \sqrt{\frac{1}{c^2} - \frac{1}{2}\frac{k}{c^2}\psi_t}$, we obtain the absorbing boundary conditions for the inviscid Westervelt equation in the potential formulation for a given angle of incidence θ:

$$c\frac{\partial \psi}{\partial n} + \sqrt{1 - \frac{k}{2}\psi_t}\,\psi_t\,\cos\theta = 0. \tag{22}$$

3.2.2. Propagation with losses

We next want to incorporate the b term into the conditions. This was not possible before since we needed $b = 0$ to make use of the pseudo-differential factorization and the dispersion relation (20). Instead, we employ a reasoning based on an energy argument.

To this end, we test the linearized equation (10) with ψ_t, integrate over space and $(0, t)$, where $t \le T$, and integrate by parts with respect to time, to arrive at the following identity:

$$\begin{aligned} &E_0[\psi](t) + \delta \int_0^t \|\nabla \psi_t\|^2_{L^2(\Omega)}\,\mathrm{d}s \\ &= E_0[\psi](0) + \int_0^t \int_\Omega \left(\tfrac{1}{2}(\alpha_0^2)_t + \alpha_1\right)\psi_t^2\,\mathrm{d}x\mathrm{d}s + \int_0^t \int_{\partial\Omega} \left(\frac{\partial \psi}{\partial n} + \delta\frac{\partial \psi_t}{\partial n}\right)\psi_t\,\mathrm{d}x\mathrm{d}s, \end{aligned} \tag{23}$$

where the energy is given by

$$E_0[\psi](t) = \frac{1}{2}\left(\|\alpha_0(t)\psi_t(t)\|^2_{L^2(\Omega)} + \|\nabla\psi(t)\|^2_{L^2(\Omega)}\right).$$

This identity suggests to modify the conditions (21) to include the sound diffusivity as follows

$$\frac{\partial \psi}{\partial n} + \delta\frac{\partial \psi_t}{\partial n} = -\alpha_0\,\psi_t\cos\theta \quad \text{on } \Gamma_{\text{abc}}. \tag{24}$$

These conditions facilitate the extraction of energy through the boundary since (23) becomes

$$\begin{aligned} &E_0[\psi](t) + \delta \int_0^t \|\nabla \psi_t\|^2_{L^2(\Omega)}\,\mathrm{d}s + \int_0^t \left\|\sqrt{\alpha_0\cos\theta}\,\psi_t\right\|^2_{L^2(\partial\Omega)}\,\mathrm{d}s \\ &= E_0[\psi](0) + \int_0^t \int_\Omega (\tfrac{1}{2}(\alpha_0^2)_t + \alpha_1)\psi_t^2\,\mathrm{d}x\mathrm{d}s, \end{aligned} \tag{25}$$

from which by employing Gronwall's inequality it follows that

$$E_0[\psi](t) + \delta \int_0^t \|\nabla \psi_t\|^2_{L^2(\Omega)}\,\mathrm{d}s + \int_0^t \left\|\sqrt{\alpha_0\cos\theta}\,\psi_t\right\|^2_{L^2(\partial\Omega)}\,\mathrm{d}s \le C(T)E_0[\psi](0),$$

provided $\frac{1}{2}(\alpha_0^2)_t + \alpha_1 \in L^\infty(0, T; L^\infty(\Omega))$.

We therefore adopt conditions (24). After returning to $\beta = \psi_t$ and $\alpha_0 = \sqrt{\frac{1}{c^2} - \frac{1}{2}\frac{k}{c^2}\psi_t}$ in (24) and recalling that $\delta = b/c^2$, we obtain the nonlinear conditions

$$c^2\frac{\partial \psi}{\partial n} + b\frac{\partial \psi_t}{\partial n} = -c\sqrt{1 - \frac{k}{2}\psi_t}\,\psi_t\,\cos\theta \quad \text{on } \Gamma_{\text{abc}}. \tag{26}$$

We note that in realistic settings the sound diffusivity b in fluids is small; see, e.g., [41]. It is also known that the presence of a large b damping in the model would imply a parabolic instead of a wave-like behavior of the equation resulting in an exponential decay of the energy; cf. [44, Theorem 3.3].

Setting k to zero in (26) corresponds to conditions for a linear, strongly damped wave equation. If in addition $b = 0$, we end up with the standard linear absorbing conditions for the angle θ

$$c\frac{\partial \psi}{\partial n} + \psi_t\,\cos\theta = 0 \quad \text{on } \Gamma_{\text{abc}}; \tag{27}$$

see [24,26].

Remark 1 *(One- and two-dimensional domains).* In a one-dimensional setting, system (18) for determining the symbols a_1 and b_1 simplifies to

$$\begin{cases} a_1 + b_1 = 0 \\ a_1 b_1 = -\alpha_0^2 (i\tau)^2. \end{cases}$$

In a two-dimensional setting, system (18) simplifies to

$$\begin{cases} a_1 + b_1 = 0 \\ a_1 b_1 = -(\alpha_0^2 (i\tau)^2 - (i\eta)^2). \end{cases}$$

It is then straightforward to show that conditions (26) hold in 1D and 2D as well, where in 1D the angle θ can be interpreted as being set to $\theta = 0°$.

Remark 2 *(A different linearization).* Employing linearization (9) would result in the following absorbing conditions

$$c^2 \frac{\partial \psi}{\partial n} + b \frac{\partial \psi_t}{\partial n} = -c \sqrt{1 - k\psi_t}\, \psi_t \cos\theta \quad \text{on } \Gamma_{\text{abc}}. \tag{28}$$

The performance of conditions (26) and (28) is compared in Section 6, where the proposed conditions (26) significantly outperform (28).

Remark 3. In our experiments, we employ the gradient information to compute the angle of incidence θ via

$$\cos\theta = \frac{|\nabla\psi \cdot n|}{\sqrt{\psi_x^2 + \psi_y^2 + \psi_z^2}} \quad \text{on } \Gamma_{\text{abc}},$$

assuming that $\nabla\psi \neq \mathbf{0}$ on the absorbing boundary. The linear conditions (27) for the angle θ are then equivalent to

$$c|\nabla\psi| + \psi_t = 0 \quad \text{on } \Gamma_{\text{abc}}. \tag{29}$$

Therefore, in the linear regime, conditions (29) can be seen as the extension of the absorbing conditions proposed in [37] for the Helmholtz equation to the linear time-dependent wave model.

4. Numerical treatment

After deriving the absorbing boundary conditions for the potential form of the Westervelt equation (6), we next focus on the numerical schemes used in simulations. We begin by formulating the initial-boundary value problem that has to be solved.

4.1. The initial-boundary value problem for the Westervelt equation

We consider the following problem for the Westervelt equation:

$$\begin{cases} \psi_{tt} - c^2\Delta\psi - b\Delta\psi_t = \dfrac{1}{c^2}(B/A + 2)\,\psi_t\psi_{tt} & \text{in } \Omega \times (0,T), \\ \psi = g & \text{on } \Gamma_{\text{exc}} \times (0,T), \\ c\dfrac{\partial\psi}{\partial n} + \dfrac{b}{c}\dfrac{\partial\psi_t}{\partial n} = -\sqrt{1-\sigma k\psi_t}\,\psi_t \cos\theta(\psi) & \text{on } \Gamma_{\text{abc}} \times (0,T), \\ \dfrac{\partial\psi}{\partial n} = 0 & \text{on } \Gamma_{\text{N}} \times (0,T), \\ \psi = \psi_t = 0 & \text{in } \Omega \times \{0\}. \end{cases} \tag{30}$$

The wave source is given in the form of inhomogeneous Dirichlet conditions on the excitation part of the domain boundary $\Gamma_{\text{exc}} \subset \partial\Omega$. In our numerical tests, the excitation signal is always taken to be a modulated sine wave, that is growing over time until its maximal amplitude is reached, i.e.,

$$g(t) = \begin{cases} (f^2/4)t^2\, \mathfrak{A} \sin(\omega t), & t < 2/f, \\ \mathfrak{A} \sin(\omega t), & t \geq 2/f, \end{cases} \tag{31}$$

where f denotes the frequency, $\omega = 2\pi f$ the angular frequency, and $\mathfrak{A}$ the maximal amplitude of the signal.

We have introduced the parameter σ within the square root of the absorbing conditions in (30). In this way, we generalized in one formula all the absorbing conditions that we want to compare. Indeed, setting $\sigma = 0$ yields the adaptive absorbing conditions for the linear strongly damped wave equation

$$c\frac{\partial \psi}{\partial n} + \frac{b}{c}\frac{\partial \psi_t}{\partial n} = -\psi_t \cos\theta(\psi), \tag{32}$$

which we denote from now on in experiments by "$\mathrm{ABC}^0_{\mathrm{W}}$ adaptive". In case also $\theta = 0$ everywhere, we denote them just by $\mathrm{ABC}^0_{\mathrm{W}}$. Setting $\sigma = 1/2$ recovers our new nonlinear adaptive conditions, denoted by "$\mathrm{ABC}^{1/2}_{\mathrm{W}}$ adaptive". If the angle is always set to zero, we denote them just by $\mathrm{ABC}^{1/2}_{\mathrm{W}}$. Finally, $\sigma = 1$ leads to conditions based on the second linearization (9), which are denoted in the experiments by "$\mathrm{ABC}^1_{\mathrm{W}}$ adaptive" and $\mathrm{ABC}^1_{\mathrm{W}}$.

We start from the weak form of the problem (30). We are looking for a solution in

$$\{\psi \in C^1([0,T]; H^2(\Omega)) \cap C^2([0,T]; H^1(\Omega)) \mid \psi = g \text{ on } \Gamma_{\mathrm{exc}} \times (0,T)\}$$

such that

$$\int_\Omega ((1-k\psi_t)\psi_{tt} v + c^2 \nabla\psi \cdot \nabla v + b\nabla\psi_t \cdot \nabla v)\,\mathrm{d}\Omega + \int_{\Gamma_{\mathrm{abc}}} c\sqrt{1-\sigma k\psi_t}\,\psi_t \cos\theta(\psi)\, v\,\mathrm{d}S = 0$$

for all test functions in $\{v \in H^1(\Omega) \mid v = 0 \text{ on } \Gamma_{\mathrm{exc}} \times (0,T)\}$ a.e. in time, with $(\psi, \psi_t)|_{t=0} = (0,0)$. We assume that the problem (30) is well-posed, although the rigorous proof is beyond the scope of the current work. Results on the well-posedness of the Westervelt equation in the pressure form with nonlinear absorbing conditions for the angle of incidence $\theta = 0°$ can be found in [17,52].

4.2. Finite element discretization and time integration

We follow the standard discretization methods for nonlinear acoustics based on finite elements [41,53–57]. The finite element method is employed in space with lowest order conforming elements on simplicial meshes.

The mass $\mathbf{M}$, stiffness $\mathbf{K}$, and damping matrix $\mathbf{C}$ as well as the nonlinearity tensor $\mathcal{T}$ are assembled in the usual manner; see [41,56]. By dividing the set of degrees of freedom into the set of Dirichlet degrees D and the set of interior degrees I, the semi-discrete problem reads as follows

$$\begin{cases} \mathbf{M}_{\mathrm{I,I}}\ddot{\underline{\psi}}_{\mathrm{I}} + \mathbf{K}_{\mathrm{I,I}}\underline{\psi}_{\mathrm{I}} + \mathbf{C}_{\mathrm{I,I}}\dot{\underline{\psi}}_{\mathrm{I}} - \mathcal{T}_{\mathrm{I,I,I}}[\ddot{\underline{\psi}}_{\mathrm{I}}, \dot{\underline{\psi}}_{\mathrm{I}}, \cdot] - \mathcal{T}_{\mathrm{I,D,I}}[\ddot{\underline{\psi}}_{\mathrm{I}}, \dot{\underline{\psi}}_{\mathrm{D}}, \cdot] & \\ -\mathcal{T}_{\mathrm{D,I,I}}[\ddot{\underline{\psi}}_{\mathrm{D}}, \dot{\underline{\psi}}_{\mathrm{I}}, \cdot] + \underline{\mathbf{A}}_{\mathrm{I}}(\underline{\psi}, \dot{\underline{\psi}}, \theta(\psi)) = F(t) & \text{in } (0,T), \\ \underline{\psi} = \dot{\underline{\psi}} = 0 & \text{at } t = 0. \end{cases} \tag{33}$$

The right-hand side of the equation is given by

$$F(t) = -\mathbf{M}_{\mathrm{I,D}}\ddot{\underline{\psi}}_{\mathrm{D}} - \mathbf{K}_{\mathrm{I,D}}\underline{\psi}_{\mathrm{D}} - \mathbf{C}_{\mathrm{I,D}}\dot{\underline{\psi}}_{\mathrm{D}} + \mathcal{T}_{\mathrm{D,D,I}}[\ddot{\underline{\psi}}_{\mathrm{D}}, \dot{\underline{\psi}}_{\mathrm{D}}, \cdot].$$

The underlined quantities $\underline{\psi}$, $\dot{\underline{\psi}}$, and $\ddot{\underline{\psi}}$ denote the coefficient vectors of ψ, ψ_t, and ψ_{tt} resulting from the spatial finite element discretization. The compact notation with index sets D and I is used to extract the respective rows and columns of matrices and vectors that belong to Dirichlet and interior degrees of freedom.

The absorbing boundary vector $\underline{\mathbf{A}}$ is formally given by

$$\begin{aligned} &\underline{\mathbf{A}}(\psi_t, \theta(\psi)) = (A_i(\psi_t, \theta(\psi)))_{i \in \mathrm{DOF}(\Gamma_{\mathrm{abc}})}, \\ &A_i(\psi_t, \theta(\psi)) = \int_{\Gamma_{\mathrm{abc}}} c\sqrt{1-\sigma k\psi_t}\,\psi_t \cos\theta(\psi)\, N_i\,\mathrm{d}S. \end{aligned} \tag{34}$$

Above, N_i stands for the finite element ansatz function of the i-th global degree of freedom, while $\mathrm{DOF}(\Gamma_{\mathrm{abc}})$ is the set of degrees of freedom belonging to the absorbing boundary.

The nonlinearity tensor $\mathcal{T}$ is used to resolve the nonlinear bulk term in the weak formulation in a fixed-point iteration. The same also holds for the absorbing boundary vector which is iteratively updated with the current values of ψ_t, ψ_{tt} as well as updates for the angle θ.

The system (33) is a nonlinear system of ordinary differential equations of second order with $|\mathrm{I}|$ components. It remains to solve it by using a suitable time integrator. Following [56], we employ the Generalized-α scheme in combination with the Newmark relations for time integration. Values of the Generalized-α parameters (α_m, α_f) and the Newmark parameters

Table 1
Time-stepping parameters.

	parameter	value
Newmark-parameters	β_{nm}	4/9
	γ_{nm}	5/6
Generalized-α parameters	α_m	0
	α_f	1/3
Nonlinear iteration parameters	TOL	10^{-6}
	$\kappa_{\max}$	100

$(\beta_{\text{nm}}, \gamma_{\text{nm}})$ that are used in experiments are chosen according to the stability and accuracy criteria stated in [58]:

$$\alpha_m = \frac{2\rho_\infty - 1}{1+\rho_\infty}, \quad \alpha_f = \frac{\rho_\infty}{1+\rho_\infty}, \quad \beta_{\text{nm}} = \frac{1}{(1+\rho_\infty)^2}, \quad \gamma_{\text{nm}} = \frac{1}{2}\frac{3-\rho_\infty}{1+\rho_\infty}$$

where we take $\rho_\infty = 1/2$; see also Table 1 for the resulting values.

In comparison to the numerical solvers proposed in [53,56], a new aspect of our method is the computation of the angle of incidence $\theta(\psi)$. The angle is computed once in every time step before the first assembly of the absorbing boundary vector. Details on how we compute the angle can be found in Section 5.

5. Computation of the angle of incidence

It remains to see how we can compute the angle of incidence θ that the local wave vector encloses with the outward normal to the absorbing boundary at a given point on Γ_{abc}. To reduce the computational cost, we compute the angle θ once per time step and do not update it within the nonlinear fixed-point iteration.

According to [33,35], the Poynting vector $\mathbf{P}(\psi)$ of a wave field ψ can be used to compute its local propagation direction. The vector $\mathbf{P}(\psi)$ is given by

$$\mathbf{P}(\psi) = -\frac{\partial \psi}{\partial t}\nabla\psi. \tag{35}$$

Since neither the sign nor the norm of the propagation vector plays a role when computing the incidence angle, we restrict ourselves to the spatial gradient alone to determine the main propagation direction of the wave. Such an approach was also taken in [31,34,36] for wave fields in an isotropic medium. In our case, this method of computing the local propagation direction works especially well since, although globally discontinuous, the element-wise gradient information is readily available at every time step in the finite element framework. We also refer to [32] for a further discussion on the use of the Poynting vector in angle decomposition methods.

We conduct experiments with zero initial data and inhomogeneous Dirichlet conditions on part of the boundary, and so most of the potential field is at rest at the beginning of the simulation. However, numerical noise of low magnitude can be present at the absorbing boundary before the wave reaches it. Such behavior could be accounted to weak ill-posedness; see [59]. To tackle this issue, we implement a switch. When going over all elements adjacent to the absorbing boundary, we only compute the element-wise angle of incidence once the local wave amplitude (in terms of absolute value of the elements degrees of freedom) exceeds a certain percentage p_1 of a reference value; see Algorithm 1, line 3. We take the reference value to be the source amplitude of the wave. In the case that the source amplitude is not known a priori, an alternative would be to compute the maximum field amplitude in the interior of the domain and take this as a reference value. As long as the criterion is not matched, the local angle of incidence is set to 0; see Algorithm 1, line 14. We note that a similar approach was taken in [28]. In all our numerical experiments, we set $p_1 = 0.1$.

Algorithm 1 summarizes our method of computing the incidence angle. Within the algorithm, indices in the exponent indicate the time step.

Note that even once the local amplitude of the wave at a given element is large enough for the angle computation to start, unreliable angle values can be computed at points where a local wave maximum or minimum hits the boundary since the gradient is close to zero. As a remedy, we propose that gradients with the Euclidean norm below some threshold should not influence the angle of incidence. Whenever such a small gradient appears, we use the angle of the last time step; see Algorithm 1, line 9. We employ a percentage p_2 of a reference value for the threshold.

As the reference value we take the local gradient history of the given element and pick the norm-wise maximum over the past time steps; see Algorithm 1, line 8. We compute a new angle of incidence only in cases where the threshold is surpassed, i.e., when the local gradient is sufficiently large; cf. Algorithm 1, line 11. To also reduce the oscillations with respect to time in the angle distribution, in all experiments we choose a relatively high threshold of $p_2 = 0.5$.

Together with the previously introduced switch, the above approach allows to steer the sensitivity of the angle computation algorithm by adapting the parameters p_1 and p_2. If these parameters are close to 1, the angle is only computed for very high amplitudes and local gradients, while for most other parts of the boundary the angle remains zero. On the other hand, small values of p_1 and p_2 would lead to highly sensitive angles that react to even small perturbations in the wave field.

Algorithm 1: Angle-computation algorithm

Initialization:

Formally **set** $|\nabla\psi_{\text{el}}^{(-1)}| = \infty$ and $\theta_{\text{el}}^{0} = 0°$ for all elements el

In time step $n = 1, 2, \ldots$ **do**

for el $\in$ {**elements** : **element has an edge/face on the absorbing boundary**}
  if $\max\{|\psi_i^n| : \text{dof}_i \textit{ belongs to } \text{el}\} > p_1 \cdot \mathfrak{A}$ **then**
    enable angle computation for el
  end
  if angle computation is enabled for el **then**
    Evaluate $\nabla\psi(\vec{x}, t^{n-1})$ within el $\rightarrow$ save as $\nabla\psi_{\text{el}}^{n-1}$
    if $|\nabla\psi_{\text{el}}^{n-1}| \leq p_2 \max_{k<n-1} |\nabla\psi_{\text{el}}^{k}|$ **then**
      set $\theta_{\text{el}}^{n} = \theta_{\text{el}}^{n-1}$
    else
      compute $\theta_{\text{el}}^{n} = \arccos\left(\frac{|\langle\nabla\psi_{\text{el}}^{n-1}, \vec{n}_{\text{el}}\rangle|}{|\nabla\psi_{\text{el}}^{n-1}|}\right)$
    end
  else
    set $\theta_{\text{el}}^{n} = 0°$
  end
end

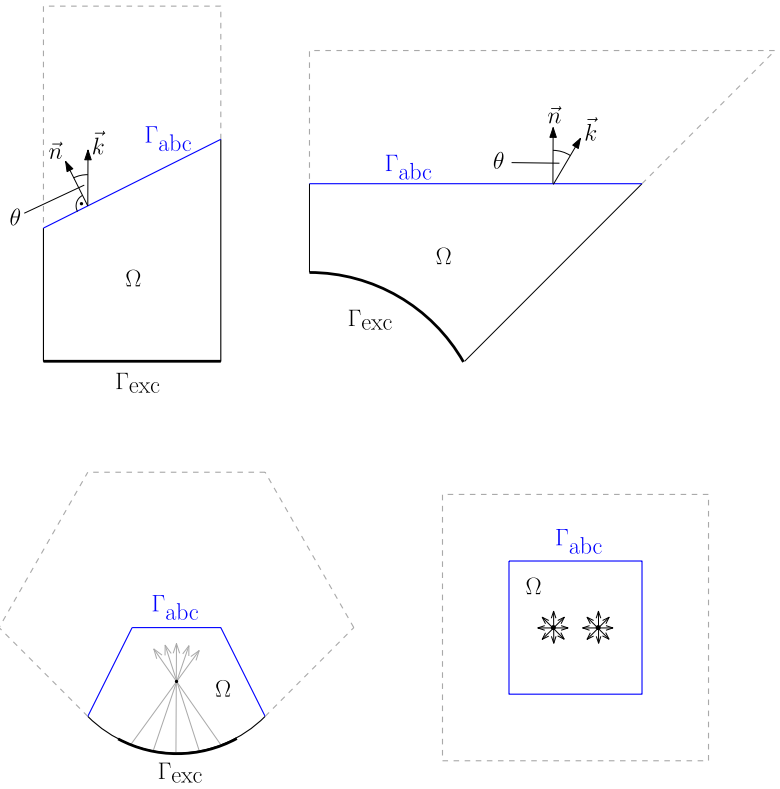

Fig. 2. Computational domains used in simulations. **(Top left)** Channel with an inclined absorbing boundary, **(Top right)** Octant of a "plate with hole" geometry, **(Bottom left)** Geometry of a focusing transducer, **(Bottom right)** Geometry with multiple sources and wave superposition.

6. Numerical results

We proceed with numerical simulations where we put our self-adaptive technique to the test. Computational domains Ω used in numerical experiments are sketched in Fig. 2. The dashed lines symbolize the boundaries of the reference domain Ω_{ref} where we compute the reference solution ψ^{ref}. The reference solution is always first computed on Ω_{ref}, then restricted to the actual domain Ω, and compared with the potential field obtained on Ω by employing the absorbing conditions.

We mention again that in all numerical simulations conforming finite elements of lowest order on simplicial meshes are used. Geometry and mesh are generated by using the Gmsh software package [60].

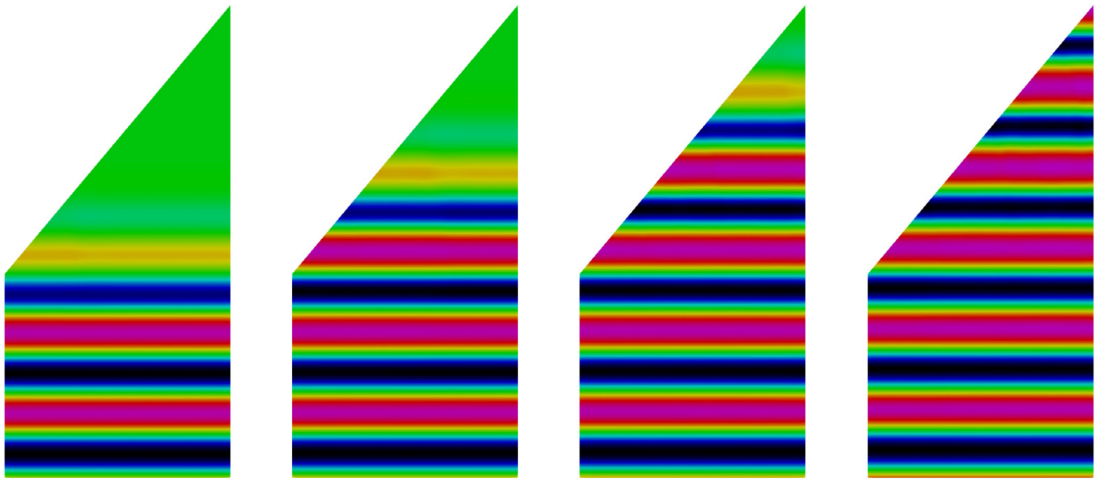

Fig. 3. Time snapshots of the potential field.

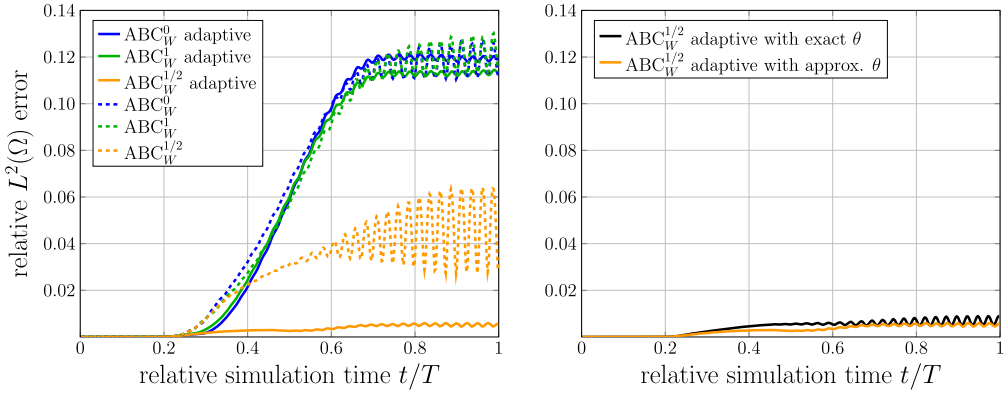

Fig. 4. Inclined plane boundary: Relative $L^2(\Omega)$ error of the potential $\psi(t)$ over the simulation time with $\theta = 20°$. **(Left)** Nonlinear vs. linear conditions with and without adaptivity, **(Right)** Performance of adaptive conditions with numerically computed vs. the exact incidence angle θ. (For interpretation of the colors in the figure(s), the reader is referred to the web version of this article.)

6.1. Domain with an inclined absorbing boundary

In our first experiment, we consider a two-dimensional channel geometry, where the upper (absorbing) boundary Γ_{abc} is tilted by a given angle of θ; see Fig. 2. The waves originate from the excitation boundary Γ_{exc} at the bottom of the rectangle and travel straight upwards. We impose homogeneous Neumann boundary conditions on the sides of the domain. The wave vector $\vec{k}$ in this setting points straight upwards. Therefore, the angle that the wave vector and the outward normal $\vec{n}$ of Ω at Γ_{abc} enclose is exactly θ for the absorbing boundary.

We compute the reference solution ψ^{ref} on a larger domain without the absorbing boundary and then conduct a simulation on Ω. To get an impression on how the wave propagates in the present setting, Fig. 3 shows the potential field ψ at different time snapshots. Material parameters were chosen to be the ones of water, i.e.

$$c = 1500\ \mathrm{m/s},\ b = 6 \cdot 10^{-9}\ \mathrm{m^2/s},\ \rho = 1000\ \mathrm{kg/m^3},\ B/A = 5;$$

see [41, Chapter 5], while the excitation (31) has an amplitude of $\mathfrak{A} = 0.01\ \mathrm{m^2/s^2}$ and a frequency of 210 kHz. The experiment was conducted for two different angles

$$\theta \in \{20°, 50°\}.$$

For spatial discretization, we take 13045 (20° case) and 13046 (50° case) degrees of freedom in space for the channel width of 0.02 m and channel length (in the middle) of 0.03 m. In time, 9800 time steps were taken to cover the interval from $t_0 = 0$ s until $T = 9.45 \cdot 10^{-5}$ s.

The error plots are given in Fig. 4. We observe that the conditions that do not take the angle of incidence into consideration significantly deteriorate when the angle increases. For the angle of incidence $\theta = 50°$, the maximal relative error is more than 20% for the linear conditions and around 17% for the nonlinear conditions with the fixed angle $\theta = 0°$. In comparison, the self-adaptive technique when combined with the nonlinear conditions (26) allows for the error to remain around 1%. Note that linearization (10) and the resulting absorbing conditions (26) clearly outperform conditions (28). We,

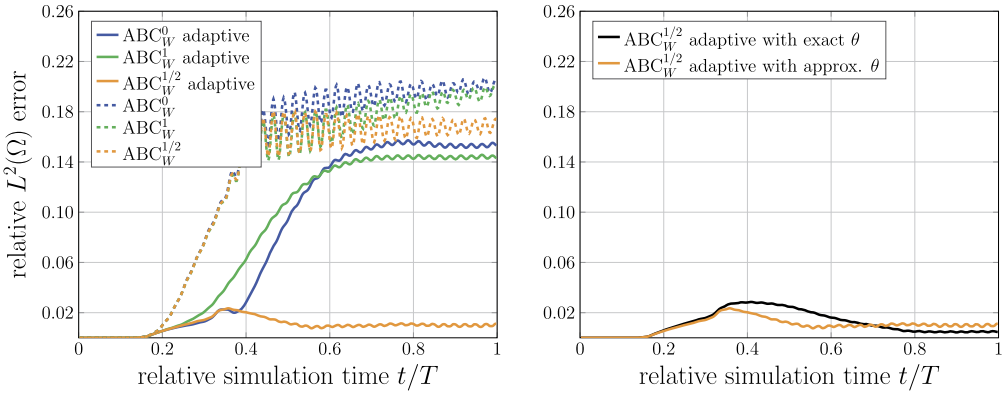

Fig. 5. Inclined plane boundary: Relative $L^2(\Omega)$ error of the potential $\psi(t)$ over the simulation time with $\theta = 50°$. **(Left)** Nonlinear vs. linear conditions with and without adaptivity, **(Right)** Performance of adaptive conditions with numerically computed vs. the exact incidence angle θ.

therefore, proceed in the following experiments with testing only (26) in combination with the self-adaptive technique. We also observe that the nonlinear conditions (26) that use an approximate angle computation via the gradient of the wave field perform similarly to the conditions that employ the exact angle.

It is also interesting to see how the errors are distributed over the domain Ω, i.e., where they originate from and how far they spread. Fig. 6 shows the error fields $|\psi(t) - \psi^{\mathrm{ref}}(t)|$ at different times for the $\mathrm{ABC}_W^{1/2}$ conditions with and without adaptivity. The first snapshots were taken just as the first wave hits the absorbing boundary. In the subsequent snapshots, we can see how the erroneous reflections travel together with the wave across the absorbing boundary. It is evident that there are fewer reflections present when using the self-adaptive absorbing boundary conditions that take the local angle information into account.

6.2. Higher source frequency

So far our experiments have been conducted with the same source excitation. After varying the domain geometry via the angle θ, we investigate the influence of the source frequency on the quality of absorbing conditions. We now test with the excitation frequency

$$f = 250\ \mathrm{kHz}.$$

All the remaining parameters being the same as before. The domain again has the upper boundary tilted with the angle of 50°. Fig. 7 shows the error plots for the higher frequency. We observe that conditions ABC_W^0 asymptotically show the same poor results as conditions ABC_W^0 with self-adaptivity. Only our combination of nonlinear conditions with the self-adaptive technique (26) allows for the relative error to stay around 1%. By comparing Fig. 5 and Fig. 7, we also notice that the difference in the error between the nonlinear and the corresponding linear conditions increases with the frequency, emphasizing the need to employ nonlinear conditions for high-frequency nonlinear sound waves.

6.3. Plate with a hole

We previously tested the new absorbing boundary conditions in a domain where the angle of incidence was constant over the absorbing boundary. To show that both our approach of computing the angle of incidence of the wave as well as the nonlinear boundary conditions work in more realistic settings, we now consider the so-called "*plate with a hole*" domain. It consists of a square with a circular hole in the center. In our case, the excitation of the wave takes place at the boundary of the hole. By using symmetry, we reduce the simulation of the whole domain to half of one of its quarters; see Fig. 2.

An analytical expression for the angle of incidence is also available here which allows us to judge the quality of our angle approximation. If the origin is at the center of the circular hole and the square has sides of length a, the angle of incidence is given by

$$\theta(x, y, t) = \arccos\left(\frac{a/2}{\sqrt{x^2 + (a/2)^2}}\right). \tag{36}$$

We set $a = 0.08$ in the experiments. The domain is resolved with 13820 degrees of freedom in space. For time discretization, we choose 8330 time steps with final time $T = 8.0325 \cdot 10^{-5}$ s.

Fig. 8 shows the angle of incidence computed by our approach at two different points in time and further illustrates our criterion on computing the incidence angle based on the amplitude of the wave on the boundary. Note that formula (36) assumes a reflection-free potential field so an exact match of our angle to the analytical angle distribution cannot

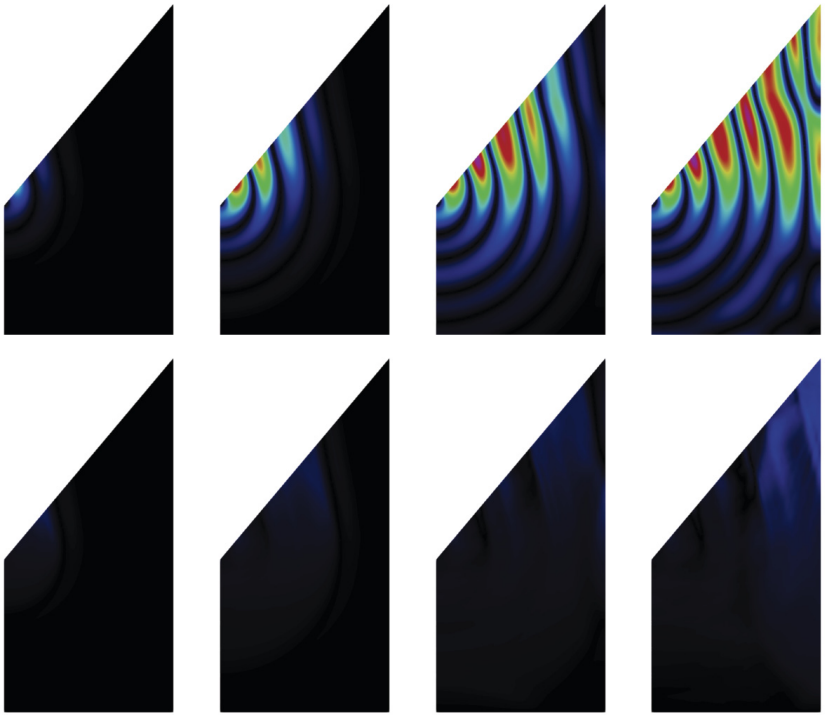

Fig. 6. Potential difference $|\psi(t) - \psi^{\text{ref}}(t)|$ plotted over time **(Horizontal)** for $\text{ABC}_W^{1/2}$ **(First row)** without adaptivity and **(Second row)** with self-adaptive angle.

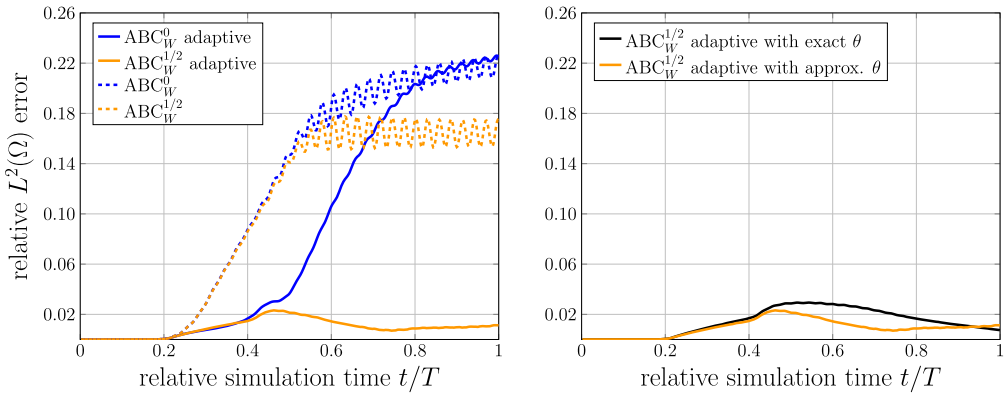

Fig. 7. Inclined plane boundary: Relative $L^2(\Omega)$ error of the potential $\psi(t)$ for $t \in [0, T]$ with $\theta = 50°$ and higher source frequency. **(Left)** Nonlinear vs. linear conditions with and without adaptivity, **(Right)** Performance of adaptive conditions with numerically computed vs. the exact incidence angle θ.

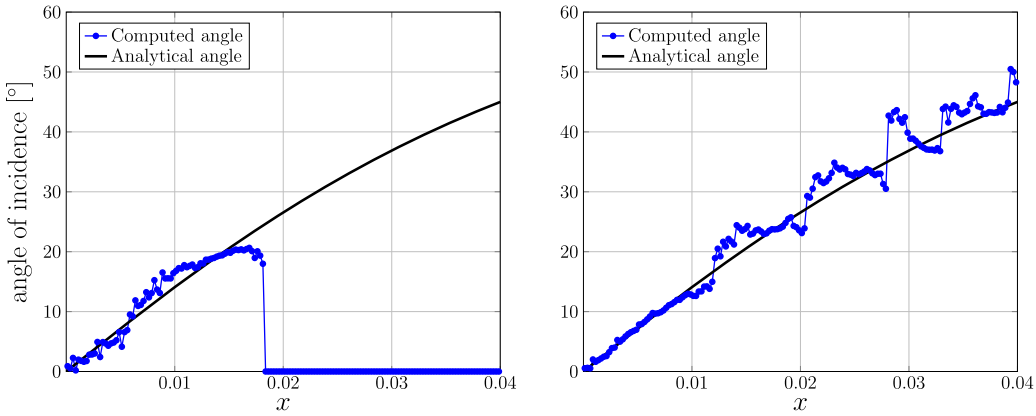

Fig. 8. Computed versus exact angle of incidence θ. **(Left)** The angle is only computed on the parts of the absorbing boundary that the wave has reached. **(Right)** Angle computation towards the end of the simulation.

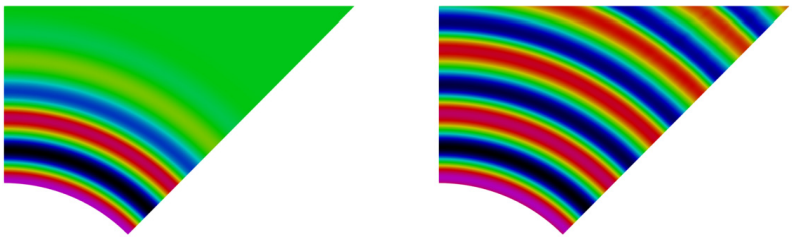

Fig. 9. Time snapshots of the pressure field $u = \rho\psi_t$.

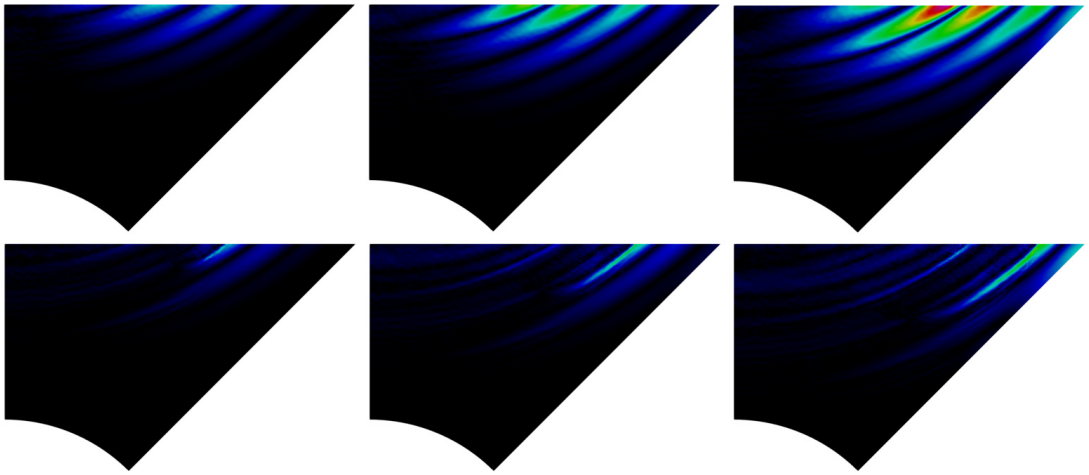

Fig. 10. Pressure difference $|u(t) - u^{\text{ref}}(t)|$ plotted over time **(Horizontal)** for $\text{ABC}_W^{1/2}$ without **(First row)** and with **(Second row)** angle consideration.

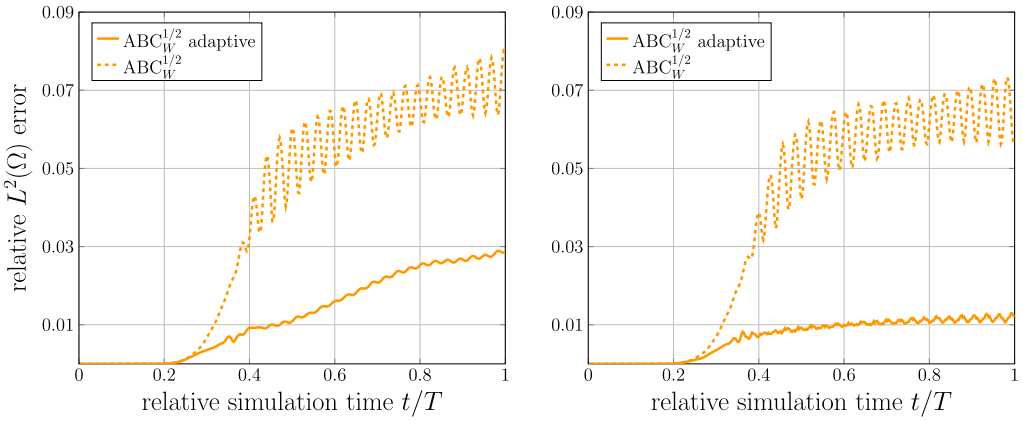

Fig. 11. Plate with a hole: Relative $L^2(\Omega)$ error of **(Left)** the potential $\psi(t)$ and **(Right)** the pressure $u(t) = \rho\psi_t(t)$ over the simulation time.

be expected. In fact, our method tries to compensate also for the waves that originate as spurious reflections from the absorbing boundary.

As in our last experiment, we proceed by showing the wave field at different time steps as well as the error comparison of different absorbing boundary conditions; see Fig. 9 and Fig. 11. This time we also compute them in terms of the acoustic pressure $u = \rho\psi_t$ due to its practical importance. We also introduce here the relative errors in the $L^2(0,T;L^2(\Omega))$ norm, i.e.

$$e_\psi = \frac{\|\psi - \psi^{\text{ref}}\|_{L^2(0,T;L^2(\Omega))}}{\|\psi^{\text{ref}}\|_{L^2(0,T;L^2(\Omega))}}, \qquad e_u = \frac{\|u - u^{\text{ref}}\|_{L^2(0,T;L^2(\Omega))}}{\|u^{\text{ref}}\|_{L^2(0,T;L^2(\Omega))}}.$$

In the present experiment, those errors amount to $e_\psi = 1.82\%$ and $e_u = 0.93\%$ for the self-adaptive conditions and $e_\psi = 5.41\%$ and $e_u = 5.17\%$ for the conditions without adaptivity, giving an overall improvement of 66.36% in the potential and 82.01% in the pressure.

Plots of the difference field $|u(t) - u^{\text{ref}}(t)|$ at different times are given in Fig. 10. We observe that with the absorbing conditions that are not adaptive, the amplitude of the error increases over the width of the domain as the angle grows.

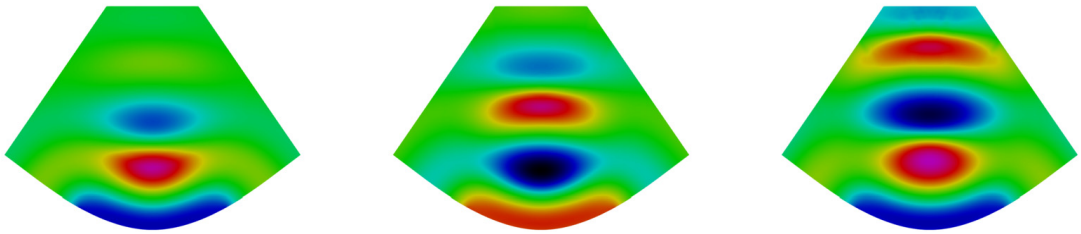

Fig. 12. Snapshots of the pressure field $u = \rho\psi_t$ of a propagating, self-focusing wave.

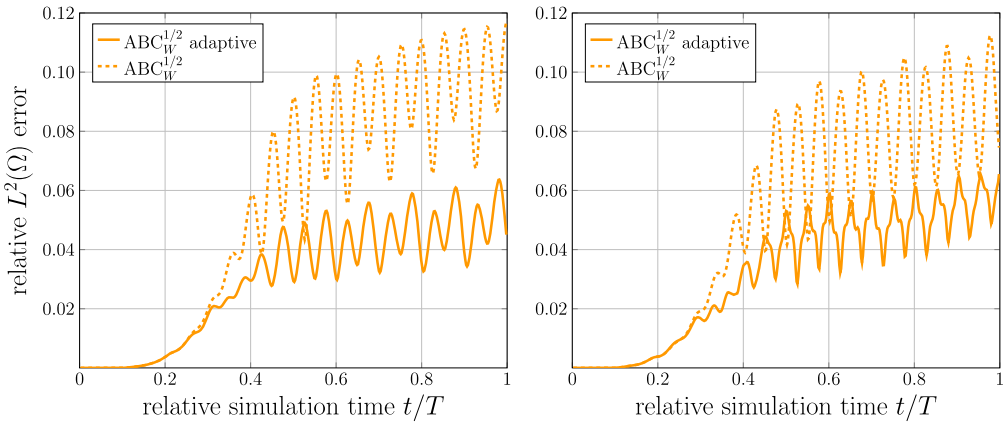

Fig. 13. HIFU transducer in 2D: Relative $L^2(\Omega)$ error of **(Left)** the potential $\psi(t)$ and **(Right)** the pressure $u(t) = \rho\psi_t(t)$ over the simulation time.

6.4. High-intensity focused ultrasound (HIFU)

We next simulate the potential field generated by a piezoelectric transducer. Such devices are made of small plates of a piezoelectric material that are aligned in an arc-shaped array pointing towards a common focal point [61,62]. When set into motion, those vibrating plates induce acoustic sound waves that propagate towards the focal point. As it travels, the wave is focused more and more the closer it comes to the focal point. This technique of generating high-pressure amplitudes at specific locations is used in medicine to treat kidney stones and certain types of cancer; see [4–8]. The pressure levels in the non-focal region are sufficiently low so that damage to the surrounding tissue is avoided.

For this experiment, the medium of propagation is again chosen to be water with the same physical parameters as before. The source frequency is again given by $f = 210$ kHz and the source amplitude by $\mathfrak{A} = 0.02$ m^2/s^2 which increases at the focal point due to focusing. As depicted in Fig. 2, the absorbing boundary here consists out of three line segments at the left, right and top. Time-snapshots of the transducer simulation can be seen in Fig. 12.

The computational domain was resolved with 13313 degrees of freedom, while for the time stepping 9800 steps and a final time of $T = 4.725 \cdot 10^{-5}$ s were used.

A comparison of the relative $L^2(\Omega)$ errors at every time step is displayed in Fig. 13. Due to the relevance of measuring the acoustic pressure in HIFU applications, we again also plot the relative error that the absorbing boundary conditions produce in the pressure $u = \rho\psi_t$. We observe that the qualitative behavior of the errors and especially also the improvement made by the new adaptive conditions remains the same. For the adaptive conditions, the relative errors in the $L^2(0, T; L^2(\Omega))$ norm are $e_\psi = 4.12\%$ and $e_u = 4.46\%$, whereas $e_\psi = 7.94\%$ and $e_u = 7.27\%$ if the adaptivity is not considered, resulting in an improvement of 51.89% in ψ and even 61.35% in u. The increase in computational time when using the adaptive absorbing conditions amounts to 1.5%.

Since even with the absorbing boundary conditions an impinging wave is not completely absorbed, there are always some spurious reflections that travel back into the interior of the domain. They then interact with the “main” wave that still travels towards the boundary and other spurious reflections originating from different parts of the boundary. Those effects together can accumulate over time, leading to an increase of the deviation from the reference solution and therefore the error, as can be observed in Fig. 13. These effects appear to be more pronounced in more complicated geometries as well as with wave focusing.

6.5. Multi-source wave superposition

Our next experiment is intended to illustrate that the adaptive method also works in scenarios with more than one wave source present and when superposition of waves occurs. In such cases, we can expect a less distinct wave propagation direction. In contrast to the other examples, here we use a source term on the right-hand side of the Westervelt equation.

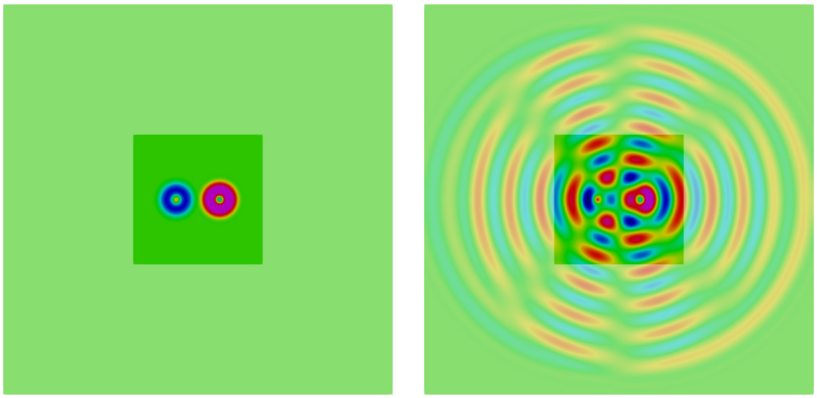

Fig. 14. Wave propagation induced by two different source terms.

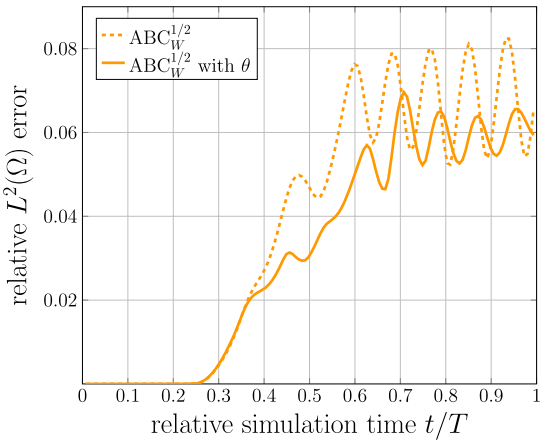

Fig. 15. Multi-source wave superposition: Relative $L^2(\Omega)$ error of the potential $\psi(t)$.

The computational domain is given by the square $\Omega = (0, 0.03)^2$ and we choose the source term as follows

$$f(x, y, t) = \mathfrak{A} \sin(\omega t) \left[\exp\left(-\left(\frac{x - x_{\mathrm{mp1}}}{\sigma_x} \right)^2 - \left(\frac{y - y_{\mathrm{mp1}}}{\sigma_y} \right)^2 \right) - \frac{2}{3} \exp\left(-\left(\frac{x - x_{\mathrm{mp2}}}{\sigma_x} \right)^2 - \left(\frac{y - y_{\mathrm{mp2}}}{\sigma_y} \right)^2 \right) \right],$$

with $\sigma_x = \sigma_y = 0.0005$, $x_{\mathrm{mp1}} = 0.02, x_{\mathrm{mp2}} = 0.01$, $y_{\mathrm{mp1}} = y_{\mathrm{mp2}} = 0.015$, and $\mathfrak{A} = 10^{11}$ $\mathrm{m}^2/\mathrm{s}^4$. Fig. 14 depicts wave propagation at two different times induced by two different source terms within the computational domain. We impose absorbing conditions on all four boundaries. The transparent region depicts the reference domain. In Fig. 15, we can see the relative L^2 errors. We observe that also in this setting the adaptive approach results in a smaller error and a better overall behavior.

6.6. 3D transducer

To also show the capability of our method in three dimensions, we perform another experiment in a transducer setting, this time in 3D. Due to the high computational costs, especially for the reference solution on the larger domain Ω^{ref}, we choose a source amplitude of $\mathfrak{A} = 0.002$ $\mathrm{m}^2/\mathrm{s}^2$, while keeping physical parameters and the excitation frequency the same. Fig. 16 shows the computational domain together with the grid, while Fig. 17 depicts the three-dimensional wave propagation in the given domain.

In Fig. 18, we compare the adaptive conditions to the nonlinear conditions with the fixed angle $\theta = 0°$. Note that in 3D, in addition to the discretization error, there is also an interpolation error caused by a mismatch between the grid for the simulation with absorbing conditions and the mesh of the reference solution. Combined with the L^2-norm of the reference solution being small at the beginning of the simulation, this results in the initial peak in the relative error for both adaptive and non-adaptive conditions. In 2D, the meshing software was able to avoid the interpolation error. In the long term behavior as well as in the absolute errors, we observe that the adaptive angle information improves the quality of the conditions. The qualitative behavior of the errors of the new adaptive conditions is similar in 3D. The relative errors in the $L^2(0, T; L^2(\Omega))$ norm are $e_\psi = 8.28\%$ and $e_u = 8.3\%$ if the adaptivity is considered, whereas $e_\psi = 10.34\%$ and $e_u = 10.39\%$ if the adaptivity is not considered, resulting in an improvement of 19.92% in ψ and 20.12% in u.

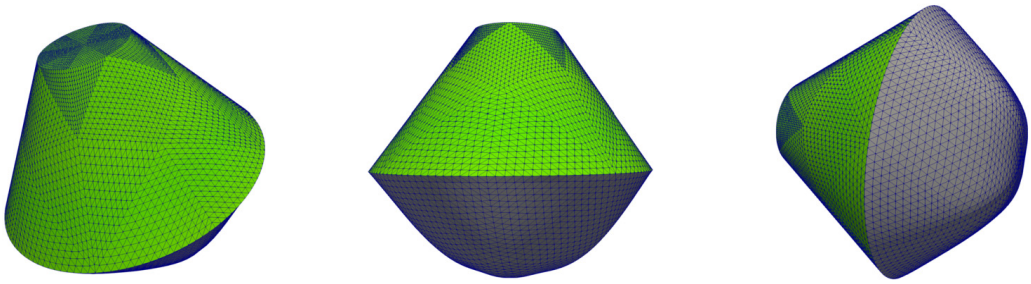

Fig. 16. Three-dimensional transducer geometry with mesh visible on the surface. Absorbing conditions are employed on the green surface, Dirichlet conditions on the grey.

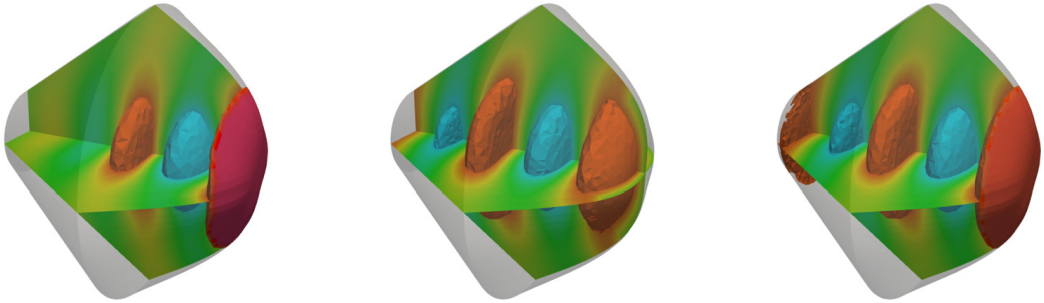

Fig. 17. Three-dimensional propagation of the pressure wave $u = \rho\psi_t$. The iso-volumes show the regions of highest (in absolute value) pressure amplitudes in 3D, while the two planes show slices through the three-dimensional pressure field.

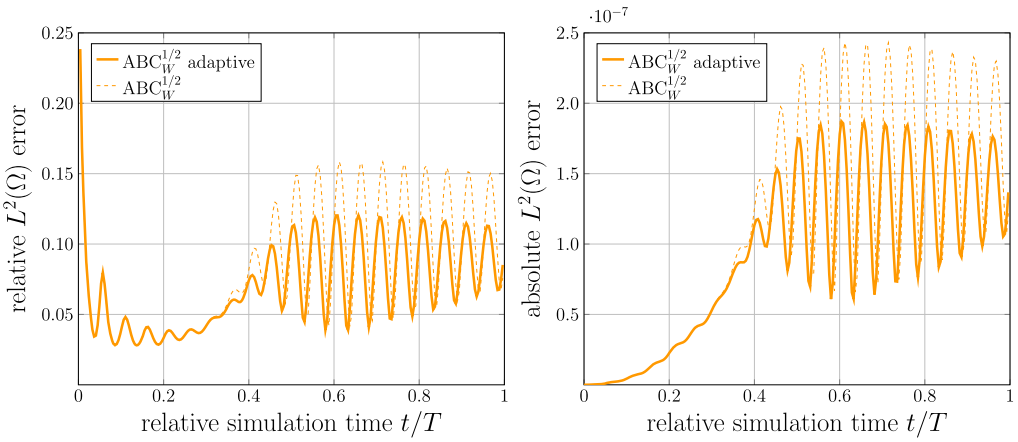

Fig. 18. HIFU transducer 3D: (Left) Relative $L^2(\Omega)$ error of the potential $\psi(t)$, **(Right)** Absolute $L^2(\Omega)$ error of the potential $\psi(t)$.

6.7. 3D acoustic horn

Nonlinear sound propagation has been widely reported to occur in wind instruments; see [63–66]. Motivated by this, for our final experiment, we consider a numerical simulation of an acoustic horn.

The excitation takes place at the bottom of the domain and the waves then travel through a waveguide with an increasing diameter; see Fig. 20. At the end of the waveguide, where the wave starts to propagate into the ambient space, we employ again the absorbing conditions to truncate the domain at a spherical boundary. In this experiment we use the physical parameters of air instead of water:

$$c = 331\,\frac{\mathrm{m}}{\mathrm{s}},\ b = 0.00005\,\frac{\mathrm{kg}}{\mathrm{m\,s}},\ B/A = 1.2,\ \varrho = 1.29\,\frac{\mathrm{kg}}{\mathrm{m}^3};$$

see [67]. The excitation has a frequency of $f = 6.5$ kHz and an amplitude of $\mathfrak{A} = 0.01\ \mathrm{m}^2/\mathrm{s}^2$. To keep the computational cost reasonable, we again use symmetry to reduce the simulation to a quarter of the actual three-dimensional acoustic horn. The two planes of symmetry are equipped with homogeneous Neumann conditions; see Fig. 19. A comparison of adaptive and non-adaptive conditions is given in Fig. 21. The relative errors in the $L^2(0, T; L^2(\Omega))$ norm are $e_\psi = 5.23\%$ and $e_u = 5.33\%$ if the adaptivity is considered, whereas $e_\psi = 6.11\%$ and $e_u = 6.07\%$ if the adaptivity is not considered, resulting in an improvement of 14.4% in ψ and 12.19% in u.

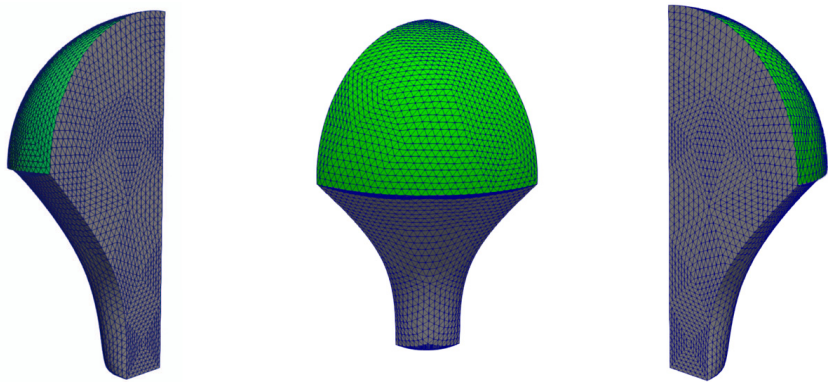

Fig. 19. Three-dimensional acoustic horn geometry with mesh visible on the surface. Absorbing conditions are employed on the green surface, homogeneous Neumann conditions on the grey and a wave excitation via inhomogeneous Dirichlet conditions at the bottom surface.

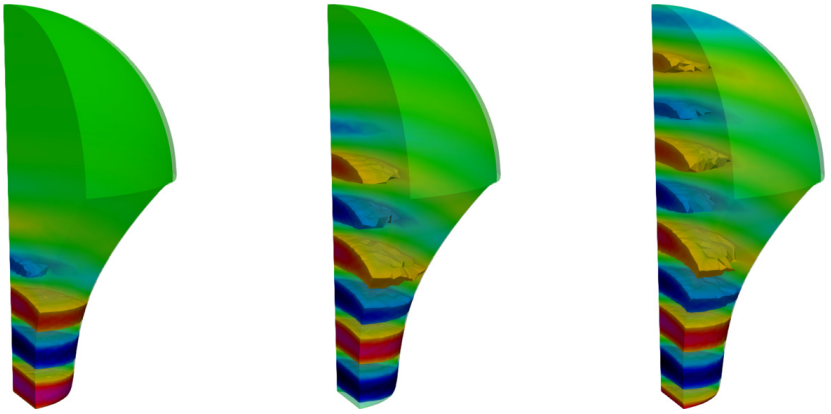

Fig. 20. Three-dimensional propagation of the pressure wave $u = \rho\psi_t$. The iso-volumes show the regions of highest (in absolute value) pressure amplitudes in 3D.

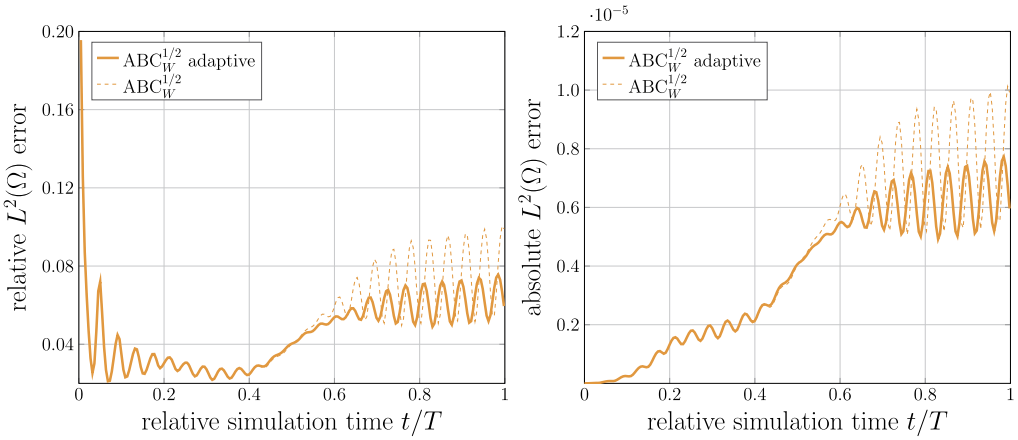

Fig. 21. Acoustic horn 3D: (Left) Relative $L^2(\Omega)$ error of the potential $\psi(t)$, **(Right)** Absolute $L^2(\Omega)$ error of the potential $\psi(t)$ over the simulation time.

We observe less of a gain in our recent examples compared to the introductory ones in 2D, which has a natural explanation. In our simplest 2D setting in Section 6.1, the angle of incidence is constant over the whole absorbing boundary and large, so the boundary conditions can significantly profit from taking the angle information into account adaptively. In the later, more advanced examples (e.g., in Section 6.3) a large portion of the wave leaves the domain with quite small incidence angles. The same also holds for the application-oriented example of the focusing transducer in Sections 6.4 and 6.6. There, most of the angles of incidence are smaller than in the introductory examples which results in a smaller improvement compared to the standard non-adaptive conditions.

7. Conclusion

We have developed a self-adaptive absorbing technique for sound propagation in the presence of nonlinearities. Within our approach, the angle of incidence of the wave is computed locally by employing the information given by the gradient of the wave-field. The absorbing conditions are then updated in real time with the angle values.

The method offers three fundamental advantages. It is sufficiently accurate over a range of angles of incidence, and it is easy to implement. Moreover, by only relying on the gradient of the wave field which is readily available in finite element simulations, we can keep the additional computational efforts low.

Acknowledgements

We thank Dr. Igor Shevchenko for helpful comments. We would also like to thank the anonymous reviewers for their valuable and constructive comments that contributed to improving the final version of the paper. The funds provided by the Deutsche Forschungsgemeinschaft under the grant number WO 671/11-1 are gratefully acknowledged.

References

[1] G.M. Fierro, F. Ciampa, D. Ginzburg, E. Onder, M. Meo, Nonlinear ultrasound modelling and validation of fatigue damage, J. Sound Vib. 343 (2015) 121–130.
[2] K.-Y. Jhang, Nonlinear ultrasonic techniques for nondestructive assessment of micro damage in material: a review, Int. J. Precis. Eng. Manuf. 10 (1) (2009) 123–135.
[3] K. Matlack, J. Wall, J.-Y. Kim, J. Qu, L. Jacobs, H.-W. Viehrig, Evaluation of radiation damage using nonlinear ultrasound, J. Appl. Phys. 111 (2012) 054911.
[4] R. Illing, J. Kennedy, F. Wu, G. Ter Haar, A. Protheroe, P. Friend, F. Gleeson, D. Cranston, R. Phillips, M. Middleton, The safety and feasibility of extra-corporeal high-intensity focused ultrasound (HIFU) for the treatment of liver and kidney tumours in a western population, Br. J. Cancer 93 (8) (2005) 890.
[5] J. Kennedy, F. Wu, G. Ter Haar, F. Gleeson, R. Phillips, M. Middleton, D. Cranston, High-intensity focused ultrasound for the treatment of liver tumours, Ultrasonics 42 (1–9) (2004) 931–935.
[6] J.E. Kennedy, High-intensity focused ultrasound in the treatment of solid tumours, Nat. Rev. Cancer 5 (4) (2005) 321.
[7] F. Wu, Z.-B. Wang, W.-Z. Chen, J. Bai, H. Zhu, T.-Y. Qiao, Preliminary experience using high intensity focused ultrasound for the treatment of patients with advanced stage renal malignancy, J. Urol. 170 (6) (2003) 2237–2240.
[8] S. Yoshizawa, T. Ikeda, A. Ito, R. Ota, S. Takagi, Y. Matsumoto, High intensity focused ultrasound lithotripsy with cavitating microbubbles, Med. Biol. Eng. Comput. 47 (8) (2009) 851–860.
[9] B. Engquist, A. Majda, Absorbing boundary conditions for the numerical simulation of waves, Proc. Natl. Acad. Sci. 74 (5) (1977) 1765–1766.
[10] D. Givoli, Non-reflecting boundary conditions, J. Comput. Phys. 94 (1) (1991) 1–29.
[11] F. Nataf, Absorbing boundary conditions and perfectly matched layers in wave propagation problems, in: Direct and Inverse Problems in Wave Propagation and Applications, vol. 14, de Gruyter, 2013, pp. 219–231.
[12] J. Szeftel, Absorbing boundary conditions for nonlinear scalar partial differential equations, Comput. Methods Appl. Mech. Eng. 195 (29–32) (2006) 3760–3775.
[13] J. Szeftel, A nonlinear approach to absorbing boundary conditions for the semilinear wave equation, Math. Comput. 75 (254) (2006) 565–594.
[14] G. Hedstrom, Nonreflecting boundary conditions for nonlinear hyperbolic systems, J. Comput. Phys. 30 (2) (1979) 222–237.
[15] H. Li, X. Wu, J. Zhang, Local absorbing boundary conditions for nonlinear wave equation on unbounded domain, Phys. Rev. E 84 (2011) 036707.
[16] I. Shevchenko, B. Kaltenbacher, Absorbing boundary conditions for nonlinear acoustics: the Westervelt equation, J. Comput. Phys. 302 (2015) 200–221.
[17] I. Shevchenko, B. Kaltenbacher, Absorbing Boundary Conditions for the Westervelt Equation, Conference Publications, 2015.
[18] J.-P. Bérenger, A perfectly matched layer for the absorption of electromagnetic waves, J. Comput. Phys. 114 (2) (1994) 185–200.
[19] S. Abarbanel, D. Gottlieb, J.S. Hesthaven, Well-posed perfectly matched layers for advective acoustics, J. Comput. Phys. 154 (2) (1999) 266–283.
[20] S. Hein, T. Hohage, W. Koch, J. Schöberl, Acoustic resonances in a high-lift configuration, J. Fluid Mech. 582 (2007) 179–202.
[21] J.S. Hesthaven, On the analysis and construction of perfectly matched layers for the linearized Euler equations, J. Comput. Phys. 142 (1) (1998) 129–147.
[22] B. Kaltenbacher, M. Kaltenbacher, I. Sim, A modified and stable version of a perfectly matched layer technique for the 3-d second order wave equation in time domain with an application to aeroacoustics, J. Comput. Phys. 235 (2013) 407–422.
[23] Q. Qi, T.L. Geers, Evaluation of the perfectly matched layer for computational acoustics, J. Comput. Phys. 139 (1) (1998) 166–183.
[24] R.L. Higdon, Absorbing boundary conditions for difference approximations to the multidimensional wave equation, Math. Comput. 47 (176) (1986) 437–459.
[25] R.L. Higdon, Numerical absorbing boundary conditions for the wave equation, Math. Comput. 49 (179) (1987) 65–90.
[26] R.G. Keys, Absorbing boundary conditions for acoustic media, Geophysics 50 (6) (1985) 892–902.
[27] Z. Xu, H. Han, X. Wu, Adaptive absorbing boundary conditions for Schrödinger-type equations: application to nonlinear and multi-dimensional problems, J. Comput. Phys. 225 (2) (2007) 1577–1589.
[28] I. Shevchenko, B. Wohlmuth, Self-adapting absorbing boundary conditions for the wave equation, Wave Motion 49 (4) (2012) 461–473.
[29] J.-M. Jin, N. Lu, Application of adaptive absorbing boundary condition to finite element solution of three-dimensional scattering, IEE Proc., Microw. Antennas Propag. 143 (1) (1996) 57–61.
[30] Y. Li, Z.J. Cendes, Adaptive absorbing boundary conditions for high accuracy scattering, in: Antennas and Propagation Society International Symposium, 1994. AP-S. Digest, Vol. 1, IEEE, 1994, pp. 402–405.
[31] X. Jia, R.-S. Wu, Calculation of the wave propagation angle in complex media: application to turning wave simulations, Geophys. J. Int. 178 (3) (2009) 1565–1573.
[32] N. Patrikeeva, P. Sava, Comparison of angle decomposition methods for wave-equation migration, in: SEG Technical Program Expanded Abstracts 2013, Society of Exploration Geophysicists, 2013, pp. 3773–3778.
[33] A. Richardson, A.E. Malcolm, Separating a wavefield by propagation direction, in: SEG Technical Program Expanded Abstracts 2015, Society of Exploration Geophysicists, 2015, pp. 4185–4189.
[34] R.-C. Ye, X.-F. Jia, An effective denoising strategy for wave equation migration based on propagation angles, Appl. Geophys. 9 (1) (2012) 33–40.
[35] K. Yoon, K.J. Marfurt, Reverse-time migration using the Poynting vector, Explor. Geophys. 37 (1) (2006) 102–107.
[36] Q. Zhang, G.A. McMechan, Direct vector-field method to obtain angle-domain common-image gathers from isotropic acoustic and elastic reverse time migration, Geophysics 76 (5) (2011) WB135–WB149.

[37] D. Gordon, R. Gordon, E. Turkel, Compact high order schemes with gradient-direction derivatives for absorbing boundary conditions, J. Comput. Phys. 297 (2015) 295–315.
[38] B. Kaltenbacher, M. Thalhammer, Fundamental models in nonlinear acoustics part I. Analytical comparison, Math. Models Methods Appl. Sci. 28 (12) (2018) 2403–2455.
[39] D.G. Crighton, Model equations of nonlinear acoustics, Annu. Rev. Fluid Mech. 11 (1) (1979) 11–33.
[40] M.F. Hamilton, D.T. Blackstock, Nonlinear Acoustics, vol. 1, Academic Press, San Diego, 1998.
[41] M. Kaltenbacher, Numerical Simulation of Mechatronic Sensors and Actuators, vol. 2, Springer, 2007.
[42] V. Kuznetsov, Equations of nonlinear acoustics, Sov. Phys. Acoust. 16 (1971) 467–470.
[43] P.J. Westervelt, Parametric acoustic array, J. Acoust. Soc. Am. 35 (4) (1963) 535–537.
[44] B. Kaltenbacher, I. Lasiecka, Global existence and exponential decay rates for the Westervelt equation, Discrete Contin. Dyn. Syst., Ser. S 2 (3) (2009) 503.
[45] B. Kaltenbacher, I. Lasiecka, Well-posedness of the Westervelt and the Kuznetsov equation with nonhomogeneous Neumann boundary conditions, Discrete Contin. Dyn. Syst.: Conference Publications 2 (2011) 763–773.
[46] S. Kawashima, Y. Shibata, Global existence and exponential stability of small solutions to nonlinear viscoelasticity, Commun. Math. Phys. 148 (1) (1992) 189–208.
[47] L. Nirenberg, Lectures on Linear Partial Differential Equations, vol. 17, American Mathematical Soc., 1973.
[48] L. Hörmander, Pseudo-differential operators, Commun. Pure Appl. Math. 18 (3) (1965) 501–517.
[49] M.W. Wong, An Introduction to Pseudo-Differential Operators, World Scientific Publishing, 1999.
[50] L. Hörmander, The Analysis of Linear Partial Differential Operators III: Pseudo-Differential Operators, vol. 274, Springer Science & Business Media, 1994.
[51] A. Majda, S. Osher, Reflection of singularities at the boundary, Commun. Pure Appl. Math. 28 (4) (1975) 479–499.
[52] G. Simonett, M. Wilke, Well-posedness and longtime behavior for the Westervelt equation with absorbing boundary conditions of order zero, J. Evol. Equ. 17 (1) (2017) 551–571.
[53] M. Fritz, V. Nikolić, B. Wohlmuth, Well-posedness and numerical treatment of the Blackstock equation in nonlinear acoustics, Math. Models Methods Appl. Sci. 28 (13) (2018) 2557–2597.
[54] J. Hoffelner, H. Landes, M. Kaltenbacher, R. Lerch, Finite element simulation of nonlinear wave propagation in thermoviscous fluids including dissipation, IEEE Trans. Ultrason. Ferroelectr. Freq. Control 48 (3) (2001) 779–786.
[55] Y. Kagawa, T. Tsuchiya, T. Yamabuchi, H. Kawabe, T. Fujii, Finite element simulation of non-linear sound wave propagation, J. Sound Vib. 154 (1) (1992) 125–145.
[56] M. Muhr, V. Nikolić, B. Wohlmuth, L. Wunderlich, Isogeometric shape optimization for nonlinear ultrasound focusing, Evol. Equ. Control Theory 8 (1) (2019) 163–202.
[57] T. Walsh, M. Torres, Finite element methods for nonlinear acoustics in fluids, J. Comput. Acoust. 15 (03) (2007) 353–375.
[58] A. Bonelli, O. Bursi, S. Erlicher, L. Vulcan, Analysis of the generalized-α method for linear and non-linear forced excited systems, in: Structural Dynamics-EURODYN, vol. 2, 2002, pp. 1523–1528.
[59] W. Mulder, Experiments with Higdon's absorbing boundary conditions for a number of wave equations, Comput. Geosci. 1 (1) (1997) 85.
[60] C. Geuzaine, J.-F. Remacle, Gmsh: a three-dimensional finite element mesh generator with built-in pre- and post-processing facilities, Int. J. Numer. Methods Eng. 79 (11) (2009) 1309–1331.
[61] T. Dreyer, W. Krauss, E. Bauer, R. Riedlinger, Investigations of compact self focusing transducers using stacked piezoelectric elements for strong sound pulses in therapy, in: Ultrasonics Symposium, 2000 IEEE, vol. 2, IEEE, 2000, pp. 1239–1242.
[62] K. Watanabe, T. Hata, K. Koyama, H. Kurosawa, Wave focusing by a spherical concave transducer, Wave Motion 20 (1) (1994) 1–12.
[63] H. Berjamin, B. Lombard, C. Vergez, E. Cottanceau, Time-domain numerical modeling of brass instruments including nonlinear wave propagation, viscothermal losses, and lips vibration, Acta Acust. Acust. 103 (1) (2017) 117–131.
[64] N. Fletcher, Nonlinear theory of musical wind instruments, Appl. Acoust. 30 (2–3) (1990) 85–115.
[65] A. Myers, R.W. Pyle Jr, J. Gilbert, D.M. Campbell, J.P. Chick, S. Logie, Effects of nonlinear sound propagation on the characteristic timbres of brass instruments, J. Acoust. Soc. Am. 131 (1) (2012) 678–688.
[66] P.L. Rendón, R. Ezeta, A. Pérez-López, Nonlinear sound propagation in trumpets, Acta Acust. Acust. 99 (4) (2013) 607–614.
[67] T. Gudra, K. Opieliński, The parametric formation of acoustic waves in the air by using ultrasonic transducers, Rev. Acust. XXXII (2002), Sevilla.

A.2. A discontinuous Galerkin coupling for nonlinear elasto-acoustics

A discontinuous Galerkin coupling for nonlinear elasto-acoustics

Markus Muhr, Vanja Nikolić and Barbara Wohlmuth

This article was inspired from the mechanical application of a piezoelectric transducer, which by elastic vibrations excites ultrasound waves in an acoustic medium. The waves then travel through an acoustic wave guide until they transition into human tissue, for which different modeling approaches are used. The key feature of the article is hereby the coupling and numerical treatment of a nonlinear acoustic- with the elastic-wave-model of the excitator and the human tissue. In case of an acoustic tissue model, jumps in the material parameters have to be considered, which are resolved using a DG approach. Elasto-acoustic interface coupling together with the application and analysis of numerical methods for it can be found in [7, 106] for the linear case. In this article we extend the considerations to the nonlinear case by combining the ideas with arguments from [IV] to treat the nonlinear terms.

We introduce the elasto-acoustic model with two options, where one of them also contains an acoustic-acoustic interface of different materials. The acoustic model equation is stated in a general form that, by picking parameters accordingly, reduces to either the Westervelt or Kuznetsov equation. The overall computational domain is divided into material sub-domains with interfaces in between. Discretization is done using sub-domain-wise conforming hexahedral finite elements of order p, where on the interfaces coupling conditions are prescribed. For the elasto-acoustic interface they take the form of mutual force-exchange Neumann conditions, in the acoustic-acoustic case continuity conditions from DG are applied. The meshes of the individual sub-domains have to fulfill some regularity assumptions. However, due to the interface DG approach, geometrically they do not have to be matching at the interfaces. The same holds for the subdomain-wise polynomial degrees. We then continue to analyze the semi-discrete problem to ultimately arrive at a convergence result. Under a sufficient *smallness of data* assumption, we can show that in the L^∞- in time and energy-norm in space the method converges w.r.t. the mesh size parameter h^{s-1}, where s depends on the regularity of the problem and the polynomial degree of the finite element ansatz functions.

After the introduction, in Sec. 2, our coupled model is introduced, in Sec. 3 the semi-discrete problem is stated. In Sec. 4 the linearized problem is analyzed involving a stability estimate. Furthermore all necessary approximation results are collected. Sec. 5 then deals with the analysis of the nonlinear problem relying on Banach's fixed point theorem making use of the linear results from before. Finally Sec. 6 shows the theoretically proven convergence rates on extensive numerical experiments and also closes the loop back to the original motivation by conducting a complex simulation of the initially mentioned transducer-wave-guide-tissue configuration in the software framework *SPEED*.

I was significantly involved in finding the ideas and carrying out the scientific work presented in this article including the write-up (except Remark 4.1, Prop. 4.10). Furthermore I was solely in charge of the numerical part of the article, i.e. design of numerical examples, realization of the implementation and the creation of the figures.

Letter of acceptance

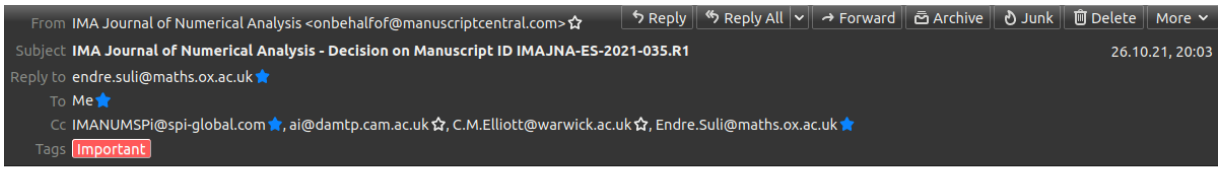

26-Oct-2021

Dear Mr. Muhr,

It is a pleasure to accept your revised manuscript entitled

"A discontinuous Galerkin coupling for nonlinear elasto-acoustics"

Received: 09-Feb-2021
Revised: 20-Aug-2021

in its current form for publication in the IMA Journal of Numerical Analysis. The comments of the reviewer(s) who reviewed your manuscript are included at the foot of this letter.

Please send the .tex file of the final version of your paper, the corresponding .pdf or .ps file, as well as any files you may have used to generate figures/images in your manuscript, to Oxford University Press' production team at the following email address:

IMANUMSPi@spi-global.com

If you have any additional questions then you can contact the UK-based production editor on:

Jnls.author.support@oup.com

In order to publish your article, Oxford University Press requires that you complete a licence agreement online. A link to the online licensing system, and instructions on how to select and complete a licence, will be provided to you by the Production Editor at Oxford University Press in due course.

Upon publication of your paper in the IMA Journal of Numerical Analysis Oxford University Press will send you a free-access link to the online version of your article. You may post the free-access link on your webpages and may also use it to link preprint versions of the paper residing in web repositories to the published version of your paper.

On behalf of the Editors of the IMA Journal of Numerical Analysis, I would like to thank you for submitting your work to our Journal.

With best wishes,

Endre Suli
Editor-in-Chief, IMA Journal of Numerical Analysis
endre.suli@maths.ox.ac.uk

Referee: 1

Comments to the Authors:
The authors have satisfactorily responded to all my questions and remarks. I have no doubts in recommending the manuscript for publication in IMAJNA.

Permission to include:

Muhr, Markus, Vanja Nikolić and Barbara Wohlmuth
A discontinuous Galerkin coupling for nonlinear elasto-acoustics
to appear in: IMA Journal of Numerical Analysis

< Access and Purchase Resource Centre
- Collection sales enquiries
- Dispatch Dates
- Keep reading
- Leavers
- ▸ Oxford Journals Archive
- ▸ Pricing and Ordering
- ▾ Rights and Permissions
  - Author self archiving policy
  - Accepted Manuscript Embargo Periods
  - Image Permissions
  - **Publication Rights**
  - Rightslink
- Changes to list

Publication rights

What is our policy?

For the majority of journals published by Oxford University Press, we have a policy of acquiring a sole and exclusive licence for all published content, rather than asking authors to transfer ownership of their copyright, which has been common practice in the past. We believe this policy more carefully balances the interests of our authors with our need to maintain the viability and reputation of the journals through which our authors are accorded status, recognition, and widespread distribution. In developing this policy we have been guided by the following principles:

- As a university press and not-for-profit academic publisher, we rely heavily on the good relationships we have with our authors. Having a licensing policy which enables an author to be identified as the owner of the copyright in an article is one of the key ways of demonstrating how highly we value these relationships.
- An exclusive licence enables the centralised and efficient management of permissions and licencing, ensuring the widest dissemination of the content through intermediaries;
- Exclusive rights also enable OUP to take measures on behalf of our authors against infringement, inappropriate use of an article, libel or plagiarism;
- At the same time, by maintaining exclusive rights, in all media for all published content, we can monitor and uphold the integrity of an article once refereed and accepted for publication to be maintained;

Please note - Although the majority of the journals published by Oxford University Press operate exclusive copyright agreements, some of our society journal may require an assignment of copyright. For further information, please refer to the Authors Guidelines sections of the Journal's homepage.

Copyright agreements

OUP cannot publish your article until a completed copyright agreement has been received. You should receive a link to our online licencing system or a hardcopy form as soon as your article is accepted for publication.

Connect

Facebook | Join our mailing list
Twitter | Blog
YouTube

Useful links

Changes to our list
Dispatch dates
Frequently asked questions

Government employees

- If you are or were a UK Crown servant and the article has been written in that capacity, we have an arrangement with HMSO to enable us to publish it while acknowledging that it is Crown Copyright. Please inform the Editorial office or Oxford University Press at the time of acceptance or as soon as possible that the article is Crown Copyright, so that we can ensure the appropriate acknowledgement and copyright line are used, as required by our arrangement with HMSO.
- If you are a US Government employee and the article has been written in that capacity, we acknowledge that the Licence to Publish applies only to the extent allowable by US law.

Re-use of third party content as part of your Oxford Journals article

- As part of your article, you may wish to reuse material sourced from third parties such as other publishers, authors, museums, art galleries etc. To assist with this process, we have a Permission Request form and accompanying Guidelines that specifies the rights required in order for third party material to be published as part of your Article. For a copy of this form, please email.
- Responsibility for clearing these third party permissions must be borne by the Author, and this process completed as soon as possible - preferably before acceptance of the manuscript, but if not possible, before the Article reaches the Production stage of the process.

Rights retained by ALL Oxford Journal authors

- The right, after publication by Oxford Journals, to use all or part of the Article and abstract, for their own personal use, including their own classroom teaching purposes;
- The right, after publication by Oxford Journals, to use all or part of the Article and abstract, in the preparation of derivative works, extension of the article into book-length or in other works, provided that a full acknowledgement is made to the original publication in the journal;
- The right to include the article in full or in part in a thesis or dissertation, provided that this is not published commercially;

For the uses specified here, please note that there is no need for you to apply for written permission from Oxford University Press in advance. Please go ahead with the use ensuring that a full acknowledgment is made to the original source of the material including the journal name, volume, issue, page numbers, year of publication, title of article and to Oxford University Press and/or the learned society.

The only exception to this is for the re-use of material for commercial purposes, e.g. republication or distribution of an article by a for-profit publisher or medical communications company etc. Permission for this kind of re-use is required and can be obtained by using Rightslink.

With Copyright Clearance Center's Rightslink ® service it's faster and easier than ever before to secure permission from OUP titles to be republished in a coursepack, book, CD-ROM/DVD, brochure or pamphlet, journal or magazine, newsletter, newspaper, make a photocopy, or translate.

- Simply visit: Oxford Academic and locate your desired content.
- Click on (Order Permissions) within the table of contents and/ or at the bottom article's abstract to open the following page:
- Select the way you would like to reuse the content
- Create an account or login to your existing account
- Accept the terms and conditions and permission is granted

For questions about using the Rightslink service, please contact Customer Support via phone 877/622-5543 (toll free) or 978/777-9929, or email Rightslink customer care.

Author self-archiving policies

Oxford Journals also offer a range of author self-archiving polices, permitting authors to share and distribute various versions of their articles. For full details of our self-archiving policies please see our Author self-archiving page.

Permissions

- All requests to reuse the article, in whole or in part, in another publication will be handled by Oxford Journals. Unless otherwise stated, any permission fees will be retained by the Journal concerned. Where possible, any requests to reproduce substantial parts of the article (including in other Oxford University Press publications) will be subject to your approval (which is deemed to be given if we have not heard from you within 4 weeks of the permission being granted).
- If copyright of the article is held by someone other than the Author, e.g. the Author's employer, Oxford Journals requires non-exclusive permission to administer any requests from third parties.
- The Journal is registered with the Copyright Licensing Agency (London) and the Copyright Clearance Center (Danvers, Massachusetts), and other Reproduction Rights Organizations. These are non-profit organizations which offer centralised licensing arrangements for photocopying on behalf of publishers such as Oxford University Press.
- Please forward requests to re-use all or part or your article, or to use figures contained within it, to the Rights and New Business Development Department.

The above pages are copies from the webpage
https://academic.oup.com/journals/pages/access_purchase/rights_and_permissions/publication_rights
Date: 21.07.2021

IMA Journal of Numerical Analysis (2021) **00**, 1–33
https://doi.org/10.1093/imanum/drab089

A discontinuous Galerkin coupling for nonlinear elasto-acoustics

Markus Muhr* and Barbara Wohlmuth
Department of Mathematics, Technical University of Munich, Boltzmannstraße 3, 85748 Garching bei München, Germany
*Corresponding author: muhr@ma.tum.de

and

Vanja Nikolić
IMAPP—Department of Mathematics, Radboud University, Heyendaalseweg 135, 6525 AJ Nijmegen, The Netherlands

[Received on 9 February 2021; revised on 20 August 2021]

Inspired by medical applications of high-intensity ultrasound we study a coupled elasto-acoustic problem with general acoustic nonlinearities of quadratic type as they arise, for example, in the Westervelt and Kuznetsov equations of nonlinear acoustics. We derive convergence rates in the energy norm of a finite element approximation to the coupled problem in a setting that involves different acoustic materials and hence jumps within material parameters. A subdomain-based discontinuous Galerkin approach realizes the acoustic-acoustic coupling of different materials. At the same time, elasto-acoustic interface conditions are used for a mutual exchange of forces between the different models. Numerical simulations back up the theoretical findings in a three-dimensional setting with academic test cases as well as in an application-oriented simulation, where the modeling of human tissue as an elastic versus an acoustic medium is compared.

Keywords: nonlinear acoustics; elasto-acoustic coupling; discontinuous Galerkin methods; Westervelt's equation; Kuznetsov's equation; ultrasonic waves.

1. Introduction

This work is devoted to the numerical analysis and simulation of coupled linear elastic-nonlinear acoustic problems, which arise in a variety of medical and industrial applications of ultrasonic waves.

Coupled problems in general play an essential role in different fields of application. Starting with fluid–structure interaction (FSI), where fluid-dynamical equations like Navier–Stokes equations are coupled to equations of solid mechanics (Hou *et al.*, 2012; Wick & Wollner, 2020), over electro/magneto-mechanical systems involving electromagnetic field equations (Kaltenbacher, 2007), to biomedical applications, such as the mathematical modeling of tumor growth and the simulation of thermo-acoustic effects (Shevchenko *et al.*, 2012), which couple wave and heat equations. All such problems have in common at least two different models—mostly in the form of partial differential equations (PDEs)—that describe, for example one a fluid part, the other a solid part of the overall problem. It is then necessary to couple the individual models to a global system. Therefore, different techniques can be used, for example by individual (volumetric) source terms or factors mutually depending on each other such as temperature and speed of sound in Shevchenko *et al.* (2012) or—in case of spatially separated modeldomains with some common interface—via a coupling using Lagrange multipliers, as discussed in Li (1998) for a simple model-problem, or in Flemisch *et al.* (2006) for an

elasto-acoustic coupling. A direct exchange via boundary conditions can also be used, as discussed in Felippa *et al.* (2011) in an FSI setting.

The coupled problem considered in this work is the elasto-acoustic problem, where elastic subdomains are modeled by an elastodynamic wave equation, whereas on (mostly) fluid subdomains a nonlinear acoustic wave equation is employed to model the propagation of pressure waves. The choice of the subdomain models often depends on the concrete application of interest. Therefore, different coupling of elastic and acoustic equations have been investigated in the literature. A Lagrange-multiplier approach for the coupling of a linear elastic equation and a linear undamped acoustic problem is considered in Flemisch *et al.* (2006), whereas the approach of Antonietti *et al.* (2020a) employs a direct exchange of forces via interface conditions.

In this work displacement-based linear elasticity is chosen to model the elastic parts of the domain, whereas a nonlinear wave equation with a general nonlinearity of quadratic type is used for the acoustic part:

$$\frac{1}{c^2}\ddot{\psi} - \Delta\psi - \frac{b}{c^2}\Delta\dot{\psi} = \frac{1}{c^2}(k_1\dot{\psi}\ddot{\psi} + k_2\nabla\psi\cdot\nabla\dot{\psi}). \tag{1.1}$$

This equation is formulated in terms of the acoustic velocity potential $\psi = \psi(x,t)$, from which the acoustic pressure can be computed using the relation $p = \varrho\dot{\psi}$, where ϱ is the mass density of the medium. In homogeneous media, depending on the choice of the parameters k_1 and k_2, the well-known Westervelt and Kuznetsov equations of nonlinear acoustics are obtained from (1.1) as special cases; see Westervelt (1963); Kuznetsov (1970); Kaltenbacher (2007) and Section 2 below for more details on the modeling aspects. Such wave equations model the propagation of sound waves with sufficiently high amplitudes and frequencies through thermoviscous media. The thermoviscous dissipation is reflected in the presence of the strong damping $-\frac{b}{c^2}\Delta\dot{\psi}$ in the equation. The magnitude of the parameter b plays a significant role in the analysis. If $b \to 0^+$ the hyperbolic character of $\frac{1}{c^2}\ddot{\psi} - \Delta\psi$ dominates the behavior of solutions. On the other hand, if the sound diffusivity b is relatively large, the parabolic character of $\frac{1}{c^2}\ddot{\psi} - \frac{b}{c^2}\Delta\dot{\psi}$ is pronounced and, in homogeneous media, one can even expect exponential decay of the energy of solutions in time; see, for example, Mizohata & Ukai (1993); Kaltenbacher & Lasiecka (2009). Thus, the presence of this strong damping will be crucial in our energy arguments.

A common medical use of high-intensity ultrasonic waves is in the noninvasive treatments of kidney stones (Lee *et al.*, 2007) and certain types of cancer (Kennedy, 2005). In such scenarios high-intensity waves are generated, for example, by vibrating piezoelectric transducers (Kaltenbacher, 2007) arranged on a part of the boundary of an acoustic medium, which might, for example, be a simple pipe filled with water. Due to the shape of the transducers, the ultrasonic waves induced into the acoustic medium are focused towards the central axis of the device, increasing the pressure amplitude there even more (Kaltenbacher & Peichl, 2016; Muhr *et al.*, 2019). Finally, on the other end of the acoustic channel, the ultrasound waves propagate into human tissue, where they further travel towards, for example, a kidney stone or tumor. Due to the fact that the waves are focused and of high power, the waves reaching, e.g., the kidney stone have enough energy to break it apart into smaller debris, thus avoiding an open surgery for the patient; see, e.g., Skolarikos *et al.* (2006).

For solving the arising PDEs finite elements are our method of choice. A full discontinuous Galerkin higher-order approach has been developed in Antonietti *et al.* (2020a) for the linear elasto-acoustic problem. In Antonietti *et al.* (2020b) the acoustic propagation in homogeneous media without the quadratic gradient nonlinearity has been treated in a discontinuous Galerkin setting. In Antonietti *et al.* (2012) the purely elastic problem has been considered using the dG approach for the coupling

of different subdomains; the developed approached was termed the discontinuous Galerkin spectral element method (DGSEM).

To our best knowledge rigorous numerical analysis of an interface coupling between linear elasticity and nonlinear acoustics has not been performed before. The available results in the literature on the numerical analysis seem to focus either on related linear coupled problems or on nonlinear (acoustic) wave propagation in homogeneous media. In particular, *a priori* analysis of a high-order discontinuous Galerkin method for a spatial discretization of the corresponding undamped linear problem ($b = k_1 = k_2 = 0$) has been conducted in Antonietti *et al.* (2020a). Error analysis of the (semi-)discrete Kuznetsov equation is seemingly still an open problem. A high-order discontinuous Galerkin method for the Westervelt equation (obtained when $k_2 = 0$ in (1.1)) in homogeneous media has been analyzed in Antonietti *et al.* (2020b). We also point out the results of Maier (2020), which as a particular case, include rigorous analysis of the semidiscrete (based on a finite-element discretization) and fully discrete Westervelt equation in pressure form in homogeneous inviscid media, where $b = 0$.

The hybrid approach developed in this work combines advantages of both the conforming and discontinuous Galerkin framework. Within regions of constant material properties and simple geometry, we use a conforming hexahedral mesh with its—conforming as well—nodal degrees of freedom located at the Gauss–Laguerre–Lobatto points known from the spectral finite element method. However, in order for more flexibility concerning the meshes being used, complex, possibly nonconforming, interfaces are resolved using a DG-paradigm, which also allows us to clearly separate blocks of different material properties, resolve jumps in the coefficients precisely and refine (material) subdomains of the overall model individually to their needs.

The rest of the paper is structured as follows. In Section 2 we discuss the modeling aspects of the problem, interface conditions and the variational formulation as well as the discrete finite element setting. Section 3 introduces the semidiscrete problem with the necessary notation for the hybrid DG-coupling approach. In Section 4 we prove stability of a linear version of the approximate problem and derive convergence rates of this numerical scheme in the energy norm, where the proof of the error-estimate is postponed to the appendix. Section 5 then presents a fixed-point argument, through which we transfer the results from the linear error estimator to the nonlinear case, under the assumption of sufficiently small data and the global mesh size. In particular, the main error estimate for the nonlinear problem is obtained in Theorem 5.3 below. Finally, Section 6 contains our three-dimensional numerical examples that illustrate the convergence results numerically in certain academic test cases as well as in more application-oriented simulations.

2. The nonlinear elasto-acoustic problem

We begin by stating the elasto-acoustic coupled problem in its strong form. The different domains of elastic as well as acoustic media are denoted using indices motivated by medical ultrasound applications as discussed in the introduction. Nevertheless, whenever the term ‘excitator’ or ‘actuator’ is used, one might also think of some general elastic domain $\Omega_e \subset \mathbb{R}^d$ being coupled to some again general ‘fluid’ domain $\Omega_f \subset \mathbb{R}^d$ representing an acoustic medium. What is here called ‘tissue’ domain $\Omega_t \subset \mathbb{R}^d$ will be a domain where both an elastic or an acoustic model could be used, depending on the concrete application. We refer to Fig. 1 below for a graphical representation of the individual domains and interfaces.

Throughout the paper we assume the elastic and acoustic domains to be polygonal and convex, so that they can be discretized exactly. Furthermore, $T > 0$ is a given fixed final time.

The coupling terms as well as the analysis of the global problem depend on the choice of the material models. For the theoretical considerations we restrict ourselves to the case of an acoustic model in the

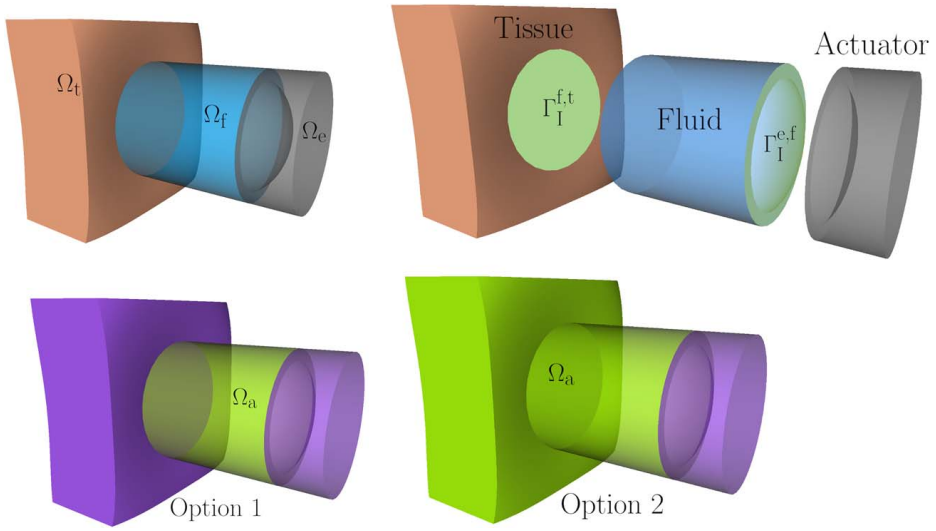

FIG. 1. **(Top left)** Actuator Ω_e, fluid Ω_f and tissue Ω_t domain in exemplary situation motivated by focused ultrasound applications. **(Top right)** Material interfaces $\Gamma_I^{e,f}$, $\Gamma_I^{f,t}$ (highlighted in green). **(Bottom left)** Option 1 with elastic tissue domain. The fluid forms the acoustic domain Ω_a alone (highlighted in green). **(Bottom right)** Option 2 with acoustic tissue domain. The acoustic domain is formed by Ω_f and Ω_t (highlighted in green) with an acoustic-acoustic interface $\Gamma_I^{a,a} = \Gamma_I^{f,t}$. Here the elasto-acoustic interface $\Gamma_I^{e,a} = \Gamma_I^{e,f}$.

tissue domain. From the point of view of analysis this is a more challenging problem, since it involves a different type of interface coupling. However, our numerical experiments will deal with both situations and compare the two models in an applicational context.

Actuator/mechanical excitator(elastic medium)

$$\begin{aligned}
&\varrho^e\,\ddot{\mathbf{u}}^e + 2\varrho^e\zeta^e\,\dot{\mathbf{u}}^e + \varrho^e(\zeta^e)^2\,\mathbf{u}^e - \operatorname{div}(\boldsymbol{\sigma}(\mathbf{u}^e)) = \boldsymbol{f}^e, && \text{in } \Omega_e \times (0,T],\\
&\mathbf{u}^e = \mathbf{0}, && \text{on } \Gamma_D^e \times (0,T],\\
&(\mathbf{u}^e, \dot{\mathbf{u}}^e)|_{t=0} = (\mathbf{u}_0^e, \mathbf{u}_1^e), && \text{in } \Omega_e,
\end{aligned}$$

Fluid(acoustic medium)

$$\begin{aligned}
&(c^f)^{-2}\ddot{\psi}^f - \Delta\psi^f - \frac{b^f}{(c^f)^2}\,\Delta\dot{\psi}^f = f^f(\dot{\psi}^f, \ddot{\psi}^f, \nabla\psi^f, \nabla\dot{\psi}^f), && \text{in } \Omega_f \times (0,T],\\
&\psi^f = 0, && \text{on } \Gamma_D^f \times (0,T],\\
&(\psi^f, \dot{\psi}^f)_{t=0} = (\psi_0^f, \psi_1^f), && \text{in } \Omega_f,
\end{aligned}$$

Tissue, Option 1(elastic medium)

$$\begin{aligned}
&\varrho^t\,\ddot{\mathbf{u}}^t + 2\varrho^t\zeta^t\,\dot{\mathbf{u}}^t + \varrho^t(\zeta^t)^2\,\mathbf{u}^t - \operatorname{div}(\boldsymbol{\sigma}(\mathbf{u}^t)) = \boldsymbol{f}^t, && \text{in } \Omega_t \times (0,T],\\
&\mathbf{u}^t = 0, && \text{on } \Gamma_D^t \times (0,T],\\
&(\mathbf{u}^t, \dot{\mathbf{u}}^t)|_{t=0} = (\mathbf{u}_0^t, \mathbf{u}_1^t), && \text{in } \Omega_t,
\end{aligned}$$

Tissue, Option 2(acoustic medium)

$$
\begin{aligned}
&(c^{\mathrm{t}})^{-2}\ddot{\psi}^{\mathrm{t}} - \Delta\psi^{\mathrm{t}} - \frac{b^{\mathrm{t}}}{(c^{\mathrm{t}})^2}\,\Delta\dot{\psi}^{\mathrm{t}} = f^{\mathrm{t}}(\dot{\psi}^{\mathrm{t}}, \ddot{\psi}^{\mathrm{t}}, \nabla\psi^{\mathrm{t}}, \nabla\dot{\psi}^{\mathrm{t}}), && \text{in } \Omega_{\mathrm{t}} \times (0,T],\\
&\psi^{\mathrm{t}} = 0, && \text{on } \Gamma_{\mathrm{D}}^{\mathrm{t}} \times (0,T],\\
&(\psi^{\mathrm{t}}, \dot{\psi}^{\mathrm{t}})_{t=0} = (\psi_0^{\mathrm{t}}, \psi_1^{\mathrm{t}}), && \text{in } \Omega_{\mathrm{t}}.
\end{aligned}
$$

The acoustic right-hand side nonlinearity is defined as

$$
f^{\mathrm{i}}(\dot{\psi}^{\mathrm{i}}, \ddot{\psi}^{\mathrm{i}}, \nabla\psi^{\mathrm{i}}, \nabla\dot{\psi}^{\mathrm{i}}) = \frac{1}{(c^{\mathrm{i}})^2}\left(k_1^{\mathrm{i}}(\dot{\psi}^{\mathrm{i}})^2 + k_2^{\mathrm{i}}|\nabla\psi^{\mathrm{i}}|^2\right)_t = \frac{2}{(c^{\mathrm{i}})^2}\left(k_1^{\mathrm{i}}\dot{\psi}^{\mathrm{i}}\ddot{\psi}^{\mathrm{i}} + k_2^{\mathrm{i}}\nabla\psi^{\mathrm{i}}\cdot\nabla\dot{\psi}^{\mathrm{i}}\right), \tag{2.1}
$$

where $\mathrm{i} \in \{\mathrm{f}, \mathrm{t}\}$. Here the notation $(\cdot)_t$ stands for the partial derivative with respect to time. The stress-tensor $\boldsymbol{\sigma}$ in the elastic domains is given by Hook's law in the framework of linear elasticity as

$$
\boldsymbol{\sigma}(\mathbf{u}) = \mathbb{C}\boldsymbol{\varepsilon}(\mathbf{u}) = \lambda\mathrm{div}(\mathbf{u})\mathbb{1} + 2\mu\boldsymbol{\varepsilon}(\mathbf{u}),
$$

where $\mathbf{u}$ stands for either $\mathbf{u}^{\mathrm{e}}$ or $\mathbf{u}^{\mathrm{t}}$. Furthermore, $\boldsymbol{\varepsilon}(\mathbf{u}) = \frac{1}{2}(\nabla\mathbf{u} + \nabla\mathbf{u}^{\top})$, $\mathbb{C}$ is the material stiffness tensor with λ and μ being the Lamé-parameters of the given material. Further, ζ^{e} and ζ^{t} are damping parameters. The source terms $\boldsymbol{f}^{\mathrm{e}}$ and $\boldsymbol{f}^{\mathrm{t}}$ denote external body forces.

Interface coupling. We next discuss the coupling conditions over different interfaces. We introduce

$$
\Gamma_{\mathrm{I}}^{\mathrm{e,f}} = \overline{\Omega_{\mathrm{e}}} \cap \overline{\Omega_{\mathrm{f}}}
$$

as the interface between the purely elastic and purely acoustic domains. Moreover, we set

$$
\Gamma_{\mathrm{I}}^{\mathrm{f,t}} = \overline{\Omega_{\mathrm{f}}} \cap \overline{\Omega_{\mathrm{t}}}
$$

as the interface between the purely acoustic domain Ω_{f} and the domain Ω_{t}, for which the *role* of the interface will differ, but not its geometry. Finally, we denote by $\mathbf{n}^{\mathrm{i}}, \mathrm{i} \in \{\mathrm{e,t,f}\}$ the outward unit normal vector field of the respective subdomain Ω_{i}.

Actuator–fluid interface. This is an elasto-acoustic interface that prescribes a normal stress/pressure on the elastic domain given by the acoustic pressure in the fluid domain, while the acoustic particle velocity is prescribed by the displacement velocity of the elastic medium

$$
\begin{aligned}
\boldsymbol{\sigma}(\mathbf{u}^{\mathrm{e}})\,\mathbf{n}^{\mathrm{e}} &= -\varrho^{\mathrm{f}}\left(\dot{\psi}^{\mathrm{f}} + \frac{b^{\mathrm{f}}}{(c^{\mathrm{f}})^2}\ddot{\psi}^{\mathrm{f}}\right)\mathbf{n}^{\mathrm{e}}, && \text{on } \Gamma_{\mathrm{I}}^{\mathrm{e,f}} \times (0,T],\\
\frac{\partial\psi^{\mathrm{f}}}{\partial\mathbf{n}^{\mathrm{f}}} + \frac{b^{\mathrm{f}}}{(c^{\mathrm{f}})^2}\,\frac{\partial\dot{\psi}^{\mathrm{f}}}{\partial\mathbf{n}^{\mathrm{f}}} &= -\dot{\mathbf{u}}^{\mathrm{e}}\cdot\mathbf{n}^{\mathrm{f}}, && \text{on } \Gamma_{\mathrm{I}}^{\mathrm{e,f}} \times (0,T].
\end{aligned}
$$

Fluid–tissue interface. The type of the interface between the fluid and tissue depends on the choice of the material model for the tissue domain Ω_{t}.

Option 1: elastic tissue In case of an elastic material Ω_t the interface has the same structure as the actuator–fluid interface.

$$\begin{aligned} \boldsymbol{\sigma}(\mathbf{u}^\mathrm{t})\,\mathbf{n}^\mathrm{t} &= -\varrho^\mathrm{f}\left(\dot{\psi}^\mathrm{f} + \frac{b^\mathrm{f}}{(c^\mathrm{f})^2}\ddot{\psi}^\mathrm{f}\right)\mathbf{n}^\mathrm{t}, && \text{on } \Gamma_\mathrm{I}^{\mathrm{f,t}} \times (0,T], \\ \frac{\partial \psi^\mathrm{f}}{\partial \mathbf{n}^\mathrm{f}} + \frac{b^\mathrm{f}}{(c^\mathrm{f})^2}\frac{\partial \dot{\psi}^\mathrm{f}}{\partial \mathbf{n}^\mathrm{f}} &= -\dot{\mathbf{u}}^\mathrm{t}\cdot\mathbf{n}^\mathrm{f}, && \text{on } \Gamma_\mathrm{I}^{\mathrm{f,t}} \times (0,T]. \end{aligned}$$

Option 2: acoustic tissue In case of an acoustic material Ω_t, the type of the interface changes to the following transmission condition respecting jumps in the acoustic material parameters, as well as enforcing continuity of the acoustic potential across the acoustic-acoustic interface in the trace sense.

$$\begin{aligned} \left(\nabla\psi^\mathrm{t} + \frac{b^\mathrm{t}}{(c^\mathrm{t})^2}\nabla\dot{\psi}^\mathrm{t}\right)\mathbf{n}^\mathrm{f} &= \left(\nabla\psi^\mathrm{f} + \frac{b^\mathrm{f}}{(c^\mathrm{f})^2}\nabla\dot{\psi}^\mathrm{f}\right)\mathbf{n}^\mathrm{f}, && \text{on } \Gamma_\mathrm{I}^{\mathrm{f,t}} \times (0,T], \\ \psi^\mathrm{t} &= \psi^\mathrm{f}, && \text{on } \Gamma_\mathrm{I}^{\mathrm{f,t}} \times (0,T]. \end{aligned}$$

As already discussed we will focus on the stability and error analysis in the case of the tissue being an acoustic medium. The analysis when the tissue is elastic follows by analogous arguments, and so we omit it here. In the numerical experiments we will extensively test both settings. We refer to Fig. 1 (bottom line) for a graphical description of the two options and corresponding domain setups.

REMARK 2.1 (On the choice of the acoustic model). Our model for acoustic propagation in media with piecewise constant coefficients can be written in the strong form on Ω_a as

$$\tfrac{1}{c^2(x)}\ddot{\psi} - \Delta\psi - \operatorname{div}\big(\tfrac{b(x)}{c^2(x)}\nabla\dot{\psi}\big) = \tfrac{1}{c^2(x)}\big(k_1(x)\dot{\psi}\ddot{\psi} + k_2(x)\nabla\psi\cdot\nabla\dot{\psi}\big). \tag{2.2}$$

This choice of the acoustic model is in part dictated by the physical interface conditions between the elastic and acoustic domain. Simplified versions of (2.2) can be found in the nonlinear acoustics literature. In particular, equation

$$\frac{1}{c^2(x)}\ddot{p} - \Delta p = \frac{\beta_\mathrm{nl}}{\varrho c^4}(p^2)_{tt}$$

for the acoustic pressure is valid when the inhomogeneity of the medium varies in one direction; see Hamilton & Blackstock (1998, §5, Eq. (40)). In such cases it can be assumed that this weak inhomogeneity of the medium results in changes only to the speed of sound, while the other parameters remain constant. Above, β_nl denotes the coefficient of nonlinearity in a given medium. Integrating with respect to time and using the relation $p = \varrho\dot{\psi}$ gives

$$\frac{1}{c^2(x)}\ddot{\psi} - \Delta\psi = \frac{\beta_\mathrm{nl}}{c^4}(\dot{\psi}^2)_t. \tag{2.3}$$

Equation (2.2) can be understood as a mathematical generalization of (2.3) that allows for a Kuznetsov-type nonlinearity and all coefficients to be piecewise constant functions.

2.1 *Notation*

Since in the analysis we assume the tissue to be an acoustic medium, we can treat both the fluid and tissue as one acoustic domain with piecewise constant parameters. We thus denote this tissue–fluid acoustic region as

$$\overline{\Omega_{\mathrm{a}}} = \overline{\Omega_{\mathrm{f}}} \cup \overline{\Omega_{\mathrm{t}}}.$$

The general elasto-acoustic interface $\Gamma_{\mathrm{I}}^{\mathrm{e,a}}$ and the acoustic-acoustic interface $\Gamma_{\mathrm{I}}^{\mathrm{a,a}}$ are then defined as

$$\Gamma_{\mathrm{I}}^{\mathrm{e,a}} = \overline{\Omega_{\mathrm{a}}} \cap \overline{\Omega_{\mathrm{e}}}, \qquad \Gamma_{\mathrm{I}}^{\mathrm{a,a}} = \overline{\Omega_{\mathrm{f}}} \cap \overline{\Omega_{\mathrm{t}}}.$$

We then define the parts of the boundary with homogeneous Dirichlet conditions prescribed as

$$\Gamma_{\mathrm{D}}^{\mathrm{a}} = \partial\Omega_{\mathrm{a}} \setminus \Gamma_{\mathrm{I}}^{\mathrm{e,a}}, \qquad \Gamma_{\mathrm{D}}^{\mathrm{e}} = \partial\Omega_{\mathrm{e}} \setminus \Gamma_{\mathrm{I}}^{\mathrm{e,a}}.$$

To facilitate the analysis we introduce the following Hilbert spaces:

$$H_{\mathrm{D}}^1(\Omega_{\mathrm{f}}) = \{u \in H^1(\Omega_{\mathrm{f}}) : \ u = 0 \text{ on } \Gamma_{\mathrm{D}}^{\mathrm{f}}\}, \qquad H_{\mathrm{D}}^1(\Omega_{\mathrm{t}}) = \{u \in H^1(\Omega_{\mathrm{t}}) : \ u = 0 \text{ on } \Gamma_{\mathrm{D}}^{\mathrm{t}}\},$$
$$H_{\mathrm{D}}^1(\Omega_{\mathrm{a}}) = \{u \in H^1(\Omega_{\mathrm{a}}) : \ u = 0 \text{ on } \Gamma_{\mathrm{D}}^{\mathrm{a}}\}, \qquad \boldsymbol{H}_{\mathrm{D}}^1(\Omega_{\mathrm{e}}) = \{\mathbf{u} \in \boldsymbol{H}^1(\Omega_{\mathrm{e}}) : \ \mathbf{u} = \mathbf{0} \text{ on } \Gamma_{\mathrm{D}}^{\mathrm{e}}\},$$

where $\boldsymbol{H}^1(\Omega_{\mathrm{e}})$ stands for the vector-valued version of the $H^1(\Omega_{\mathrm{e}})$ Sobolev space. By $\|\cdot\|_{\Omega_{\mathrm{a}}}$ and $\|\cdot\|_{\Omega_{\mathrm{e}}}$ we denote the norm in $L^2(\Omega_{\mathrm{a}})$ and $\boldsymbol{L}^2(\Omega_{\mathrm{e}})$ again being the vector-valued version of $L^2(\Omega_{\mathrm{e}})$:

$$\|\phi\|_{\Omega_{\mathrm{a}}} = \left\{\int_{\Omega_{\mathrm{a}}} |\phi|^2 \,\mathrm{d}x\right\}^{1/2}, \qquad \|\mathbf{u}\|_{\Omega_{\mathrm{e}}} = \left\{\int_{\Omega_{\mathrm{e}}} \|\mathbf{u}\|^2 \,\mathrm{d}x\right\}^{1/2}.$$

Similarly, $\|\cdot\|_{\Omega_{\mathrm{f}}}$ and $\|\cdot\|_{\Omega_{\mathrm{t}}}$ denote the norms in $L^2(\Omega_{\mathrm{f}})$ and $L^2(\Omega_{\mathrm{t}})$, respectively.

2.2 *Assumptions on the medium parameters*

We assume all the medium parameters to be piecewise constant functions:

$$c(x) := \begin{cases} c^{\mathrm{f}}, & x \in \Omega_{\mathrm{f}}, \\ c^{\mathrm{t}}, & x \in \Omega_{\mathrm{t}}, \end{cases} \quad b(x) := \begin{cases} b^{\mathrm{f}}, & x \in \Omega_{\mathrm{f}}, \\ b^{\mathrm{t}}, & x \in \Omega_{\mathrm{t}}, \end{cases} \quad k_1(x) := \begin{cases} k_1^{\mathrm{f}}, & x \in \Omega_{\mathrm{f}}, \\ k_1^{\mathrm{t}}, & x \in \Omega_{\mathrm{t}}, \end{cases} \quad k_2(x) := \begin{cases} k_2^{\mathrm{f}}, & x \in \Omega_{\mathrm{f}}, \\ k_2^{\mathrm{t}}, & x \in \Omega_{\mathrm{t}}. \end{cases}$$

Furthermore, we assume that $c^{\mathrm{f}}, c^{\mathrm{t}} > 0$ and $b^{\mathrm{f}}, b^{\mathrm{t}} > 0$. As mentioned in the introduction the presence of strong b-damping in the nonlinear acoustic equation is crucial for the validity of our error estimates. The sign of k does not play an important role in the analysis, and we can assume that $k_i^{\mathrm{f}}, k_i^{\mathrm{t}} \in \mathbb{R}$ for $i = 1, 2$. The piecewise acoustic nonlinearity is given by

$$f^{\mathrm{a}}(\dot\psi, \psi, \nabla\psi, \nabla\dot\psi) := \begin{cases} f^{\mathrm{f}}(\dot\psi^{\mathrm{f}}, \psi^{\mathrm{f}}, \nabla\psi^{\mathrm{f}}, \nabla\dot\psi^{\mathrm{f}}), & x \in \Omega_{\mathrm{f}}, \\ f^{\mathrm{t}}(\dot\psi^{\mathrm{t}}, \psi^{\mathrm{t}}, \nabla\psi^{\mathrm{t}}, \nabla\dot\psi^{\mathrm{t}}), & x \in \Omega_{\mathrm{t}}. \end{cases} \tag{2.4}$$

Since in the analysis we work with one elastic domain, from now on we drop the superscript e from the notation of the elastic solution and its derivatives, and use, for example, just $\mathbf{u}$ in place of $\mathbf{u}^{\mathrm{e}}$. We also set $\zeta = \zeta^{\mathrm{e}} > 0$. The material density ρ is the only parameter appearing in both elastic and acoustic media, hence we introduce the piecewise constant function

$$\varrho(x) = \begin{cases} \varrho^{\mathrm{a}}(x) = \begin{cases} \varrho^{\mathrm{f}}, & x \in \Omega_{\mathrm{f}}, \\ \varrho^{\mathrm{t}}, & x \in \Omega_{\mathrm{t}}, \end{cases} \\ \varrho^{\mathrm{e}}, \qquad\qquad x \in \Omega_{\mathrm{e}}, \end{cases}$$

which is assumed to be positive as well.

2.3 *Weak formulation*

We can now introduce the bilinear form

$$a^{\mathrm{a}} : \{\psi \in L^2(\Omega_{\mathrm{a}}) : \psi_{|\Omega_{\mathrm{f}}} \in H^1_{\mathrm{D}}(\Omega_{\mathrm{f}}),\ \psi_{|\Omega_{\mathrm{t}}} \in H^1_{\mathrm{D}}(\Omega_{\mathrm{t}})\}^2 \to \mathbb{R}$$

as

$$a^{\mathrm{a}}(\psi, \phi) = (\nabla\psi^{\mathrm{f}}, \nabla\phi^{\mathrm{f}})_{\Omega_{\mathrm{f}}} + (\nabla\psi^{\mathrm{t}}, \nabla\phi^{\mathrm{t}})_{\Omega_{\mathrm{t}}},$$

where $\psi|_{\Omega_{\mathrm{f}}} = \psi^{\mathrm{f}}$ and $\psi|_{\Omega_{\mathrm{t}}} = \psi^{\mathrm{t}}$. The bilinear form $a^{\mathrm{e}} : \boldsymbol{H}^1_{\mathrm{D}}(\Omega_{\mathrm{e}}) \times \boldsymbol{H}^1_{\mathrm{D}}(\Omega_{\mathrm{e}}) \to \mathbb{R}$ corresponding to the elastic medium is given by

$$a^{\mathrm{e}}(\mathbf{u}, \mathbf{v}) = (\mathbb{C}\boldsymbol{\varepsilon}(\mathbf{u}), \boldsymbol{\varepsilon}(\mathbf{v}))_{\Omega_{\mathrm{e}}}.$$

Going forward we assume that our problem has a solution in the following sense. Let the solution space for the displacement be given by

$$X^{\mathrm{e}} = C^1([0,T]; \boldsymbol{H}^1_{\mathrm{D}}(\Omega_{\mathrm{e}})) \cap H^2(0,T; \boldsymbol{H}^s(\Omega_{\mathrm{e}})),$$

and the solution space for the acoustic velocity potential by

$$X^{\mathrm{a}} = \{\psi \in C^1([0,T]; H^1_{\mathrm{D}}(\Omega_{\mathrm{a}})) \cap H^2(0,T; L^2(\Omega_{\mathrm{a}})) : \psi|_{\Omega_{\mathrm{i}}} \in H^2(0,T; H^s(\Omega_{\mathrm{i}}))\},$$

where $s > 1 + d/2$, d being the spatial dimension of the problem. We note that the choice of the regularity index s is dictated by the nonlinear error analysis below; see Theorem 5.3 for details.

We assume that there exists $(\mathbf{u}, \psi) \in X^{\mathrm{e}} \times X^{\mathrm{a}}$ such that

$$\begin{aligned} &(\varrho^{\mathrm{e}}\ddot{\mathbf{u}}, \mathbf{v})_{\Omega_{\mathrm{e}}} + (2\varrho^{\mathrm{e}}\zeta\dot{\mathbf{u}}, \mathbf{v})_{\Omega_{\mathrm{e}}} + (\varrho^{\mathrm{e}}\zeta^2\mathbf{u}, \mathbf{v})_{\Omega_{\mathrm{e}}} + a^{\mathrm{e}}(\mathbf{u}, \mathbf{v}) \\ &\quad + \mathscr{I}(\varrho^{\mathrm{f}}(\dot{\psi} + \tfrac{b}{c^2}\ddot{\psi}), \mathbf{v}) - \mathscr{I}(\phi, \dot{\mathbf{u}}) + (c^{-2}\ddot{\psi}, \phi)_{\Omega_{\mathrm{a}}} + a^{\mathrm{a}}(\psi + \tfrac{b}{c^2}\dot{\psi}, \phi) \\ &= (\boldsymbol{f}^{\mathrm{e}}, \mathbf{v})_{\Omega_{\mathrm{e}}} + (f^{\mathrm{a}}(\dot{\psi}, \ddot{\psi}, \nabla\psi, \nabla\dot{\psi}),\ \phi)_{\Omega_{\mathrm{a}}} \end{aligned}$$

for a.e. $t \in (0,T)$ and all test functions $(\mathbf{v},\phi) \in \boldsymbol{H}^1_{\mathrm{D}}(\Omega_{\mathrm{e}}) \times \{\phi \in L^2(\Omega_{\mathrm{a}}) : \phi_{|\Omega_{\mathrm{f}}} \in H^1_{\mathrm{D}}(\Omega_{\mathrm{f}}),\ \phi_{|\Omega_{\mathrm{t}}} \in H^1_{\mathrm{D}}(\Omega_{\mathrm{t}})\}$, supplemented by the initial conditions

$$(\mathbf{u},\dot{\mathbf{u}})|_{t=0} = (\mathbf{u}_0,\mathbf{u}_1), \qquad (\psi,\dot{\psi})_{t=0} = (\psi_0,\psi_1).$$

The interface form $\mathscr{I} : H^1_{\mathrm{D}}(\Omega_{\mathrm{a}}) \times \boldsymbol{H}^1_{\mathrm{D}}(\Omega_{\mathrm{e}}) \to \mathbb{R}$ above is defined as

$$\mathscr{I}(\psi,\mathbf{v}) = (\psi\mathbf{n}^{\mathrm{e}},\mathbf{v})_{\Gamma_{\mathrm{I}}^{\mathrm{e,a}}}.$$

Well-posedness of this coupled nonlinear problem appears to still be an open problem. The main difficulties in its analysis lie in the quasi-linear nature of the acoustic wave equation and the quadratic gradient nonlinearity, which, in general, requires the use of high-order energies in the analysis. However, some results on related linear coupled and nonlinear acoustic problems can be found in the literature. In particular, well-posedness of the linear undamped version ($b = k_1 = k_2 = 0$) of the coupled problem with $f^{\mathrm{a}} = f^{\mathrm{a}}(x,t)$ is proven in Antonietti *et al.* (2020a, Theorem 1.1). Small-data global well-posedness of the Kuznetsov equation has been established in Mizohata & Ukai (1993), whereas the Westervelt equation expressed in terms of the acoustic pressure has been analyzed in, for example, Kaltenbacher & Lasiecka (2009) and Meyer & Wilke (2011). We also point out the analysis of a nonlinear elasto-acoustic problem in Brunnhuber *et al.* (2014), where the acoustic field is modeled by the Westervelt equation with an additional strong nonlinear damping.

2.4 *Discrete setting*

Before introducing the semidiscrete version of the above problem, we state the assumptions on the finite element mesh used in the discretization (with $d = 3$). Each subdomain Ω_{e}, Ω_{f} and Ω_{t} is individually meshed in a conforming way by trilinear hexahedral Lagrange elements, where the element mapping for element κ will be denoted by

$$F_\kappa : (-1,1)^3 \to \mathbb{R}^3, \quad F_\kappa((-1,1)^3) = \kappa.$$

This gives rise to the subdomain-wise tessellations $\mathscr{T}_{h_{\mathrm{e}},\mathrm{e}}$, $\mathscr{T}_{h_{\mathrm{f}},\mathrm{f}}$ and $\mathscr{T}_{h_{\mathrm{t}},\mathrm{t}}$, where we have defined $h_{\mathrm{i}} := \max_{\kappa\in\mathscr{T}_{h_{\mathrm{i}},\mathrm{i}}} h_\kappa$, $\mathrm{i} \in \{\mathrm{e},\mathrm{f},\mathrm{t}\}$, and the global mesh $\mathscr{T}_h$ with global mesh size

$$h = \max\{h_{\mathrm{e}},h_{\mathrm{f}},h_{\mathrm{t}}\}.$$

At the interfaces the subdomain meshes *do not* have to match, which allows for a more flexible grid generation as well as different levels of refinement. For $\mathrm{i} \in \{\mathrm{e},\mathrm{f},\mathrm{t}\}$ we make the following assumptions on the families $\{\mathscr{T}_{h_{\mathrm{i}},\mathrm{i}}\}$:

- Shape-regularity subdomain-wise: there exists $\sigma_{\mathrm{i}} > 0$ such that each element $\kappa \in \mathscr{T}_{h_{\mathrm{i}},\mathrm{i}}$ contains a ball with the radius $\rho_\kappa \geqslant \frac{h_\kappa}{\sigma_{\mathrm{i}}}$, where h_κ denotes the diameter of the element κ.
- Uniformity (subdomain-wise): there exist $\hat{\sigma}_{\mathrm{i}} > 0$, such that: $\frac{h_{\mathrm{i}}}{\min_{\kappa\in\mathscr{T}_{h_{\mathrm{i}},\mathrm{i}}} h_\kappa} \leqslant \hat{\sigma}_{\mathrm{i}}$.
- Comparability of subdomains: there exists $\hat{\varsigma}_{\mathrm{i}} > 0$ such that: $h \leqslant \hat{\varsigma}_{\mathrm{i}} h_{\mathrm{i}}$.

- Face nondegeneracy: let $\kappa \in \mathscr{T}_{h_\mathrm{i},\mathrm{i}}$ and F be any face of κ, then there exists some constant ι_i such that $|F| \geqslant \frac{h_\kappa^2}{\iota_\mathrm{i}}$.

REMARK 2.2 We remark that the assumed face nondegeneracy is applied *only* subdomain-wise, and does *not* exclude grids that are for example staggered by a length-parameter ϵ w.r.t. each other. The 'comparability of subdomain' assumption can easily be satisfied even for individually generated submeshes, as only the global mesh-size information needs to be exchanged.

Besides the computational domain's volumetric tessellation, we also define the sets of mesh faces that belong to the interfaces. As mentioned before the analysis deals with Option 2, where the tissue is an acoustic medium. Hence, we classify the interfaces into elasto-acoustic and acoustic-acoustic. To deal with meshes that are nonmatching at the interfaces, we follow ideas and notation of mortar methods and classify master and slave sides for the subdomains meeting at the interfaces; see, for example, Brivadis *et al.* (2015). In the case of the elasto-acoustic interface the acoustic fluid region will be considered the master side, the elastic excitation domain the slave side. The fluid will be regarded as the master and the tissue domain as the slave side for the acoustic-acoustic interface again. We define the interface-face-collection now only for the master side, where later summation/integration over them, of course, incorporates the respective slave sides contributions as well, e.g. via jump terms.

$$\text{Elasto-Acoustic interface faces (master side): } \mathscr{F}_h^{\mathrm{e,a}} = \{F : F \text{ face of some } \kappa \in \mathscr{T}_{h,\mathrm{f}} \wedge F \subset \Gamma_\mathrm{I}^{\mathrm{e,a}}\},$$
$$\text{Acoustic-Acoustic interface faces: } \mathscr{F}_h^{\mathrm{a,a}} = \{F : F \text{ face of some } \kappa \in \mathscr{T}_{h,\mathrm{f}} \wedge F \subset \Gamma_\mathrm{I}^{\mathrm{a,a}}\}.$$

If we talk about faces on a generic interface (e.g. any of elasto-acoustic or acoustic-acoustic) we use $\mathscr{F}_h^{\mathrm{I}}$. We can now use the following physical-domain elementwise ansatz-spaces:

$$\mathscr{Q}_p^F(\kappa) = \{\varphi : \kappa \to \mathbb{R} \,:\, \varphi = \hat{\varphi} \circ F_\kappa^{-1}, \text{ with some } \hat{\varphi} \in \mathscr{Q}_p((-1,1)^3)\},$$
$$\underline{\mathscr{Q}}_p^F(\kappa) = \{v : \kappa \to \mathbb{R}^3 \,:\, v = \hat{v} \circ F_\kappa^{-1}, \text{ with some } \hat{v} \in \underline{\mathscr{Q}}_p((-1,1)^3)\},$$

where $\mathscr{Q}_p$ denotes the tensor-product polynomial space of degree $\leqslant p$ in each direction and $\underline{\mathscr{Q}}_p$ its vector-valued version. Furthermore, we introduce the finite-element spaces as

$$V_h^{\mathrm{f}} := \{\psi \in H_\mathrm{D}^1(\Omega_\mathrm{f}) : \psi|_\kappa \in \mathscr{Q}_p^F(\kappa)\, \forall\, \kappa \in \mathscr{T}_{h,\mathrm{f}}\}, \qquad V_h^{\mathrm{t}} := \{\psi \in H_\mathrm{D}^1(\Omega_\mathrm{t}) : \psi|_\kappa \in \mathscr{Q}_p^F(\kappa)\, \forall\, \kappa \in \mathscr{T}_{h,\mathrm{t}}\},$$
$$V_h^{\mathrm{a}} := \{\psi \in L^2(\Omega_\mathrm{a}) : \psi|_{\Omega_\mathrm{f}} \in V_h^{\mathrm{f}}, \psi|_{\Omega_\mathrm{t}} \in V_h^{\mathrm{t}}\}, \qquad \boldsymbol{V}_h^{\mathrm{e}} := \{v \in \boldsymbol{H}_\mathrm{D}^1(\Omega_\mathrm{e}) : v|_\kappa \in \underline{\mathscr{Q}}_p^F(\kappa)\, \forall\, \kappa \in \mathscr{T}_{h,\mathrm{e}}\}.$$

REMARK 2.3 Having different polynomial degrees p_f, p_t and p_e within the individual subdomains would be possible. However, for simplicity of notation, we restrict ourselves here to a single polynomial degree p.

We use $x \lesssim y$ to denote $x \leqslant Cy$, where the constant $C > 0$ does not depend on the mesh size, however, might still depend on the material parameters and on the polynomial degree. For better readability we do not track this dependency on material parameters in this work. In an easier, purely acoustic setting such constant tracking was performed in Antonietti *et al.* (2020b).

3. The semidiscrete problem

To state our hybrid semidiscrete problem we introduce the following average and jump operators on the fluid–tissue interface. For sufficiently smooth ψ we set the gradient average on $F \in \mathscr{F}_h^{\mathrm{a,a}}$ and define the jump of the normal trace as follows:

$$\{\!\{\nabla\psi\}\!\} = \frac{\nabla\psi^{\mathrm{f}} + \nabla\psi^{\mathrm{t}}}{2}, \qquad [\![\psi]\!] = \psi^{\mathrm{f}}\mathbf{n}^{\mathrm{f}} + \psi^{\mathrm{t}}\mathbf{n}^{\mathrm{t}}.$$

Moreover, we introduce the short-hand notations

$$\langle \psi,\ \phi\rangle_{\mathscr{F}_h^{\mathrm{a,a}}} = \sum_{F\in\mathscr{F}_h^{\mathrm{a,a}}} (\psi,\phi)_{L^2(F)}, \qquad \text{and} \qquad \|\psi\|_{\mathscr{F}_h^{\mathrm{a,a}}} = \langle \psi,\ \psi\rangle_{\mathscr{F}_h^{\mathrm{a,a}}}^{1/2}.$$

The semidiscrete problem is given by

$$\begin{aligned}
&(\varrho^{\mathrm{e}}\ddot{\mathbf{u}}_h(t),\mathbf{v}_h)_{\Omega_{\mathrm{e}}} + (2\varrho^{\mathrm{e}}\zeta\dot{\mathbf{u}}_h(t),\mathbf{v}_h)_{\Omega_{\mathrm{e}}} + (\varrho^{\mathrm{e}}\zeta^2\mathbf{u}_h(t),\mathbf{v}_h)_{\Omega_{\mathrm{e}}} + a^{\mathrm{e}}(\mathbf{u}_h(t),\mathbf{v}_h)\\
&\qquad + (c^{-2}\ddot{\psi}_h(t),\phi_h)_{\Omega_{\mathrm{a}}} + a_h^{\mathrm{a}}(\psi_h(t) + \tfrac{b}{c^2}\dot{\psi}_h(t),\phi_h)\\
&\qquad\qquad + \mathscr{I}(\varrho^{\mathrm{f}}(\dot{\psi}_h(t) + \tfrac{b}{c^2}\ddot{\psi}_h(t)),\mathbf{v}_h) - \mathscr{I}(\phi_h,\dot{\mathbf{u}}_h(t))\\
&= (\mathbf{f}_{\mathrm{e}}(t),\mathbf{v}_h)_{\Omega_{\mathrm{e}}} + (f_h^{\mathrm{a}}(\dot{\psi}_h(t),\ddot{\psi}_h(t),\nabla\psi_h(t),\nabla\dot{\psi}_h(t)),\ \phi_h)_{\Omega_{\mathrm{a}}}
\end{aligned} \tag{3.1}$$

a.e. in time for all $(\mathbf{v}_h,\phi_h) \in \boldsymbol{V}_h^{\mathrm{e}} \times V_h^{\mathrm{a}}$ and supplemented with initial conditions

$$(\mathbf{u}_h(0),\dot{\mathbf{u}}_h(0),\psi_h(0),\dot{\psi}_h(0)) \in \boldsymbol{V}_h^{\mathrm{e}} \times \boldsymbol{V}_h^{\mathrm{e}} \times V_h^{\mathrm{a}} \times V_h^{\mathrm{a}}.$$

The acoustic gradient terms on the right-hand side of (3.1) should be understood as

$$\begin{aligned}
&(f_h^{\mathrm{a}}(\dot{\psi}_h(t),\ddot{\psi}_h(t),\nabla\psi_h(t),\nabla\dot{\psi}_h(t)),\ \phi_h)_{\Omega_{\mathrm{a}}}\\
&= (f_h^{\mathrm{f}}(\dot{\psi}_h^{\mathrm{f}}(t),\ddot{\psi}_h^{\mathrm{f}}(t),\nabla\psi_h^{\mathrm{f}}(t),\nabla\dot{\psi}_h^{\mathrm{f}}(t)),\ \phi_h)_{\Omega_{\mathrm{f}}} + (f_h^{\mathrm{t}}(\dot{\psi}_h^{\mathrm{t}}(t),\ddot{\psi}_h^{\mathrm{t}}(t),\nabla\psi_h^{\mathrm{t}}(t),\nabla\dot{\psi}_h^{\mathrm{t}}(t)),\ \phi_h)_{\Omega_{\mathrm{t}}},
\end{aligned}$$

where f_h^f and f_h^t are defined analogously to f^t and f^t in (2.1) just over the discrete spaces. This is used for a compact notation of the difference $\|f^a - f_h^a\|$ later in Sec. 4 and 5. The discrete acoustic bilinear form $a_h^{\mathrm{a}} : V_h^{\mathrm{a}} \times V_h^{\mathrm{a}} \to \mathbb{R}$ is given by

$$\begin{aligned}
a_h^{\mathrm{a}}(\psi_h,\varphi_h) &= (\nabla\psi_h^{\mathrm{f}},\nabla\varphi_h)_{\Omega_{\mathrm{f}}} + (\nabla\psi_h^{\mathrm{t}},\nabla\varphi_h)_{\Omega_{\mathrm{t}}}\\
&\quad - \langle\{\!\{\nabla\psi_h\}\!\},\ [\![\varphi_h]\!]\rangle_{\mathscr{F}_h^{\mathrm{a,a}}} - \langle\{\!\{\nabla\varphi_h\}\!\},\ [\![\psi_h]\!]\rangle_{\mathscr{F}_h^{\mathrm{a,a}}} + \langle\chi[\![\psi_h]\!],\ [\![\varphi_h]\!]\rangle_{\mathscr{F}_h^{\mathrm{a,a}}}.
\end{aligned}$$

Finally, the stabilization parameter χ is defined face-wise on $F \in \mathscr{F}_h^{\mathrm{a,a}}$:

$$\chi = \beta\frac{p^2}{h_F}, \qquad h_F = \min\{h_\kappa : \kappa \in \mathscr{T}_{h,\mathrm{t}},\ \lambda^2(\overline{\kappa}\cap\overline{\kappa}_F) > 0\}, \tag{3.2}$$

where κ_F is the element that F belongs to as a face and $\lambda^2(\cdot)$ is the two-dimensional Lebesgue measure. By that h_F is the minimal h of all elements from the slave-side (tissue domain) that have a nontrivial intersection with the face F, while $\beta > 0$ is a suitable DG penalty parameter that will be chosen as sufficiently large to guarantee stability of the semidiscrete method. Finally, we also incorporate the p-dependency in the stabilization parameter in the standard way via p^2, see Schötzau *et al.* (2002); Epshteyn & Rivière (2007); Antonietti *et al.* (2020a), where p is again the polynomial degree of the finite element ansatz functions.

4. Stability analysis and *a priori* bounds of the linearized semidiscrete formulation

We first perform the stability analysis in the case

$$f_h^{\mathrm{a}} = f_h^{\mathrm{a}}(x,t).$$

To facilitate the later study of the nonlinear problem the following points are important:

(i) Discretization errors $f^{\mathrm{a}} - f_h^{\mathrm{a}}$ of the acoustic source terms should be taken into account.

(ii) An error estimate of $\ddot{\psi}_h$ and not only of the approximate potential field ψ_h and its first time derivative $\dot{\psi}_h$ is needed.

The second point implies that we have to involve the second time derivative of the approximate acoustic velocity potential as a test function in the energy analysis.

Motivated by the analysis in Antonietti *et al.* (2020b), we define the higher-order acoustic energy

$$\|\psi_h(t)\|_{\mathrm{E}^{\mathrm{a}}}^2 = \|\dot{\psi}_h(t)\|_{\Omega_{\mathrm{a}}}^2 + \int_0^t \|\ddot{\psi}_h(\tau)\|_{\Omega_{\mathrm{a}}}^2 \,\mathrm{d}\tau + \|\nabla\tilde{\psi}_h(t)\|_{\Omega_{\mathrm{a}}}^2 + \|\sqrt{\chi}\,[\![\tilde{\psi}_h(t)]\!]\,\|_{\mathscr{F}_h^{\mathrm{a,a}}}^2, \tag{4.1}$$

where we have introduced the short-hand tilde notation

$$\tilde{\psi}_h = \psi_h + \frac{b}{c^2}\dot{\psi}_h.$$

The gradient term should be understood in a broken sense as

$$\begin{aligned}\|\nabla\tilde{\psi}_h(t)\|_{\Omega_{\mathrm{a}}}^2 &= a^{\mathrm{a}}(\tilde{\psi}_h(t),\tilde{\psi}_h(t)) \\ &= \left\|\nabla\left(\psi_h^{\mathrm{f}} + \frac{b^{\mathrm{f}}}{(c^{\mathrm{f}})^2}\dot{\psi}_h^{\mathrm{f}}\right)(t)\right\|_{\Omega_{\mathrm{f}}}^2 + \left\|\nabla\left(\psi_h^{\mathrm{t}} + \frac{b^{\mathrm{t}}}{(c^{\mathrm{t}})^2}\dot{\psi}_h^{\mathrm{t}}\right)(t)\right\|_{\Omega_{\mathrm{t}}}^2.\end{aligned}$$

For convenience of notation we also introduce the broken H^s-norm on the total acoustic domain as

$$\|\phi\|_{s,\mathrm{a}}^2 = \|\phi\|_{H^s(\Omega_{\mathrm{f}})}^2 + \|\phi\|_{H^s(\Omega_{\mathrm{t}})}^2, \quad s \geqslant 0.$$

We further recall that

$$\|\sqrt{\chi}\,[\![\tilde{\psi}_h(t)]\!]\,\|_{\mathscr{F}_h^{\mathrm{a,a}}}^2 = \langle \chi\,[\![\tilde{\psi}_h]\!],\ [\![\tilde{\psi}_h]\!]\rangle_{\mathscr{F}_h^{\mathrm{a,a}}}$$

with

$$[\![\tilde{\psi}_h]\!] = (\psi_h^{\mathrm{f}} + \tfrac{b^{\mathrm{f}}}{(c^{\mathrm{f}})^2}\dot{\psi}_h^{\mathrm{f}})\mathbf{n}^{\mathrm{f}} + (\psi_h^{\mathrm{t}} + \tfrac{b^{\mathrm{t}}}{(c^{\mathrm{t}})^2}\dot{\psi}_h^{\mathrm{t}})\mathbf{n}^{\mathrm{t}}$$

and the stabilization parameter χ defined in (3.2). The elastic energy is given by

$$\|\mathbf{u}_h(t)\|_{\mathrm{E^e}}^2 = \|\dot{\mathbf{u}}_h(t)\|_{\Omega_{\mathrm{e}}}^2 + \|\mathbf{u}_h(t)\|_{\Omega_{\mathrm{e}}}^2 + \|\boldsymbol{\varepsilon}(\mathbf{u}_h(t))\|_{\Omega_{\mathrm{e}}}^2. \tag{4.2}$$

We can then set the total energy as

$$\|(\mathbf{u}_h(t), \psi_h(t))\|_{\mathrm{E}}^2 = \|\psi_h(t)\|_{\mathrm{E^a}}^2 + \|\mathbf{u}_h(t)\|_{\mathrm{E^e}}^2.$$

Note that, except for the term $b/c^2\dot{\psi}_h$, the norms within energies are chosen without scaling that would involve material parameters. For careful tracking of material parameters within the hidden constants in the numerical analysis, we refer to Antonietti *et al.* (2020a,b).

REMARK 4.1 For the upcoming estimates it is useful to note that a bound on the acoustic energy of a function ψ at time t will give us a bound on $\|\nabla\psi(t)\|_{\Omega_{\mathrm{a}}}$ and $\|\nabla\dot{\psi}(t)\|_{\Omega_{\mathrm{a}}}$ as well. Indeed, let

$$\|\psi(t)\|_{\mathrm{E^a}}^2 \leqslant M$$

for some $M > 0$. Then by

$$\begin{aligned}\|\nabla\tilde{\psi}(t)\|_{\Omega_{\mathrm{a}}}^2 = \|\nabla\psi(t)\|_{\Omega_{\mathrm{a}}}^2 &+ \frac{(b^{\mathrm{f}})^2}{(c^{\mathrm{f}})^4}\|\nabla\dot{\psi}^{\mathrm{f}}(t)\|_{\Omega_{\mathrm{f}}}^2 + 2\frac{b^{\mathrm{f}}}{(c^{\mathrm{f}})^2}(\nabla\psi_h^{\mathrm{f}}(t), \nabla\dot{\psi}_h^{\mathrm{f}}(t))_{\Omega_{\mathrm{f}}} \\ &+ \frac{(b^{\mathrm{t}})^2}{(c^{\mathrm{t}})^4}\|\nabla\dot{\psi}^{\mathrm{t}}(t)\|_{\Omega_{\mathrm{f}}}^2 + 2\frac{b^{\mathrm{t}}}{(c^{\mathrm{t}})^2}(\nabla\psi_h^{\mathrm{t}}(t), \nabla\dot{\psi}_h^{\mathrm{t}}(t))_{\Omega_{\mathrm{t}}} \leqslant M,\end{aligned}$$

and Hölder's and Young's inequalities, we have

$$\begin{aligned}\|\nabla\psi(t)\|_{\Omega_{\mathrm{a}}}^2 + \frac{\underline{b}^2}{\overline{c}^4}\|\nabla\dot{\psi}(t)\|_{\Omega_{\mathrm{a}}}^2 &\leqslant M + \frac{2\overline{b}}{\underline{c}^2}\|\nabla\psi(t)\|_{\Omega_{\mathrm{a}}}\|\nabla\dot{\psi}(t)\|_{\Omega_{\mathrm{a}}} \\ &\leqslant M + \frac{2}{\epsilon}\|\nabla\psi(t)\|_{\Omega_{\mathrm{a}}}^2 + \epsilon\frac{\overline{b}^2}{2\underline{c}^4}\|\nabla\dot{\psi}(t)\|_{\Omega_{\mathrm{a}}}^2,\end{aligned} \tag{4.3}$$

where $\underline{b} = \min\{b^{\mathrm{f}}, b^{\mathrm{t}}\}$, $\overline{b} = \max\{b^{\mathrm{f}}, b^{\mathrm{t}}\}$ and similarly $\underline{c} = \min\{c^{\mathrm{f}}, c^{\mathrm{t}}\}$, $\overline{c} = \max\{c^{\mathrm{f}}, c^{\mathrm{t}}\}$. We can choose $\epsilon > 0$ small enough so that the last term on the right in (4.3) is absorbed by the left side. By additionally relying on the bound

$$\|\nabla\psi(t)\|_{\Omega_{\mathrm{a}}}^2 \leqslant 2T\int_0^t \|\nabla\dot{\psi}(\tau)\|_{\Omega_{\mathrm{a}}}^2 \mathrm{d}\tau + 2\|\nabla\psi(0)\|_{\Omega_{\mathrm{a}}}^2$$

and Gronwall's inequality, we then have

$$\|\nabla\psi(t)\|^2_{\Omega_\mathrm{a}} + \|\nabla\dot{\psi}(t)\|^2_{\Omega_\mathrm{a}} \leqslant \tilde{C}(T,b)\left(M + \|\nabla\psi(0)\|^2_{\Omega_\mathrm{a}}\right), \quad t\in[0,T], \tag{4.4}$$

where the constant $\tilde{C}$ tends to infinity as $T\to\infty$ or $\underline{b}\to 0^+$, but does not depend on h.

4.1 *Preliminary theoretical results*

In this subsection we collect several well-known results on interpolation, trace inequalities and standard estimates used in the (discontinuous) Galerkin framework that we will later need to employ in our proofs.

LEMMA 4.2 Let $p\in\mathbb{N}$ be a given polynomial degree and let $\kappa\in\mathscr{T}_h$. Then for $v\in\mathscr{Q}^F_p(\kappa)$, it holds

$$\begin{aligned}\|v\|_{L^\infty(\kappa)} &\leqslant C_\mathrm{inv} h_\kappa^{-d/2}\|v\|_{L^2(\kappa)},\\ \|v\|_{L^2(\partial\kappa)} &\lesssim h_\kappa^{-1/2}\|v\|_{L^2(\kappa)}.\end{aligned} \tag{4.5}$$

Note that the constants in Lemma 4.2 depend on the polynomial degree of v. However, this dependency is suppressed here just as the material parameter dependencies.

LEMMA 4.3 Let χ be the stabilization parameter defined in 3.2 with parameter β. Then it holds

$$\|\chi^{-1/2}\{\!\{\nabla\tilde{\psi}_h(t)\}\!\}\|_{\mathscr{F}_h^{\mathrm{a,a}}} \lesssim \frac{1}{\sqrt{\beta}}\|\nabla\tilde{\psi}_h(t)\|_{\Omega_\mathrm{a}}, \quad t\in[0,T].$$

Proof. The proof follows analogously to the proof of Antonietti *et al.* (2020a, Lemma A.1). □

LEMMA 4.4 Let $\psi_h\in H^2(0,T;V_h^\mathrm{a})$ and let C_1 and C_2 be two given positive constants. For a sufficiently large penalty parameter β in (3.2), the following estimates hold:

$$\begin{aligned}C_1\|\psi_h(t)\|^2_{\mathrm{E}^\mathrm{a}} - \langle\{\!\{\nabla\tilde{\psi}_h(t)\}\!\},\,[\![\tilde{\psi}_h(t)]\!]\rangle_{\mathscr{F}_h^{\mathrm{a,a}}} &\gtrsim \|\psi_h(t)\|^2_{\mathrm{E}^\mathrm{a}},\\ C_2\|\psi_h(0)\|^2_{\mathrm{E}^\mathrm{a}} - \langle\{\!\{\nabla\tilde{\psi}_h(0)\}\!\},\,[\![\tilde{\psi}_h(0)]\!]\rangle_{\mathscr{F}_h^{\mathrm{a,a}}} &\lesssim \|\psi_h(0)\|^2_{\mathrm{E}^\mathrm{a}}.\end{aligned}$$

Proof. Note that $\psi_h\in H^2(0,T;V_h^\mathrm{a})\hookrightarrow C^1([0,T];V_h^\mathrm{a})$. The proof can then be carried out analogously to the proof of Lemma A.2 in Antonietti *et al.* (2020a). □

The following lemmas summarize standard interpolation and stability estimates in the L^2, H^1 and L^∞ norms.

LEMMA 4.5 (see Theorem 4.6.14 in Brenner & Scott, 2008) Let $\mathrm{i}\in\{\mathrm{f},\mathrm{t}\}$. There exists a subdomain-wise interpolation operator

$$\Pi^p : H^s(\Omega_\mathrm{i}) \to V_h^\mathrm{i},$$

which satisfies the following bounds:

- $\|\phi - \Pi^p\phi\|_{L^2(\Omega_\mathrm{i})} \leqslant C_{\mathrm{app}2} h^s\|\phi\|_{H^s(\Omega_\mathrm{i})} \qquad \forall\, s=0,1,...,p+1,$

- $|\phi - \Pi^p\phi|_{H^1(\Omega_\mathrm{i})} \lesssim h^{s-1}\|\phi\|_{H^s(\Omega_\mathrm{i})} \qquad \forall\, s = 1, 2, ..., p+1,$
- $\|\phi - \Pi^p\phi\|_{L^\infty(\Omega_\mathrm{i})} \lesssim h^{s-d/2}\|\phi\|_{H^s(\Omega_\mathrm{i})} \qquad \forall\, d/2 < s \leqslant p+1.$

Component-wise application allows to extend the definition to vector-valued functions; i.e., there exists $\Pi^p : \boldsymbol{H}^s(\Omega_\mathrm{e}) \to \boldsymbol{V}_h^e$ with the same orders of approximation.

Due to the regularity assumptions on the exact solution to our problem we can employ the Lagrange interpolation operator. Restriction to a single element $\kappa \in \mathscr{T}_h$ yields the following stability estimate.

LEMMA 4.6 (See Lemma 4.4.1 in Brenner & Scott, 2008). The interpolation operator introduced in Lemma 4.5 fulfills the following stability estimate in the $W^{k,\infty}(\kappa)$ norm:

$$\|\Pi^p\psi\|_{W^{k,\infty}(\kappa)} \leqslant C_\mathrm{st}\|\psi\|_{C^0(\overline{\kappa})}.$$

We also recall the following multiplicative trace inequality, which will be used to derive error estimates.

LEMMA 4.7 Let $\kappa \in \mathscr{T}_h$ be a mesh element with diameter h_κ satisfying our mesh assumptions. Furthermore, let F be any face of κ. Then for $v \in H^1(\kappa)$, it holds

$$\|v\|^2_{L^2(F)} \lesssim \|v\|_{L^2(\kappa)}\left(|v|_{H^1(\kappa)} + h_\kappa^{-1}\|v\|_{L^2(\kappa)}\right).$$

Proof. The statement follows by Lemma 1.49 in Di Pietro & Ern (2012). □

LEMMA 4.8 Let $\phi_h \in V_h^\mathrm{a}$ and let χ be the stabilization parameter defined in (3.2) with parameter β. Then for the global polynomial interpolant $\phi_I \in V_h^\mathrm{a}$ of degree p of $\phi \in H^s(\Omega_\mathrm{a})$, $d/2 < s \leqslant p+1$, it holds

$$\|\chi^{-1/2}\{\!\{\nabla(\phi - \phi_I)\}\!\}\|^2_{\mathscr{F}_h^{\mathrm{a,a}}} \lesssim h^{2(s-1)}\|\phi\|^2_{s,\mathrm{a}}.$$

Proof. The statement follows by Lemmas 3 and 4 in Antonietti *et al.* (2020b). □

LEMMA 4.9 For any element $\kappa \in \mathscr{T}_h$ and polynomial degree $p \in \mathbb{N}$, let $\phi \in H^s(\kappa)$ for some $d/2 < s \leqslant p+1$ and let F be a face of κ. Then, the following interpolation estimate on the face F holds true:

$$\|\phi - \Pi^p\phi\|_{L^2(F)} \lesssim \sqrt{|F|}\, h_\kappa^{s-d/2}\,\|\phi\|_{H^s(\kappa)}, \qquad \forall\, d/2 < s \leqslant p+1.$$

Proof. The statement follows as a special case of the more general result of Lemma 4.2 in Cangiani *et al.* (2014); see also Lemma 1.59 in Di Pietro & Ern (2012). □

With these technical results at hand we now proceed with considering stability and error estimate for the linearization of the coupled problem.

4.2 *Stability of the semidiscrete formulation in the energy norm*

We first prove that our linearized semidiscrete approximation is uniquely solvable and stable in the energy norm.

PROPOSITION 4.10 Let $\boldsymbol{f}^{\mathrm{e}} \in L^2(0,T;\boldsymbol{L}^2(\Omega))$, $f_h^{\mathrm{f}} \in L^2(0,T;V_h^{\mathrm{f}})$ and $f_h^{\mathrm{t}} \in L^2(0,T;V_h^{\mathrm{t}})$. The following estimate holds:

$$\|(\mathbf{u}_h(t),\psi_h(t))\|_{\mathrm{E}}^2 \lesssim \|(\mathbf{u}_h(0),\psi_h(0)\|_{\mathrm{E}}^2) + \int_0^t (\|\boldsymbol{f}^{\mathrm{e}}(\tau)\|_{\Omega_{\mathrm{e}}}^2 + \|f_h^{\mathrm{a}}(\tau)\|_{\Omega_{\mathrm{f}}}^2)\,\mathrm{d}\tau, \tag{4.6}$$

for a.e. $t \in [0,T]$, provided the penalty parameter β in (3.2) is sufficiently large. The hidden constant depends on the material parameters and the polynomial degree p, and tends to ∞ as $T \to \infty$, but does not depend on the mesh size.

Proof. We note that the existence of a unique $(\mathbf{u}_h,\psi_h) \in H^1(0,T;\boldsymbol{V}_h^{\mathrm{e}}) \times H^2(0,T;V_h^{\mathrm{a}})$ follows by standard arguments for linear ordinary differential equations and the energy bounds derived below; see, for example, Nikolić & Wohlmuth (2019), Antonietti *et al.* (2020b). The proof then follows by testing the problem by $\mathbf{v}_h = \dot{\mathbf{u}}_h$ and

$$\phi_h = \varrho^{\mathrm{f}}\dot{\tilde{\psi}}_h = \varrho^{\mathrm{f}}(\dot{\psi}_h + \tfrac{b}{c^2}\ddot{\psi}_h).$$

Note that we have the same factor ϱ^{f} on both subdomains,

$$\phi_h = \begin{cases} \varrho^{\mathrm{f}}(\dot{\psi}_h^{\mathrm{f}} + \frac{b^{\mathrm{f}}}{(c^{\mathrm{f}})^2}\ddot{\psi}_h^{\mathrm{f}}) & \text{in } \Omega_{\mathrm{f}}, \\ \varrho^{\mathrm{f}}(\dot{\psi}_h^{\mathrm{t}} + \frac{b^{\mathrm{t}}}{(c^{\mathrm{t}})^2}\ddot{\psi}_h^{\mathrm{t}}) & \text{in } \Omega_{\mathrm{t}}. \end{cases}$$

The reason for this choice of test functions is that they lead to the canceling out of the elasto-acoustic interface terms in (3.1):

$$(\varrho^{\mathrm{f}}(\dot{\psi}_h^{\mathrm{f}} + \tfrac{b^{\mathrm{f}}}{(c^{\mathrm{f}})^2}\ddot{\psi}_h^{\mathrm{f}})\mathbf{n}^{\mathrm{e}}, \dot{\mathbf{u}}_h)_{\Gamma_{\mathrm{I}}^{\mathrm{e,a}}} = -(\dot{\mathbf{u}}_h \cdot \mathbf{n}^{\mathrm{a}}, \varrho^{\mathrm{f}}(\dot{\psi}_h^{\mathrm{f}} + \tfrac{b^{\mathrm{f}}}{(c^{\mathrm{f}})^2}\ddot{\psi}_h^{\mathrm{f}}))_{\Gamma_{\mathrm{I}}^{\mathrm{e,a}}}$$

because $\mathbf{n}^{\mathrm{a}} = -\mathbf{n}^{\mathrm{e}}$ on $\Gamma_{\mathrm{I}}^{\mathrm{e,a}}$. Moreover, scaling the acoustic test function by the constant ϱ^{f} (as opposed to ϱ) will not cause issues with the symmetry of dG terms across the acoustic interface. Standard computations then lead to (4.6). We omit the details here. □

4.3 *Error analysis of the linearized semidiscrete problem*

To facilitate the error analysis of the linearization we define suitable norms in space and time, as well as decompose the overall error into interpolation and discretization parts, which are then estimated separately. We introduce the following norms:

$$\|\mathbf{v}\|_{L^\infty \mathrm{E}^{\mathrm{e}}} = \operatorname*{ess\,sup}_{t\in(0,T)} \|\mathbf{v}(t)\|_{\mathrm{E}^{\mathrm{e}}}, \qquad \|\phi\|_{L^\infty \mathrm{E}^{\mathrm{a}}} = \sup_{t\in(0,T)} \|\phi(t)\|_{\mathrm{E}^{\mathrm{a}}} \tag{4.7}$$

as well as the overall energy norm

$$\|(\mathbf{v},\phi)\|_{L^\infty \mathrm{E}}^2 = \|\mathbf{v}\|_{L^\infty \mathrm{E}^{\mathrm{e}}}^2 + \|\phi\|_{L^\infty \mathrm{E}^{\mathrm{a}}}^2. \tag{4.8}$$

As standard the total error between the solution and its approximation

$$e = (e_{\mathbf{u}}, e_{\psi}) = (\mathbf{u} - \mathbf{u}_h, \psi - \psi_h)$$

can be decomposed into two parts as follows:

$$\begin{aligned} e = (e_{\mathbf{u}}, e_{\psi}) &= (e_{\mathbf{u},I} - e_{\mathbf{u},h}, e_{\psi,I} - e_{\psi,h}) \\ &= ((\mathbf{u} - \mathbf{u}_I) - (\mathbf{u}_I - \mathbf{u}_h), (\psi - \psi_I) - (\psi_I - \psi_h)), \end{aligned} \tag{4.9}$$

where $\mathbf{u}_I$ and ψ_I are the subdomain-wise defined, global interpolants of $(\mathbf{u}, \psi) \in X^{\mathrm{e}} \times X^{\mathrm{a}}$ given by Lemma 4.5; i.e., $\mathbf{u}_I\big|_{\Omega_{\mathrm{e}}} = \Pi^p\, \mathbf{u}\big|_{\Omega_{\mathrm{e}}}$, $\psi_I\big|_{\Omega_{\mathrm{f}}} = \Pi^p\, \psi\big|_{\Omega_{\mathrm{f}}}$ and $\psi_I\big|_{\Omega_{\mathrm{t}}} = \Pi^p\, \psi\big|_{\Omega_{\mathrm{t}}}$.

With these assumptions and the technical results from Subsection 4.1 at hand, we can derive an approximation bound for the global interpolants.

LEMMA 4.11 Given $(\mathbf{u}, \psi) \in X^{\mathrm{e}} \times X^{\mathrm{a}}$ the global interpolants satisfy the following error estimates:

$$\|\psi - \psi_I\|^2_{L^\infty \mathrm{E}^{\mathrm{a}}} \lesssim h^{2(s-1)} \left\{ \sup_{t\in(0,T)} \left(\|\psi(t)\|^2_{s,\mathrm{a}} + \|\dot\psi(t)\|^2_{s,\mathrm{a}} \right) + \int_0^t \|\ddot\psi(\tau)\|^2_{s,\mathrm{a}}\, \mathrm{d}\tau \right\},$$

$$\|\mathbf{u} - \mathbf{u}_I\|^2_{L^\infty \mathrm{E}^{\mathrm{e}}} \lesssim h^{2(s-1)} \sup_{t\in(0,T)} \left(\|\mathbf{u}(t)\|^2_{H^s(\Omega_{\mathrm{e}})} + \|\dot{\mathbf{u}}(t)\|^2_{H^s(\Omega_{\mathrm{e}})} \right).$$

Proof. Directly follows from Lemma 4.7 and the interpolation estimates from Lemma 4.5. □

We approximate initial conditions by applying the subdomain-wise global interpolation operators to the given data. In other words, we take $(\mathbf{u}_h(0), \dot{\mathbf{u}}_h(0), \psi_h(0), \dot\psi_h(0)) \in \boldsymbol{V}^{\mathrm{e}}_h \times \boldsymbol{V}^{\mathrm{e}}_h \times V^{\mathrm{a}}_h \times V^{\mathrm{a}}_h$ such that

$$\begin{aligned} \mathbf{u}_h(0) &= \mathbf{u}_{0,I}, \quad \dot{\mathbf{u}}_h(0) = \mathbf{u}_{1,I}, \\ \psi_h(0) &= \psi_{0,I}, \quad \dot\psi_h(0) = \psi_{1,I}. \end{aligned} \tag{4.10}$$

We can now state the error bound in the energy norm for the linearized problem.

THEOREM 4.12 Let $(\mathbf{u}, \psi) \in X^{\mathrm{e}} \times X^{\mathrm{a}}$ and let the discrete initial conditions be obtained by interpolation of the exact ones; that is, let (4.10) hold. Then the approximation error $e = (e_{\mathbf{u}}, e_{\psi}) = (\mathbf{u} - \mathbf{u}_h, \psi - \psi_h)$ can be bounded as follows:

$$\begin{aligned} \|e\|^2_{L^\infty E} \lesssim h^{2(s-1)} \Bigg[&\sup_{t\in(0,T)} \left(\|\mathbf{u}(t)\|^2_{H^s(\Omega_{\mathrm{e}})} + \|\psi(t)\|^2_{s,\mathrm{a}} + \|\dot\psi(t)\|^2_{s,\mathrm{a}} \right) \\ &+ \int_0^T \left(\|\dot{\mathbf{u}}\|^2_{H^s(\Omega_{\mathrm{e}})} + \|\ddot{\mathbf{u}}\|^2_{H^s(\Omega_{\mathrm{e}})} + \|\ddot\psi\|^2_{s,\mathrm{a}} \right) \mathrm{d}\tau \Bigg] + \int_0^T \|f^{\mathrm{a}} - f^{\mathrm{a}}_h\|^2_{\Omega_{\mathrm{a}}}\, \mathrm{d}\tau, \end{aligned} \tag{4.11}$$

provided the penalty parameter β in (3.2) is sufficiently large. The hidden constant in the estimate tends to infinity as $T \to \infty$, but does not depend on h.

The proof follows by combining the arguments from the proof of Theorem 5.2 in Antonietti *et al.* (2020a) (with respect to treating the elastic and coupling terms) with our particular choice of

test functions, as already seen in Proposition 4.10, and allowing for the error in the source term. For a worked out version of the proof see Appendix A in Muhr *et al.* (2021).

5. *A priori* analysis of the nonlinear coupled problem

We next analyze the nonlinear problem by relying on the Banach fixed-point theorem; see, for example, Ortner & Süli (2007); Antonietti *et al.* (2020b) for similar techniques used in the numerical analysis of nonlinear wave equations. To this end, we introduce the mapping

$$\mathscr{S} : \mathscr{B}_h \ni (\tilde{\mathbf{u}}_h, w_h) \mapsto (\mathbf{u}_h, \psi_h),$$

where $(\mathbf{u}_h, \psi_h)$ solves the linear problem

$$\begin{aligned}
&(\varrho^{\mathrm{e}}\ddot{\mathbf{u}}_h(t), \mathbf{v}_h)_{\Omega_{\mathrm{e}}} + (2\varrho^{\mathrm{e}}\zeta\dot{\mathbf{u}}_h(t), \mathbf{v}_h)_{\Omega_{\mathrm{e}}} + (\varrho^{\mathrm{e}}\zeta^2\mathbf{u}_h(t), \mathbf{v}_h)_{\Omega_{\mathrm{e}}} + a^{\mathrm{e}}(\mathbf{u}_h(t), \mathbf{v}_h) \\
&\qquad + (c^{-2}\ddot{\psi}_h(t), \phi_h)_{\Omega_{\mathrm{a}}} + a_h^{\mathrm{a}}(\psi_h(t) + \tfrac{b}{c^2}\dot{\psi}_h(t), \phi_h) \\
&\qquad + \mathscr{I}(\varrho^{\mathrm{f}}(\dot{\psi}_h(t) + \tfrac{b}{c^2}\ddot{\psi}_h), \mathbf{v}_h) - \mathscr{I}(\phi_h, \dot{\mathbf{u}}_h(t)) \\
&= (\boldsymbol{f}^{\mathrm{e}}(t), \mathbf{v}_h)_{\Omega_{\mathrm{e}}} + (f_h^{\mathrm{a}}(\dot{w}_h(t), \ddot{w}_h(t), \nabla w_h(t), \nabla\dot{w}_h(t)),\ \phi_h)_{\Omega_{\mathrm{a}}},
\end{aligned} \tag{5.1}$$

a.e. in time for all test functions $(\mathbf{v}_h, \phi_h) \in \boldsymbol{V}_h^{\mathrm{e}} \times V_h^{\mathrm{a}}$ and supplemented with initial conditions (4.10). Recall that

$$f_h^{\mathrm{a}}(\dot{w}_h, \ddot{w}_h, \nabla w_h, \nabla\dot{w}_h) = \frac{2}{c^2}\left(k_1\dot{w}_h\ddot{w}_h + k_2\nabla w_h \cdot \nabla\dot{w}_h\right)$$

with material parameter jumps allowed at the fluid-tissue interface; cf. (2.4).

Furthermore, given $C_\star > 0$, $\mathscr{B}_h$ is the ball containing all $(\tilde{\mathbf{u}}_h, w_h) \in H^1(0,T;\boldsymbol{V}_h^{\mathrm{e}}) \times H^2(0,T;V_h^{\mathrm{a}})$ such that

$$\|(\mathbf{u} - \tilde{\mathbf{u}}_h, \psi - w_h)\|_{L^\infty E} \leqslant C_\star h^{s-1}\left\{|||\mathbf{u}|||_{s,\mathrm{e}} + |||\psi|||_{s,\mathrm{a}}\right\},$$

with initial conditions

$$(w_h(0), \dot{w}_h(0)) = (\psi_{0,I}, \psi_{1,I}), \qquad (\tilde{\mathbf{u}}_h(0), \dot{\tilde{\mathbf{u}}}_h(0)) = (\mathbf{u}_{0,I}, \mathbf{u}_{1,I}).$$

Above, we have introduced the following short-hand notation:

$$|||\mathbf{u}|||_{s,\mathrm{e}}^2 = \sup_{t\in(0,T)} \|\mathbf{u}(t)\|_{H^s(\Omega_{\mathrm{e}})}^2 + \int_0^T (\|\dot{\mathbf{u}}\|_{H^s(\Omega_{\mathrm{e}})}^2 + \|\ddot{\mathbf{u}}\|_{H^s(\Omega_{\mathrm{e}})}^2)\,\mathrm{d}\tau,$$

and

$$|||\psi|||_{s,\mathrm{a}}^2 = \sup_{t\in(0,T)} \left(\|\psi(t)\|_{s,\mathrm{a}}^2 + \|\dot{\psi}(t)\|_{s,\mathrm{a}}^2\right) + \int_0^T \|\ddot{\psi}\|_{s,\mathrm{a}}^2\,\mathrm{d}\tau,$$

where we recall that the s-regularity above should be understood subdomain-wise:

$$\|\phi\|_{s,\mathrm{a}}^2 = \|\phi\|_{H^s(\Omega_\mathrm{f})}^2 + \|\phi\|_{H^s(\Omega_\mathrm{t})}^2.$$

The constant $C_\star = C_\star(\mathbf{u}, \psi)$ in the error estimate will be specified below. The set $\mathscr{B}_h$ is nonempty because the solution of the linear problem belongs to it when $f_h^\mathrm{a} = f^\mathrm{a}$ for a suitably chosen $C_\star$.

On account of the existence and uniqueness result for the linear problem this mapping is well-defined. Furthermore, the space $(\mathscr{B}_h, d)$ is complete with respect to the metric $d((\mathbf{u}, \psi), (\mathbf{v}, \phi)) = \|(\mathbf{u} - \mathbf{v}, \psi - \phi)\|_\mathrm{E}$. We first determine sufficient conditions for $\mathscr{S}$ to be self-mapping. To simplify notation we use $\|\cdot\|_{L^pL^q}$ below in place of $\|\cdot\|_{L^p(0,T;L^q(\Omega_\mathrm{i}))}$ for $p, q \in \{2, \infty\}$. We will also rely on the continuous embedding

$$H^s(\Omega_\mathrm{i}) \hookrightarrow W^{1,\infty}(\Omega_\mathrm{i}), \quad s > 1 + d/2,$$

with the embedding constant denoted by C_emb.

PROPOSITION 5.1 Let $1+d/2 < s \leqslant p+1$ and $\boldsymbol{f}^\mathrm{e} \in L^2(0,T;\boldsymbol{L}^2(\Omega))$. Assume that the penalty parameter β in (3.2) is chosen as sufficiently large according to Proposition 4.10 and Theorem 4.12. Then there exist $\overline{h} > 0$ and $\delta > 0$, such that for

$$|||\mathbf{u}|||_{s,\mathrm{e}} + |||\psi|||_{s,\mathrm{a}} \leqslant \delta$$

and $0 < h \leqslant \overline{h}$, the mapping $\mathscr{S}$ satisfies

$$\mathscr{S}(\mathscr{B}_h) \subset \mathscr{B}_h.$$

Proof. For a given $(\tilde{\mathbf{u}}_h, w_h) \in \mathscr{B}_h$ and $(\mathbf{u}_h, \psi_h)$ solving (5.1), we know from the linear result that there exists $C_\mathrm{lin} > 0$ such that

$$\|(\mathbf{u} - \mathbf{u}_h, \psi - \psi_h)\|_{L^\infty\mathrm{E}} \leqslant C_\mathrm{lin}\left(h^{s-1}\left(|||\mathbf{u}|||_{s,\mathrm{e}} + |||\psi|||_{s,\mathrm{a}}\right) + \|f^\mathrm{a} - f_h^\mathrm{a}\|_{L^2L^2}\right) \tag{5.2}$$

provided $\beta > 0$ in (3.2) is large enough. Since

$$\begin{aligned} f^\mathrm{a} - f_h^\mathrm{a} &= \frac{2}{c^2}\left(k_1(\dot\psi\ddot\psi - \dot w_h\ddot w_h) + k_2(\nabla\psi\cdot\nabla\dot\psi - \nabla w_h\cdot\nabla\dot w_h)\right) \\ &= \frac{2}{c^2}\left(k_1(\dot\psi(\ddot\psi - \ddot w_h) + \ddot w_h(\dot\psi - \dot w_h)) + k_2(\nabla w_h\cdot\nabla(\dot\psi - \dot w_h) + \nabla\dot\psi\cdot\nabla(\psi - w_h))\right), \end{aligned}$$

we can estimate the error in the acoustic source term using $|\overline{k_i}| := \max\{|k_i^\mathrm{f}|, |k_i^\mathrm{t}|\}, i = 1, 2$ as follows:

$$\begin{aligned} \|f^\mathrm{a} - f_h^\mathrm{a}\|_{L^2L^2} \leqslant{}& \frac{2|\overline{k_1}|}{\underline{c}^2}\left(\|\dot\psi(\ddot\psi - \ddot w_h)\|_{L^2L^2} + \|\ddot w_h(\dot\psi - \dot w_h)\|_{L^2L^2}\right) \\ &+ \frac{2|\overline{k_2}|}{\underline{c}^2}\left(\|\nabla w_h\cdot\nabla(\dot\psi - \dot w_h)\|_{L^2L^2} + \|\nabla\dot\psi\cdot\nabla(\psi - w_h)\|_{L^2L^2}\right), \end{aligned}$$

where the gradient should be understood in a broken $\Omega_{\mathrm{f}} \cup \Omega_{\mathrm{t}}$ sense. Recall that $\underline{c} = \min\{c^{\mathrm{f}}, c^{\mathrm{t}}\}$. Therefore, we infer

$$\begin{aligned}\|f^{\mathrm{a}} - f_h^{\mathrm{a}}\|_{L^2L^2} \leqslant \frac{2|\overline{k_1}|}{\underline{c}^2} \big(\|\dot\psi\|_{L^\infty L^\infty}\|\ddot\psi - \ddot w_h\|_{L^2L^2} + \|\ddot w_h\|_{L^2L^\infty}\|\dot\psi - \dot w_h\|_{L^\infty L^2}\big) \\ + \frac{2|\overline{k_2}|}{\underline{c}^2} \big(\|\nabla w_h\|_{L^2L^\infty}\|\nabla(\dot\psi - \dot w_h)\|_{L^\infty L^2} + \|\nabla\dot\psi\|_{L^2L^\infty}\|\nabla(\psi - w_h)\|_{L^\infty L^2}\big). \quad (5.3)\end{aligned}$$

We know the approximation error of $(\tilde{\mathbf{u}}_h, w_h) \in \mathscr{B}_h$, so we can further deduce

$$\|f^{\mathrm{a}} - f_h^{\mathrm{a}}\|_{L^2L^2} \leqslant \frac{2\overline{k}}{\underline{c}^2} \big(\|\dot\psi\|_{L^\infty L^\infty} + \|\ddot w_h\|_{L^2L^\infty} + \|\nabla w_h\|_{L^2L^\infty} + \|\nabla\dot\psi\|_{L^2L^\infty}\big) C_\star h^{s-1} \big(|||\mathbf{u}|||_{s,\mathrm{e}} + |||\psi|||_{s,\mathrm{a}}\big),$$

where $\overline{k} = \max\{|\overline{k_1}|, |\overline{k_2}|\}$. From (5.2) we see that for the self-mapping property to hold, we have to guarantee that

$$\check{C} := C_{\mathrm{lin}}\left[1 + \frac{2\overline{k}}{\underline{c}^2}\Big(\|\dot\psi\|_{L^\infty L^\infty} + \|\ddot w_h\|_{L^2L^\infty} + \|\nabla w_h\|_{L^2L^\infty} + \|\nabla\dot\psi\|_{L^2L^\infty}\Big)C_\star\right] \leqslant C_\star.$$

We will next further bound the w_h terms by relying on the inverse estimates together with the stability and approximation properties of the interpolant. Note first that

$$\|\dot\psi\|_{L^\infty L^\infty} \leqslant C_{\mathrm{emb}}|||\psi|||_{s,\mathrm{a}}, \qquad \|\nabla\dot\psi\|_{L^2L^\infty} \leqslant \sqrt{T}C_{\mathrm{emb}}|||\psi|||_{s,\mathrm{a}}.$$

Let $\kappa \in \mathscr{T}_{h_{\mathrm{f}},\mathrm{f}} \cup \mathscr{T}_{h_{\mathrm{t}},\mathrm{t}}$ be the element such that

$$\|\nabla w_h\|_{L^2L^\infty} = \|\nabla w_h\|_{L^2L^\infty(\kappa)} \leqslant \|\nabla w_h - \nabla\Pi^p\psi\|_{L^2L^\infty(\kappa)} + \|\nabla\Pi^p\psi\|_{L^2L^\infty(\kappa)}.$$

Then thanks to the inverse estimate (4.5), we find that

$$\begin{aligned}\|\nabla w_h\|_{L^2L^\infty} &\leqslant h^{-d/2}C_{\mathrm{inv}}\|\nabla w_h - \nabla\Pi^p\psi\|_{L^2L^2(\kappa)} + \|\nabla\Pi^p\psi\|_{L^2L^\infty(\kappa)} \\ &\leqslant \tilde{C}C_{\mathrm{inv}}h^{-d/2}\|w_h - \psi_I\|_{L^2\mathrm{E}^{\mathrm{a}}} + \|\nabla\Pi^p\psi\|_{L^2L^\infty(\kappa)}, \quad (5.4)\end{aligned}$$

where in the second line we have used the bound (4.4) on the gradient via the acoustic energy and relied on our choice of approximate initial data. Recall that the constant $\tilde{C} = \tilde{C}(T, b)$ tends to infinity as $T \to +\infty$ or $\underline{b} \to 0^+$; cf. Remark 4.1. From here we have

$$\begin{aligned}\|\nabla w_h\|_{L^2L^\infty} &\leqslant \tilde{C}C_{\mathrm{inv}}h^{-d/2}\|w_h - \psi + \psi - \psi_I\|_{L^2\mathrm{E}^{\mathrm{a}}} + \|\nabla\Pi^p\psi\|_{L^2L^\infty(\kappa)} \\ &\leqslant \tilde{C}C_{\mathrm{inv}}h^{-d/2}\sqrt{T}C_\star h^{s-1}(|||\mathbf{u}|||_{s,\mathrm{e}} + |||\psi|||_{s,\mathrm{a}}) \\ &\quad + \tilde{C}C_{\mathrm{inv}}h^{-d/2}\sqrt{T}C_{\mathrm{app}}h^{s-1}|||\psi|||_{s,\mathrm{a}} + C_{\mathrm{st}}\|\psi\|_{L^2L^\infty}, \quad (5.5)\end{aligned}$$

where we have relied on the approximation properties of the global interpolant in the energy norm with C_{app} being the hidden constant therein; see Lemma 4.11. Also we have used the stability of the local interpolant in the $W^{1,\infty}$ norm; see Lemma 4.6. Finally,

$$C_{\mathrm{st}}\|\psi\|_{L^2L^\infty} \leqslant \sqrt{T}C_{\mathrm{st}}C_{\mathrm{emb}}|||\psi|||_{s,\mathrm{a}}.$$

Similarly, it holds that

$$\begin{aligned}\|\ddot{w}_h\|_{L^2L^\infty} &\leqslant C_{\mathrm{inv}}h^{-d/2}\left(\|\ddot{w}_h-\ddot{\psi}\|_{L^2L^2}+\|\ddot{\psi}-(\ddot{\psi})_I\|_{L^2L^2}\right)+\|\Pi^p\ddot{\psi}\|_{L^2L^\infty(\kappa)}\\ &\leqslant C_{\mathrm{inv}}h^{-d/2}\big(C_\star h^{s-1}(|||\mathbf{u}|||_{s,\mathrm{e}}+|||\psi|||_{s,\mathrm{a}})+C_{\mathrm{app}}h^{s-1}|||\psi|||_{s,\mathrm{a}}\big)+C_{\mathrm{st}}\|\ddot{\psi}\|_{L^2L^\infty},\end{aligned} \tag{5.6}$$

where the last term can be further bounded as follows:

$$C_{\mathrm{st}}\|\ddot{\psi}\|_{L^2L^\infty} \leqslant C_{\mathrm{st}}C_{\mathrm{emb}}|||\psi|||_{s,\mathrm{a}}.$$

Let us collect the embedding, stability and approximation constants appearing above into one constant given by

$$\mathscr{C}(T) = C_{\mathrm{emb}}(C_{\mathrm{st}}+1)(1+\sqrt{T})+C_{\mathrm{inv}}(C_{\mathrm{app}}+1)(1+\tilde{C}\sqrt{T}).$$

Altogether, we then have

$$\check{C} \leqslant C_{\mathrm{lin}}\left\{1+\frac{2\bar{k}}{\underline{c}^2}(|||\mathbf{u}|||_{s,\mathrm{e}}+|||\psi|||_{s,\mathrm{a}})\mathscr{C}(T)\left[1+h^{s-1-d/2}C_\star+h^{s-1-d/2}\right]C_\star\right\}.$$

Observe that if $h^{s-1-d/2} \leqslant 1$ and $h^{s-1-d/2}C_\star \leqslant 1$ then

$$\check{C} \leqslant C_{\mathrm{lin}}\left\{1+\frac{2\bar{k}}{\underline{c}^2}(|||\mathbf{u}|||_{s,\mathrm{e}}+|||\psi|||_{s,\mathrm{a}})\cdot 3\mathscr{C}(T)C_\star\right\} \leqslant C_{\mathrm{lin}}\left(1+\frac{6\bar{k}}{\underline{c}^2}\delta\mathscr{C}(T)C_\star\right).$$

In order to fulfill the desired property that $\check{C} \leqslant C_\star$ we demand the bound δ for $|||\mathbf{u}|||_{s,\mathrm{e}}+|||\psi|||_{s,\mathrm{a}}$ to be small enough, so that

$$1-6\frac{\bar{k}}{\underline{c}^2}C_{\mathrm{lin}}\mathscr{C}(T)\delta > 0 \tag{5.7}$$

and then set

$$C_\star(\delta,T) = \frac{C_{\mathrm{lin}}}{1-6\dfrac{\bar{k}}{\underline{c}^2}C_{\mathrm{lin}}\mathscr{C}(T)\delta}. \tag{5.8}$$

Finally, we take $\overline{h}$ small enough, so that

$$\overline{h}^{s-1-d/2} \leqslant \min\left\{1, \frac{1}{C_\star(\delta,T)}\right\}.$$

Altogether, for $1 + d/2 < s \leqslant p + 1$, we then have

$$\sup_{t\in(0,T)} \|(\mathbf{u}-\mathbf{u}_h, \psi-\psi_h)(t)\|_E \leqslant C_\star(\delta,T) h^{s-1}(|||\mathbf{u}|||_{s,\mathrm{e}} + |||\psi|||_{s,\mathrm{a}}).$$

□

The smallness condition (5.7) is mitigated in practice by the fact that the factor $\frac{\overline{k}}{\underline{c}^2}$ is quite small; see Section 6 for typical values of the acoustic medium parameters. We next provide sufficient conditions under which $\mathscr{S}$ is strictly contractive.

PROPOSITION 5.2 Let $1 + d/2 < s \leqslant p + 1$. Assume that the penalty parameter β in (3.2) is chosen sufficiently large according to Proposition 4.10 and Theorem 4.12. There exist $\overline{h} > 0$ and $\delta > 0$, such that for $0 < h \leqslant \overline{h}$ and $|||\mathbf{u}|||_{s,\mathrm{e}} + |||\psi|||_{s,\mathrm{a}} \leqslant \delta$, the mapping $\mathscr{S}$ is strictly contractive on $\mathscr{B}_h$ in the topology induced by the L^∞E norm; cf. (4.8).

Proof. To prove contractivity take $(\tilde{\mathbf{u}}_h^{(1)}, w_h^{(1)})$, $(\tilde{\mathbf{u}}_h^{(2)}, w_h^{(2)}) \in \mathscr{B}_h$ and set

$$(\mathbf{u}_h^{(1)}, \psi_h^{(1)}) = \mathscr{S}(\tilde{\mathbf{u}}_h^{(1)}, w_h^{(1)}), \qquad (\mathbf{u}_h^{(2)}, \psi_h^{(2)}) = \mathscr{S}(\tilde{\mathbf{u}}_h^{(2)}, w_h^{(2)}).$$

The difference $(\bar{\mathbf{u}}_h, \bar{\psi}_h)$, where $\bar{\psi}_h = \psi_h^{(1)} - \psi_h^{(2)}$ and $\bar{\mathbf{u}}_h = \mathbf{u}_h^{(1)} - \mathbf{u}_h^{(2)}$, then satisfies the weak form

$$\begin{aligned}
&(\varrho^{\mathrm{e}} \ddot{\bar{\mathbf{u}}}_h(t), \mathbf{v}_h)_{\Omega_\mathrm{e}} + (2\varrho^{\mathrm{e}}\zeta \dot{\bar{\mathbf{u}}}_h(t), \mathbf{v}_h)_{\Omega_\mathrm{e}} + (\varrho^{\mathrm{e}}\zeta^2 \bar{\mathbf{u}}_h(t), \mathbf{v}_h)_{\Omega_\mathrm{e}} + a^{\mathrm{e}}(\bar{\mathbf{u}}_h(t), \mathbf{v}_h) \\
&\qquad + (c^{-2}\ddot{\bar{\psi}}_h(t), \phi_h)_{\Omega_\mathrm{a}} + a_h^{\mathrm{a}}(\bar{\psi}_h(t) + \tfrac{b}{c^2}\dot{\bar{\psi}}_h(t), \phi_h) \\
&\qquad + \mathscr{I}(\varrho^{\mathrm{f}}(\dot{\bar{\psi}}_h(t) + \tfrac{b}{c^2}\ddot{\bar{\psi}}_h(t)), \mathbf{v}_h) - \mathscr{I}(\phi_h, \dot{\bar{\mathbf{u}}}_h(t)) \\
= \; &(f_h^{\mathrm{a}}(\dot{w}_h^{(1)}(t), \ddot{w}_h^{(1)}(t), \nabla w_h^{(1)}(t), \nabla \dot{w}_h^{(1)}(t)), \phi_h)_{\Omega_\mathrm{a}} \\
&- (f_h^{\mathrm{a}}(\dot{w}_h^{(2)}(t), \ddot{w}_h^{(2)}(t), \nabla w_h^{(2)}(t), \nabla \dot{w}_h^{(2)}(t)), \phi_h)_{\Omega_\mathrm{a}}
\end{aligned}$$

for all $(\mathbf{v}_h, \phi_h) \in \boldsymbol{V}_h^{\mathrm{e}} \times V_h^{\mathrm{a}}$ a.e. in time, and supplemented with zero initial conditions. We can then rely on the linear stability result of Proposition 4.10 with $\boldsymbol{f}^{\mathrm{e}}$ and the initial conditions set to zero, and the right-hand side taken as the above difference of the f_h^{a} terms. This immediately yields

$$\begin{aligned}
&\|\mathscr{S}(\tilde{\mathbf{u}}_h^{(1)}, w_h^{(1)})(t) - \mathscr{S}(\tilde{\mathbf{u}}_h^{(2)}, w_h^{(2)})(t)\|_{\mathrm{E}} \\
\lesssim\; &\frac{1}{\underline{c}^2} \|2k_1(\dot{w}_h^{(1)}\ddot{w}_h^{(1)} - \dot{w}_h^{(2)}\ddot{w}_h^{(2)}) + 2k_2(\nabla w_h^{(1)} \cdot \nabla \dot{w}_h^{(1)} - \nabla w_h^{(2)} \cdot \nabla \dot{w}_h^{(2)})\|_{L^2(0,t;L^2)},
\end{aligned}$$

for all $t \in (0,T)$. Then analogously to deriving (5.3), we have the estimate

$$\begin{aligned}
&\|\mathscr{S}(\tilde{\mathbf{u}}_h^{(1)}, w_h^{(1)})(t) - \mathscr{S}(\tilde{\mathbf{u}}_h^{(2)}, w_h^{(2)})(t)\|_{\mathrm{E}} \\
&\lesssim \|\dot{w}_h^{(1)}\|_{L^\infty L^\infty} \|\ddot{w}_h^{(1)} - \ddot{w}_h^{(2)}\|_{L^2L^2} + \|\ddot{w}_h^{(2)}\|_{L^2L^\infty} \|\dot{w}_h^{(1)} - \dot{w}_h^{(2)}\|_{L^\infty L^2} \\
&\quad + \|\nabla \dot{w}_h^{(1)}\|_{L^2L^\infty} \|\nabla w_h^{(1)} - \nabla w_h^{(2)}\|_{L^\infty L^2} + \|\nabla w_h^{(2)}\|_{L^2L^\infty} \|\nabla \dot{w}_h^{(1)} - \nabla \dot{w}_h^{(2)}\|_{L^\infty L^2}.
\end{aligned}$$

By taking the supremum over $t \in (0,T)$, we obtain

$$\begin{aligned}
&\sup_{t\in(0,T)} \|\mathscr{S}(\tilde{\mathbf{u}}_h^{(1)}, w_h^{(1)})(t) - \mathscr{S}(\tilde{\mathbf{u}}_h^{(2)}, w_h^{(2)})(t)\|_{\mathrm{E}} \\
&\lesssim \left(\|\dot{w}_h^{(1)}\|_{L^\infty L^\infty} + \|\ddot{w}_h^{(2)}\|_{L^2L^\infty} + \|\nabla w_h^{(2)}\|_{L^2L^\infty} + \|\nabla \dot{w}_h^{(1)}\|_{L^2L^\infty} \right) \\
&\qquad \times \sup_{t\in(0,T)} \|(\tilde{\mathbf{u}}_h^{(1)} - \tilde{\mathbf{u}}_h^{(2)}, w_h^{(1)} - w_h^{(2)})\|_{\mathrm{E}}, \qquad (5.9)
\end{aligned}$$

where we have again relied on estimate (4.4). In view of estimates (5.5)–(5.6) and analogous ones that can be derived for $\|\dot{w}_h^{(1)}\|_{L^\infty L^\infty}$ and $\|\nabla \dot{w}_h^{(1)}\|_{L^2L^\infty}$, we can reduce the terms in the bracket on the right-hand side of (5.9) by assuming smallness of $|||\mathbf{u}|||_{s,\mathrm{e}} + |||\psi|||_{s,\mathrm{a}}$ and h. In this way we obtain strict contractivity of the mapping $\mathscr{S}$ in the $L^\infty\mathrm{E}$ norm, as claimed. □

Similarly to before the hidden constant in (5.9) has the form $\frac{\bar{k}}{c^2} \cdot C$, which helps to fulfill the strict contractivity condition in more realistic ultrasonic settings. By virtue of the previous two results and the Banach fixed-point theorem, we obtain a unique approximate solution $(\mathbf{u}_h, \psi_h)$ in $\mathscr{B}_h$.

THEOREM 5.3 Under the assumptions of Propositions 5.1 and 5.2 there exist $\bar{h} > 0$ and $\delta > 0$, such that for $0 < h \leqslant \bar{h}$ and $|||\mathbf{u}|||_{s,\mathrm{e}} + |||\psi|||_{s,\mathrm{a}} \leqslant \delta$, approximate solution $(\mathbf{u}_h, \psi_h)$ of the nonlinear elasto-acoustic problem (4.10) satisfies the following error bound:

$$\|(\mathbf{u} - \tilde{\mathbf{u}}_h, \psi - w_h)\|_{L^\infty E} \leqslant C_\star(\delta, T) h^{s-1} (|||\mathbf{u}|||_{s,\mathrm{e}} + |||\psi|||_{s,\mathrm{a}}),$$

where the constant $C_\star(\delta, T)$ is given in (5.8).

6. Numerical simulation

In this chapter we perform numerical simulations with the method proposed and analyzed before. We begin with synthetic experiments to back up the proven convergence results with numerical data. Therefore, we conduct several mesh analysis scenarios, where we test the numerical solution against a known analytical one. Later we will come back to the initial motivation for this work and use the proposed method to simulate ultrasound excitation, propagation and transition into human tissue in a more natural setting with physical parameters and more realistic domains. The simulations are conducted with the software *SPEED*, Stupazzini *et al.* (2009); Antonietti *et al.* (2012); Mazzieri *et al.* (2013), in detail its elasto-acoustic development branch (Antonietti *et al.*, 2020b). In order to focus on the numerical results, for precise details, e.g. about the used material parameter values, artificial solutions, boundary data and geometry measures, we refer to the extended arxiv version (Muhr *et al.*, 2021).

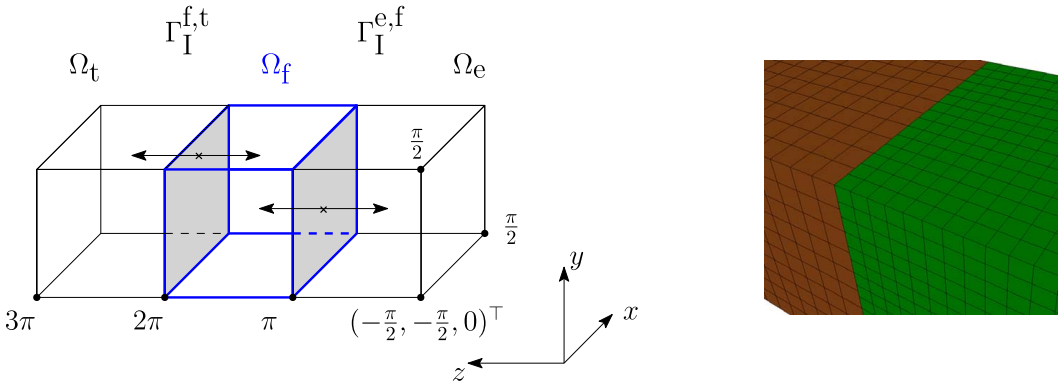

FIG. 2. **(Left)** '*Three stacked cubes*' artificial domains for elasto-acoustic coupled problem with analytical solution available. **(Right)** Exemplary nonconforming mesh at the interfaces between the subdomains.

6.1 *Numerical experiment 1: test against analytical solution*

In this first numerical experiment we employ artificial domain sizes, boundary conditions and external forces, in order to enforce a known analytical solution to the full coupled problem. We then conduct a convergence study comparing our numerical solutions against that analytical one. We consider the following domains: $\Omega_{\mathrm{e}} := (-\frac{\pi}{2}, \frac{\pi}{2})^2 \times (0, \pi)$, $\Omega_{\mathrm{f}} := (-\frac{\pi}{2}, \frac{\pi}{2})^2 \times (\pi, 2\pi)$ and $\Omega_{\mathrm{t}} := (-\frac{\pi}{2}, \frac{\pi}{2})^2 \times (2\pi, 3\pi)$, which are depicted in Fig. 2.

Option 1: elastic tissue As the first option we choose the tissue domain Ω_{t} to be an elastic material. On the three domains we then define the following analytical solutions:

$$\mathbf{u}^{\mathrm{i}}(x,y,z,t) = \begin{pmatrix} \sin(x)\cos(y)\sin(z) \\ \cos(x)\sin(y)\sin(z) \\ \cos(x)\cos(y)\cos(z) \end{pmatrix} a^{\mathrm{e}}(t) \qquad \text{in } \Omega_{\mathrm{i}} \times (0,T], \quad \mathrm{i} \in \{\mathrm{e,t}\}$$

$$\psi(x,y,z,t) = \quad \cos(x)\cos(y)\sin(z) \quad a^{\mathrm{a}}(t) \qquad \text{in } \Omega_{\mathrm{f}} \times (0,T],$$

where the time-dependent amplitudes of the elastic and acoustic fields $a^{\mathrm{e}}(t)$ and $a^{\mathrm{a}}(t)$ are given by

$$a^{\mathrm{i}}(t) = E^{\mathrm{i}} \sin(t) + D^{\mathrm{i}} \cos(t), \quad E^{\mathrm{i}}, D^{\mathrm{i}} \in \mathbb{R}, \quad \mathrm{i} \in \{\mathrm{e,a}\}.$$

In order for these solutions to fulfill the coupling conditions on the elasto-acoustic interfaces, certain conditions on the choice of the material parameters and the prescribed solution amplitudes have to be considered. The right-hand sides $f^{\mathrm{i}}, \mathrm{i} \in \{\mathrm{e,t,f}\}$ enforcing the given solutions can be obtained by insertion into the PDEs. To analyze convergence of the proposed numerical scheme, we conduct the simulation on a sequence of meshes with h tending to zero. Time integration is always conducted with a final time $T = 2\pi$ and small enough time step size, such that on all meshes in use, the overall errors are all dominated by their spatial components. For the time integration we employ the Newmark scheme in its predictor-corrector form using $\beta = 0.25$ and $\gamma = 0.5$ as in Kaltenbacher (2007, §5) for the nonlinear acoustic components, while the leapfrog scheme is used for the elastic ones. The meshes are chosen to be *nonconforming* at the subdomain interfaces *on purpose* for this artificial data experiment to show convergence also in this general situation. In order to guarantee the nonconformance, the whole

mesh-sequence is generated with a 3:2 ratio in mesh size between the central and the two outer blocks, cf. Fig. 2.

Convergence results are collectively plotted at the end of this subsection in order to be directly compared with modeling Option 2.

Option 2: acoustic tissue We use the same geometry and subdomains as before (cf. Fig. 2), only with the tissue domain being modeled as an acoustic medium this time. This corresponds to the case analyzed in the theoretical part of this work. The analytical solutions are defined as before just with $\mathbf{u}$ (dropping the index e for the elastic displacement $\mathbf{u}$) only being defined on Ω_{e}, while ψ extends to Ω_{a} now. The amplitudes are again scaled with $a^{\mathrm{a}}(t) = E^{\mathrm{a}}\sin(t) + D^{\mathrm{a}}\cos(t)$ and $a^{\mathrm{e}}(t) = E^{\mathrm{e}}\sin(t) + D^{\mathrm{e}}\cos(t)$. However, this time the acoustic amplitudes are allowed to attain different values in the two individual acoustic domains; i.e.,

$$E^{\mathrm{a}} = \begin{cases} E^{\mathrm{f}}, & \text{in } \Omega_{\mathrm{f}} \\ E^{\mathrm{t}}, & \text{in } \Omega_{\mathrm{t}} \end{cases}, \qquad D^{\mathrm{a}} = \begin{cases} D^{\mathrm{f}}, & \text{in } \Omega_{\mathrm{f}} \\ D^{\mathrm{t}}, & \text{in } \Omega_{\mathrm{t}}. \end{cases}$$

In order for these functions to be indeed solutions to the coupled problem, we employ the same conditions and right-hand side forcing terms as before, but in addition, to satisfy the acoustic-acoustic interface flux condition, additional constraints on the material parameters are imposed. It should be noted that due to Ω_{f} and Ω_{t} having *different* material parameters, the forcing term f^{a} also differs/jumps in between the acoustic subdomains. Convergence results can be found in Fig. 3. We note that the simulation with polynomial degree $p = 1$ is not included in our theory. However, the numerical experiment suggests that, at least in this synthetic setting, the convergence rate $\mathcal{O}(h^{s-1})$ can also be obtained for $p = 1$.

REMARK 6.1 Note that for Parameter set 1 the factor k_2 in front of the quadratic gradient type nonlinearity is set to zero, reducing the model to Westervelt's equation in potential form (with synthetic material parameters) in the acoustic sub-domains. For Parameter set 2 the parameter k_2 is nonzero, and hence inclusion of the quadratic gradient nonlinearity leads to Kuznetsov's equation of nonlinear acoustics (Kuznetsov, 1970), with synthetic material parameters as well.

6.2 *Numerical experiment 2: focused ultrasound propagation into human tissue*

For the final numerical example we come back to our motivation for the present work, the simulation of medical ultrasound applications involving human tissue. Due to the presence of different boundary conditions (i.e., not only homogeneous Dirichlet data) this experiment lies beyond the theory of this work. Nevertheless, it adheres to the structure of subdomains and coupling given before. Figure 4 depicts the mechanical device design lying behind the subdomain partition and boundary conditions used.

Geometry and boundary data setup We set up a computational domain consisting out of the following three subdomains and data.

- **Curved transducer/excitation array** is modeled as an elastic body made of silicone rubber, where at the bottom side an excitation signal is applied via a (displacement) Dirichlet condition. Using our previous notation this subdomain takes the role of the purely elastic part Ω_{e}. The excitation signal takes the space-time factorized form $u_d(t,x,y) = u_d^{(t)}(t)u_d^{(x)}(x,y)$, where $u_d^{(x)}$ models the spatial distribution of the excitator plates (cf. Fig. 4), while $u_d^{(t)}$ is a sine-pulse signal.

  The remaining surfaces of the excitator block have homogeneous Dirichlet conditions

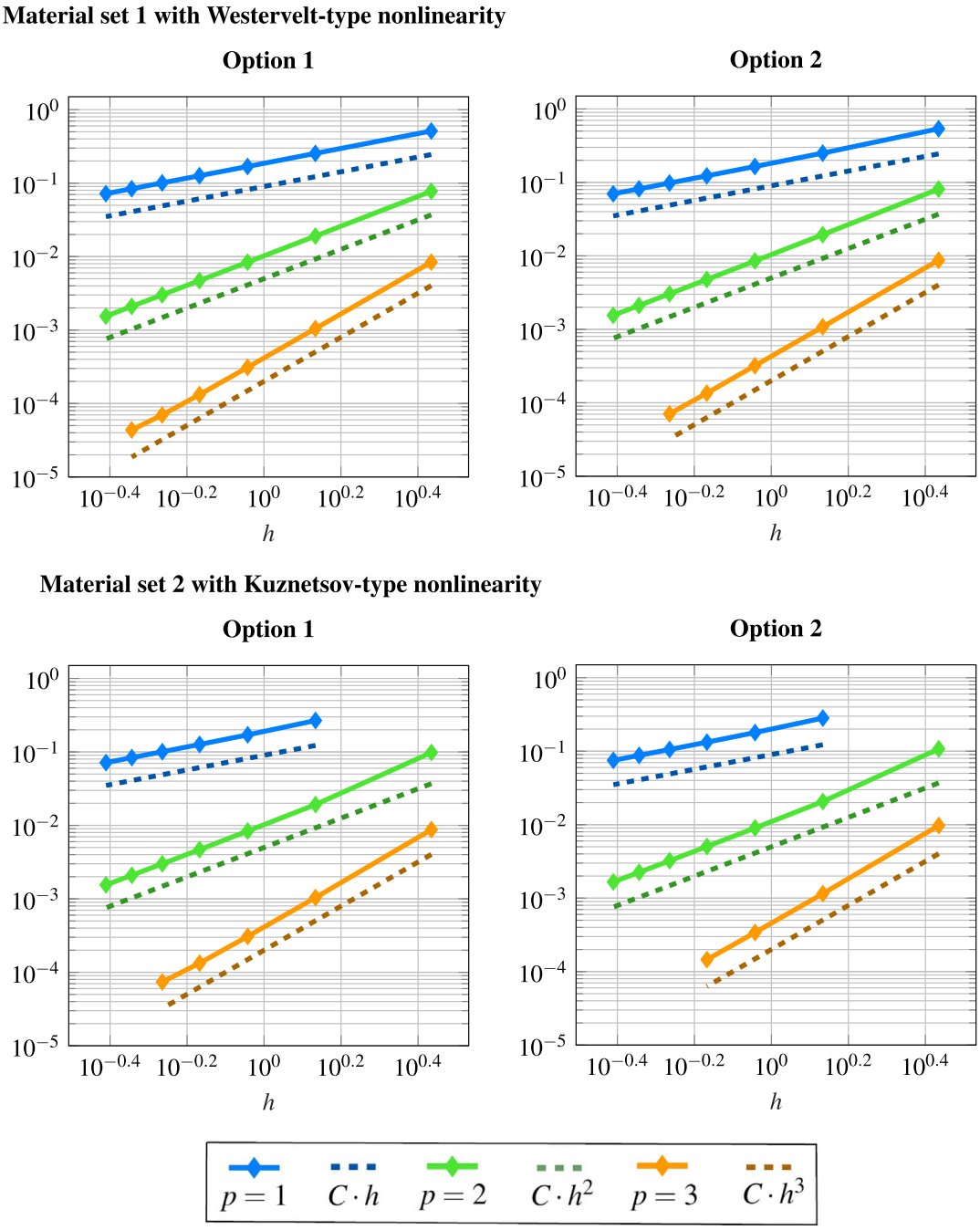

FIG. 3. Relative errors in $L^\infty E$-norm. **(Top)** Material set 1, **(Bottom)** Material set 2. In each we have **(Left)** convergence plots for Option 1 (elastic tissue) and **(Right)** convergence plots for Option 2 (acoustic tissue) with simulations using different polynomial degrees p.

prescribed for the displacement, which can be interpreted as a rigid fixation of the silicon rubber part within the rest of the mechanical device; cf. Fig. 4. For a graphical depiction of different parts of the boundary and used conditions we refer to Fig. 4.

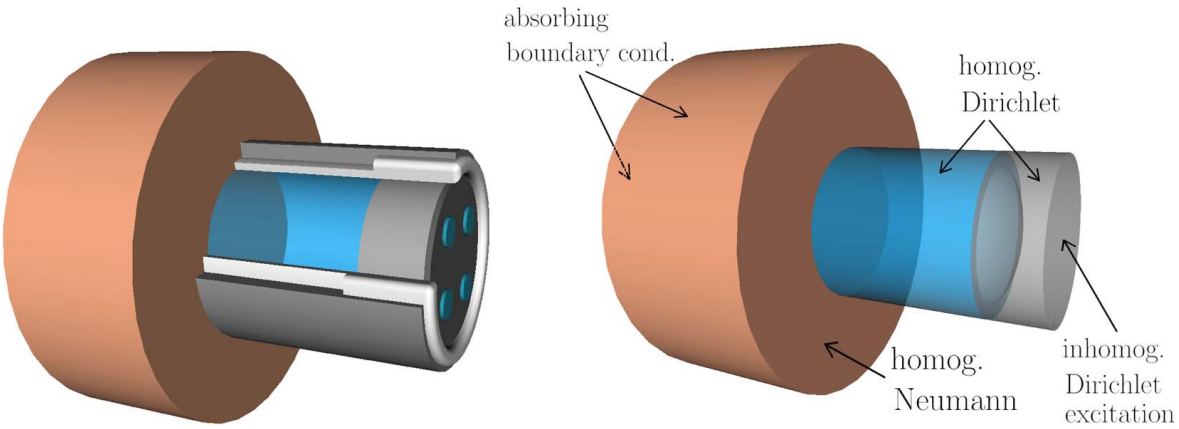

FIG. 4. **(Left)** Depiction of the computational domain embedded into the device framework with walls (270° cut-out view), bearings and excitator plates **(Right)** actual computational domain. The remaining device parts are not numerically resolved, but incorporated via boundary conditions.

- **Acoustic conductor pipe** is modeled as an acoustic/fluid body filled with water. This subdomain takes the role of the purely acoustic/fluid part Ωf from before. On its bottom end the subdomain aligns with the elastic excitator domain on the interface $\Gamma_{\mathrm{I}}^{\mathrm{e,f}}$. On its top end the interface $\Gamma_{\mathrm{I}}^{\mathrm{f,t}}$ with the tissue domain is placed. The cylinder mantle surface has homogeneous Dirichlet conditions for the acoustic potential prescribed, modeling the devices rigid walls encasing the water (compare to Fig. 4).
- **The tissue domain** resides on top of the acoustic conductor. It can be modeled as an elastic or acoustic body, corresponding to the two previously discussed options. In both cases the computational tissue domain has the shape of a cylinder cut out of the larger physical tissue domain, being (part of) the human body. To avoid unphysical reflections on the mantle and top surfaces resulting from that truncation procedure absorbing boundary conditions of Engquist–Majda type (Engquist & Majda, 1977) (in the acoustic case) or as in (Stacey, 1988; Antonietti *et al.*, 2018) (in the elastic case) are employed on these surfaces. The remaining surface is the (skin) surface of the human body without the interface $\Gamma_{\mathrm{I}}^{\mathrm{f,t}}$, equipped with homogeneous Neumann conditions.

For this numerical experiment the simulation starts from the zero initial conditions $(\psi, \dot{\psi})_{t=0} = (0, 0)$, $(\mathbf{u}, \dot{\mathbf{u}})_{t=0} = (\mathbf{0}, \mathbf{0})$; in other words, solid and fluid bodies being at rest. Furthermore, no additional external forces are applied; that is, $\boldsymbol{f}^{\mathrm{e}} = f^{\mathrm{t}} = 0$ and all the dynamics of the system is induced via the excitation/Dirichlet conditions described above.

Material parameters In contrast to the synthetic test case parameters for realistic materials are often given, not in terms of the Lamé-parameters λ and μ, but rather in terms of the elastic modulus E and Poisson ratio ν. Similarly in nonlinear acoustics, the coefficient of nonlinearity $\beta = 1 + \frac{1}{2}B/A$ is commonly used to indicate the nonlinear wave behavior. Here the ratio B/A denotes the parameter of nonlinearity, which arises from the Taylor expansion of the variations of the pressure in terms of variations of the density in a given medium; cf. Hamilton & Blackstock (1998, §2).

We can choose between two different well-established models. The choice $k_1 = \frac{2+B/A}{2c^2}$ and $k_2 = 0$ leads to Westervelt's equation, while $k_1 = \frac{B/A}{2c^2}, k_2 = 1$ leads to Kuznetsov's equation; see Hamilton & Blackstock (1998); Kaltenbacher (2007).

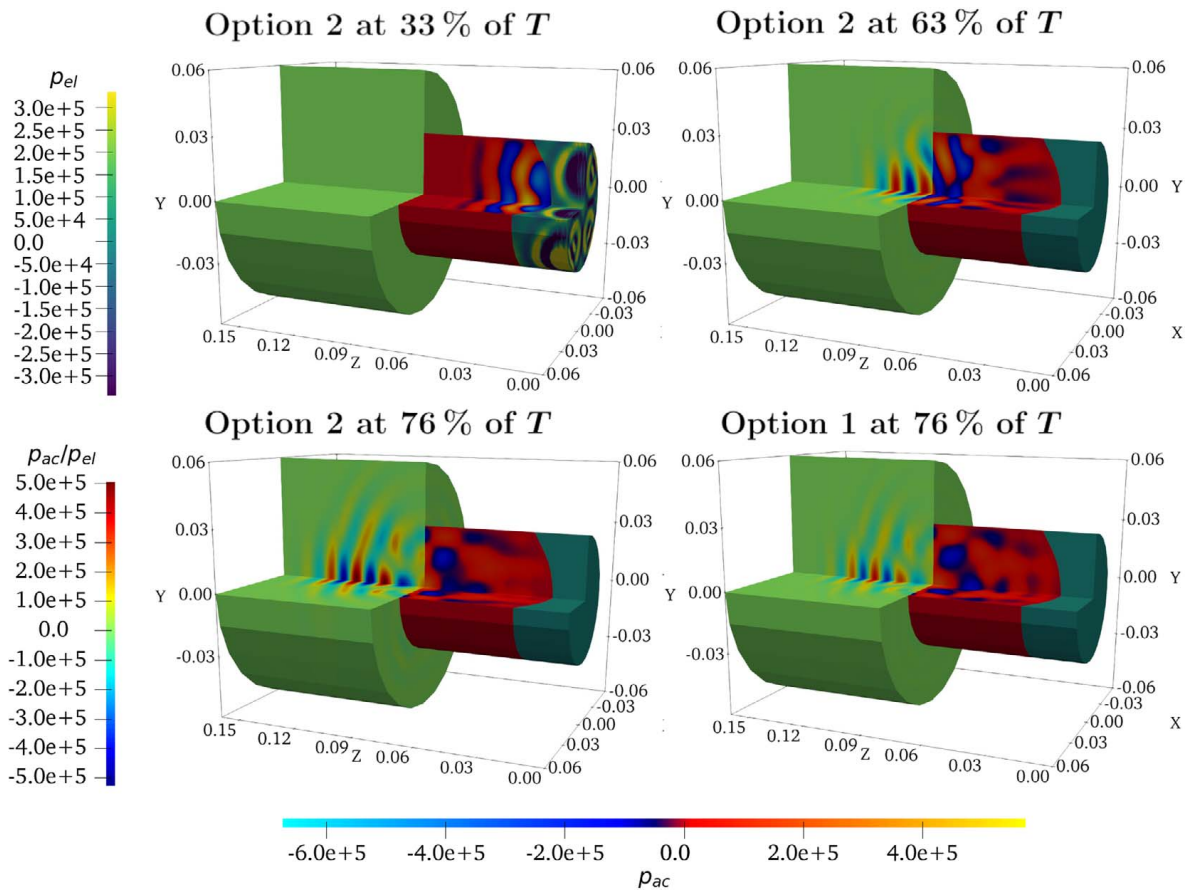

FIG. 5. Pressure field over time using Westervelt's equation as acoustic model. **(Top left–Bottom left)** Option 2, **(Bottom right)** Option 1 and Westervelt's equation only in the fluid domain.

Discretization As a final time for this simulation we have chosen $T = 1.5 \cdot 10^{-4}$ s, which is resolved by 15000 time steps of 10 ns each. For the nonlinear acoustic part, we employ the generalized α scheme as in Antonietti *et al.* (2020b) to damp high-frequency oscillations that might appear in a Gibb phenomenon-like manner near a steep wavefront. In detail, we use the method parameters $\beta = 4/9, \gamma = 5/6, \alpha_m = 0$ and $\alpha_f = 1/3$. We refer to Chung & Hulbert (1993); Erlicher *et al.* (2002) for a deeper insight into this time-stepping method. For the elastic part again the leapfrog scheme is employed. In this experiment the meshes of the subdomain were chosen to be conforming at the interfaces. Spatial discretization is done using 686937 degrees of freedom with polynomial basis functions of degree $p = 3$.

Results From the computed acoustic potential ψ and displacement field $\mathbf{u}$, from our numerical simulation we post-process the acoustic and elastic pressure values relevant for the application according to $p_{\text{ac}} = \varrho\dot{\psi}$ and $p_{\text{el}} = -\frac{1}{3}\sum_{i=1}^{3}\boldsymbol{\sigma}_{ii}$, respectively, depending on whether a subdomain contains an acoustic or elastic material. Herein $\boldsymbol{\sigma}(\mathbf{u}) = \lambda \text{div}(\mathbf{u})\mathbb{1} + 2\mu\varepsilon(\mathbf{u})$ is the stress-tensor, as defined before. Figure 5 shows the pressure wave propagation within the computational domain over different time steps for Option 2 (acoustic) choice for the tissue using the Westervelt equation as the acoustic wave model.

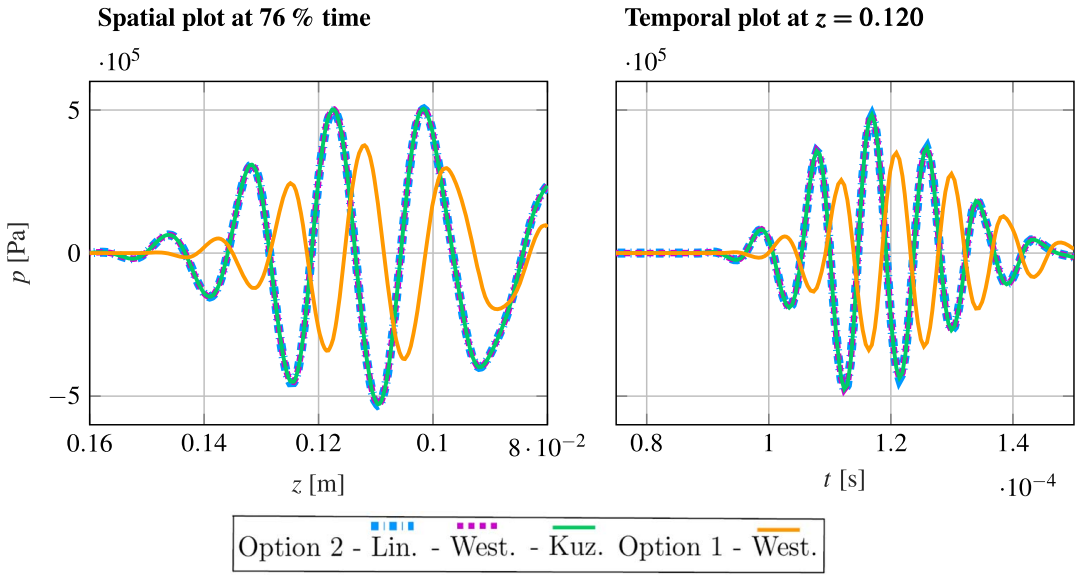

FIG. 6. Model comparison of pressure signal at **(Left)** axis of symmetry of tissue domain at 76 % of simulation time. **(Right)** Same comparison, but over time at fixed point $p = (0, 0, 0.12)^\top$ m.

Further, the pressure field within the tissue is compared with Option 1 of having an elastic tissue model. Figure 6 then compares different choices for the acoustic wave equation being the linear wave equation, the Westervelt or the Kuznetsov equation.

First it can be seen that, while qualitatively behaving similar, Options 1 and 2 differ in amplitude and propagation velocity of the wave, which is due to the material parameters for the two options stemming from different references, with some of them being available only approximately.

In contrast to that, one observes almost no visible difference among the different acoustic models (i.e, the linear wave equation, Westervelt's and Kuznetsov's equations) in the given pressure regime. This observation changes once we employ higher excitation amplitudes and hence increase the influence of the nonlinear terms of the models. Figures 7 and 8 directly compare the acoustic models with each other for a simulation with an excitation amplitude of $a = 0.075$ m. We note that this amplitude might be exaggerated from this application/experiment point of view. However, it shows very accurately the wave steepening effect modeled by the nonlinear terms in the higher pressure regime in contrast to the linear model. Even in Option 1 simulations with the linear elastic tissue model, a small steepening and amplitude increase of the pressure wave is visible once the nonlinear wave equations are used in the fluid region compared to a completely linear simulation.

The comparably quite small difference between the Westervelt and Kuznetsov equation's results further shows that the approximative assumption of $\nabla\psi \cdot \nabla\dot{\psi} \approx \frac{1}{c^2}\dot{\psi}\ddot{\psi}$, which is made in the derivation of the Westervelt equation as a simplification of Kuznetsov's equation and which holds with equality in the case of a linear plane wave, is still reasonable in the given regime of nonlinearity.

7. Conclusion

In this work we have considered a coupled elasto-acoustic problem with thermoviscous dissipation and general nonlinearities of quadratic type in the acoustic regime. The mathematical model was in

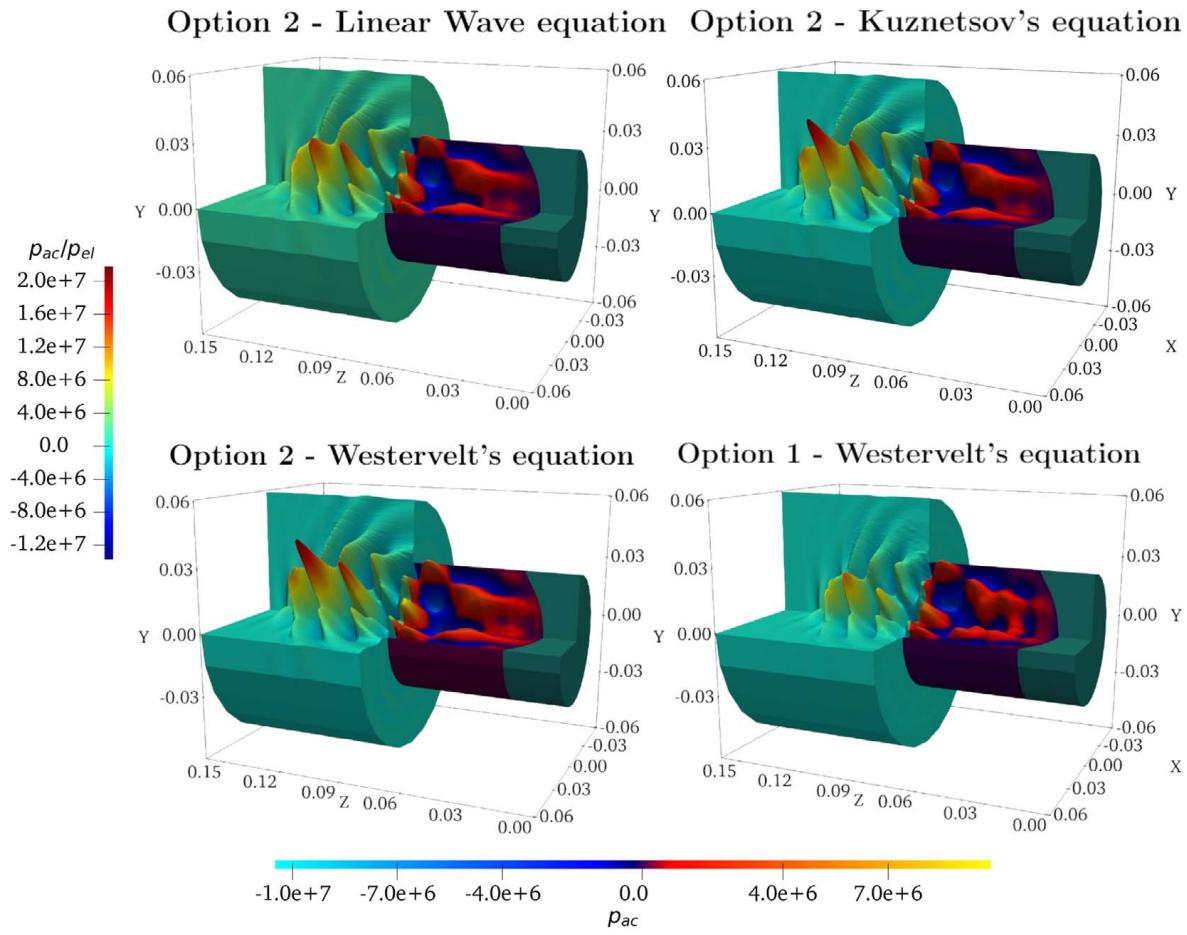

FIG. 7. Comparison of acoustic models in high pressure regime, all at 76 % simulation time in tissue domain. **(Top left)** Linear wave equation, **(Top right)** Kuznetsov's equation, **(Bottom left)** Westervelt's equation. **(Bottom right)** Option 1 with Westervelt's equation only in the fluid domain.

particular motivated by the medical applications of high-intensity ultrasound, which tend to involve different elastic and acoustic subdomains with possible jumps in the material parameters. The elasto-acoustic interface was resolved by a coupling based on force-exchange via Neumann conditions, while the acoustic-acoustic interfaces were treated using a discontinuous Galerkin approach, resulting in a fully coupled initial boundary-value problem. We discretized the problem in space using hexahedral elements of degree p being conform within each material subdomain, but with the option of nonmatching grids across interfaces. By a careful choice of test functions, taking into account the thermoviscous dissipation term, we proved stability and error bounds for the linearized approximation in a suitable energy norm. Under regularity and smallness assumptions on the exact solution in an appropriate norm and smallness of the mesh size parameter h, we derived an error estimate in the energy norm for the nonlinear problem by employing the Banach fixed-point theorem.

Additionally, we have conducted extensive convergence studies to support our theoretical findings for different options, with respect to modeling the tissue and material parameters of the discussed model. Finally, a three-dimensional simulation using realistic material data and geometries showing

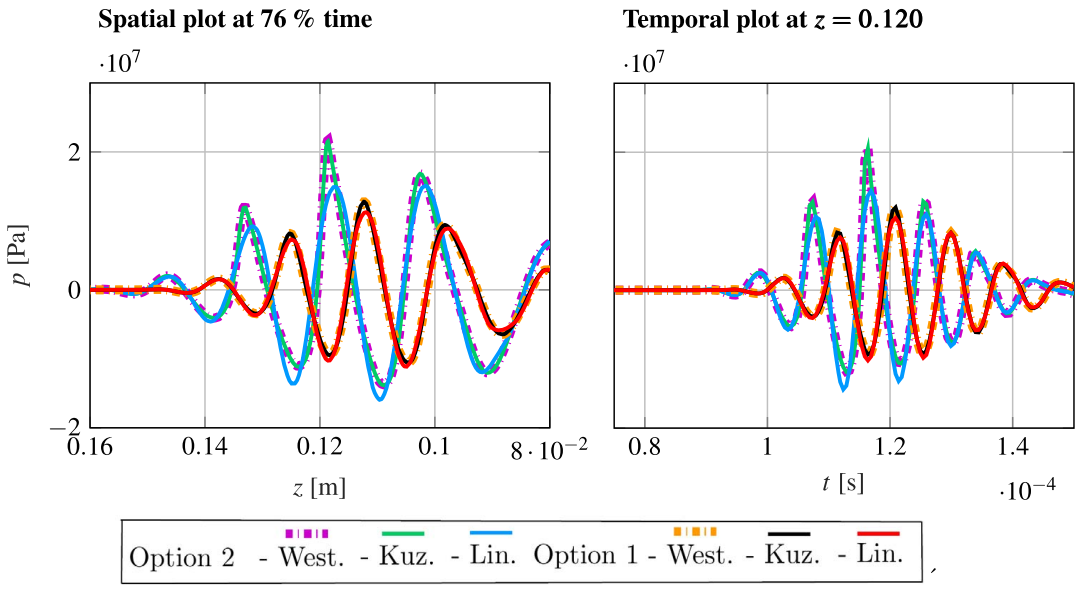

FIG. 8. Model comparison of pressure signal at **(Left)** axis of symmetry of tissue domain at 76 % of simulation time. **(Right)** Same comparison, but over time at fixed point $p = (0, 0, 0.12)^\top$ m.

the propagation of ultrasound waves into human tissue closes the loop to the original motivation of the work.

Future research on the topic will be concerned with the analysis and simulation of problems including nonlinear effects, not only in the acoustic, but also elastic regime, and the simulation of ultrasound heating by an additional coupling with a temperature model.

Acknowledgements

We would like to thank the reviewers for their careful reading of our manuscript and for the insightful remarks. M. Muhr and B. Wohlmuth acknowledge the financial support provided by the Deutsche Forschungsgemeinschaft under the grant number WO 671/11-1.

References

ANTONIETTI, P. F., BONALDI, F. & MAZZIERI, I. (2020a) A high-order discontinuous Galerkin approach to the elasto-acoustic problem. *Comput. Methods Appl. Mech. Eng.*, **358**, 112634.

ANTONIETTI, P. F., MAZZIERI, I., MUHR, M., NIKOLIĆ, V. & WOHLMUTH, B. (2020b) A high-order discontinuous Galerkin method for nonlinear sound waves. *J. Comput. Phys.*, **415**, 109484.

ANTONIETTI, P. F., FERRONI, A., MAZZIERI, I., PAOLUCCI, R., QUARTERONI, A., SMERZINI, C. & STUPAZZINI, M. (2018) Numerical modeling of seismic waves by discontinuous spectral element methods. *ESAIM Proc. Surv.*, **61**, 1–37.

ANTONIETTI, P. F., MAZZIERI, I., QUARTERONI, A. & RAPETTI, F. (2012) Non-conforming high order approximations of the elastodynamics equation. *Comput. Methods Appl. Mech. Eng.*, **209**, 212–238.

BRENNER, S. & SCOTT, R. (2008) *The Mathematical Theory of Finite Element Methods*, vol. 15. New York: Springer Science & Business Media.

Brivadis, E., Buffa, A., Wohlmuth, B. & Wunderlich, L. (2015) Isogeometric mortar methods. *Comput. Methods Appl. Mech. Eng.*, **284**, 292–319.

Brunnhuber, R., Kaltenbacher, B. & Radu, P. (2014) Relaxation of regularity for the Westervelt equation by nonlinear damping with application in acoustic–acoustic and elastic–acoustic coupling. *Evol. Equ. Control Theory*, **3**, 595–626.

Cangiani, A., Georgoulis, E. H. & Houston, P. (2014) *hp*-version discontinuous Galerkin methods on polygonal and polyhedral meshes. *Math. Models Methods Appl. Sci.*, **24**, 2009–2041.

Chung, J. & Hulbert, G. (1993) A time integration algorithm for structural dynamics with improved numerical dissipation: the Generalized-α method. *J. Appl. Mech.*, **60**, 371–375.

Di Pietro, D. A. & Ern, A. (2012) *Mathematical Aspects of Discontinuous Galerkin Methods*, vol. 69. Berlin, Heidelberg: Springer.

Engquist, B. & Majda, A. (1977) Absorbing boundary conditions for numerical simulation of waves. *Proc. Natl. Acad. Sci.*, **74**, 1765–1766.

Epshteyn, Y. & Rivière, B. (2007) Estimation of penalty parameters for symmetric interior penalty Galerkin methods. *J. Comput. Appl. Math.*, **206**, 843–872.

Erlicher, S., Bonaventura, L. & Bursi, O. S. (2002) The analysis of the generalized-α method for non-linear dynamic problems. *Comput. Mech.*, **28**, 83–104.

Felippa, C. A., Park, K. & Ross, M. (2011) A classification of interface treatments for FSI. *Fluid Structure Interaction II*. Berlin, Heidelber: Springer, pp. 27–51.

Flemisch, B., Kaltenbacher, M. & Wohlmuth, B. I. (2006) Elasto–acoustic and acoustic–acoustic coupling on non-matching grids. *Int. J. Numer. Methods Eng.*, **67**, 1791–1810.

Hamilton, M. F. & Blackstock, D. T. (1998) *Nonlinear Acoustics*, volume 1. San Diego: Academic Press.

Hou, G., Wang, J. & Layton, A. (2012) Numerical methods for fluid–structure interaction—a review. *Commun. Comput. Phys.*, **12**, 337–377.

Kaltenbacher, B. & Lasiecka, I. (2009) Global existence and exponential decay rates for the Westervelt equation. *Discrete Contin. Dyn. Syst. Ser. S*, **2**, 503.

Kaltenbacher, B. & Peichl, G. (2016) The shape derivative for an optimization problem in lithotripsy. *Evol. Equ. Control Theory*, **5**, 399.

Kaltenbacher, M. (2007) *Numerical Simulation of Mechatronic Sensors and Actuators*, vol. 2. Berlin, Heidelberg: Springer.

Kennedy, J. E. (2005) High-intensity focused ultrasound in the treatment of solid tumours. *Nat. Rev. Cancer*, **5**, 321–327.

Kuznetsov, V. P. (1970) Equations of nonlinear acoustics. *Sov. Phys. Acoustics*, **16**, 467–470.

Lee, D., Koizumi, N., Ota, K., Yoshizawa, S., Ito, A., Kaneko, Y., Matsumoto, Y. & Mitsuishi, M. (2007) Ultrasound-based visual servoing system for lithotripsy. *2007 IEEE/RSJ International Conference on Intelligent Robots and Systems*. San Diego, CA: IEEE, pp. 877–882.

Li, Z. C. (1998) *Lagrange Multipliers and Other Coupling Techniques*. Boston, MA: Springer US, pp. 209–224.

Maier, B. (2020) Error analysis for space and time discretizations of quasilinear wave-type equations. *Ph.D. Thesis*, Karlsruhe Institute of Technology, Germany.

Mazzieri, I., Stupazzini, M., Guidotti, R. & Smerzini, C. (2013) SPEED: SPectral elements in elastodynamics with discontinuous Galerkin: a non-conforming approach for 3D multi-scale problems. *Int. J. Numer. Methods Fluids*, **95**, 991–1010.

Meyer, S. & Wilke, M. (2011) Optimal regularity and long-time behavior of solutions for the Westervelt equation. *Appl. Math. Optim.*, **64**, 257–271.

Mizohata, K. & Ukai, S. (1993) The global existence of small amplitude solutions to the nonlinear acoustic wave equation. *J. Math. Kyoto Univ.*, **33**, 505–522.

Muhr, M., Nikolić, V. & Wohlmuth, B. (2021). A discontinuous Galerkin coupling for nonlinear elasto-acoustics. arXiv preprint arXiv:2102.04311v2. Extended arXiv version.

MUHR, M., NIKOLIĆ, V., WOHLMUTH, B. & WUNDERLICH, L. (2019) Isogeometric shape optimization for nonlinear ultrasound focusing. *Evol. Equ. Control Theory*, **8**, 163–202.

NIKOLIĆ, V. & WOHLMUTH, B. (2019) A priori error estimates for the finite element approximation of Westervelt's quasi-linear acoustic wave equation. *SIAM J. Numer. Anal.*, **57**, 1897–1918.

ORTNER, C. & SÜLI, E. (2007) Discontinuous Galerkin finite element approximation of nonlinear second-order elliptic and hyperbolic systems. *SIAM J. Numer. Anal.*, **45**, 1370–1397.

SCHÖTZAU, D., SCHWAB, C. & TOSELLI, A. (2002) Mixed hp-dgfem for incompressible flows. *SIAM J. Numer. Anal.*, **40**, 2171–2194.

SHEVCHENKO, I., KALTENBACHER, M. & WOHLMUTH, B. (2012) A multi-time stepping integration method for the ultrasound heating problem. *ZAMM J. Appl. Math. Mech./Zeit. Angew. Math. Mech.*, **92**, 869–881.

SKOLARIKOS, A., ALIVIZATOS, G. & DE LA ROSETTE, J. (2006) Extracorporeal shock wave lithotripsy 25 years later: complications and their prevention. *Eur. Urol.*, **50**, 981–990.

STACEY, R. (1988) Improved transparent boundary formulations for the elastic-wave equation. *Bull. Seismol. Soc. Amer.*, **78**, 2089–2097.

STUPAZZINI, M., PAOLUCCI, R. & IGEL, H. (2009) Near-fault earthquake ground-motion simulation in the Grenoble valley by a high-performance spectral element code. *Bull. Seismol. Soc. Amer.*, **99**, 286–301.

WESTERVELT, P. J. (1963) Parametric acoustic array. *J. Acoust. Soc. Amer.*, **35**, 535–537.

WICK, T. & WOLLNER, W. (2020) Optimization with nonstationary, nonlinear monolithic fluid–structure interaction. *Int. J. Numer. Methods Eng.*, **122**, 5430–5449.

B. Further Articles

B.1. Elasto-acoustic modelling and simulation for the seismic response of structures: The case of the Tahtalı dam in the 2020 İzmir earthquake

Elasto-acoustic modelling and simulation for the seismic response of structures: The case of the Tahtalı dam in the 2020 İzmir earthquake

Ilario Mazzieri, **Markus Muhr**, Marco Stupazzini and Barbara Wohlmuth

---

Seismic hazard analysis, especially in regions of high ground motion activity, is crucial for risk assessment and seismic design of building structures. This article deals with the construction and application of a numerical, elasto-acoustic model to simulate the effects a seismic event has on dam structures. As a concrete case study the response of the Tahtalı dam, located in Turkey near the city of İzmir, during the magnitude $M_w = 7$ earthquake from the 30^{th} of October 2020 is analyzed [59]. Real topography and ground data [155, 290] is used to create a realistic model, which is then validated against actual seismograph-measurements [1] from the event. Due to the generality of the model, the achieved simulation capabilities lay the foundations for further simulation based seismic analyses.

For this article we utilize the elasto-acoustic- and DG-coupling capabilities of *SPEED* in order to simulate the dam, the underlying layers of ground, each with possibly different material parameters, as well as the reservoir lake behind the dam. The elasto-acoustic model and discretization hereby are adopted from [7, II], where in this article the focus lies on the application and the incorporation of real data. First of all, the topography of the surrounding area of the dam is resolved from satellite altitude data [155]. A CAD-model of the dam is then placed in the topography and a complex mesh is generated to capture the necessary features of the solid/elastic geometry. The elasto-acoustic interface is used to incorporate the influence of the water in the reservoir-lake, being the acoustic medium. To model the seismic source, inversion-data about the actual seismic fault plane are used for a stress-glut source model. The final source-to-site model spans several length scales, which are resolved by means of local mesh refinement and the DG approach to couple non-matching sub-meshes. The resulting all-in-one simulation is compared also to a more classical approach using a deconvolved seismograph signal as a plane wave input. Outputs of the simulations feature peak ground maps of e.g. displacement and velocity and deformations of the dam, relevant from a seismological and engineering point of view to judge the safety of the dam.

After the introduction, Sec. 2 introduces the elasto-acoustic mathematical model and Sec. 3 the numerical methods used for spatial and temporal discretization. In Sec. 4, a description of the seismic event, the region of interest and the dam itself is given, placing it into a broader context. Sec. 5 then contains a description of the real-data based geometry acquisition and the meshing. In Sec. 6, the different numerical experiments are then conducted, evaluated and compared. Sec. 7 finally gives a conclusion and an outlook to further work to be done in this direction ultimately aiming for the goal of a seismic hazard analysis of the whole region.

I was significantly involved in finding the ideas and carrying out the scientific work presented in this article including the write-up, except for Sec. 4. Furthermore I was in charge of the numerical part of the article, i.e. acquisition, treatment and evaluation of data, implementation and conduction of the simulations and the creation of the figures.

Permission to include:

Mazzieri, Ilario, Markus Muhr, Marco Stupazzini, and Barbara Wohlmuth
Elasto-acoustic modelling and simulation for the seismic response of structures: The case of the Tahtalı dam in the 2020 İzmir earthquake
submitted to: *Journal of Computational Physics*

Included is the arXiv preprint version.

arXiv Submittal Agreement Terms and Conditions

Any person submitting a work for deposit in arXiv is required to assent to the following terms and conditions. The Submitter is an original author of the Work, or a proxy pre-approved by arXiv administrators acting on behalf of an original author. If the Submitter is signing and accepting the terms on behalf of another individual, the Submitter represents and warrants that the Submitter has been granted the authority to make the submittal by that individual and that the Submitter's acceptance of the terms binds that other individual.

Representations and Warranties

The Submitter makes the following representations and warranties:

- The Submitter is an original author of the Work, or a proxy pre-approved by arXiv administrators acting on behalf of an original author.
- If the Work was created by multiple authors, that all of them have consented to the submission of the Work to arXiv.
- The Submitter has the right to include any third-party materials used in the Work.
- The use of any third-party materials is consistent with scholarly and academic standards of proper citation and acknowledgement of sources.
- The Work is not subject to any agreement, license or other claim that could interfere with the rights granted herein.
- The distribution of the Work by arXiv will not violate any rights of any person or entity, including without limitation any rights of copyright, patent, trade secret, privacy, or any other rights, and it contains no defamatory, obscene, or other unlawful matter.
- The Submitter has authority to make the statements, grant the rights, and take the actions described above.

Grant of the License to arXiv

The Submitter grants to arXiv upon submission of the Work a non-exclusive, perpetual, and royalty-free license to include the Work in the arXiv repository and permit users to access, view, and make other uses of the work in a manner consistent with the services and objectives of arXiv. This License includes without limitation the right for arXiv to reproduce (e.g., upload, backup, archive, preserve, and allow online access), distribute (e.g., allow access), make available, and prepare versions of the Work (e.g., , abstracts, and metadata or text files, formats to support accessibility, machine-readable formats) in analog, digital, or other formats as arXiv may deem appropriate. The rights granted will move with arXiv if arXiv moves to another steward.

Waiver of Rights and Indemnification

The Submitter waives the following claims on behalf of themselves and all other authors:

- Any claims against arXiv or Cornell University, or any officer, employee, or agent thereof, based upon the use of the Work by arXiv consistent with the License.
- Any claims against arXiv or Cornell University, or any officer, employee, or agent thereof, based upon actions taken by any such party with respect to the Work, including without limitation decisions to include the Work in, or exclude the Work from, the repository; editorial decisions or changes affecting the Work, including the identification of Submitters and their affiliations or titles; the classification or characterization of the Work; the content of any metadata; the availability or lack of availability of the Work to researchers or other users of arXiv, including any decision to include the Work initially or remove or disable access.
- Any rights related to the integrity of the Work under Moral Rights principles.
- Any claims against arXiv or Cornell University, or any officer, employee, or agent thereof based upon any loss of content or disclosure of information provided in connection with a submission.
- The Submitter will indemnify, defend, and hold harmless arXiv, Cornell University and its officers, employees, agents, and other affiliated parties from any loss, damage, or claim arising out of or related to: (a) any breach of any representations or warranties herein; (b) any failure by Submitter to perform any of Submitter's obligations herein; and (c) any use of the Work as anticipated in the License and terms of submittal.

Management of Copyright

This grant to arXiv is a non-exclusive license and is not a grant of exclusive rights or a transfer of the copyright. The authors retain their copyright and may enter into publication agreements or other arrangements, so long as they do not conflict with the ability of arXiv to exercise its rights under the License. arXiv has no obligation to protect or enforce any copyright in the Work, and arXiv has no obligation to respond to any permission requests or other inquiries regarding the copyright in or other uses of the Work.

The Submitter may elect to make the Work available under one of the following Creative Commons licenses that the Submitter shall select at the time of submission: Creative Commons Attribution license (CC BY 4.0); Creative Commons Attribution-ShareAlike license (CC BY-SA 4.0); Creative Commons Attribution-Noncommercial-ShareAlike license (CC BY-NC-SA 4.0); Creative Commons Attribution-NonCommercial-NoDerivatives license (CC BY-NC-ND 4.0); arXiv license (https://arxiv.org/licenses/nonexclusive-distrib/1.0/license.html); or Creative Commons Public Domain Dedication (CC0 1.0).

If you wish to use a different CC license, then select arXiv's non-exclusive license to distribute in the arXiv submission process and indicate the desired Creative Commons license in the actual article.

The Creative Commons licenses are explained here: https://creativecommons.org/licenses/.

Metadata license

To the extent that the Submitter or arXiv has a copyright interest in metadata accompanying the submission, a Creative Commons CC0 1.0 Universal Public Domain Dedication will apply. Metadata includes title, author, abstract, and other information describing the Work.

General Provisions

This Agreement will be governed by and construed in accordance with the substantive and procedural laws of the State of New York and the applicable federal law of the United States without reference to any conflicts of laws principles. The Submitter agrees that any action, suit, arbitration, or other proceeding arising out of or related to this Agreement must be commenced in the state or federal courts serving Tompkins County, New York. The Submitter hereby consents on behalf of the Submitter and any other authors to the personal jurisdiction of such courts.

The above page is a copy from the webpage
https://arxiv.org/help/policies/submission_agreement
Date: 22.11.2021

ELASTO-ACOUSTIC MODELLING AND SIMULATION FOR THE SEISMIC RESPONSE OF STRUCTURES: THE CASE OF THE TAHTALI DAM IN THE 2020 İZMIR EARTHQUAKE

ILARIO MAZZIERI[1], MARKUS MUHR[*,2], MARCO STUPAZZINI[3], AND BARBARA WOHLMUTH[2]

[1]MOX, Dipartimento di Matematica, Politecnico di Milano, Milano, Italy
[2]Department of Mathematics, Technical University of Munich, Garching, Germany
[3]Munich RE, Münchener Rückversicherungs-Gesellschaft, Munich, Germany

Abstract. As a mean to assess the risk dam structures are exposed to during earthquakes, we employ an abstract mathematical, three dimensional, elasto-acoustic coupled wave-propagation model taking into account (i) the dam structure itself, embedded into (ii) its surrounding topography, (iii) different material soil layers, (iv) the seismic source as well as (v) the reservoir lake filled with water treated as an acoustic medium. As a case study for extensive numerical simulations we consider the magnitude 7 seismic event of the 30^{th} of October 2020 taking place in the Icarian Sea (Greece) and the Tahtalı dam around 30 km from there (Turkey). A challenging task is to resolve the multiple length scales that are present due to the huge differences in size between the dam building structure and the area of interest, considered for the propagation of the earthquake. Interfaces between structures and highly non-conforming meshes on different scales are resolved by means of a discontinuous Galerkin approach. The seismic source is modeled using inversion data about the real fault plane. Ultimately, we perform a real data driven, multi-scale, full source-to-site, physics based simulation based on the discontinuous Galerkin spectral element method, which allows to precisely validate the ground motion experienced along the Tahtalı dam, comparing the synthetic seismograms against actually observed ones. A comparison with a more classical computational method, using a plane wave with data from a deconvolved seismogram reading as an input, is discussed.

1. Introduction

With the continuous growth of computational power in the last decades, physics based simulation (PBS) emerged as an aspiring, alternative approach to ground motion prediction equations (GMPEs), which has already been applied to seismic scenarios at various sites including the United States [80, 81], Japan [37, 45], New-Zealand [26, 52], Turkey [44], China [4], the Netherlands [64], Italy [32]. PBS aims at describing, as reliably as possible, the seismic wave propagation problem and therefore it is crucial, on the one hand, to properly characterize the mechanical properties of the different portion of the computational domain and, on the other, to have a reliable seismic excitation source, see, e.g. [18, 38, 44, 64, 68, 87]. Because of the intrinsically high epistemic uncertainties involved in the construction of 3D numerical models, those need to be verified and validated against available earthquake recordings, cf. e.g. [12, 19, 65]. Nowadays, thanks to the availability of openly accessible data, as for example [30, 83], this challenge can be tackled in specific regions of the world. PBS generates synthetic time histories of displacement, velocity, acceleration and also other engineering relevant quantities, such as strains, stresses and rotations. The numerical methods used are most often finite differences [24, 56, 69], finite elements [11], finite volumes [17, 28, 29, 67] or, as used here in combination with a linear

Key words and phrases. Earthquake simulation, elasto-acoustic coupling, DG-method, water-dam-structure.

*Corresponding author: Markus Muhr, muhr@ma.tum.de.

visco-elastic model, spectral elements in conforming [38, 49, 77] but also discontinuous ways [7, 25, 34].

In this work, we simulate within a single computational model a full seismic event, from source-to-site, and study the effects of ground shaking on a larger building structure. We therefore employ a, mathematically general seismic wave-popagation model to a computational domain consisting of several layers of soil, each with its own material properties and with lengths up to the 100 km scale. On the small scale of 10-100 m, with the same mathematical model, we consider a, comparably small, dam structure in order to analyze its performance under the seismic impact of an earthquake. Together this results in a large, multi-scale problem. The challenge of coupling the multiple, non-conforming meshes of different sizes [57] is tackled by means of the discontinuous Galerkin spectral element method [8]. In addition, two more important factors are considered for properly simulating a dam subjected to seismic excitation: (i) the structure is embedded into its surrounding and therefore the topography should be accurately described, resulting in complex geometries and hence mesh structures, (ii) in contrast to free-standing typical edifices [48] where the surrounding air is most often ignored, the seismic behaviour of the reservoir lake located behind the dam cannot be neglected, and therefore a coupled elasto-acoustic wave-propagation problem needs to be solved. These two factors are considered in this work by making use of digital elevation maps, that can be obtained freely from [46, 70], to obtain a realistic topographic profile and second by resolving the reservoir lake behind the dam as well. As a matter of fact, within the reservoir lake the propagation of acoustic waves will be modeled by a scalar wave equation. The elasto-acoustic dam-water- and ground-water-interfaces are equipped with force exchange coupling conditions. For a mathematical discussion of the coupled problem, we refer to [5, 35], while [60] considers the problem even in a nonlinear, acoustic context. As a seismic source we consider a kinematic rupture model with a prescribed slip-vector and moment-tensor distribution across a fault plane [33]. The model is also compared to another sourcing mechanism using a plane wave input of a recorded seismogram.

The mathematical model and the numerical simulation are validated with respect to the specific magnitude 7 seismic event that took place on the 30^{th} of October in 2020 at around 11:51 h. Its hypocenter lies at 37.8973° N, 26.7953° E in the Icarian Sea northern the isle of Samos, Greece. Approximately 30 km north-east of it on Turkish mainland there lies the Tahtalı-dam with its fresh-water reservoir. Due to its proximity to the source, the dam was severely threatened by the seismic event; however, the reconnaissance team provided the evidence that no severe damages occurred [23]. Besides the topography data mentioned above, in this work, we make use of the large amount of available data regarding the seismic fault source [83] for a realistic simulation of the earthquake's origin, recorded seismograms made freely available by the Turkish Disaster & Emergency Management Authority AFAD [1] and ground material data [83], in order to validate our model and to yield a realistic description of and reliable results for the considered case study.

Our simulations have been obtained using the code *SPEED* [8, 55, 77] employing hexahedral meshes with higher order spectral elements. Sub-meshes with non-matching grids, e.g., at material interfaces with different refinements are coupled using a discontinuous Galerkin approach. Real case simulations as in the present case can easily result in millions of degrees of freedom in space and time, especially when considering higher polynomial orders. Therefore *SPEED* employs a hybrid MPI/OpenMP parallel implementation allowing to harness a large amount of computational resources.

We organize the rest of the paper as follows. Section 2 introduces the elasto-acoustic mathematical model, the equations, boundary- and coupling conditions used. In Section 3, we discuss the adopted discretization in space and time. We derive the semi-discrete form of the model equations by means of spectral elements and introduce a standard time integration scheme. In Section 4, we briefly describe the seismic event adopted as a case study in this work. Section 5, is then devoted to the geometry acquisition (topography/mechanical properties) from real data, and some comments on the mesh generation are given. Finally, the numerical simulations and results are discussed in Section 6, where different simulation methods are presented, validated and finally compared.

2. Mathematical model

We begin by defining the mathematical models used to describe the seismic problem, being the elastic model for the solid parts (soil layers and dam in the specific case study) and acoustic model equations for the fluid part (reservoir lake) each with their corresponding sets of boundary, initial and interface conditions. The computational domain together with its individual material subdomains is then also introduced where, without loss of generality, we refer to the specific case study of the Tahtalı-dam considered in this work. For the whole manuscript, we will denote scalar quantities by regular, greek or latin characters, vectorial quantities will be bold and underlined and tensorial quantities will just be bold.

Mathematical model. As a mathematical model for the description of the individual solid parts/subdomains $\Omega_{\mathrm{e},i}, i = 1, 2, \ldots, N_{\mathrm{e}}$ of the problem, we use the equations of displacement-based linear elasticity (2.1) subdomain-wise with Hook's law $\boldsymbol{\sigma} = \lambda \mathrm{tr}(\boldsymbol{\varepsilon})\mathbb{1} + 2\mu\boldsymbol{\varepsilon}$ as constitutive relation [48, 53], $\boldsymbol{\varepsilon} = \frac{1}{2}\left(\nabla\underline{\mathbf{u}} + \nabla\underline{\mathbf{u}}^{\top}\right)$ being the symmetric gradient of the displacement $\underline{\mathbf{u}}$, and λ and μ being subdomain-wise constant Lamé-parameters, reading

$$\lambda = \lambda(\underline{\mathbf{x}}) = \lambda_i, \text{ for } \underline{\mathbf{x}} \in \Omega_{\mathrm{e},i} \text{ and } i = 1, 2, \ldots, N_{\mathrm{e}},$$
$$\mu = \mu(\underline{\mathbf{x}}) = \mu_i, \text{ for } \underline{\mathbf{x}} \in \Omega_{\mathrm{e},i} \text{ and } i = 1, 2, \ldots, N_{\mathrm{e}}.$$

Parts of $\partial\Omega_{\mathrm{e}}$ on the top surface with *no* overlying body of water (green and white visible surfaces in Fig. 1, right), summarized as $\Gamma_{\mathrm{e,N}}$ are treated as free surfaces (2.2), the four artificial boundaries in x and y directions as well as the plane bottom surface in z-direction (brown in Fig. 1) are equipped with absorbing boundary conditions (2.3). Herein $\underline{\mathbf{t}}^*$ is a fictitious traction force reducing the amount of artificial reflections originating from these surfaces [8, 33, 76]. Parts of $\partial\Omega_{\mathrm{e}}$ that are interfaces to the acoustic domain Ω_{a}, denoted by Γ_{EA} (orange in Fig. 1), are equipped with non-homogeneous Neumann conditions (2.4) acting as force-exchange interface conditions to the acoustic field [5, 60]. Here the short hand notation of

$$\tilde{\psi} := \psi + \frac{b}{c^2}\dot{\psi}$$

is introduced. On internal interfaces between the individual elastic sub-domains $\Omega_{\mathrm{e},i}$, collectively denoted by Γ_{DG} (not visible in Fig. 1, however analogously to elasto-acoustic-interfaces but between ground and dam subdomain), transmission conditions (2.5) are employed, where

$$[\![\boldsymbol{\sigma}]\!] := (\boldsymbol{\sigma}^{+} - \boldsymbol{\sigma}^{-})\underline{\mathbf{n}}, \qquad [\![\underline{\mathbf{u}}]\!] := (\underline{\mathbf{u}}^{+} - \underline{\mathbf{u}}^{-}) \otimes \underline{\mathbf{n}}.$$

Hereby $\underline{\mathbf{n}}$ is the interface normal with arbitrary but fixed orientation and $\iota^{\pm}(\underline{\mathbf{x}}) := \lim_{t\downarrow 0} \iota(\underline{\mathbf{x}} \pm t\underline{\mathbf{n}}), \iota \in \{\boldsymbol{\sigma}, \underline{\mathbf{u}}\}$. Finally suitable initial conditions (2.6) for displacement and velocity $\underline{\mathbf{v}} = \dot{\underline{\mathbf{u}}}$ are prescribed, completing the elastic problem.

$$\rho_{\mathrm{e},i}\left(\ddot{\underline{\mathbf{u}}} + 2\zeta_i\dot{\underline{\mathbf{u}}} + \zeta_i^2\underline{\mathbf{u}}\right) - \nabla\cdot\boldsymbol{\sigma}(\underline{\mathbf{u}}) = \underline{\mathbf{f}}, \qquad \text{in } \Omega_{\mathrm{e},i}\times(0,T], \tag{2.1}$$

$$\boldsymbol{\sigma}\underline{\mathbf{n}} = \underline{\mathbf{0}}, \qquad \text{on } \Gamma_{\mathrm{e,N}}\times(0,T], \tag{2.2}$$

$$\boldsymbol{\sigma}\underline{\mathbf{n}} = \underline{\mathbf{t}}^*, \qquad \text{on } \Gamma_{\mathrm{e,ABC}}\times(0,T], \tag{2.3}$$

$$\boldsymbol{\sigma}\underline{\mathbf{n}} = -\rho_{\mathrm{a}}\dot{\tilde{\psi}}\underline{\mathbf{n}}, \qquad \text{on } \Gamma_{\mathrm{EA}}\times(0,T], \tag{2.4}$$

$$[\![\boldsymbol{\sigma}]\!] = \underline{\mathbf{0}}, [\![\underline{\mathbf{u}}]\!] = \mathbf{0}, \qquad \text{on } \Gamma_{\mathrm{DG}}\times(0,T], \tag{2.5}$$

$$(\underline{\mathbf{u}},\dot{\underline{\mathbf{u}}}) = (\underline{\mathbf{u}}_0,\underline{\mathbf{u}}_1), \qquad \text{at } \Omega_{\mathrm{e}}\times\{0\}. \tag{2.6}$$

In the above system of equations $\rho_{\mathrm{e},i}$ are the mass densities of the subdomains $\Omega_{\mathrm{e},i}, i = 1,2,\dots,N_{\mathrm{e}}$, ρ_{a} is the mass density for the acoustics domain and ζ_i, $i = 1,\dots,N_{\mathrm{e}}$ are viscous damping factors proportional to the inverse of time. For future use, we also introduce the compressional v_p and shear $v_s$wave velocities defined as $v_{p,i} = \sqrt{(\lambda_i + 2\mu_i)/\rho_{\mathrm{e},i}}$ and $v_{s,i} = \sqrt{\mu_i/\rho_{\mathrm{e},i}}$ for $i = 1,\dots,N_{\mathrm{e}}$, respectively.

In the acoustic subdomain Ω_{a}, the linear, damped wave equation (2.7) in potential form, ψ being the acoustic potential, is used to model the propagation of pressure waves with speed of sound c and damping coefficient b. On free water-surfaces (Fig. 1 left, blue) homogeneous Neumann conditions (2.8), on artificially generated surfaces, resulting from the cut-out of Ω from the Earth (Fig. 1 backside, where the lake is cut-off), absorbing boundary conditions (2.9) [31, 75] and on interfaces with the elastic bodies $\Omega_{\mathrm{e},i}$ (Fig. 1 right, orange) interface conditions (2.10) once more as in [5, 60] are imposed. Again, suitable initial conditions (2.11) complete the acoustic problem.

$$\frac{1}{c^2}\ddot{\tilde{\psi}} - \Delta\tilde{\psi} = 0, \qquad \text{in } \Omega_{\mathrm{a},i}\times(0,T], \tag{2.7}$$

$$\nabla\tilde{\psi}\cdot\underline{\mathbf{n}} = 0, \qquad \text{on } \Gamma_{\mathrm{a,N}}\times(0,T], \tag{2.8}$$

$$\nabla\tilde{\psi}\cdot\underline{\mathbf{n}} = -\frac{1}{c}\dot{\tilde{\psi}}, \qquad \text{on } \Gamma_{\mathrm{a,ABC}}\times(0,T], \tag{2.9}$$

$$\nabla\tilde{\psi}\cdot\underline{\mathbf{n}} = -\dot{\underline{\mathbf{u}}}\cdot\underline{\mathbf{n}}, \qquad \text{on } \Gamma_{\mathrm{EA}}\times(0,T], \tag{2.10}$$

$$(\tilde{\psi},\dot{\tilde{\psi}}) = (\psi_0,\psi_1), \qquad \text{at } \Omega_{\mathrm{a}}\times\{0\} \tag{2.11}$$

Note that for all material parameters $\iota \in \{\rho_{\mathrm{e},i}, \rho_{\mathrm{a}}, \zeta_i, \lambda_i, \mu_i, c, b\}$ defined above, we assume the existence of uniformly positive and finite bounds above and below. Note that quantities of interest like acoustic or seismic/elastic pressure can be computed from the solutions of the above models via $p_{\mathrm{ac}} = \rho_{\mathrm{a}}\dot{\tilde{\psi}}$, $p_{\mathrm{el}} = -\frac{1}{3}\sum_{i=1}^{3}\boldsymbol{\sigma}_{ii}$ in a post processing step.

Remark 1. *We remark that Γ_{DG} does not have to contain all internal elastic interfaces necessarily and hence the (discontinuous Galerkin) transmission conditions do not have to be applied to all of them. As an alternative, if grids are matching, also a conforming coupling would be possible.*

Computational domain. For the computational core-domain Ω in the specific case study we choose an, in $x-y$ direction rectangular, cut-out of the Earth around the location of the dam. In z-direction Ω is limited by a plane surface at a given depth below the Earth surface at bottom, while on top the topographic profile of the Earth is used. In a second step, Ω is divided into an acoustic part Ω_{a} consisting of a portion of the dam reservoir lake lying within Ω, and the remaining part Ω_{e} consisting of solid ground (mountain range, soil layers) and the dam itself. The elastic subdomain Ω_{e} is then further divided into individual subdomains $\Omega_{\mathrm{e},i}, i = 1,2,\dots,N_{\mathrm{e}}$, each representing an individual material block, with its own set of constant material parameters, which are possibly discontinuous across the interfaces between the blocks. As a prime example, the dam structure would be one such subdomain while the surrounding ground would be an other. See Fig. 1, left, for a graphical

depiction of the domain of interest with $N_e = 2$ elastic subdomains.

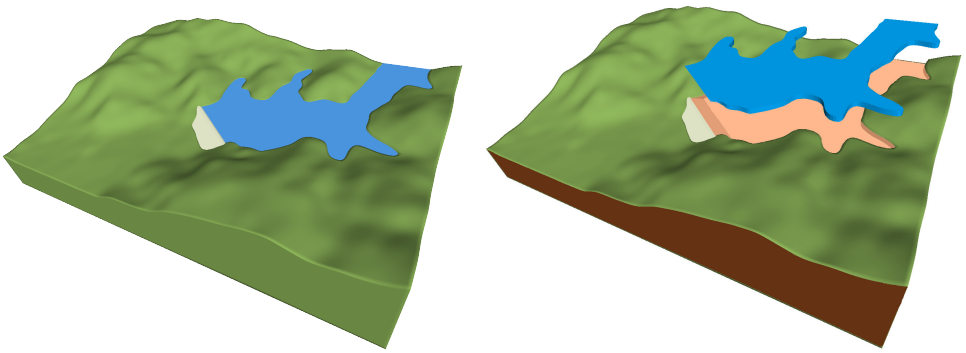

FIGURE 1. **(left)** Computational domain with three subdomains. **Green:** Solid ground $\Omega_{e,1}$, **White:** Solid dam structure $\Omega_{e,2}$, **Blue:** Acoustic water domain Ω_a. **(right)** Highlighting boundary/interface conditions: **Brown:** Absorbing boundary conditions (all 4 sides, incl. the water cut-off surface plus bottom surface), **Orange:** Elasto-Acoustic coupling interface., **Green, White, Water top surface**: Free surfaces, **Non visible:** Interfaces between $\Omega_{e,1}$ and $\Omega_{e,2}$; they are analogous to the elasto-acoustic interfaces.

3. Numerical methods

This section starts with a description of the spatially discrete setting used to approximate a weak solution to the seismic problem (2.1)-(2.11). We then derive the semi-discrete equation in variational and matrix-vector form and end with some notes about the used time integration scheme.

3.1. Spatial discretization

In this subsection, the mesh(es) to be used and the finite element spaces built on them are introduced. We hereby closely follow [60], where more details on mesh assumptions being sufficient to prove convergence in a similar setting are given.

Meshing. The meshing of the computational domain Ω is done sub-domain wise. This means that each $\Omega_{e,i}$ as well as Ω_a is subdivided into a mesh $\mathcal{T}_{e,i}$, resp. $\mathcal{T}_a$ of hexahedral elements individually. While we assume that also after meshing the discrete interface manifolds do coincide - seen from both sides of the interfaces - the individual meshes on those manifolds do *not* have to. Hence, on the interface the mesh from one side could be a refinement of the mesh from the other side or, for example at a flat interface, could also be a staggered or even completely different mesh. Such non-conformities will be treated by a discontinuous Galerkin approach for the interface coupling.

Discrete spaces. Our goal is to approximate a weak solution to the seismic problem by means of spectral finite elements. Within each subdomain $\Omega_{e,i}$ and Ω_a, this is done in a conforming way, while only at (part of) the interfaces the aforementioned DG approach will be used. This goes hand in hand with the different material properties of the individual sub-domains, and it also allows to keep the amount of degrees of freedom low within the sub-domains, while being flexible at the interfaces.

We denote by $\underline{\mathbf{V}}_h^{e,i}$ the space of discrete ansatz-functions on the i-th elastic subdomain, $i = 1, 2, \ldots, N_e$, which are elementwise polynomials of order p_i when transformed back to the reference element. By $\underline{\mathbf{V}}_h^e$ we denote the space of global elastic ansatz-functions, which, restricted to any of the subdomains, are within the subdomain's ansatz-space. Similar V_h^a

denotes the ansatz-space for the acoustic subdomain. The setting hence directly corresponds to the one in [60] where the overall coupled elasto-acoustic problem, even though in a medical ultrasound setting, including additional non-linear acoustic terms, was analyzed regarding stability and convergence w.r.t. spatial refinement. Therein also further mathematical details are given in a similar setting.

Semi-discrete form. With introducing the mean operator defined as:

$$\{\!\{\boldsymbol{\sigma}\}\!\} = \frac{1}{2}(\boldsymbol{\sigma}^+ + \boldsymbol{\sigma}^-), \qquad \{\!\{\underline{\mathbf{u}}\}\!\} = \frac{1}{2}(\underline{\mathbf{u}}^+ + \underline{\mathbf{u}}^-).$$

in addition to the already defined jump operator, the semi-discrete variational problem is given by:

For any time $t \in (0,T]$ find $(\underline{\mathbf{u}}_h, \psi_h) \in \underline{\mathbf{V}}_h^{\mathrm{e}} \times V_h^{\mathrm{a}}$ such that for all $(\underline{\mathbf{w}}_h, \phi_h) \in \underline{\mathbf{V}}_h^{\mathrm{e}} \times V_h^{\mathrm{a}}$ there holds:

$$\begin{aligned}
&\sum_{i=1}^{N_{\mathrm{e}}} \left[(\rho_{\mathrm{e},i} \ddot{\underline{\mathbf{u}}}_h, \underline{\mathbf{w}}_h)_{\Omega_{\mathrm{e},i}} + (\rho_{\mathrm{e},i} 2\zeta_i \dot{\underline{\mathbf{u}}}_h, \underline{\mathbf{w}}_h)_{\Omega_{\mathrm{e},i}} + (\rho_{\mathrm{e},i} \zeta_i^2 \underline{\mathbf{u}}_h, \underline{\mathbf{w}}_h)_{\Omega_{\mathrm{e},i}} + (\boldsymbol{\sigma}(\underline{\mathbf{u}}_h), \boldsymbol{\varepsilon}(\underline{\mathbf{w}}_h))_{\Omega_{\mathrm{e},i}} \right] \\
&-(\underline{\mathbf{t}}_h^*, \underline{\mathbf{w}}_h)_{\Gamma_{\mathrm{e,ABC}}} - \langle \{\!\{\boldsymbol{\sigma}(\underline{\mathbf{u}}_h)\}\!\}, [\![\underline{\mathbf{v}}_h]\!] \rangle_{\Gamma_{\mathrm{DG}}} - \langle [\![\underline{\mathbf{u}}_h]\!], \{\!\{\boldsymbol{\sigma}(\underline{\mathbf{v}}_h)\}\!\} \rangle_{\Gamma_{\mathrm{DG}}} + \langle \chi\, [\![\underline{\mathbf{u}}_h]\!], [\![\underline{\mathbf{v}}_h]\!] \rangle_{\Gamma_{\mathrm{DG}}} \\
&\qquad + \left(\rho_{\mathrm{a}} \dot{\tilde{\psi}}_h \underline{\mathbf{n}}, \underline{\mathbf{w}}_h \right)_{\Gamma_{\mathrm{EA}}} + (\dot{\underline{\mathbf{u}}}_h \cdot \underline{\mathbf{n}}, \phi_h)_{\Gamma_{\mathrm{EA}}} \\
&\qquad + \left(c^{-2} \ddot{\tilde{\psi}}_h, \phi_h \right)_{\Omega_{\mathrm{a}}} + (\nabla \tilde{\psi}_h, \nabla \phi_h)_{\Omega_{\mathrm{a}}} + \left(c^{-1} \dot{\tilde{\psi}}_h, \phi_h \right)_{\Gamma_{\mathrm{a,ABC}}} = (\underline{\mathbf{f}}_h, \underline{\mathbf{w}}_h)_{\Omega_{\mathrm{e}}}
\end{aligned} \tag{3.1}$$

and $\underline{\mathbf{u}}_h(0) = \underline{\mathbf{u}}_0 = \underline{\mathbf{0}}$, $\dot{\underline{\mathbf{u}}}_h(0) = \underline{\mathbf{u}}_1 = \underline{\mathbf{0}}, \psi_h(0) = \psi_0 = 0$ and $\dot{\psi}_h(0) = \psi_1 = 0$, which corresponds to an initial state at rest for the solid as well as for the acoustic quantities.

Finally, for any face in Γ_{DG}, defined as the intersection between opposite elemental faces, we define the penalty parameter χ as:

$$\chi|_F := \{\lambda + 2\mu\}_A \frac{p_F^2}{h_F}$$

being F a DG face shared by the mesh elements E^+ and E^-, $p_F = \max\{p^+, p^-\}$, $h_F = \min\{h^+, h^-\}$, $\{q\}_A$ the harmonic average of the quantity q, and β a positive real number at our disposal, cf. [8, 25, 60].

Matrix-Vector form. After representing the discrete trial functions $\underline{\mathbf{u}}_h$ and ψ_h as well as their temporal derivatives in the nodal finite element basis, denoting the coefficient vectors by (abuse of notation) also $\underline{\mathbf{u}}_h$ and $\underline{\psi}_h$, the following system of ODEs in matrix-vector form is directly obtained from (3.1):

$$\begin{aligned}
\begin{pmatrix} \mathbf{M}_{\mathrm{e}}^{(2)} & 0 \\ 0 & \mathbf{M}_{\mathrm{a}}^{(2)} \end{pmatrix} \begin{pmatrix} \ddot{\underline{\mathbf{u}}}_h \\ \ddot{\underline{\psi}}_h \end{pmatrix} &= - \begin{pmatrix} \mathbf{M}_{\mathrm{e}}^{(1)} & 0 \\ 0 & 0 \end{pmatrix} \begin{pmatrix} \dot{\underline{\mathbf{u}}}_h \\ \dot{\underline{\psi}}_h \end{pmatrix} - \begin{pmatrix} \mathbf{M}_{\mathrm{e}}^{(0)} & 0 \\ 0 & 0 \end{pmatrix} \begin{pmatrix} \underline{\mathbf{u}}_h \\ \underline{\psi}_h \end{pmatrix} \\
&\quad + \begin{pmatrix} -\mathbf{K}_{\mathrm{e}} + \mathbf{D} + \mathbf{D}^\top - \mathbf{P} & 0 \\ 0 & -\mathbf{K}_{\mathrm{a}} \end{pmatrix} \begin{pmatrix} \underline{\mathbf{u}}_h \\ \underline{\psi}_h \end{pmatrix} \\
&\quad - \begin{pmatrix} 0 & \mathbf{E} \\ \mathbf{A} & 0 \end{pmatrix} \begin{pmatrix} \dot{\underline{\mathbf{u}}}_h \\ \dot{\underline{\psi}}_h \end{pmatrix} - \begin{pmatrix} 0 & 0 \\ 0 & \mathbf{C}_{\mathrm{a}} + \mathbf{C}_{\mathrm{a},ABC} \end{pmatrix} \begin{pmatrix} \dot{\underline{\mathbf{u}}}_h \\ \dot{\underline{\psi}}_h \end{pmatrix} + \begin{pmatrix} \underline{\mathbf{T}}_h^* \\ 0 \end{pmatrix} + \begin{pmatrix} \underline{\mathbf{F}}_h \\ 0 \end{pmatrix}
\end{aligned} \tag{3.2}$$

$$\text{with initial conditions:} \quad \begin{pmatrix} \underline{\mathbf{u}} \\ \underline{\psi} \end{pmatrix} = \begin{pmatrix} \dot{\underline{\mathbf{u}}} \\ \dot{\underline{\psi}} \end{pmatrix} = \begin{pmatrix} \underline{\mathbf{0}} \\ \underline{0} \end{pmatrix}$$

Herein $\mathbf{M}_{\mathrm{e}}^{(1)}$ and $\mathbf{M}_{\mathrm{e}}^{(0)}$ are subdomain-wise scaled versions of the standard mass-matrix $\mathbf{M}_{\mathrm{e}}^{(2)}$ for the elastic part of the problem. Due to the DG approach for the interface coupling,

they are block-diagonal with one block per subdomain. In fact, due to the use of spectral elements, they even become diagonal. This property is not only advantageous to be exploited by the time stepping scheme but also allows to denote the aforementioned scaling using the diagonal matrix $\mathbf{Z}$, which has entries ζ_i for each degree of freedom belonging to the elastic subdomain $\Omega_{\mathrm{e},i}$. With that, the scaled mass matrices read $\mathbf{M}_{\mathrm{e}}^{(1)} = 2\mathbf{Z}\mathbf{M}_{\mathrm{e}}^{(2)}$ and $\mathbf{M}_{\mathrm{e}}^{(0)} = \mathbf{Z}^2\mathbf{M}_{\mathrm{e}}^{(2)}$. Analogously $\mathbf{M}_{\mathrm{a}}^{(2)}$ is the standard mass-matrix for the acoustic part. $\mathbf{K}_{\mathrm{a}}$ resp. $\mathbf{K}_{\mathrm{e}}$ denote stiffness-matrices for the scalar resp. vectorial case, $\mathbf{C}_a$ incorporates the b-damping of the acoustic equation. On the right hand side $\mathbf{D}$ and $\mathbf{P}$ are the matrices stemming from the inter-elastic DG coupling, where $\mathbf{P}$ contains the penalization term, while $\mathbf{E}$ and $\mathbf{A}$ contain the coupling terms between the elastic and acoustic domains. Finally $\mathbf{C}_{\mathrm{a},ABC}$ is a boundary mass-matrix used in the implementation of the acoustic absorbing boundary conditions, $\underline{\mathbf{T}}_h^*$ incorporates the elastic absorbing boundary conditions and $\underline{\mathbf{F}}_h$ the elastic source term inducing the earthquake (cf. Sec. 6 for different source models).

3.2. **Time integration**

The basis scheme used for time integration is the Leap-Frog scheme in its full-step predictor-corrector form [42]. After the prediction step

$$\underline{\phi}^{(n+1)} = \underline{\phi}_{\mathrm{pred}} = \underline{\phi}^{(n)} + \Delta t\dot{\underline{\phi}}^{(n)} + \frac{1}{2}\Delta t^2\ddot{\underline{\phi}}^{(n)}, \qquad \dot{\underline{\phi}}_{\mathrm{pred}} = \dot{\underline{\phi}}^{(n)} + \frac{1}{2}\Delta t\ddot{\underline{\phi}}^{(n)}$$

for $\underline{\phi} \in \{\underline{\mathbf{u}}_h, \underline{\psi}_h\}$ the right hand side of (3.2) can be evaluated using the predicted values (and the previous timestep value for $\ddot{\underline{\psi}}_h$ within $\dot{\underline{\psi}}_h$). One then conducts a solver step for the left hand side variables $\ddot{\underline{\mathbf{u}}}_h^{(n+1)}$ and $\ddot{\underline{\psi}}_h^{(n+1)}$ followed by the correction step

$$\dot{\underline{\phi}}^{(n+1)} = \dot{\underline{\phi}}_{\mathrm{pred}} + \frac{1}{2}\Delta t\ddot{\underline{\phi}}^{(n+1)}$$

again $\underline{\phi} \in \{\underline{\mathbf{u}}_h, \underline{\psi}_h\}$.

To take into account the multiscale nature in time, we also employ a simple local time-stepping approach for the acoustic part of the problem similar to [74]. Especially in the vicinity of the inclined dam surface that is under water (cf. Fig. 4, right) water elements become quite thin hence requiring small timesteps that are not necessary in the remaining region of the problem, especially the huge land masses $\Omega_{\mathrm{e},i}$ of seismic propagation. Hence, within each regular time step of size Δt the solution of the acoustic equation within Ω_{a} consisting of prediction, evaluation, solving and correction is internally repeated within a loop of n_{loc} timesteps of size $\frac{\Delta t}{n_{\mathrm{loc}}}$ before the next regular step for the elastic portion of the problem is conducted. In the presented simulation cases a value of $n_{\mathrm{loc}} = 10$ yields good results.

4. **Seismic scenario description**

We now provide some selected information about the specific, real seismic event that will serve as a case study for the mathematical model and numerical methods described in Sec. 2 and 3. The event was chosen due to the large amount of seismograms recorded and therefore allowing a proper validation of the simulation.

The Samos Island (Aegean Sea) earthquake struck at 14:51 local time in Turkey, on 30 October 2020. Severe damages have been observed in some densely populated districts of İzmir (Bayraklı, Bornova, Karşıyaka and Konak), and 118 fatalities have been reported. The present event occurred in the cross-border region between the eastern Aegean Sea islands and Western Turkey, which is among the most seismically active areas in Eastern Mediterranean and has been the site of devastating earthquakes in both recent and historical

times, see [40]. The fault that ruptured during the mainshock is located offshore the northern coast of Samos Island, and it was previously identified as Kaystrios Fault (see GreDaSS database [20] and the GEM-Faults database [78]). The geometric characteristics of the Kaystrios Fault are: strike in the range 260° to 290°, dip 45° to 70° and rake in the range -100° to -80°, while the maximum depth of the fault is estimated as 14.5 km.

The mainshock was well recorded by the broadband seismic networks of Greece and Turkey, and 35 records are located within 100 km distance from the epicenter [22, 23, 27, 63, 88]. Between October 31st and November 6th a group of engineers assembled by the İzmir Regional Directorate of State Hydraulic Works (DSI) and a reconnaissance team from METU visited dam sites to document the performance of earth-fill and rock-fill dams shaken by the event. After a detailed inspection of six small to medium size earth-fill and rock-fill dams including the Tahtalı dam, no apparent damage was reported by reconnaissance teams.

As reported by [82], the Tahtalı dam is a rockfill dam on the Tahtalı River near Gumuldur County in the İzmir Metropolitan Area. It has a 54.4 m height from river bed. When the reservoir is at maximum capacity, the facility impounds 306.6 hm^3 of water in its reservoir. Its construction was finished in 1999. It was designed to provide domestic water with an active volume of 287 hm^3. As reported by [82], the Tahtalı dam is only 1.9 km away from an active fault and, according to the seismic hazard analyses performed, it will be subjected to a peak ground acceleration of 0.277 g by an earthquake of M_w 5.7. The Tahtalı dam is at second place, after Gordes dam, when regarding the total capacity of the reservoir and one of the most critical dams in the İzmir Metropolitan Area.

5. Geometry acquisition and mesh generation

The methods described in this section are general and can easily be adopted to different scenarios. However, the individual steps are motivated and illustrated based on the case study discussed in Sec. 4.

Digital elevation map data. In the presently examined case study, the topography of the surrounding area of the Tahtalı-dam is obtained from the *SRTM Digital Elevation Database* of CGIARCSI [46], which contains topographic elevation data in a 3 arc second grid.
On the left-hand side of Fig. 2 a contour plot of a roughly 3 km×2 km area around the Tahtalı-dam is shown, while on the right-hand side of Fig. 2, the respective area in a satellite view for a clear image of the dam location is given.

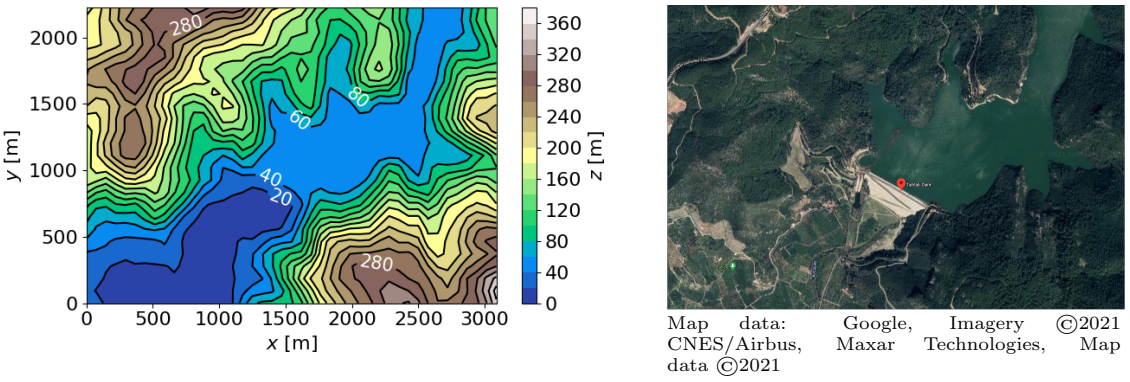

FIGURE 2. **(left)** Topographic map of the region around the Tahtalı-dam with reference coordinate-system. Data source [46]. **(right)** Satellite view of the same area. The red marker is located at 38.0888 °N, 27.0415 °E. Image source [39].

CAD model construction. Starting from the elevation point-cloud data, a volumetric object is constructed and afterwards modified in order to add the dam and the water, and finally proceeding with the meshing. To tackle this challenge the software Cubit [13, 21], which also features some CAD-capabilities, was used firstly for the surface- and then volume-reconstruction.
Using the point cloud elevation data, a spline-surface approximating the topography is created, see Fig. 3. For the bottom surface a rectangle in the x-y-plane directly below the topographic spline-surface at depth $z = -300\,\mathrm{m}$ is used. The four sides remaining to close the volume are flat surfaces and connect the four boundary curves of bottom and top surfaces.

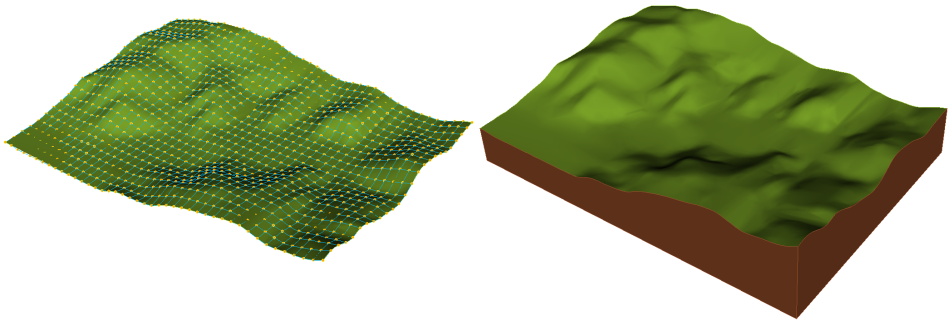

FIGURE 3. **(left)** Orange: Elevation point data obtained from [46], Blue: $x-y$-spline curves, Green: Spline net-surface approximation of topography. **(right)** Volumetric ground object with closing sides (and bottom surface at $z = -300\,\mathrm{m}$) in brown.

Once the topography is available, the dam is added, see Fig. 4, left. The dam is placed in the proper location within the topography and, by means of simple boolean intersection/subtraction as well as downward extrusion operations between the two volumes, is *"naturally"* finally embedded into the surrounding area. Fig. 4, middle, shows the portion of the dam after the operations within the topography.

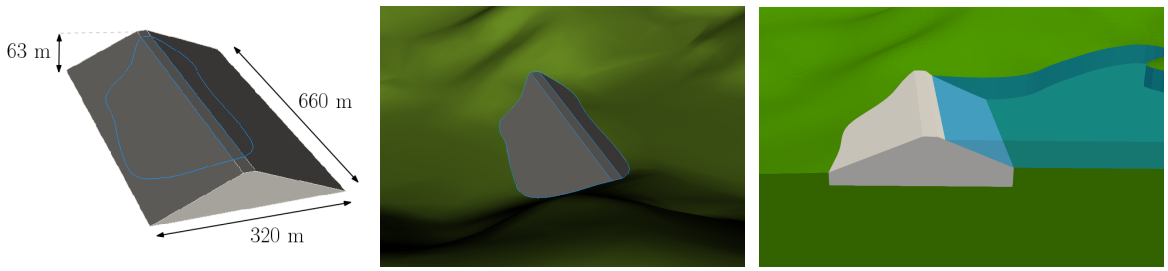

FIGURE 4. **(left)** CAD-model of a gravitational dam. The blue lines (compare to figure right) are the intersection curves between the dam and ground model. **(middle)** Dam-structure embedded into surface topography. **(right)** Cross section View on CAD-model of ground, dam and water. Due to the embedding into the topography the dam measures reduce to approximately $L \approx 570\,\mathrm{m}$, $B \approx 250\,\mathrm{m}$ and $H \approx 50\,\mathrm{m}$ of visible size.

Having placed ground and dam, only the acoustic water-subdomain - the reservoir lake - is missing. It is created by "flooding" the ground block behind the dam and again some downward extrusion followed by a boolean subtraction from the ground block. The resulting water block can be seen in Fig. 1, right, as a whole, Fig. 4, right, gives a cross-sectional view. It should be observed that the inclined dam surface interfacing with the water block

is explicitly created as part of the model, again by means of boolean CAD operations. The final model, consisting of the blocks ground, dam and water can be seen in Fig. 1, left.

Meshing. The usage of a complete hexahedral mesh, with matching interfaces, bears a much more difficult task in mesh generation than a tetrahedral mesh. Even though the software Cubit offers automatic hex-mesh routines like *sculpt* [62], the resulting mesh quality turned out to be not fully satisfactory in the present case, especially in the proximity of interfaces or corners with sharp angles. The process of mesh generation for this work was done in a semi-automatic way, where in a manual pre-processing step the three blocks of the CAD model were subdivided into even more smaller blocks, each with an easily meshable form. Fig. 5, left, shows all those sub-blocks used. The meshing of the sub-blocks was then

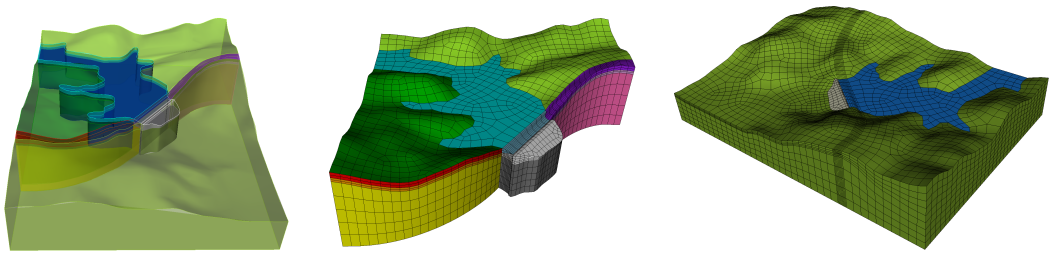

FIGURE 5. **(left)** Division into sub-blocks for the *pave-and-sweep* meshing approach. **(middle)** Meshed sub-blocks with free view on critical water-dam interface. **(right)** Complete mesh of the computational domain, divided into three blocks: Ground, dam and water. Compare to Fig. 1, left.

conducted automatically by a *pave-and-sweep* approach [14, 15, 58]. Special care had to be taken for the inclined water-dam interface (cf. Fig. 4, right).

After successful meshing of all sub-blocks by the aforementioned strategy, sub-block meshes of the same material were merged again to conforming meshes such that in the end (non-conforming) interfaces only remain, where introduced in Sec. 2. Fig. 5, right, shows a complete mesh of the three material blocks, cf. Fig. 1, left.

6. Numerical simulation results

In this section, we present the numerical results obtained. We conduct essentially three numerical simulations: The first one considers the seismic event on a regional scale and ignores the dam or the reservoir lake but takes into account the topography in order to validate the seismic source and numerical wave-propagation model against observed seismograms. In the second scenario, the vicinity region of the dam/reservoir from Fig. 1 and 5 is excited by a simple plane wave input at the bottom of the domain where the time history of the adopted input signal corresponds to the seismogram recorded in the proximity, namely AFAD # 3536. Finally, a full source-to-site simulation of the considered event is conducted, spanning the multiple length scales from the seismic fault plane up to the dam structure including the complete domain from the second analysis as a sub-domain.

As previously mentioned, the dam and other details are ignored in the regional simulation; this allows to have sufficient degrees of freedom and computational resources available to span a broader region and therefore being capable to incorporate 10 seismograph stations for comparison. In the following source-to-site simulation, the domain is tailored around the optimal size that encompasses the fault plane and the dam region and the thereby saved resources are used to adequately simulate the details in the dam vicinity region.

We would like to point out that previously, different verification tests have been considered in order to evaluate the accuracy of the numerical discretization adopted. In particular,

we refer the reader to [6] for the linear elasto-acoustic case and to [60] for the non-linear and viscous elasto-acoustic case.

It is important to recall the concepts of verification and validation [54, 59]: verification of a numerical method may be defined as the demonstration of the consistency of the numerical method with the original mathematical–physical problem defined by the controlling equation, constitutive law, and initial and boundary conditions. The quantitative analysis of accuracy should be a part of the verification. Once the numerical method is analyzed and verified for accuracy, it should be validated using observations. In general, the validation may be defined as the demonstration of the capability of the theoretical model (i.e., the mathematical–physical model and its numerical approximation) to predict and reproduce observations. Normally the criteria and the metrics adopted for the verification and the validation phase are different, given the complexity of the physical problem analyzed.

6.1. **Large scale validation-simulation**

For the aforementioned validation step, we first conduct a large scale simulation in the domain Ω_{large}, depicted in Fig. 6, without the fine scaled dam structure.

Simulation parameters. The domain Ω_{large} contains not only the area around the Tahtalı-dam but also the seismic fault location where the considered event originated from (cf. Sec. 4) as well as the locations of ten selected stations of the AFAD network [1], see Fig. 6. The mesh used for this large scale simulation is coarser by a factor of around 13 (measured between two average elements with edge lengths 75 m vs. 1000 m), compared to the dam mesh from Fig. 5, and ignores the dam structure as a detail in order to effectively span a volume of roughly $135 \times 100 \times 35$ km. In order to properly describe the mechanical properties of the area along the Earth's crust, layered materials have been employed, which are assumed to be parallel to the x-y-plane. The adopted mechanical parameters as well as the layer depths used can be found in Tab. 1.

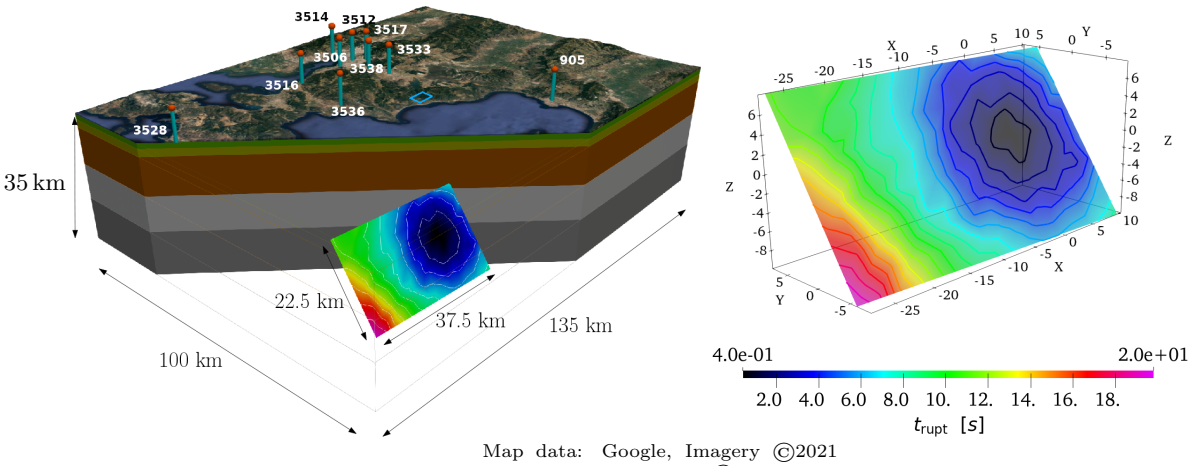

FIGURE 6. Domain for the large scale simulation. Cross-section view with different material layers and the seismic fault plane showing iso-lines of rupture time (see also right figure for a zoom with time scale). The red pins mark the locations of the seismographic measurement stations with their AFAD ID numbers being printed next to them. The blue box is the dam vicinity region from Fig. 2.

The final large-scale mesh contains $N_{\text{el,large}} = 536.105$ elements with polynomial degree of $p = 3$ for the ansatz functions. Time discretization is done with $N_{T,\text{large}} = 40.000$ timesteps of size $\Delta t_{\text{large}} = 10^{-3}$ s.

Mat. par.	**material block**						
parameter	**Layer 1**	**Layer 2**	**Layer 3**	**Layer 4**	**Layer 5**	**Layer 6**	**unit**
depth	$0-0.3$	$0.3-1.7$	$1.7-3.7$	$3.7-13.7$	$13.7-23.2$	$23.2-35.0$	km
ρ	2355	2200	2300	2700	2900	3100	$\frac{\text{kg}}{\text{m}^3}$
v_p	1695	2300	3200	6000	6600	7200	$\frac{\text{m}}{\text{s}}$
v_s	1130	1600	3400	3700	3700	4000	$\frac{\text{m}}{\text{s}}$
Q_s	113	160	340	370	370	400	–

TABLE 1. **Layers and material parameters** used for the large-scale simulations. Data derived and adapted from the original data-set taken from [83]. The quality factor $Q_s = \pi f_0/\zeta$, where f_0 is a frequency reference value here chosen equal to $f_0 = 1\,\text{Hz}$.

Seismic fault data and kinematic source mechanism. The source mechanism is described by means of a set of double-couple moment-tensors $\boldsymbol{M}_i(t), i = 1, 2, \ldots, 160$ distributed along the fault plane, each with its own set of source parameters being slip-vector $\underline{\mathbf{s}}_i$, rupture- and rise-times $t_{\text{rup},i}$ and $t_{\text{rise},i}$ as well as the released moment magnitude $M_{0,i}$. Data have been obtained by [83] on a grid of 10×16 points p_i across the seismic fault plane depicted in Fig. 7. The moment tensors $\boldsymbol{M}_i$ are then associated with the numerical

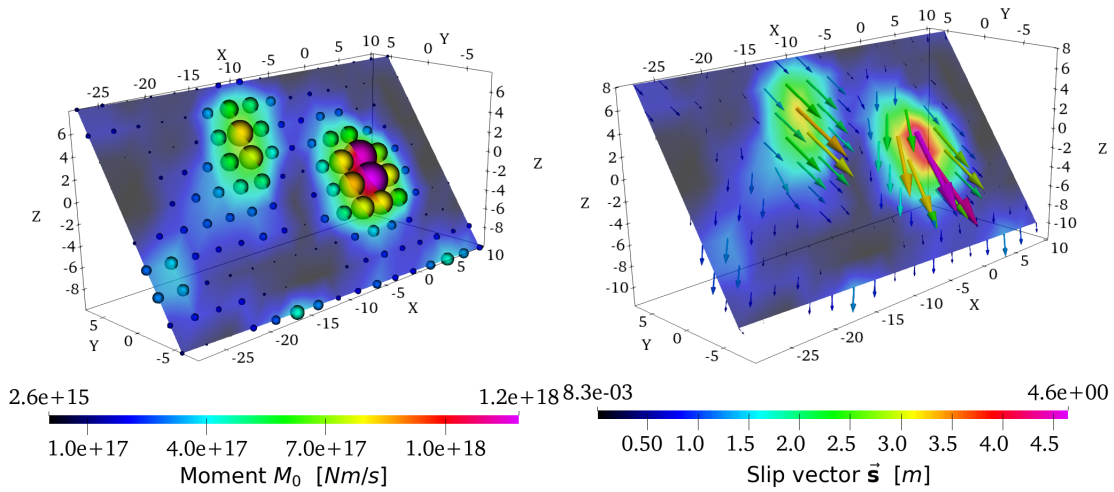

FIGURE 7. Seismic fault plane with coordinates relative to the hypocenter measured in km. **(left)** Seismic moment magnitude M_0, **(right)** slip vector field $\underline{\mathbf{s}}$ (vectors scaled by a factor of 2000), rupture time t_{rupt} can be found in Fig. 6.

quadrature node closest to the data point p_i and can be computed as:

$$\boldsymbol{M}_i(t) = M_{0,i} \cdot m_i\left(\frac{t - t_{\text{rupt},i}}{t_{\text{rise},i}}\right) \cdot \left[(\underline{\mathbf{s}}_i \otimes \underline{\mathbf{n}}) + (\underline{\mathbf{s}}_i \otimes \underline{\mathbf{n}})^\top\right]$$

where $\underline{\mathbf{n}}$ is the fault plane normal computed from the provided data-set, and $m_i(\hat{t})$ is a normalized moment-function monotonically increasing from 0 to 1 that models the moment-release over time at the point p_i respecting the available data of rupture- and rise-time, hence the individual distance from the hypocenter. We refer the reader to [72] for the precise definition of the moment-rate functions $\dot{m}_i$ from which m_i are computed.

Numerical results and validation. In order to assess the maximal (over time) displacement, resp. velocity that is attained at each point $\underline{\mathbf{p}}$ on the computational domain's surface,

we introduce the so called ***g**eometric **m**ean **h**orizontal peak ground displacement* $\mathrm{PGU}_{\mathrm{gmh}}$ and *velocity* $\mathrm{PGV}_{\mathrm{gmh}}$ at point $\underline{\mathbf{p}} \in \Omega$ [16] as quantities of interest:

$$\mathrm{PGU}_{\mathrm{gmh}}(\underline{\mathbf{p}}) := \sqrt{\sup_{t\in(0,T)} \underline{\mathbf{u}}_x(t,\underline{\mathbf{p}}) \cdot \sup_{t\in(0,T)} \underline{\mathbf{u}}_y(t,\underline{\mathbf{p}})}, \quad \mathrm{PGV}_{\mathrm{gmh}}(\underline{\mathbf{p}}) := \sqrt{\sup_{t\in(0,T)} \underline{\mathbf{v}}_x(t,\underline{\mathbf{p}}) \cdot \sup_{t\in(0,T)} \underline{\mathbf{v}}_y(t,\underline{\mathbf{p}})}$$

Fig. 8 then shows the PGV-map of the large scale simulation. The location of the dam, fault and hypocenter as well as the AFAD stations available are reported (see also Fig. 6). The latters are color coded, according to the values retrieved from the observed seismograms. The filtered time-history of simulated and measured seismograms are also listed and compared in the time domain in Fig. 9 and in the frequency domain in Fig. 10. Both for the subset of the six stations closest to the hypocenter.

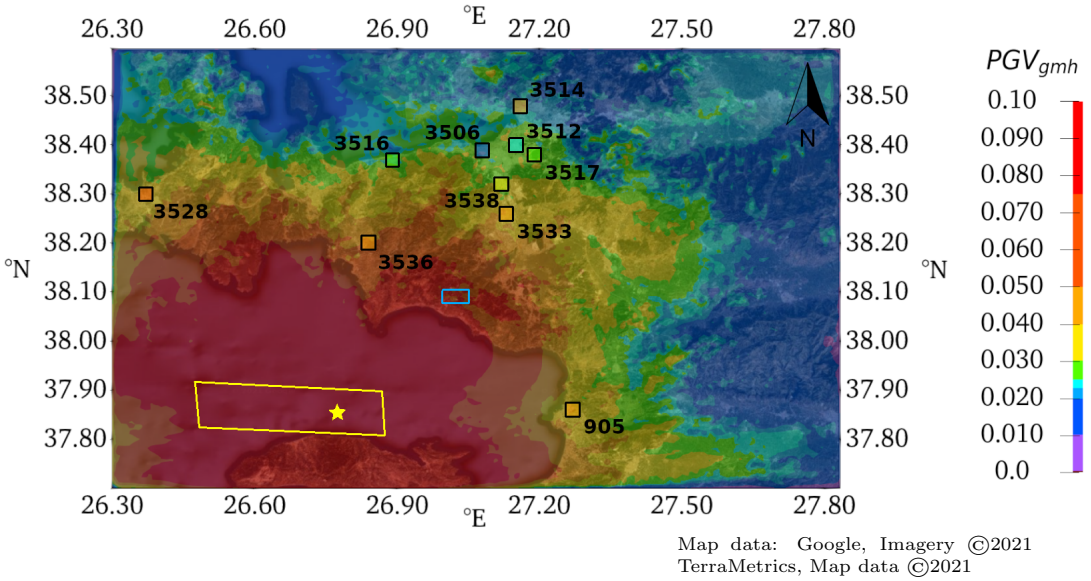

FIGURE 8. PGV-map for the large scale simulation. Color scale is cut-off at $0.1\,\frac{\mathrm{m}}{\mathrm{s}}$. AFAD stations are marked by their ID number, peak ground velocity values of measurements are color coded. The blue rectangle shows the dam vicinity region of Fig. 1, the hypocenter and the fault are marked in yellow. *(original map image overlayed with simulation colormap)*

Given the relatively simplistic model adopted, Fig. 9 shows a satisfactory agreement between the observed and simulated velocities, in terms of arrival time, duration of the signal, phase and amplitude of the waves. The goodness of these results is also confirmed by the PGV map, showed in Fig. 8. Referring to the comparison in terms of Fourier spectra, cf. Fig. 10, it turns out that, in general, there is a satisfactory agreement between simulated and recorded amplitudes for frequencies up to about 1 Hz, although synthetic tends sometimes to underestimate the observed amplitudes.

To give a quantitative measure of the overall performance of the numerical simulation we adopt the Goodness of Fit (GoF) criteria proposed by [3], being this latter widely followed and recognized for this kind of evaluation. For the frequency band of interest (i.e. $0.1 - 1\,\mathrm{Hz}$), a GoF score from 0 to 10 (< 4, poor; $4 - 6$, fair; $6 - 8$, good; ≥ 8, excellent) is estimated on five metrics of interest for engineering purposes, namely: energy duration (ED), Peak Ground Velocity (PGV), Peak Ground Displacement (PGU), Response Spectral (RS) acceleration and Fourier Amplitude Spectrum (FAS). Note that FAS and RS criteria are evaluated considering only the frequencies and structural periods within the range $0.1 - 1\,\mathrm{Hz}$ of validity of the numerical simulations. The GoF scores, computed for each criterion and for the three components of motion, are shown in Fig. 11 for the whole set of ten recording stations considered in Fig. 8. These results confirm that with few exceptions,

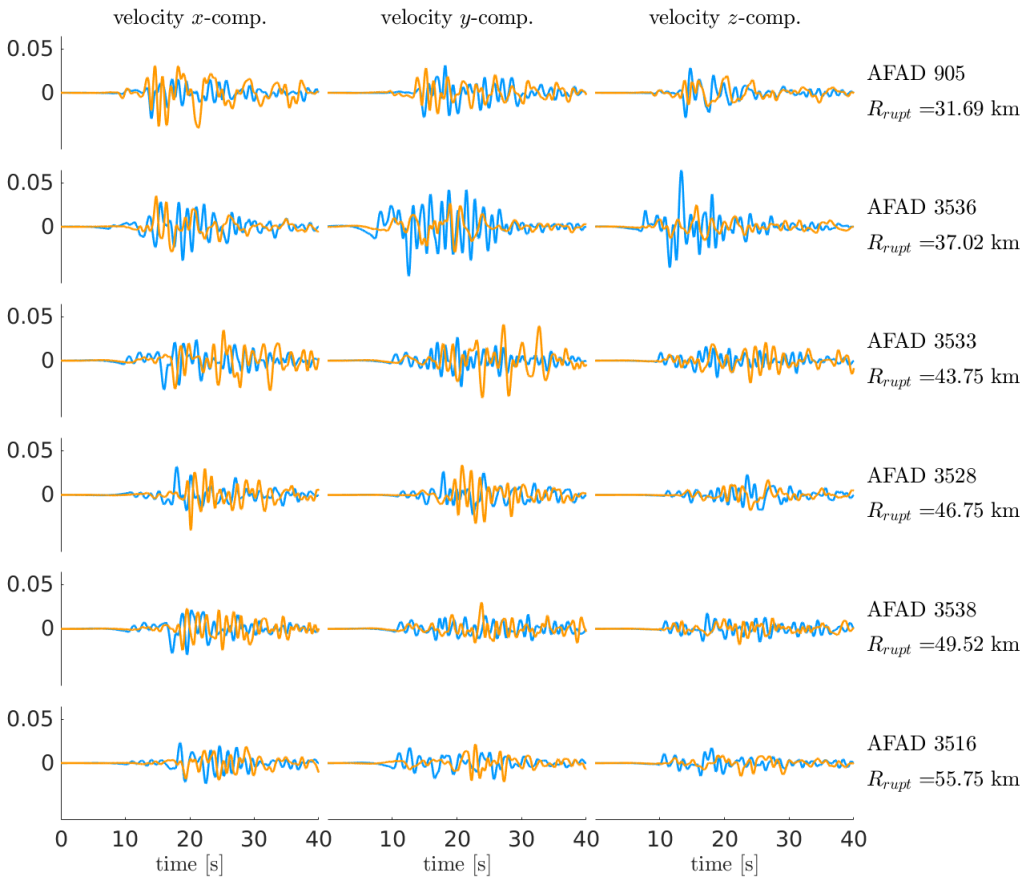

FIGURE 9. **(rows)** Comparison of numerically evaluated velocity seismograms (blue) and records (orange) for the six AFAD-stations closest to the hypocenter. Stations are sorted by increasing R_{rupt} (see label on the right, also for station ID). **(columns)** First column x-component, second y-component, third z-component. All data filtered to $[0.1, 1]$ Hz with 2^{nd} order Butterworth filter.

the numerical model provides predictions that are in overall good agreement (from fair to excellent) with the records. By taking inspiration from [61] we not only compute the average GoF value for each ground motion component but also the average between the components in order to summarize the results into a single final score for each station. Hence, in Fig. 11, we additionally present that score as an overview of the misfit between records and simulated results at territorial scale. We found that for the majority of the stations the agreement between simulations and observations is from fair to good. These results are aligned with those obtain for other, different earthquake scenarios as, e.g., [41, 65].

6.2. Plane-wave excitation using nearby seismogram

Measurement data and source mechanism. For our second numerical simulation, we use input data for the ground motion from recorded measurements. Namely the station AFAD # 3536, located at 38.1968 °N, 26.8384 °E , (cf. Figs. 6, 8) and positioned approximately 30 km from the Tahtalı-dam. In Fig. 9, second row, the x, y and z components $v^{\text{ref}}_{x,y,z}(t)$ (orange lines) of the ground motion velocity $\underline{\mathbf{v}}^{\text{ref}}(t)$ recorded at AFAD # 3536 during the seismic event [1] can be seen. They were deconvolved to a certain depth, since it was observed on the free surface, and subsequently it was adopted as input for the plane wave excitation, following [33]. Therein the equivalent body force

$$\underline{\mathbf{f}} = 2\rho_{\text{e}} v_p \delta(z - z_0) \underline{\mathbf{v}}^{\text{ref}}(t)$$

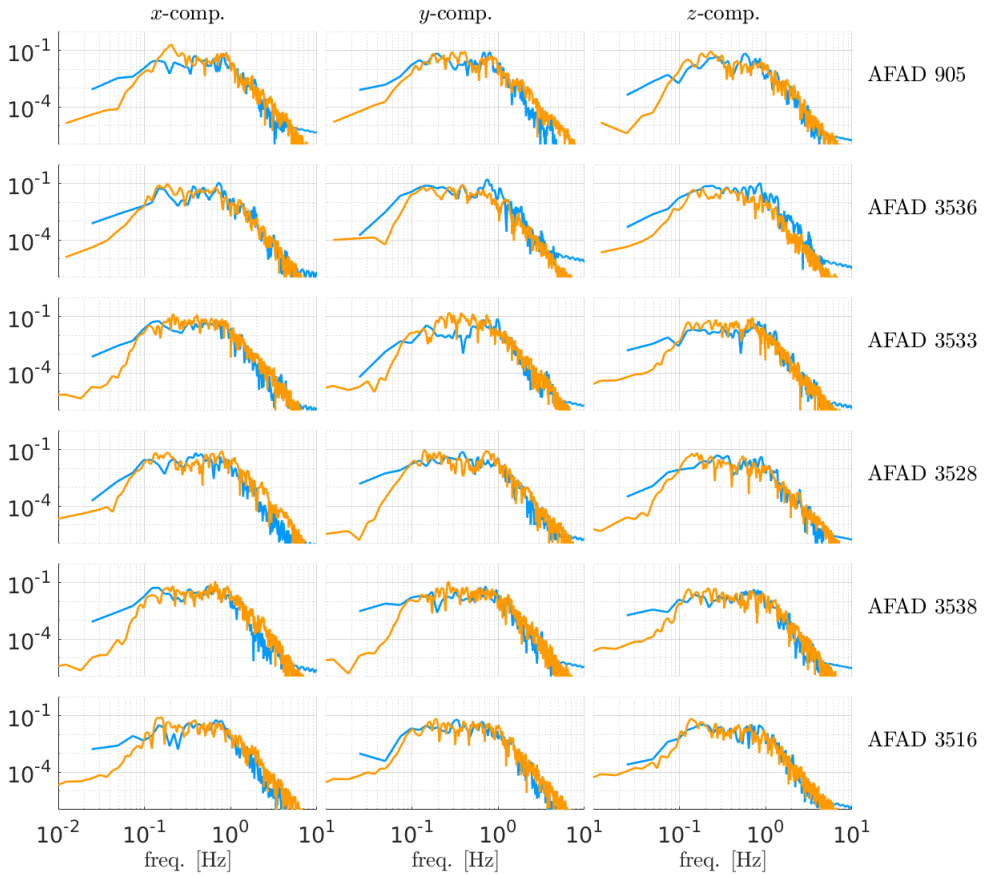

FIGURE 10. Amplitude power spectra of the velocity signals in Fig. 9. Again (blue) are the numerical data, (orange) the filtered measurement data.

is applied on a horizontal plane located at $z = z_0$. The seismic wave generated by it will rise and yields an approximation to the actual ground motion of the event. The realization of this approach is based on an additional layer of same material properties below the bottom surface of the mesh in Fig. 5, right, which has a thickness of only one element and z_0 being its mean depth, in which the body force is applied. This approach is often used in engineering analysis aiming at simulating the so-called "dynamic soil structure interaction" problem (DSSI). In fact, due to scarcity of numerical code capable of taking into account the entire problem (from source-to-site) and/or having only limited computational resources available, the state-of-the-art engineering approach considers, typically, only the region in the immediate proximity to the dam and assumes that at this scale the excitation can be properly approximated by a plane wave [9, 79]. Obviously this approach presents a series of limitations that are even more relevant when, as often happens operationally, the dam is studied in 2D [10].

Simulation parameters. Tab. 2 shows the material parameters used for the different zones of the numerical simulations. Since "in-situ" measured values were not available it was decided to adopt reliable literature values.

The numerical simulation was conducted with $N_T = 10^6$ timesteps of size $\Delta t = 5 \cdot 10^{-5}$ on a spacial grid using $N_{\text{el}} = 18.948$ elements with a polynomial degree of $p = 2$ for the ansatz functions. The DG penalty-parameter was chosen as $\beta = 250$.

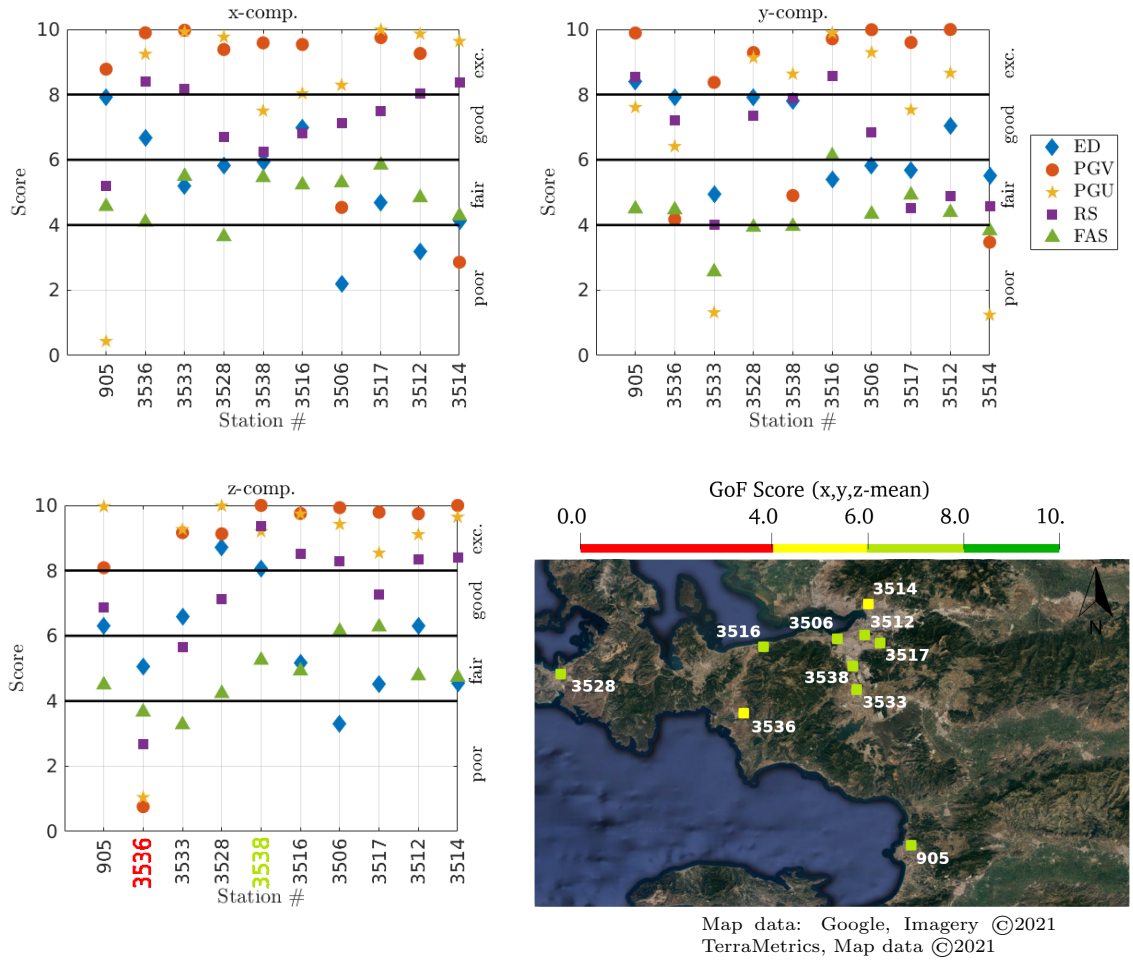

FIGURE 11. Evaluation of Anderson GoF-criteria to assess the similarity of the seismographs in Fig. 9. **(top left, right, bottom left)** Energy duration (ED), peak ground velocity (PGV), peak ground displacement (PGU), response spectrum (RS) and Fourier amplitude spectrum (FAS) evaluated for x, y and z-components at the presented stations. Extreme values marked in red and green: z-comp. of #3536 at ≈ 2.637 (poor) to z-comp. of #3538 at ≈ 8.372 (excellent). **(bottom right)** Station-wise mean of x, y and z component's presented Anderson criteria.

Numerical results. Fig. 12 (top) shows a snapshot of the simulated displacement-field $\underline{\mathbf{u}}$ in the elastic, and acoustic pressure field p_{ac} in the acoustic domain. The bottom row shows a corresponding snapshot of the upcoming source-to-site simulation from Sec. 6.3 which highlights the different scales of magnitude of the simulations. In addition to the time-snapshot picture, we can also employ the time-history of the simulation at certain points of interest (cf. Fig. 14) and again compute peak-ground maps of the conducted simulation, which will also be depicted later in Fig. 15 for a comparative discussion with the results of the full source-to-site simulation. Fig. 14 contains the numerical seismograms of the components of $\underline{\mathbf{v}}$ (oriented orthogonal, parallel and vertical to the dam, compare Fig. 16 for orientation) of the simulation at three distinct locations around the dam. One of them is located on the ground in front of the dam, the other directly on top of the dam and the third at the right dam ambutment. The exact locations of these synthetical seismographs are depicted in Fig. 12 via the red pin-needles. In order to compare the signals with similar frequency content, the signals are again frequency filtered based on a second order Butterworth filter with a frequency-band of $[0.1, 1]$ Hz, eliminating high frequency (numerical) artifacts and measurement oscillations.

Material parameters		**material block**			
type	**parameter**	**Ground**	**Dam**	**Water**	**unit**
all	ρ	2355	2000	998.23	$\frac{\text{kg}}{\text{m}^3}$
elastic	v_p	1695	525	/	$\frac{\text{m}}{\text{s}}$
	v_s	1130	350	/	$\frac{\text{m}}{\text{s}}$
	Q_s	500	500	/	-
acoustic	c	/	/	1500	$\frac{\text{m}}{\text{s}}$
	b	/	/	$6 \cdot 10^{-9}$	$\frac{\text{m}^2}{\text{s}}$

TABLE 2. **Material parameters** used for the numerical simulations. Ground consists of Rock/Limestone and the Dam is mostly modelled as Gravel/Sand material . The quality factor $Q_s = \pi f_0/\zeta$, where f_0 is a frequency reference value here chosen equal to $f_0 = 1\,\text{Hz}$.

Plane wave:

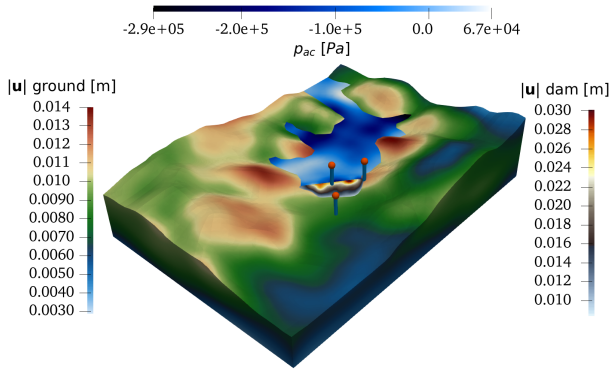

Source-to-site:

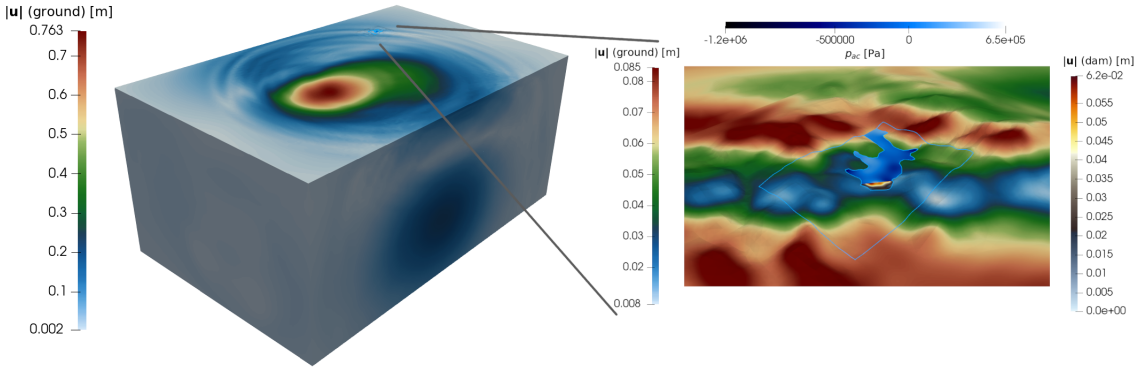

FIGURE 12. Time snapshot of displacement-field in **(top)** plane wave simulation, **(bottom)** source-to-site simulation where in the zoomed in picture the blue frame of the dam-vicinity region Ω is visible. The pin-needles (top picture) show the locations of the synthetic seismographs evaluated in Fig. 14.

6.3. **Full source-to-site simulation**

The final simulation setup consists of a full source-to-site simulation using a domain Ω_{s2s} containing the Tahtalı-dam area as well as the seismic fault just as Ω_{large}. By respecting the

dam-structure, the topography in its vicinity and the presence of water behind the dam, Ω becomes a subset of Ω_{s2s} and hence the original mesh (cf. Fig. 5) a submesh as well. The resulting grid contains multiple length-scales in element size from the larger elements having an edge length in the order of a kilometer to the smaller ones measuring only few meters. The geometry is created by embedding the domain Ω from Fig. 1 on top of a rectangular block of an approximate size of $88 \times 55 \times 40\,\text{km}$. In order to have a smooth top-surface, a transition zone was used, in which the detailed topography of the dam-area gets flattened down to the level $z = 0$ such that it is accurately resolved only in the proximity of the dam. Fig. 13 shows the resulting geometry, which was then meshed with a locally refined mesh consisting out of around 100.000 elements in total. The mesh is also depicted in Fig. 13 and takes advantage of the DG coupling approach by individually meshing the surrounding, transition and core blocks in a not-necessarily matching way, then coupling them together to arrive at a locally refined final mesh. This strategy allows for an easy local grid refinement in the vicinity of the structure while the mesh further away stays relatively coarse. In combination with the elaborate fine structure mesh (cf. Fig. 5), this keeps the overall amount of elements relatively low while retaining well behaved element shapes. These blockwise meshes also easily allow to assign different polynomial degrees p_i to the individual blocks.

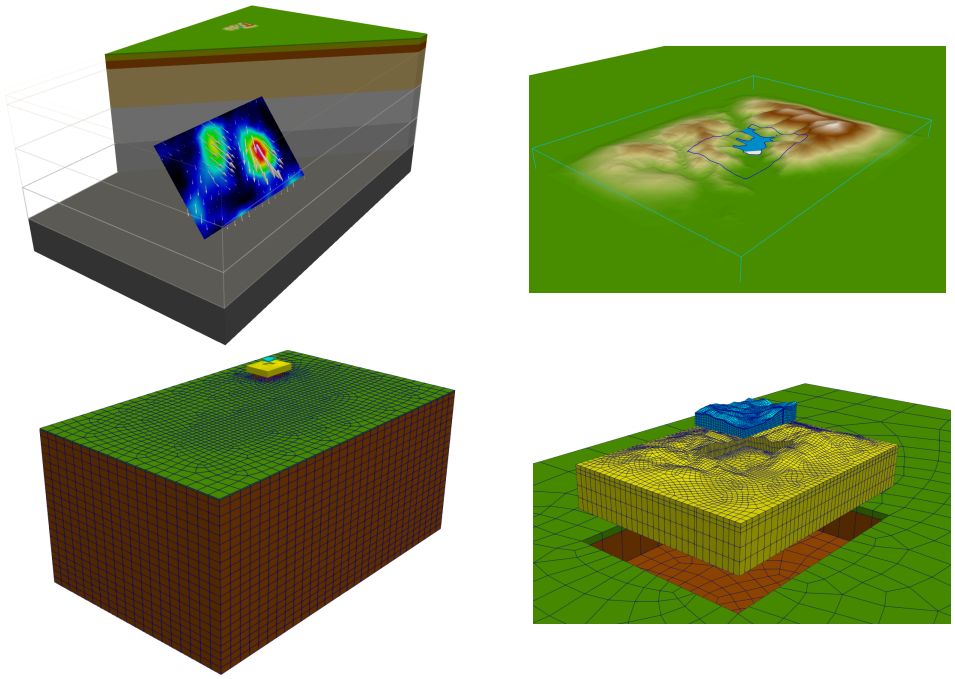

FIGURE 13. **(top left)** Full source-to-site domain in cross-section view with different material layers as well as the seismic fault plane and slip distribution (cf. Fig. 7) visible. **(top right)** Zoom into the region of the dam. The dark blue lines mark Ω as a sub-region with resolved topography (cf. Fig. 1), the light blue frame marks the transition zone. **(bottom left)** Hexahedral mesh of the complete source-to-site domain Ω_{s2s}. The brown surfaces carry absorbing boundary conditions. **(bottom right)** Zoom into the region of the dam. The transition zone (yellow) and the core blocks (blue) with their individual meshes are elevated here in order to see the (non matching) DG interfaces between each of them.

As within the large scale simulation, also the source-to-site simulation adopts the layered materials, presented in Tab. 1, and the seismic fault rupture mechanism and slip distribution as previously described (see Fig. 7). Both the layers and the location of the fault plane w.r.t. the dam structure are depicted in Fig. 13.

The simulation was conducted using a polynomial degree of $p = 2$ in the core- (water, dam, dam-vicinity) and the transition-blocks and $p = 3$ in the outer layers and 920.000 timesteps of size $5 \cdot 10^{-5}$. Fig. 14 shows the comparison between the synthetic seismograms computed on (i) ground, (ii) crest and (iii) abutment of the dam, as obtained with the source-to-site simulation (present paragraph) and with the plane-wave approach (previous simulation from Sec. 6.2). Note that the orthogonal, parallel and up-down synthetic time histories of displacement and velocity are considered; the directions are w.r.t to the orientation of the dam (see Fig. 16 for the orientations). Furthermore, Fig. 15 compares the respective peak ground maps of the two simulations: on the left-hand side the plane-wave model and, on the right-hand side, the source-to-site model.

Finally Fig. 16 shows the maximum orthogonal displacement along the dam over different cross sections. The quantity $u_{\perp,\max} := \sup_{t\in(0,T)} |\underline{u}_\perp|$, is presented along the four sections depicted in the nearby sketch.

6.4. **Discussion of results**

The results obtained so far deserve some comments, since at first glance the large difference in terms of displacement and velocity, experienced by the Tahtalı dam adopting the plane-wave model and the source-to-site one, is evident. It is worth noting that the Tahtalı dam and station AFAD #3536 are located both at about 30 km away from the hypocenter, therefore in the so-called near-field region, however the azimuthal difference is around 30°. Radiation pattern [51] and rupture directivity [36, 71] effects might play a significant role in this region and therefore the large variability observed can be at least partially explained by these effects. Thanks to the validations accomplished (see Sec. 6.1) we are confident about the reliability of our simulations up to 1 Hz, and therefore we consider the source-to-site simulation not only a state-of-the-art modelling approach but also the more reliable one, in terms of the excitation experienced by the Tahtalı dam during the seismic event analysed in this study.

Regarding the magnitude of the ground motion observed, it is important to mention that nor the plane-wave model neither the source-to-site simulation seems to be capable to produce shaking levels that might endanger the dam itself. In fact, according to the exhaustive literature examined, both based on numerical studies [2, 9, 10, 79] or empirical observations [66, 73, 84–86, 89] the shaking level simulated seems to be incapable of producing significant damages to the infrastructure. This findings are coherent with the empirical observation as witnessed by the reconnaissance team [23, 63].

Furthermore, as highlighted by [66], there are more than 59,000 large dams worldwide, and more than three quarters employ earthfill and rockfill construction [43]. Several large earthquakes were recorded at embankment dams, for example, during the 2008 Wenchuan earthquake (M_w 7.9), the 156-meter-high Zipingpu concrete-faced rockfill dam (CFRD) was damaged partially without any collapse or freeboard deficiency. The dam, designed with peak ground acceleration of $0.26\,g$ at its foundation bedrock, recorded data exceeding $0.5\,g$ [50, 90]. During the 2011 Tohoku earthquake (M_w 9.0), the Aratozawa rockfill dam experienced a PGA of $1.04\,g$ at foundation rock and in spite of that the safety was not endangered [47]. According to [86] most modern embankment dams are capable of withstanding significant seismic shaking with no detrimental consequences in the past events. This leads to the conclusion that further analyses are necessary to predict more accurately which seismic event may involve a dangerous shaking for the structural safety of the building during earthquakes. The full source-to-site simulation provides an example of what our tool is capable of and must be properly exploited in the future.

7. **Conclusion and Outlook**

Starting from a general mathematical description of a coupled elasto-acoustic wave propagation problem, we have studied a realistic earthquake event for which we have analyzed

Displacement:

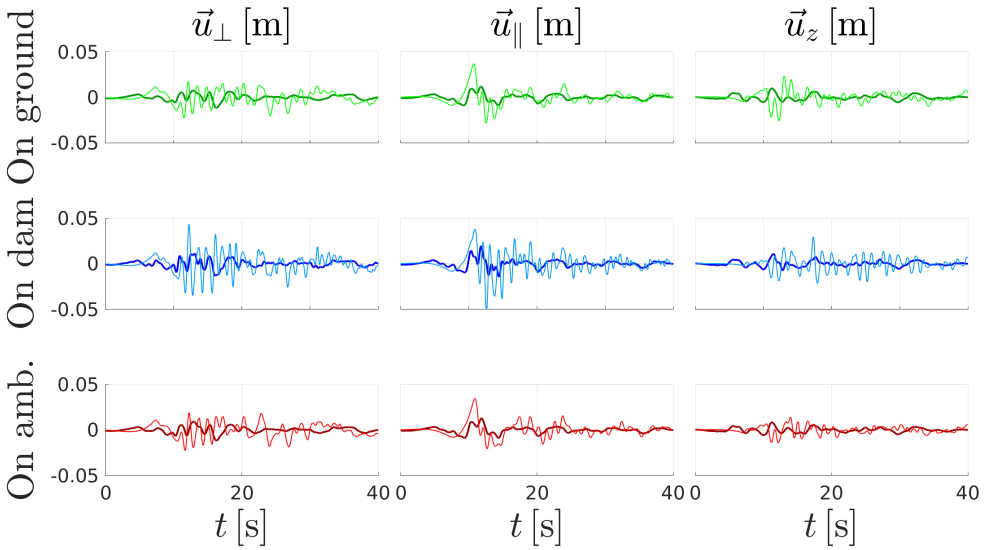

Velocity:

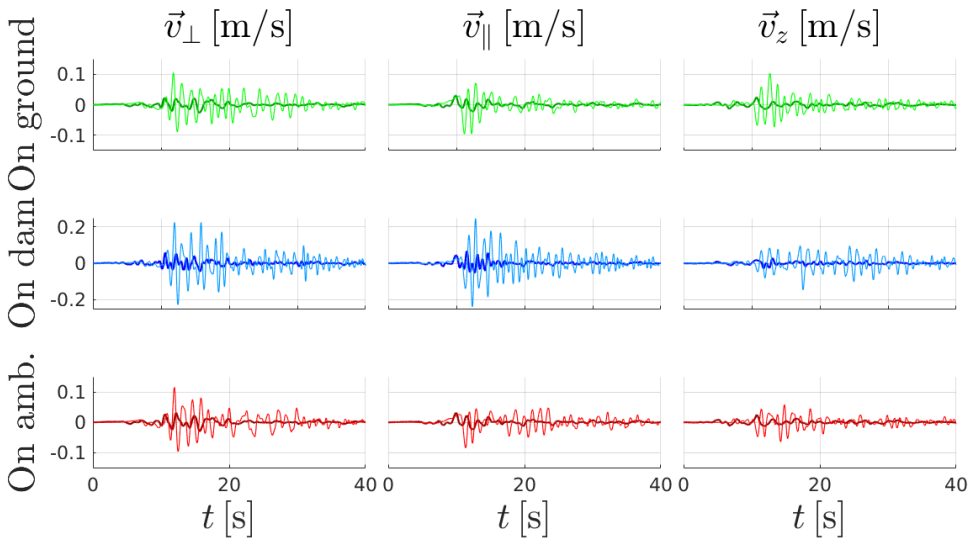

FIGURE 14. Comparison of synthetical displacement **(top block)** and velocity **(bottom block)** seismograms between plain wave **(bold lines)** and source-to-site simulation **(thin lines)**. Each quantity is decomposed into dam-orthogonal, -parallel and vertical components and is compared at three physical locations (ground, dam-crest and ambutment), see Fig. 12 for locations. All data again filtered to $[0.1, 1]$ Hz with 2^{nd} order Butterworth filter.

the seismic response of a dam. The computational model comprises the actual topography around the dam, its reservoir lake as well as a simplified one dimensional crustal model. Regarding this last aspect, it is worth mentioning that, by taking into account a more accurate seismic tomography it will be possible to improve the computational model so far adopted. Eventual taking into account local soil heterogeneities in the proximity of the dam, as well as a more detailed characterisation of the material of the dam will also contribute to that. The generation and analysis of the latter will be the subject of future studies. Due to the comparably small ground motions recorded during the seismic event, we considered for the solid portion of the domain a relatively simple but rather realistic,

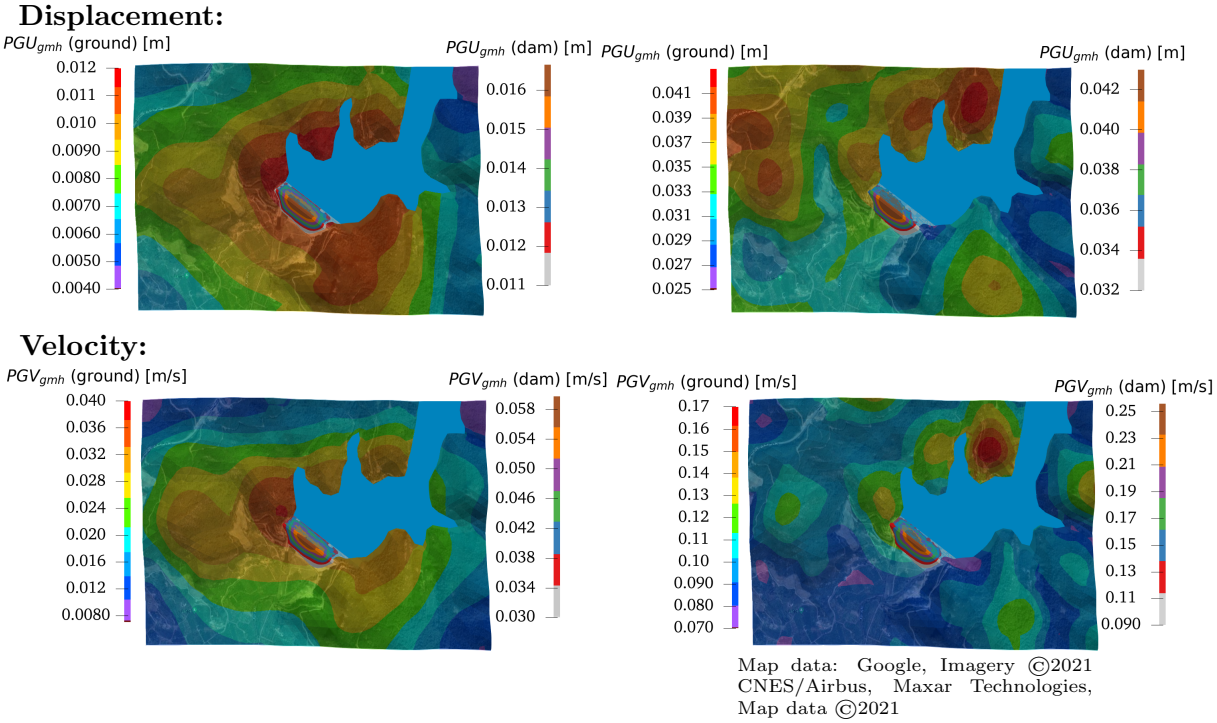

FIGURE 15. Comparison of **(top row)** PGU and **(bottom row)** PGV maps between the **(left column)** plain wave simulation of Sec. 6.2 and **(right column)** the full source-to-site simulation both in the vicinity region of the dam. *(original map image overlayed with simulation colormap)*

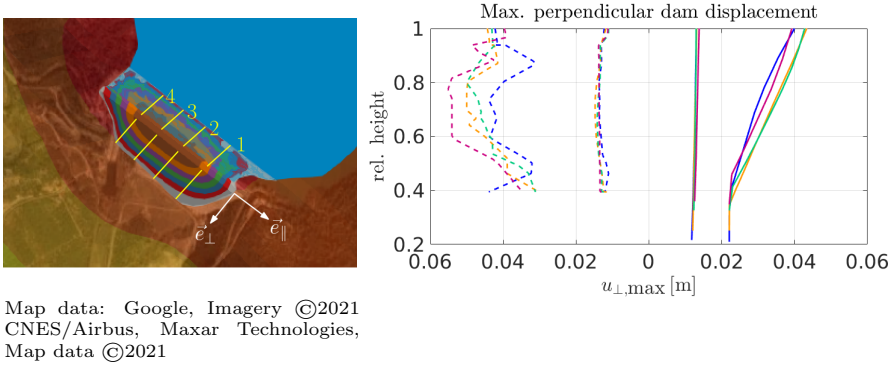

FIGURE 16. Evaluation of maximal orthogonal dam displacement $u_{\perp,\max}$ across four slices depicted in **(left)** image *(original map image overlayed with simulation colormap)*. The image also shows the unit vectors in $\underline{e}_\perp$ in orthogonal and $\underline{e}_\parallel$ in parallel direction. Results show the **(middle strands)** plain wave simulation and **(outer strands)** source-to-site simulation with dashed lines for the reservoir side, continuous lines for the free side of the dam. (blue) slice 1, (orange) slice 2, (green) slice 3, (red) slice 4.

visco-elastodynamic model; this latter should be enhanced to a plastic one, for an analysis focusing on individual features of the dam, especially in case of higher ground motions (i.e.: local events in the immediate proxmity of the dam). Having said that and precisely due to the model's simplicity, the conducted simulations turn out to be in good agreement with the recorded seismograms and are capable to produce reliable results in the frequency range of up to 1 Hz at manageable computational costs. This resulted in a flexible and robust computational numerical model.

The final, state-of-the-art, fully-coupled source-to-site simulation makes use of local and independent grid-refinements, treated with a discontinuous Galerkin approach, in order to accurately resolve the multiple length scales adopted in the model. With one single simulation the source-to-site approach allows to obtain numerical data at site, such as maximum displacement or peak velocities, that can be used for engineering purposes. The source-to-site model presented here could be used for a better assessment of the seismic risk associated to the dam and its nearby region by investigating the ground motion wave field generated by (i) different earthquake realizations along the Kaystrios fault and/or (ii) different seismogenic faults. Due to its generality the model can be also easily employed and further adapted for the seismic risk assessment in other active regions and for different structures with additional uncertainties being considered.

Acknowledgements

M. Muhr and B. Wohlmuth acknowledge the financial support provided by the Deutsche Forschungsgemeinschaft under the grant number WO 671/11-1. I. Mazzieri is member of the INdAM Research group GNCS and this work is partially funded by INdAM-GNCS.

References

[1] AFAD, Seismographic measurement station records, Retrieval date 01.06.2021. https://tadas.afad.gov.tr/event-detail/11995.

[2] A. Anastasiadis, N. Klimis, K. Makra, and B. Margaris. On seismic behavior of a 130m high rockfill dam: An integrated approach. *Proceedings of the 13th World Conference on Earthquake Engineering, Vancouver, BC, Canada*, pages 1–6, 08 2004.

[3] J. G. Anderson. Quantitative measure of the goodness-of-fit of synthetic seismograms. In *Proceedings of the 13th World Conference on Earthquake Engineering*, volume 243, pages 1–14. 13 WCEE Secretariat, International Association for Earthquake Engineering, 2004.

[4] P. Antonietti, I. Mazzieri, L. Melas, R. Paolucci, A. Quarteroni, C. Smerzini, and M. Stupazzini. Three-dimensional physics-based earthquake ground motion simulations for seismic risk assessment in densely populated urban areas. *Mathematics in Engineering*, 3:1–31, 2021.

[5] P. F. Antonietti, F. Bonaldi, and I. Mazzieri. A high-order discontinuous Galerkin approach to the elasto-acoustic problem. *Computer Methods in Applied Mechanics and Engineering*, 358:112634, 2020.

[6] P. F. Antonietti, F. Bonaldi, and I. Mazzieri. Simulation of three-dimensional elastoacoustic wave propagation based on a discontinuous Galerkin spectral element method. *International Journal for Numerical Methods in Engineering*, 121(10):2206–2226, 2020.

[7] P. F. Antonietti, A. Ferroni, I. Mazzieri, R. Paolucci, A. Quarteroni, C. Smerzini, and M. Stupazzini. Numerical modeling of seismic waves by discontinuous spectral element methods. *ESAIM: Proceedings and Surveys*, 61:1–37, 2018.

[8] P. F. Antonietti, I. Mazzieri, A. Quarteroni, and F. Rapetti. Non-conforming high order approximations of the elastodynamics equation. *Computer Methods in Applied Mechanics and Engineering*, 209:212–238, 2012.

[9] A. Bayraktar, A. Altunişik, B. Sevim, M. Kartal, T. Türker, and Y. Bilici. Comparison of near- and far-fault ground motion effect on the nonlinear response of dam–reservoir–foundation systems. *Nonlinear Dynamics*, 58:655–673, 12 2009.

[10] A. Bayraktar, M. Kartal, and H. Başağa. Reservoir water effects on earthquake performance evaluation of Torul concrete-faced rockfill dam. *Water Science and Engineering*, 2, 03 2009.

[11] J. Bielak, O. Ghattas, and E. Kim. Parallel octree-based finite element method for large-scale earthquake ground motion simulation. *Computer Modeling in Engineering and Sciences*, 10(2):99–112, 2005.

[12] J. Bielak, R. W. Graves, K. B. Olsen, R. Taborda, L. Ramírez-Guzmán, S. M. Day, G. P. Ely, D. Roten, T. H. Jordan, P. J. Maechling, et al. The ShakeOut earthquake scenario: Verification of three simulation sets. *Geophys. J. Int.*, 180(1):375–404, 2010.

[13] T. D. Blacker, S. J. Owen, M. L. Staten, W. R. Quadros, B. Hanks, B. W. Clark, R. J. Meyers, C. Ernst, K. Merkley, R. Morris, C. McBride, C. Stimpson, M. Plooster, and S. Showman. Cubit geometry and mesh generation toolkit 15.2 user documentation. 5 2016. Sandia National Lab.(SNL-NM), Albuquerque, NM (United States).

[14] T. D. Blacker and M. B. Stephenson. Paving: A new approach to automated quadrilateral mesh generation. *International journal for numerical methods in engineering*, 32(4):811–847, 1991.

[15] T. D. Blacker, M. B. Stephenson, and S. Canann. Analysis automation with paving: a new quadrilateral meshing technique. *Advances in engineering software and workstations*, 13(5-6):332–337, 1991.

[16] D. Boore and J. Bommer. Processing of strong-motion accelerograms: Needs, options and consequences. *Soil Dynamics and Earthquake Engineering*, 25:93–115, 02 2005.
[17] A. Breuer, A. Heinecke, and Y. Cui. EDGE: Extreme scale fused seismic simulations with the discontinuous Galerkin method. In *International Supercomputing Conference*, pages 41–60. Springer, 2017.
[18] A. Breuer, A. Heinecke, S. Rettenberger, M. Bader, A. Gabriel, and C. Pelties. Sustained petascale performance of seismic simulations with SeisSol on SuperMUC. In J. M. Kunkel, T. Ludwig, and H. W. Meuer, editors, *Supercomputing*, pages 1–18. Springer International Publishing, 2014.
[19] L. S. Burks and J. W. Baker. Validation of Ground-Motion Simulations through Simple Proxies for the Response of Engineered Systems. *Bulletin of the Seismological Society of America*, 104(4):1930–1946, 2014.
[20] R. Caputo, A. Chatzipetros, S. Pavlides, and S. Sboras. The greek database of seismogenic sources (gredass): state-of-the-art for northern greece. *Annals of Geophysics*, 55:859–894, 2013.
[21] E. Casarotti, M. Stupazzini, S. J. Lee, D. Komatitsch, A. Piersanti, and J. Tromp. Cubit and seismic wave propagation based upon the spectral-element method: An advanced unstructured mesher for complex 3d geological media. In *Proceedings of the 16th International Meshing Roundtable*, pages 579–597. Springer, 2008.
[22] C. Cauzzi, S. Custódio, C. P. Evangelidis, G. Lanzano, L. Luzi, L. Ottemöller, H. Pedersen, and R. Sleeman. Preface to the Focus Section on European Seismic Networks and Associated Services and Products. *Seismological Research Letters*, 92(3):1483–1490, 2021.
[23] K. Çetin, G. Mylonakis, A. Sextos, J. Stewart, and T. Irmak. Seismological and engineering effects of the M 7.0 Samos Island (Aegean sea) earthquake. Technical report, 2020.
[24] E. Chaljub, E. Maufroy, P. Moczo, J. Kristek, F. Hollender, P.-Y. Bard, E. Priolo, P. Klin, F. de Martin, Z. Zhang, W. Zhang, and X. Chen. 3-D numerical simulations of earthquake ground motion in sedimentary basins: testing accuracy through stringent models. *Geophys. J. Int.*, 201(1):90–111, 2015.
[25] J. D. De Basabe, M. K. Sen, and M. F. Wheeler. The interior penalty discontinuous Galerkin method for elastic wave propagation: grid dispersion. *Geophysical Journal International*, 175(1):83–93, 2008.
[26] D. Dempsey, J. D. Eccles, J. Huang, S. Jeong, E. Nicolin, A. Stolte, L. Wotherspoon, and B. A. Bradley. Ground motion simulation of hypothetical earthquakes in the upper North Island of New Zealand. *New Zealand Journal of Geology and Geophysics*, 64(4):570–588, 2021.
[27] Disaster And Emergency Management Presidency - Turkish Accelerometric Database and Analysis System, Retrieval date 07.10.2021. https://tadas.afad.gov.tr/.
[28] M. Dumbser, M. Käser, and E. F. Toro. An arbitrary high-order Discontinuous Galerkin method for elastic waves on unstructured meshes-V. Local time stepping and p-adaptivity. *Geophys. J. Int.*, 171(2):695–717, 2007.
[29] K. Duru, L. Rannabauer, A.-A. Gabriel, G. Kreiss, and M. Bader. A stable discontinuous Galerkin method for the perfectly matched layer for elastodynamics in first order form. *Numerische Mathematik*, 146(4):729–782, 2020.
[30] Earthquake Source Model Database, Retrieval date 01.06.2021. http://equake-rc.info/srcmod/.
[31] B. Engquist and A. Majda. Absorbing boundary conditions for numerical simulation of waves. *Proceedings of the National Academy of Sciences*, 74(5):1765–1766, 1977.
[32] L. Evangelista, S. Del Gaudio, C. Smerzini, A. d'Onofrio, G. Festa, I. Iervolino, L. Landolfi, R. Paolucci, A. Santo, and F. Silvestri. Physics-based seismic input for engineering applications: a case study in the Aterno river valley, Central Italy. *Bulletin of Earthquake Engineering*, 15(7):2645–2671, 2017.
[33] E. Faccioli, F. Maggio, R. Paolucci, and A. Quarteroni. 2d and 3d elastic wave propagation by a pseudo-spectral domain decomposition method. *Journal of seismology*, 1(3):237–251, 1997.
[34] A. Ferroni, P. F. Antonietti, I. Mazzieri, and A. Quarteroni. Dispersion-dissipation analysis of 3-D continuous and discontinuous spectral element methods for the elastodynamics equation. *Geophys. J. Int.*, 211:1554–1574, 2017.
[35] B. Flemisch, M. Kaltenbacher, and B. I. Wohlmuth. Elasto–acoustic and acoustic–acoustic coupling on non-matching grids. *International Journal for Numerical Methods in Engineering*, 67(13):1791–1810, 2006.
[36] Y. Fukushima, G. Ichinose, P. Somerville, and K. Koketsu. Characterizing near-field rupture directivity effects at low to intermediate frequencies. *AGU Fall Meeting Abstracts*, 12 2003.
[37] E. Fukuyama, R. Ando, C. Hashimoto, S. Aoi, and M. Matsu'ura. A physics-based simulation of the 2003 Tokachi-oki, Japan, earthquake to predict strong ground motions. *Bulletin of the Seismological Society of America*, 99(6):3150–3171, 2009.
[38] P. Galvez, J.-P. Ampuero, L. A. Dalguer, S. N. Somala, and T. Nissen-Meyer. Dynamic earthquake rupture modelled with an unstructured 3-D spectral element method applied to the 2011 M 9 Tohoku earthquake. *Geophys. J. Int.*, 198(2):1222–1240, 2014.
[39] Google Maps, Retrieval date 24.03.2021, Search term: Tahtali Dam. https://www.google.com/maps/place/Keler,+Tahtal%C4%B1-Talsperre,+35471+Menderes%2F%C4%B0zmir,+T%C3%

BCrkei/@38.0877507,27.0359917,2413m/data=!3m1!1e3!4m5!3m4!1s0x14bbf9719bd48b7d:0xbaea9fc6a5837e1!8m2!3d38.0884!4d27.0417, Imagery ©2021 CNES/Airbus, Maxar Technologies, Map data ©2021.

[40] E. Guidoboni, A. Comastri, and G. Traina. *Catalogue of ancient earthquakes in the Mediterranean area up to the 10th century (Vol. 1)*. SGA, Istituto nazionale di geofisica Rome, 1994.

[41] R. Guidotti, M. Stupazzini, C. Smerzini, R. Paolucci, and P. Ramieri. Numerical Study on the Role of Basin Geometry and Kinematic Seismic Source in 3D Ground Motion Simulation of the 22 February 2011 Mw 6.2 Christchurch Earthquake. *Seismological Research Letters*, 82(6):767–782, 2011.

[42] E. Hairer, C. Lubich, and G. Wanner. Geometric numerical integration illustrated by the Störmer–Verlet method. *Acta numerica*, 12:399–450, 2003.

[43] ICOLD. World register of dams, International Commission on large dams, 2020. http://www.icold-cigb.net/GB/world_register/general_synthesis.asp.

[44] M. Infantino, I. Mazzieri, A. G. Özcebe, R. Paolucci, and M. Stupazzini. 3d physics-based numerical simulations of ground motion in Istanbul from earthquakes along the Marmara segment of the North Anatolian Fault. *Bulletin of the Seismological Society of America*, 110(5):2559–2576, 2020.

[45] A. Iwaki, T. Maeda, N. Morikawa, H. Miyake, and H. Fujiwara. Validation of the recipe for broadband ground-motion simulations of japanese crustal earthquakes. *Bulletin of the Seismological Society of America*, 106:2214–2232, 2016.

[46] A. Jarvis, H. Reuter, A. Nelson, and E. Guevara. Hole-filled seamless srtm data v4, international centre for tropical agriculture (ciat), available from https://srtm.csi.cgiar.org. 2008.

[47] JCOLD. Acceleration records on dams and foundations no. 3, Japan commission on large dams, Tokyo, Japan. 2014.

[48] B. Kato and G. Wang. Regional seismic responses of shallow basins incorporating site-city interaction analyses on high-rise building clusters. *Earthquake Engineering & Structural Dynamics*, 50(1):214–236, 2021.

[49] D. Komatitsch, Q. Liu, J. Tromp, P. Suss, C. Stidham, and J. H. Shaw. Simulations of ground motion in the Los Angeles basin based upon the spectral-element method. *Bulletin of the Seismological Society of America*, 94(1):187–206, 2004.

[50] X.-J. Kong, Y. Zhou, B. Xu, and D.-G. Zou. Analysis on seismic failure mechanism of Zipingpu dam and several reflections of aseismic design for high rock-fill dam. *Earth and Space*, page 3177–3189, 2010.

[51] S. R. Kotha, F. Cotton, and D. Bindi. Empirical models of shear-wave radiation pattern derived from large datasets of ground-shaking observations. *Scientific Reports*, 01 2019.

[52] R. L. Lee, B. A. Bradley, P. J. Stafford, R. W. Graves, and A. Rodriguez-Marek. Hybrid broadband ground motion simulation validation of small magnitude earthquakes in Canterbury, New Zealand. *Earthquake Spectra*, 36(2):673–699, 2020.

[53] G. W. F. Lorenzo, M. P. S. d'Avila, A. Deschamps, E. Bertrand, E. D. Mercerat, L. Foundotos, and F. Courboulex. Numerical and empirical simulation of linear elastic seismic response of a building: The case of Nice prefecture. *Earthquake Spectra*, 34(1):169–196, 2018.

[54] E. Maufroy, E. Chaljub, F. Hollender, J. Kristek, P. Moczo, P. Klin, E. Priolo, A. Iwaki, T. Iwata, V. Etienne, F. De Martin, N. Theodoulidis, M. Manakou, C. Guyonnet-Benaize, K. Pitilakis, and P.-Y. Bard. Earthquake ground motion in the mygdonian basin, greece: The e2vp verification and validation of 3d numerical simulation up to 4 hz. *Bulletin of the Seismological Society of America*, 105, 06 2015.

[55] I. Mazzieri, M. Stupazzini, R. Guidotti, and C. Smerzini. SPEED: SPectral Elements in Elastodynamics with discontinuous Galerkin: A non-conforming approach for 3d multi-scale problems. *International Journal for Numerical Methods in Engineering*, 95(12):991–1010, 2013.

[56] D. McCallen, A. Petersson, A. Rodgers, A. Pitarka, M. Miah, F. Petrone, B. Sjogreen, N. Abrahamson, and H. Tang. EQSIM—a multidisciplinary framework for fault-to-structure earthquake simulations on exascale computers part i: Computational models and workflow. *Earthquake Spectra*, 37(2):707–735, 2021.

[57] L. Melas. Three-dimensional physics-based numerical simulations of earthquake ground motion for advanced seismic risk assessment. 2021. http://hdl.handle.net/10589/177110.

[58] L. Mingwu, S. E. Benzley, G. Sjaardema, and T. Tautges. A multiple source and target sweeping method for generating all hexahedral finite element meshes. In *Proceedings, 5th International Meshing Roundtable*, volume 96, pages 217–225. Citeseer, 1996.

[59] P. Moczo, J. Kristek, and M. Galis. The finite-difference modelling of earthquake motions: Waves and ruptures. 2014.

[60] M. Muhr, V. Nikolić, and B. Wohlmuth. A discontinuous Galerkin coupling for nonlinear elasto-acoustics. *arXiv preprint arXiv:2102.04311*, 2021.

[61] K. B. Olsen and J. E. Mayhew. Goodness-of-fit Criteria for Broadband Synthetic Seismograms, with Application to the 2008 Mw 5.4 Chino Hills, California, Earthquake. *Seismological Research Letters*, 81(5):715–723, 2010.

[62] S. J. Owen, J. A. Brown, C. D. Ernst, H. Lim, and K. N. Long. Hexahedral mesh generation for computational materials modeling. *Procedia engineering*, 203:167–179, 2017.
[63] A. A. Özacar, Z. Gülerce, E. Sopacı, A. Askan, A. Altındal, G. Can, . . . , and A. Caner. The october 30, 2020 İzmir-Seferihisar Offshore (Samos) earthquake Mw=6.6 reconnaissance observations and findings. Technical report, 2020. Report No: METU/EERC 2020-03.
[64] R. Paolucci, I. Mazzieri, G. Piunno, C. Smerzini, M. Vanini, and A. Özcebe. Earthquake ground motion modeling of induced seismicity in the Groningen gas field. *Earthquake Engineering & Structural Dynamics*, 50(1):135–154, 2021.
[65] R. Paolucci, I. Mazzieri, and C. Smerzini. Anatomy of strong ground motion: near-source records and three-dimensional physics-based numerical simulations of the Mw 6.0 2012 May 29 Po Plain earthquake, Italy. *Geophys. J. Int.*, 203(3):2001–2020.
[66] D. Park and T. Kishida. Seismic response of embankment dams based on recorded strong-motion data in Japan. *Earthquake Spectra*, 35, 11 2018.
[67] C. Pelties, J. Puente, J.-P. Ampuero, G. Brietzke, and M. Käser. Three-dimensional dynamic rupture simulation with a high-order discontinuous Galerkin method on unstructured tetrahedral meshes. *J. Geophys. Res. Solid Earth*, 117(B2), 2012.
[68] N. A. Petersson and B. Sjögreen. High Order Accurate Finite Difference Modeling of Seismo-Acoustic Wave Propagation in a Moving Atmosphere and a Heterogeneous Earth Model Coupled Across a Realistic Topography. *J. Sci. Comput.*, 74(1):209–323, 2018.
[69] A. Pitarka, A. Akinci, P. De Gori, and M. Buttinelli. Deterministic 3D Ground-Motion Simulations (0–5 Hz) and Surface Topography Effects of the 30 October 2016 Mw 6.5 Norcia, Italy, Earthquake. *Bulletin of the Seismological Society of America*, 2021.
[70] GEBCO Compilation Group (2020). Gebco 2020 grid (doi:10.5285/a29c5465-b138-234d-e053-6c86abc040b9).
[71] J. Ripperger, P. Mai, and J. P. Ampuero. Variability of near-field ground motion from dynamic earthquake rupture simulations. *Bulletin of the Seismological Society of America*, 98, 06 2008.
[72] J. Schmedes, R. J. Archuleta, and D. Lavallée. A kinematic rupture model generator incorporating spatial interdependency of earthquake source parameters. *Geophys. J. Int.*, 192(3):1116–1131, 2013.
[73] H. Seed, F. Makdisi, and P. de Alba. Performance of dams during earthquakes. *Journal of the Geotechnical Engineering Division*, 992, 1978.
[74] I. Shevchenko, M. Kaltenbacher, and B. Wohlmuth. A multi-time stepping integration method for the ultrasound heating problem. *ZAMM-Journal of Applied Mathematics and Mechanics/Zeitschrift für Angewandte Mathematik und Mechanik*, 92(11-12):869–881, 2012.
[75] I. Shevchenko and B. Wohlmuth. Self-adapting absorbing boundary conditions for the wave equation. *Wave motion*, 49(4):461–473, 2012.
[76] R. Stacey. Improved transparent boundary formulations for the elastic-wave equation. *Bulletin of the Seismological Society of America*, 78(6):2089–2097, 1988.
[77] M. Stupazzini, R. Paolucci, and H. Igel. Near-fault earthquake ground-motion simulation in the Grenoble valley by a high-performance spectral element code. *Bulletin of the Seismological Society of America*, 99(1):286–301, 2009.
[78] R. Styron and M. Pagani. The gem global active faults database. *Earthquake Spectra*, 36(1_suppl):160–180, 2020.
[79] A. B. Sunbul, M. Çavuşli, M. Kartal, and F. Sunbul. A case study on 3d non-linear analysis of a clay core rockfill dam. *The Eurasia Proceedings of Science, Technology, Engineering & Mathematics (EPSTEM)*, 1:388–396, 12 2017.
[80] R. Taborda and D. Roten. Physics-based ground-motion simulation. *Encyclopedia of Earthquake Engineering, Springer-Verlag, Berlin Heidelberg*, 2015.
[81] G. Teng and J. Baker. Evaluation of scec cybershake ground motions for engineering practice. *Earthquake Spectra*, 35(3):1311–1328, 2019.
[82] H. Tosun and V. Tosun. Earthquake safety of large dams located in Kucuk Menderes basin, West Turkey. In *Proceedings of the* 5^{th} *International Symposium on Dam Safety*, pages 1–12. Turkish Society of Dam Safety, 2018.
[83] U.S. Geological Survey, 2021, Earthquake Event page, accessed May 26, 2021. https://earthquake.usgs.gov/earthquakes/eventpage/us7000c7y0/finite-fault.
[84] USCOLD. Observed performance of dams during earthquakes. 1992.
[85] USSD. Observed performance of dams during earthquakes. volume ii, ussd committee on earthquakes. *United States Society on Dams*, 2000.
[86] USSD. Observed performance of dams during earthquakes. volume iii, ussd committee on earthquakes. *United States Society on Dams*, 2014.
[87] I. van Zelst, S. Wollherr, A.-A. Gabriel, E. H. Madden, and Y. van Dinther. Modeling Megathrust Earthquakes Across Scales: One-way Coupling From Geodynamics and Seismic Cycles to Dynamic

Rupture. *J. Geophys. Res. Solid Earth*, 124(11):11414–11446, 2019.

[88] A. Yakut, H. Sucuoğlu, B. Binici, E. Canbay, C. Donmez, A. İlki, A. Caner, O. C. Celik, and B. Ö. Ay. Performance of structures in İzmir after the samos island earthquake. *Bulletin of Earthquake Engineering*, pages 1–26, 2021.

[89] Y. Yamaguchi, M. Kondo, and T. Kobori. Safety inspections and seismic behavior of embankment dams during the 2011 off the Pacific Coast of Tohoku earthquake. *Soils and Foundations*, 52:945–955, 10 2012.

[90] J.-M. Zhang, Z. Yang, X. Gao, and J. Zhang. Geotechnical aspects and seismic damage of the 156-m-high Zipingpu concrete-faced rockfill dam following the ms 8.0 Wenchuan earthquake. *Soil Dynamics and Earthquake Engineering*, 76, 04 2015.

E-mail address: ilario.mazzieri@polimi.it
E-mail address: muhr@ma.tum.de
E-mail address: MStupazzini@munichre.com
E-mail address: wohlmuth@ma.tum.de

B.2. A high-order discontinuous Galerkin method for nonlinear sound waves.

A high-order discontinuous Galerkin method for nonlinear sound waves

Paola F. Antonietti, Ilario Mazzieri, **Markus Muhr**, Vanja Nikolić, Barbara Wohlmuth

---

The Westervelt equation of nonlinear acoustics plays an important role when it comes to the modeling of high amplitude ultrasound waves. Such waves appear for example in the medical treatment of kidney stones via extracorporeal shockwave lithotripsy. Therefore accurate numerical simulations of such processes, often in complex, multi-material domains, is of relevance. This article deals with the application of a DG finite element method to the Westervelt equation, derives an a priori error estimate for polynomial degrees $p \geq 2$ and also shows the numerical applicability of the method in a hybrid continuous/discontinuous way. To keep the analysis general, polytopic elements in 2D and 3D are considered.

The proof of the error estimate is based on Banach's fixed point theorem. First, a linearized version of Westervelt's equation is studied, where a reference solution is used in the nonlinear terms. We first prove stability and then an priori error estimate in a suitable energy norm. Then, in order to extend the argument to the nonlinear equation, a fixed point mapping is defined, which maps the reference solution from the linearized argument to the nonlinear solution. The rest of the proof consists of showing the necessary prerequisites for Banach's fixed point theorem for the defined mapping. In order to support the general polytopic elements careful assumptions on the meshes have to be made. The implementation of the method treats the nonlinearity via a fixed-point iteration, time integration is done with a generalized-α scheme in order to avoid Gibbs oscillations at the steep wave-fronts. A first numerical example with synthetic data shows the proven error-rates numerically and also the feasibility of the method in case of nearly degenerate mesh edges, covered by the general polygonal case. More elaborated 3D examples feature the method also in a hybrid way, where the DG approach is only used at sub-domain interfaces, also with jumping coefficients, while a conforming approach is used within the individual subdomains.

After the introduction, Sec. 2 shortly introduces the acoustic model equation. In Sec. 3 the assumptions on the polytopic meshes are stated and basic estimates from the DG literature are collected, while in Sec. 4 the DG discretization of the equation is performed. The analysis of the method is then done in Sec. 5 for the linear case, and Sec. 6 for the nonlinear case. Sec. 7 describes the computational approach and Sec. 8 finally contains the numerical experiments.

I was significantly involved in finding the ideas and carrying out the scientific work presented in this article including the write-up. I was in charge of the numerical sections of the work, i.e. Sec. 3, 4, 7 and 8. Furthermore I was in charge of the computational part of the article, i.e. design of numerical examples, realization of the implementation and the creation of the figures.

Permission to include:

Paola F. Antonietti, Ilario Mazzieri, Markus Muhr, Vanja Nikolić and Barbara Wohlmuth
A high-order discontinuous Galerkin method for nonlinear sound waves.
Journal of Computational Physics 415 (2020): 109484

Copyright

Overview

In order for Elsevier to publish and disseminate research articles, we need certain publishing rights from authors, which are determined by a publishing agreement between the author and Elsevier.

For articles published open access, the authors license exclusive publishing rights to Elsevier.

For articles published under the subscription model, the authors transfer copyright to Elsevier.

Regardless of whether they choose to publish open access or subscription with Elsevier, authors have many of the same rights under our publishing agreement, which support their need to share, disseminate and maximize the impact of their research.

For open access articles, authors will also have additional rights, depending on the Creative Commons end user license that they select. This Creative Commons license sets out the rights that readers (as well as the authors) have to re-use and share the article: please see here for more information on how articles can be re-used and shared under these licenses.

This page aims to summarise authors' rights when publishing with Elsevier; these are explained in more detail in the ↓ publishing agreement between the author and Elsevier.

Irrespective of how an article is published, Elsevier is committed to protect and defend authors' works and their reputation. We take allegations of infringement, plagiarism, ethical disputes, and fraud very seriously.

Author rights

The below table explains the rights that authors have when they publish with Elsevier, for authors who choose to publish either open access or subscription. These apply to the corresponding author and all co-authors.

Author rights in Elsevier's proprietary journals	Published open access	Published subscription
Retain patent and trademark rights	√	√
Retain the rights to use their research data freely without any restriction	√	√
Receive proper attribution and credit for their published work	√	√
Re-use their own material in new works without permission or payment (with full acknowledgement of the original article): 1. Extend an article to book length 2. Include an article in a subsequent compilation of their own work 3. Re-use portions, excerpts, and their own figures or tables in other works.	√	√
Use and share their works for scholarly purposes (with full acknowledgement of the original article): 1. In their own classroom teaching. Electronic and physical distribution of copies is permitted 2. If an author is speaking at a conference, they can present the article and distribute copies to the attendees 3. Distribute the article, including by email, to their students and to research colleagues who they know for their personal use 4. Share and publicize the article via Share Links, which offers 50 days' free access for anyone, without signup or registration 5. Include in a thesis or dissertation (provided this is not published commercially) 6. Share copies of their article privately as part of an invitation-only work group on commercial sites with which the publisher has a hosting agreement	√	√
Publicly share the preprint on any website or repository at any time.	√	√
Publicly share the accepted manuscript on non-commercial sites	√	√ using a CC BY-NC-ND license and usually only after an embargo period (see Sharing Policy for more information)
Publicly share the final published article	√ in line with the author's choice of end user license	×
Retain copyright	√	×

Institution rights

Regardless of how the author chooses to publish with Elsevier, their institution has the right to use articles for classroom teaching and internal training. Articles can be used for these purposes throughout the author's institution, not just by the author:

Institution rights in Elsevier's proprietary journals (providing full acknowledgement of the original article is given)	**All articles**
Copies can be distributed electronically as well as in physical form for classroom teaching and internal training purposes	√
Material can be included in coursework and courseware programs for use within the institution (but not in Massive Open Online Courses)	√
Articles can be included in applications for grant funding	√
Theses and dissertations which contain embedded final published articles as part of the formal submission can be posted publicly by the awarding institution with DOI links back to the formal publication on ScienceDirect	√

Government rights

For US government employees, works created within the scope of their employment are considered to be public domain and Elsevier's publishing agreements do not require a transfer or license of rights for such works.

In the UK and certain commonwealth countries, a work created by a government employee is copyrightable, but the government may own the copyright (Crown copyright). Click here for information about UK government employees publishing open access.

Find out more

- Download a sample publishing agreement for articles financed by journal subscriptions in ↓ English and ↓ French.
- Download a sample publishing agreement for articles published open access with a↓ commercial user license (CC BY) and a↓ non-commercial user license. (CC BY-NC-ND)
- For authors who wish to self-archive see our sharing guidelines.
- See our author pages for further details about how to promote your article.
- See our hosting page for additional information on hosting research published by Elsevier.
- For use of Elsevier material not defined here please see our permissions page or visit the Permissions Support Center ↗ .
- If an author has become aware of a possible plagiarism, fraud or infringement we recommend contacting their Elsevier publishing contact who can then liaise with our in-house legal department.
- If you are publishing in a society or third party owned journal, they may have different publishing agreements. Please see the journal's Guide for Authors for journal specific copyright information.

The above pages are copies from the webpage
https://www.elsevier.com/about/policies/copyright
Date: 08.06.2021

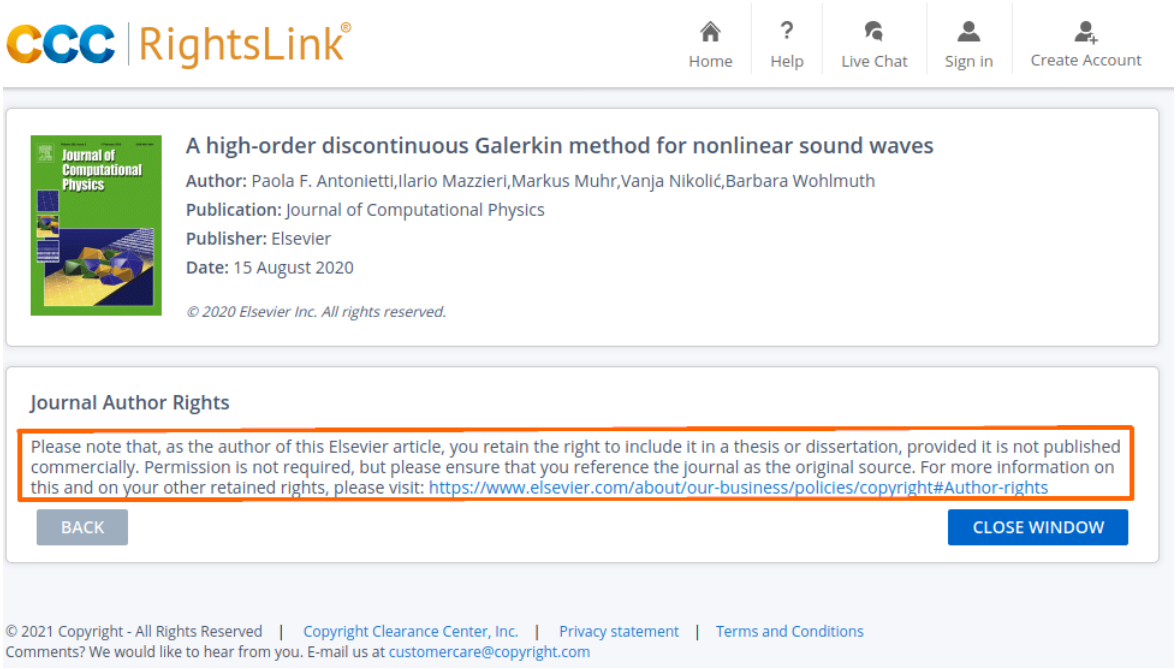

The above pages are copies from the webpage
https://s100.copyright.com/AppDispatchServlet
Date: 08.06.2021

Journal of Computational Physics 415 (2020) 109484

Contents lists available at ScienceDirect

Journal of Computational Physics

www.elsevier.com/locate/jcp

A high-order discontinuous Galerkin method for nonlinear sound waves

Paola F. Antonietti [a], Ilario Mazzieri [a], Markus Muhr [b,*], Vanja Nikolić [c], Barbara Wohlmuth [b]

[a] MOX, Dipartimento di Matematica, Politecnico di Milano, Milano, Italy
[b] Department of Mathematics, Technical University of Munich, Germany
[c] Department of Mathematics, Radboud University, the Netherlands

ARTICLE INFO

Article history:
Received 5 December 2019
Received in revised form 16 April 2020
Accepted 17 April 2020
Available online 28 April 2020

Keywords:
Discontinuous Galerkin methods
Nonlinear acoustics
Westervelt's equation

ABSTRACT

We propose a high-order discontinuous Galerkin scheme for nonlinear acoustic waves on polytopic meshes. To model sound propagation with losses through homogeneous media, we use Westervelt's nonlinear wave equation with strong damping. Challenges in the numerical analysis lie in handling the nonlinearity in the model, which involves the derivatives in time of the acoustic velocity potential, and in preventing the equation from degenerating. We rely in our approach on the Banach fixed-point theorem combined with a stability and convergence analysis of a linear wave equation with a variable coefficient in front of the second time derivative. By doing so, we derive an *a priori* error estimate for Westervelt's equation in a suitable energy norm for the polynomial degree $p \geq 2$. Numerical experiments carried out in two-dimensional settings illustrate the theoretical convergence results. In addition, we demonstrate efficiency of the method in a three-dimensional domain with varying medium parameters, where we use the discontinuous Galerkin approach in a hybrid way.

1. Introduction

Nonlinear sound waves arise in many different applications, such as medical ultrasound [22,39,50], fatigue crack detection [52,55], or musical acoustics of brass instruments [12,26,42]. Although considerable work has been devoted to their analytical studies [33,34,37,41] and their computational treatment [31,38,48,58], rigorous numerical analysis of nonlinear acoustic phenomena is still largely missing from the literature. The goal of our work is to develop a high-order discontinuous Galerkin (DG) scheme for nonlinear sound waves in homogeneous media that is rigorously justified through a stability and convergence analysis.

The DG method was first introduced in the seventies for the numerical approximation of hyperbolic problems [47], and, independently, in the context of elliptic [21] and parabolic [6] equations. Since then DG methods have been successfully developed and applied to a wide range of problems arising in computational sciences and engineering; cf. the books [19, 30,49] for a comprehensive overview. In relation to our setting, we point out in particular the works on the Euler and Navier–Stokes equations [10] and on a class of nonlinear elliptic and second-order hyperbolic problems [44].

* Corresponding author.
E-mail addresses: paola.antonietti@polimi.it (P.F. Antonietti), ilario.mazzieri@polimi.it (I. Mazzieri), muhr@ma.tum.de (M. Muhr), vanja.nikolic@ru.nl (V. Nikolić), wohlmuth@ma.tum.de (B. Wohlmuth).

https://doi.org/10.1016/j.jcp.2020.109484
0021-9991/

The finite-dimensional DG space consists of piecewise discontinuous polynomial functions defined over a computational tessellation of the domain. As a consequence, the DG paradigm can naturally support finite element spaces built upon meshes consisting of arbitrarily shaped polygonal/polyhedral elements, thus generalizing the paradigm that stands at the basis of classical Finite Elements on triangles, quadrilaterals, or their combinations in two dimensions (2D), and tetrahedra, prisms, pyramids, and hexahedra or their combinations in three dimensions (3D), and gaining flexibility in the process of mesh generation. DG methods on polygonal/polyhedral grids (PolyDG methods for short) have received a lot of attention in the last years; we give here only an incomplete list [3,8,9,14–16] and refer the reader to the references therein for a comprehensive overview. In PolyDG methods, high order accuracy can be achieved in any space dimension by introducing suitable modal basis functions defined directly in the physical frame configuration. Finally, PolyDG methods can be seen as extensions of the classical DG approach and they are naturally oriented towards 3D scalable implementations.

We organize the rest of the paper as follows. In Section 2, we first discuss the continuous initial-boundary value problem for a classical model of nonlinear acoustics–Westervelt's wave equation. Section 3 contains some theoretical preliminaries that are useful for the numerical analysis. In Section 4, we propose and discuss a high-order discontinuous Galerkin scheme for the Westervelt equation. Section 5 is devoted to the stability analysis of a linearized semi-discrete problem and its *a priori* error analysis. In Section 6, we use the Banach fixed-point theorem to prove an *a priori* estimate for the approximate solution of the Westervelt equation. Section 7 describes in detail our numerical solver. Finally, in Section 8, we carry out several numerical experiments, both in two and three dimensions, to illustrate the theory from previous sections. In a three-dimensional setting, we use the discontinuous Galerkin approach in a hybrid way to demonstrate that the method can also handle varying medium parameters.

2. The continuous problem

We employ Westervelt's wave equation [59] to model nonlinear sound propagation through a homogeneous medium, given in terms of the acoustic velocity potential ψ by

$$(1 - 2k\dot{\psi})\ddot{\psi} - c^2\Delta\psi - b\Delta\dot{\psi} = 0. \tag{2.1}$$

The constant c denotes the speed of sound and b is the so-called sound diffusivity. The constant k is given by $k = \beta_a/c^2$ where β_a is the coefficient of nonlinearity of the medium. For the derivation of nonlinear acoustic models and their physical background, we refer the interested reader to, e.g., [18,23,29,54]. The acoustic pressure u can be obtained via the relation $u = \varrho\dot{\psi}$, where ϱ denotes the mass density of the medium.

Westervelt's equation is a nonlinear acoustic wave equation, which we couple with initial conditions and homogeneous Dirichlet data, and investigate the following problem:

$$\begin{cases} (1 - 2k\dot{\psi})\ddot{\psi} - c^2\Delta\psi - b\Delta\dot{\psi} = 0 \quad \text{in } \Omega \times (0, T], \\ \psi = 0 \quad \text{on } \partial\Omega \times [0, T], \\ (\psi, \dot{\psi}) = (\psi_0, \psi_1) \quad \text{on } \Omega \times \{t = 0\} \end{cases} \tag{2.2}$$

on a bounded domain $\Omega \subset \mathbb{R}^d$ for $d \in \{2, 3\}$ and for a given final time $T > 0$.

If $b > 0$, then Westervelt's equation is strongly damped. With enough dissipation (i.e., b large enough), it exhibits a parabolic-like behavior. The initial-boundary value problem (2.2) is then known to be globally well-posed for sufficiently small and smooth initial data on regular domains, provided that appropriate compatibility conditions at the initial time are satisfied. We refer to [37, Theorem 2.2], from which global well-posedness of (2.2) follows as a special case. We mention also the local-in-time well-posedness result from [35, Section 7] that relaxes the regularity assumptions on the initial data.

If we consider propagation in inviscid media, then $b = 0$ in (2.2). It is expected and numerically observed [17,36] that now smooth solutions of (2.2) exist only for a short time before the shock develops due to nonlinear steepening. A rigorous proof of the short-term well-posedness is available for propagation in unbounded domains as a particular case of a general quasi-linear hyperbolic system of second order in [32, Theorem 1]. For the inviscid Westervelt equation reformulated in terms of the acoustic pressure u, the local well-posedness on bounded domains follows from a special case of a general quasi-linear wave equation studied in [20, Theorem 4.1].

We point out here another important feature of Westervelt's equation. The factor $1 - 2k\dot{\psi}$ in front of the second time derivative can degenerate if the acoustic pressure is too high. To avoid that this happens, we have to prove that $\dot{\psi}$ stays below $1/(2k)$. In the continuous analysis, this is commonly achieved by having sufficiently smooth data such that the solution space for the pressure embeds continuously into $L^\infty(\Omega)$ almost everywhere in time and by additionally assuming that the data are sufficiently small in an appropriate norm; see [33–35,41]. Our non-conforming discretization approach prevents this strategy. Since our approximate solution is only piecewise smooth, we have to rely on an inverse inequality to avoid degeneracy. On the other hand, we do not want a bound that degenerates as h converges to 0, and so we will need to involve additionally the (local) interpolant in the estimate and employ its approximation and stability properties.

3. Assumptions and preliminaries

Let $\Omega \subset \mathbb{R}^d$ for $d \in \{2, 3\}$ be a convex polygonal or polyhedral domain. We consider a family of meshes $\mathcal{T}_h$ made of disjoint open *polygonal/polyhedral* elements κ with diameter h_κ.

Following [3,14,16], we introduce the concept of mesh *interface*, defined as the intersection of the $(d-1)$-dimensional facets of two neighboring elements. When $d = 3$, each interface consists of a general polygon which we assume can be decomposed into a set of co-planar triangles. We assume that a sub-triangulation of each interface is provided and we denote the set of all these triangles by $\mathcal{F}_h$. We then use the terminology *face* to refer to one of the triangular elements in $\mathcal{F}_h$. When $d = 2$, each interface simply consists of a line segment, so that the concept of faces and interfaces coincides in this case. We denote by $\mathcal{F}_h$ the set of all faces of $\mathcal{T}_h$, decomposed into the set of internal faces $\mathcal{F}_h^i$ and the set of boundary faces $\mathcal{F}_h^b$ so that $\mathcal{F}_h = \mathcal{F}_h^i \cup \mathcal{F}_h^b$.

We assume a fixed uniform polynomial degree $p \geq 1$ and introduce the following finite-dimensional space:

$$V_h = \{\psi \in L^2(\Omega) : \psi_{|\kappa} \in \mathcal{P}_p(\kappa)\ \forall \kappa \in \mathcal{T}_h\},$$

where $\mathcal{P}_p(\kappa)$ is the space of polynomials of total degree p defined on κ, as well as the broken Sobolev spaces

$$H^n(\mathcal{T}_h) = \{\psi \in L^2(\Omega) :\ \psi_{|\kappa} \in H^n(\kappa)\ \forall \kappa \in \mathcal{T}_h\}$$

for $n \geq 1$. It is natural to employ the broken gradient operator $\nabla_h \cdot$ on the space $H^1(\mathcal{T}_h)$; see [19, Definition 1.21].

For sufficiently smooth ψ, we introduce jumps and averages on an interior face $F \in \mathcal{F}_h^i$, $F \subset \partial\kappa^+ \cap \partial\kappa^-$ with κ^+ and κ^- any two neighboring elements in $\mathcal{T}_h$, as follows:

$$[\![\psi]\!] = \psi^+ \mathbf{n}^+ + \psi^- \mathbf{n}^-, \qquad \{\!\{\psi\}\!\} = \frac{\psi^+ + \psi^-}{2}, \tag{3.1}$$

where $\psi^\pm$ denotes the trace of ψ on F taken within the interior of $\kappa^\pm$, and $\mathbf{n}^\pm$ denotes the unit normal vector to $\partial\kappa^\pm$ pointing outwards from $\partial\kappa^\pm$. On the boundary face $F \in \mathcal{F}^b$, we set $[\![\psi]\!] = \psi\mathbf{n}$ and $\{\!\{\psi\}\!\} = \psi$. For a (smooth enough) vector-valued function $\boldsymbol{\psi}$, definition (3.1) extends analogously.

For later use, we also define here the stabilization function $\chi \in L^\infty(\mathcal{F}_h)$ as follows:

$$\chi_{|F} = \begin{cases} c^2\,\beta \max\limits_{\kappa \in \{\kappa^+, \kappa^-\}} \dfrac{p^2}{h_\kappa} & \text{for all } F \in \mathcal{F}_h^i, \quad F \subset \partial\kappa^+ \cap \partial\kappa^-, \\ c^2\,\beta\,\dfrac{p^2}{h_\kappa} & \text{for all } F \in \mathcal{F}_h^b, \quad F \subset \partial\kappa. \end{cases} \tag{3.2}$$

The parameter $\beta > 0$ will be chosen in a convenient manner in the following proofs.

For an open subset D of $\mathbb{R}^d$, where $d \in \{1, 2, 3\}$, and a function $v \in H^n(D)$, where $n \geq 0$, we denote by $\|v\|_{H^n(D)}$ and $|v|_{H^n(D)}$ the standard norm and seminorm, respectively, with the convention that $H^0(D) \equiv L^2(D)$. When $D \equiv \Omega$, we simply write $\|\nabla v\|_{H^n}$ and $|v|_{H^n}$. We use the short-hand notation

$$\langle \psi, v \rangle_{\mathcal{F}} = \sum_{F \in \mathcal{F}} (\psi, v)_{L^2(F)}, \quad \|\psi\|_{\mathcal{F}} = \langle \psi, \psi \rangle_{\mathcal{F}}^{1/2}$$

for a generic collection of faces $\mathcal{F} \subset \mathcal{F}_h$, and regular enough functions ψ and v. Here $(\cdot, \cdot)_{L^2(F)}$ denotes the inner product in $L^2(F)$.

We occasionally use the notation $x \lesssim y$ and $x \gtrsim y$ instead of $x \leq Cy$ and $x \geq Cy$, respectively, when the hidden constant $C > 0$ does not depend on the coefficients in the equation c, b, and k, the mesh size, and the number of faces of a mesh element, but can depend on the polynomial degree p and the final time T.

3.1. Grid assumptions and preliminary estimates

Throughout the paper, we make the following assumptions on the family of polytopic decompositions $\mathcal{T}_h$, which allow to extend the trace-inverse and inverse inequalities on simplices to polytopic elements.

Mesh assumptions. For any $\kappa \in \mathcal{T}_h$, we assume that

$$h_\kappa^d \geq |\kappa| \gtrsim h_\kappa^d$$

for $d = 2, 3$, where $|\kappa|$ denotes the Hausdorff measure of $\kappa \in \mathcal{T}_h$. We also assume that there exists a positive number m, such that every polytopic element $\kappa \in \mathcal{T}_h$ admits a sub-triangulation into at most $\mathtt{m}_\kappa \leq m$ shape-regular simplices $\mathtt{s}_i$ for $i = 1, 2, \ldots, \mathtt{m}_\kappa$, such that

$$\bar{\kappa} = \cup_{i=1}^{\mathrm{m}_\kappa} \bar{\mathrm{s}}_i \ \text{ and } \ |\mathrm{s}_i| \gtrsim |\kappa|,$$

where the hidden constant is independent of κ and $\mathcal{T}_h$. Finally, we assume that

$$\frac{\max_\kappa h_\kappa}{\min_\kappa h_\kappa} \lesssim 1.$$

Under these mesh assumptions, the following trace-inverse and inverse inequalities hold on polytopic domains.

Lemma 1. *For any $v \in \mathcal{P}_p(\kappa)$, $\kappa \in \mathcal{T}_h$, the following trace-inverse and inverse inequalities hold:*

$$\|v\|_{L^2(\partial\kappa)} \lesssim h_\kappa^{-1/2} \, \|v\|_{L^2(\kappa)}, \tag{3.3}$$

$$\|v\|_{L^\infty(\kappa)} \lesssim h_\kappa^{-d/2} \, \|v\|_{L^2(\kappa)}. \tag{3.4}$$

Proof. The statement follows from, e.g., [15, Lemma 6] combined with our mesh assumptions. □

Remark 1 *(On the mesh assumptions).* We choose to simplify our mesh assumptions for the clarity of exposition. However, for the trace-inverse inequality (3.3) to hold, these assumptions are slightly more restrictive than needed, and can be weakened by employing the arguments of [13]. Indeed, the inequality holds provided that, for any $\kappa \in \mathcal{T}_h$, there exists a set of non-overlapping d-dimensional simplices $\kappa_\flat^F \subset \kappa$ such that, for any face $F \subset \partial\kappa$, $\overline{F} = \partial\overline{\kappa} \cap \partial\overline{\kappa_\flat^F}$, and $\bigcup_{F\subset\partial\kappa} \overline{\kappa_\flat^F} \subset \overline{\kappa}$, and the diameter h_κ of κ can be bounded by

$$h_\kappa \lesssim \frac{d|\kappa_\flat^F|}{|F|}$$

for all $F \subset \partial\kappa$, where $|F|$ and $|\kappa_\flat^F|$ denote the Hausdorff measure of F and $\kappa_\flat^F$, respectively. This latter assumption does not put a restriction on either the number of faces that an element possesses, or indeed the measure of a face of an element $\kappa \in \mathcal{T}_h$, relative to the measure of the element itself; cf. also [3,14–16]. As pointed out in [13], meshes obtained by agglomeration of a finite number of polygons that are uniformly star-shaped with respect to the largest inscribed ball will automatically satisfy the above weak requirement.

The inverse inequality (3.4) also holds under weaker assumptions: if, for any point $x \in \kappa$, there exists a shape-regular simplex containing x and contained in κ, with diameter comparable to that of κ. In other words, for any point $x \in \kappa$, there exists $\mathrm{s}_\kappa(x)$, such that $x \in \mathrm{s}_\kappa(x) \subseteq \kappa$ and $h_{\mathrm{s}(x)} \gtrsim h_\kappa$. The proof follows by relying on the L^∞ inverse estimates on shape-regular simplexes; cf. [25, equation (3.8)], [53, Theorem 4.76].

3.2. Interpolation bounds on polytopic meshes

For future reference, we also state here the specific interpolation bounds on polytopic meshes we will rely on in the proofs.

Lemma 2. *Let $v \in H^n(\kappa)$, where $\kappa \in \mathcal{T}_h$. Then, there exists $\Pi_{\kappa,p} : H^n(\kappa) \to \mathcal{P}_p(\kappa)$ such that*

$$\begin{aligned}
\left\| v - \Pi_{\kappa,p} v \right\|_{L^2(\kappa)} &\lesssim h_\kappa^{\mu} |v|_{H^n(\kappa)}, && n \geq 0, \\
|v - \Pi_{\kappa,p} v|_{H^1(\kappa)} &\lesssim h_\kappa^{\mu-1} |v|_{H^n(\kappa)}, && n \geq 1, \\
\left\| v - \Pi_{\kappa,p} v \right\|_{L^\infty(\kappa)} &\lesssim h_\kappa^{\mu-d/2} |v|_{H^n(\kappa)}, && n > d/2,
\end{aligned} \tag{3.5}$$

where $\mu = \min\{n, p+1\}$.

Proof. The statement follows by employing our mesh assumptions and classical interpolation bounds on quadrilateral/hexahedral and simplicial elements; cf. [7,11,16]. □

We can now also state a result on the interpolation error for time-dependent piecewise smooth functions. Let $\psi \in C([0,T]; H^n(\mathcal{T}_h))$, where $n \geq 2$. For any time $t \in [0,T]$, we define the global interpolant ψ_I element-wise as

$$\psi_{I\,|\kappa}(t) = \psi_{I,\kappa}(t), \quad \kappa \in \mathcal{T}_h, \tag{3.6}$$

where $\psi_{I,\kappa}(t) = \Pi_{\kappa,p}\psi(t)$ is the local interpolant of Lemma 2.

Lemma 3. *Let $\psi \in C([0,T];H^n(\mathcal{T}_h))$, where $n \geq 2$. Then, there exists an interpolant $\psi_I \in C([0,T];V_h)$, defined as in (3.6), such that the error $e_I = \psi - \psi_I$ satisfies*

$$c^2\|\nabla_h e_I(t)\|_{L^2}^2 + \|\sqrt{\chi}[\![e_I(t)]\!]\|_{\mathcal{F}_h}^2 \lesssim c^2 \sum_{\kappa\in\mathcal{T}_h} h_\kappa^{2\mu-2}\,|\psi(t)|_{H^n(\kappa)}^2,$$

for all $t \in [0,T]$, where $\mu = \min\{n, p+1\}$ and χ is defined in (3.2); we recall that $c > 0$ denotes the speed of sound. Moreover, the following estimate holds:

$$\|\chi^{-1/2}\{\!\{\nabla_h e_I(t)\}\!\}\|_{\mathcal{F}_h}^2 \lesssim \frac{1}{c^2}\sum_{\kappa\in\mathcal{T}_h} h_\kappa^{2\mu-2}\,|\psi(t)|_{H^n(\kappa)}^2, \quad \text{for } 0 \leq t \leq T. \tag{3.7}$$

Proof. The statement follows by relying on the mesh assumptions, estimates (3.5), and the following multiplicative trace inequality on shape-regular simplices $\mathfrak{s}$:

$$\|\eta\|_{L^2(\partial\mathfrak{s})}^2 \lesssim \|\eta\|_{L^2(\mathfrak{s})}\|\nabla\eta\|_{L^2(\mathfrak{s})} + h_{\mathfrak{s}}^{-1}\|\eta\|_{L^2(\mathfrak{s})}^2 \text{ for all } \eta \in H^1(\mathfrak{s});$$

cf. [7] and [15, Lemma 33]. □

4. The DG approximation in space of the Westervelt equation

In this section, we introduce and discuss the semi-discrete approximation of the initial-boundary value problem (2.2) for the Westervelt equation. To motivate our approximate weak form, we rewrite the Westervelt equation as

$$(1-2k\dot\psi)\ddot\psi - c^2\Delta(\psi + \tfrac{b}{c^2}\dot\psi) = 0.$$

Together with the fact that sound diffusivity b is relatively small in realistic applications, this suggests to introduce an auxiliary state

$$\tilde\psi = \psi + \frac{b}{c^2}\dot\psi, \tag{4.1}$$

which allows us to formally write the Westervelt equation as

$$(1-2k\dot\psi)\ddot\psi - c^2\Delta\tilde\psi = 0. \tag{4.2}$$

We are interested in the solutions of this problem in the sense of the equation

$$((1-2k\dot\psi)\ddot\psi, v)_{L^2} + a(\tilde\psi, v) = 0 \tag{4.3}$$

being satisfied for all $v \in H_0^1(\Omega)$ and almost all times $t \in (0,T)$, with $(\psi,\dot\psi)|_{t=0} = (\psi_0,\psi_1)$. The bilinear form $a : H_0^1(\Omega)\times H_0^1(\Omega) \to \mathbb{R}$ is given by

$$a(\psi, v) = c^2(\nabla\psi, \nabla v)_{L^2}.$$

We introduce the corresponding DG bilinear form $a_h : H^2(\mathcal{T}_h)\times V_h \to \mathbb{R}$ by

$$\begin{aligned} a_h(\psi, v_h) = {} & c^2(\nabla_h\psi, \nabla_h v_h)_{L^2} - \langle\{\!\{c^2\nabla_h\psi\}\!\}, [\![v_h]\!]\rangle_{\mathcal{F}_h} \\ & - \langle[\![\psi]\!], \{\!\{c^2\nabla_h v_h\}\!\}\rangle_{\mathcal{F}_h} + \langle\chi[\![\psi]\!], [\![v_h]\!]\rangle_{\mathcal{F}_h}, \end{aligned}$$

where the stabilization function χ is defined as in (3.2). We then look for the approximate solution $\psi_h \in C^2([0,T];V_h)$ of equation (4.3), such that

$$((1-2k\dot\psi_h)\ddot\psi_h, v_h)_{L^2} + a_h(\tilde\psi_h, v_h) = 0 \tag{4.4}$$

holds for all $v_h \in V_h$, a.e. $t \in (0,T)$, supplemented with the approximate initial data

$$(\psi_h(0), \dot\psi_h(0)) = (\psi_{0,h}, \psi_{1,h}) \in V_h \times V_h.$$

In equation (4.4), we have used, analogously to (4.1), the notation

$$\tilde\psi_h = \psi_h + \frac{b}{c^2}\dot\psi_h, \tag{4.5}$$

and therefore our weak form (4.4) is equivalent to

$$
\begin{aligned}
((1-2k\dot{\psi}_h)\ddot{\psi}_h, v_h)_{L^2} + c^2(\nabla_h\psi_h, \nabla_h v_h)_{L^2} + b(\nabla_h\dot{\psi}_h, \nabla_h v_h)_{L^2} \\
-\langle\{\!\{c^2\nabla_h\psi_h\}\!\}, [\![v_h]\!]\rangle_{\mathcal{F}_h} - \langle\{\!\{b\nabla_h\dot{\psi}_h\}\!\}, [\![v_h]\!]\rangle_{\mathcal{F}_h} \\
-\langle[\![\psi_h]\!], \{\!\{c^2\nabla_h v_h\}\!\}\rangle_{\mathcal{F}_h} - \langle[\![\tfrac{b}{c^2}\dot{\psi}_h]\!], \{\!\{c^2\nabla_h v_h\}\!\}\rangle_{\mathcal{F}_h} \\
+\langle\chi[\![\psi_h]\!], [\![v_h]\!]\rangle_{\mathcal{F}_h} + \langle\chi[\![\tfrac{b}{c^2}\dot{\psi}_h]\!], [\![v_h]\!]\rangle_{\mathcal{F}_h} = 0.
\end{aligned}
\tag{4.6}
$$

Recall that in (3.2) the stabilization function χ has a c^2 scaling, and thus the two stabilization terms in (4.6) effectively scale by c^2 and b.

We note that in the case of sound propagation without losses, where $b = 0$ in the Westervelt equation, (4.4) formally corresponds to the standard DG formulations for second-order undamped wave equations; see, for example, [28].

5. Analysis of the linearized semi-discrete problem

As a first step in the analysis, we consider a non-degenerate linearization of (2.2) that is given by the following initial-boundary value problem for a linear strongly damped wave equation:

$$
\begin{cases}
\alpha(x,t)\ddot{\tilde{\psi}} - c^2\Delta\tilde{\psi} = 0 \quad \text{in } \Omega\times(0,T], \\
\psi = 0 \quad \text{on } \partial\Omega\times[0,T], \\
(\psi, \dot{\psi}) = (\psi_0, \psi_1) \quad \text{on } \Omega\times\{t=0\},
\end{cases}
\tag{5.1}
$$

where it is assumed that there exist α_0, $\alpha_1 > 0$ such that

$$
\alpha_0 \le \alpha(x,t) \le \alpha_1 \ \text{ in } \overline{\Omega}\times[0,T],
$$

and the relation (4.1) holds. Sufficient conditions for the well-posedness of (5.1) in the case that $b > 0$ can be found in [35, Proposition 3.2]. The weak form of this problem is given by

$$
(\alpha\ddot{\tilde{\psi}}, v)_{L^2} + a(\tilde{\psi}, v) = 0
$$

for all $v \in H_0^1(\Omega)$, $0 < t \le T$ with $(\psi, \dot{\psi})|_{t=0} = (\psi_0, \psi_1)$. We analyze its semi-discrete approximation, given by equation

$$
(\alpha_h\ddot{\tilde{\psi}}_h, v_h)_{L^2} + a_h(\tilde{\psi}_h, v_h) = 0
\tag{5.2}
$$

which should hold for all $v_h \in V_h$, $0 < t \le T$, supplemented with the approximate initial data

$$
(\psi_h(0), \dot{\psi}_h(0)) = (\psi_{0,h}, \psi_{1,h}) \in V_h \times V_h.
$$

In equation (5.2), the coefficient α_h denotes a discrete version of the coefficient α such that

$$
\alpha_0 \le \alpha_h(x,t) \le \alpha_1 \ \text{ in } \overline{\Omega}\times[0,T].
\tag{5.3}
$$

The main idea behind studying this linearized problem is to later choose

$$
\alpha_h = 1 - 2k\dot{w}_h
$$

with w_h in a neighborhood of ψ, and define a map $\mathcal{J} : w_h \mapsto \psi_h$, where ψ_h solves the linear semi-discrete problem (5.2). The fixed point of this map will be the solution of the nonlinear problem (4.4). Our approach here follows, in spirit, the strategy taken in [44], where nonlinear hyperbolic systems in divergence form are considered.

5.1. Existence and stability

Our first task is to prove that the semi-discrete problem (5.2) has a unique solution that remains bounded in a suitable energy norm. We begin by recalling a useful inequality for functions in V_h.

Lemma 4. *For any $v_h \in V_h$, the following inequality holds:*

$$
\|\chi^{-1/2}\{\!\{\nabla_h v_h\}\!\}\|_{\mathcal{F}_h} \lesssim \frac{1}{c\sqrt{\beta}}\|\nabla_h v_h\|_{L^2},
$$

where $\beta > 0$ is the stability parameter that appears in the definition (3.2) of the stabilization function χ.

Proof. The statement follows by a straightforward modification of the arguments in [5, Lemma 3.2]; cf. also [4]. □

By relying on Lemma 4, we can show that

$$\begin{aligned} c^2\|\langle\{\!\{\nabla_h v_h\}\!\},[\![v_h]\!]\rangle_{\mathcal{F}_h}\| &\lesssim c\frac{1}{\sqrt{\beta}}\|\nabla_h v_h\|_{L^2}\|\sqrt{\chi}\,[\![v_h]\!]\,\|_{\mathcal{F}_h} \\ &\lesssim c^2\frac{1}{4\varepsilon}\frac{1}{\beta}\|\nabla_h v_h\|_{L^2}^2+\varepsilon\|\sqrt{\chi}\,[\![v_h]\!]\,\|_{\mathcal{F}_h}^2 \end{aligned} \tag{5.4}$$

for functions $v_h \in V_h$, which we can rely on in the proofs by choosing $\varepsilon > 0$ in a convenient manner.

In order to state our results, we introduce the discrete energy function

$$\begin{aligned} E[\psi_h](t) := &\|\sqrt{\alpha_h(t)}\,\dot{\psi}_h(t)\|_{L^2}^2+\tfrac{b}{c^2}\int_0^t\|\sqrt{\alpha_h}\,\ddot{\psi}_h\|_{L^2}^2\,\mathrm{d}s \\ &+c^2\|\nabla_h\tilde{\psi}_h(t)\|_{L^2}^2+\|\sqrt{\chi}\,[\![\tilde{\psi}_h(t)]\!]\,\|_{\mathcal{F}_h}^2, \end{aligned}$$

for $t \in [0,T]$. We note that in the case $b = 0$, we have $\tilde{\psi}_h = \psi_h$, and we formally recover the energy of undamped linear wave equations.

Theorem 1. *Let $c > 0$, $b \geq 0$, and let $T > 0$ be a fixed time horizon. Let the coefficient $\alpha_h \in H^1(0,T;V_h)$ be such that the non-degeneracy condition (5.3) holds, where α_0 and α_1 are independent of the discretization parameters. Moreover, assume that there exists $\gamma \in (0,1)$ such that*

$$\|\dot{\alpha}_h/\alpha_h\|_{L^1L^\infty} = \int_0^T \sup_\Omega|\dot{\alpha}_h/\alpha_h|\,\mathrm{d}s \leq \gamma. \tag{5.5}$$

Then the semi-discrete problem (5.2) has a unique solution ψ_h such that it holds

$$\max_{t\in[0,T]} E[\psi_h](t) \leq C_{\mathrm{Th1}}\,E[\psi_h](0), \tag{5.6}$$

provided that the parameter β in (3.2) is sufficiently large. The constant $C_{\mathrm{Th1}} > 0$ does not depend on the mesh size, the number of faces of a mesh element, or the coefficients in the equation, but depends on the polynomial degree and on γ.

We postpone the proof of the theorem to the appendix.

Before moving to the error analysis, let us discuss how to obtain a bound on $c^2|\nabla_h\psi_h(t)|_{L^2}$ and $\frac{b}{c^2}|\nabla_h\dot{\psi}_h(t)|_{L^2}$ from the available bound on $c^2|\nabla_h\tilde{\psi}_h(t)|_{L^2}$. From the energy estimate (5.6), by recalling that $\tilde{\psi}_h = \psi_h + \frac{b}{c^2}\dot{\psi}_h$, we have

$$\begin{aligned} c^2\|\nabla_h\tilde{\psi}_h(t)\|_{L^2}^2 &= c^2\|\nabla_h\psi_h(t)\|_{L^2}^2+\tfrac{b^2}{c^2}\|\nabla_h\dot{\psi}_h(t)\|_{L^2}^2-2c^2(\nabla_h\psi_h(t),\tfrac{b}{c^2}\nabla_h\dot{\psi}_h(t))_{L^2} \\ &\lesssim E[\psi_h](0) \end{aligned} \tag{5.7}$$

for all $t \in [0,T]$. We can rely on the Fundamental theorem of calculus to show that

$$\begin{aligned} \|\nabla_h\psi_h(t)\|_{L^2} &= \left\|\int_0^t\nabla_h\dot{\psi}_h\,\mathrm{d}s+\nabla_h\psi_h(0)\right\|_{L^2} \\ &\leq \int_0^t\|\nabla_h\dot{\psi}_h\|_{L^2}\,\mathrm{d}s+\|\nabla_h\psi_h(0)\|_{L^2} \\ &\leq \sqrt{t}\|\nabla_h\dot{\psi}_h\|_{L^2(0,t;L^2)}+\|\nabla_h\psi_h(0)\|_{L^2}. \end{aligned} \tag{5.8}$$

By employing Young's inequality together with inequality (5.8) in estimate (5.7), we arrive at

$$\begin{aligned} &c^2\|\nabla_h\psi_h(t)\|_{L^2}^2+\tfrac{b^2}{c^2}\|\nabla_h\dot{\psi}_h(t)\|_{L^2}^2 \\ &\leq 2c^2\|\nabla_h\psi_h(t)\|_{L^2}^2+\tfrac{1}{2}\tfrac{b^2}{c^2}\|\dot{\psi}_h(t)\|_{L^2}^2+E[\psi_h](0) \\ &\lesssim 4c^2T\int_0^t\|\nabla_h\dot{\psi}_h\|_{L^2}^2\,\mathrm{d}s+4c^2\|\nabla_h\psi_h(0)\|_{L^2}^2+\tfrac{1}{2}\tfrac{b^2}{c^2}\|\dot{\psi}_h(t)\|_{L^2}^2+E[\psi_h](0). \end{aligned}$$

Therefore, we can conclude that

$$c^2\|\nabla_h\psi_h(t)\|_{L^2}^2+\tfrac{1}{2}\tfrac{b^2}{c^2}\|\nabla_h\dot{\psi}_h(t)\|_{L^2}^2\lesssim c^2T\int_0^t\|\nabla_h\dot{\psi}_h\|_{L^2}^2\,\mathrm{d}s+c^2\|\nabla_h\psi_h(0)\|_{L^2}^2+E[\psi_h](0).$$

Remark 2 *(Assuming $b>0$).* Let $b>0$. We have from above

$$c^2\|\nabla_h\psi_h(t)\|_{L^2}^2+\tfrac{1}{2}\tfrac{b^2}{c^2}\|\nabla_h\dot{\psi}_h(t)\|_{L^2}^2\lesssim c^2T\tfrac{c^2}{b^2}\int_0^t\tfrac{1}{2}\tfrac{b^2}{c^2}\|\nabla_h\dot{\psi}_h\|_{L^2}^2\,\mathrm{d}s+c^2\|\nabla_h\psi_h(0)\|_{L^2}^2+E[\psi_h](0).$$

By making use of Gronwall's inequality, we obtain

$$c^2\|\nabla_h\psi_h(t)\|_{L^2}^2+\tfrac{b^2}{c^2}\|\nabla_h\dot{\psi}_h(t)\|_{L^2}^2\lesssim\exp\left(CT^2\tfrac{c^4}{b^2}\right)(c^2\|\nabla_h\psi_{0,h}\|_{L^2}^2+E[\psi_h](0)).$$

We observe that this bound, however, degenerates as $b\to 0$.

5.2. Error analysis of the linearization

In this subsection, we state an *a priori* error estimate for the linear semi-discrete problem (5.2). We note that we also have to take the error of the variable coefficient α into account to be able to later employ a fixed-point argument and prove a convergence result for the Westervelt equation as well.

5.2.1. Error estimate in the energy norm

We decompose the approximation error by involving the interpolant as follows:

$$e=\underbrace{(\psi-\psi_I)}_{e_I}-\underbrace{(\psi_h-\psi_I)}_{e_h},$$

where ψ solves (5.1), ψ_h solves (5.2), and ψ_I is the interpolant introduced in Lemma 3. To simplify the exposition, we introduce the following auxiliary variables:

$$\tilde{e}=\tilde{\psi}-\tilde{\psi}_h,\quad \tilde{\psi}_I=\psi_I+\tfrac{b}{c^2}\dot{\psi}_I,\quad \tilde{e}_h=\tilde{\psi}_h-\tilde{\psi}_I,\quad \tilde{e}_I=\tilde{\psi}-\tilde{\psi}_I.$$

In order to formulate the convergence result, we also define the energy norm

$$||\psi_h||_E:=\left(\max_{t\in[0,T]}\|\dot{\psi}_h(t)\|_{L^2}^2+\tfrac{b}{c^2}\int_0^T\|\ddot{\psi}_h\|_{L^2}^2\,\mathrm{d}s+c^2\max_{t\in[0,T]}\|\nabla_h\tilde{\psi}_h(t)\|_{L^2}^2+\max_{t\in[0,T]}|\sqrt{\chi}\,[\![\tilde{\psi}_h(t)]\!]|_{\mathcal{F}_h}^2\right)^{1/2}.\tag{5.9}$$

Thanks to Lemma 3, we can estimate the interpolation error in this norm by

$$\|e_I\|_E^2\lesssim\max_{t\in[0,T]}\sum_{\kappa\in\mathcal{T}_h}h_\kappa^{2\mu-2}\left(c^2|\psi(t)|_{H^n(\kappa)}^2+(1+\tfrac{b^2}{c^2})|\dot{\psi}(t)|_{H^n(\kappa)}^2\right)+\tfrac{b}{c^2}\int_0^T\sum_{\kappa\in\mathcal{T}_h}h_\kappa^{2\mu-2}|\ddot{\psi}|_{H^n(\kappa)}^2\,\mathrm{d}s.\tag{5.10}$$

We are now ready to state the convergence result.

Theorem 2. *Let the assumptions of Theorem 1 hold. Let $\psi\in H^2(0,T;H_0^1(\Omega)\cap H^n(\Omega))$, where $n\geq 2$, be the solution of the linear initial-boundary value problem (5.1). Let ψ_h be the solution of the corresponding semi-discrete problem (5.2) with the approximate initial data given by*

$$(\psi_h(0),\dot{\psi}_h(0))=((\psi_0)_I,(\psi_1)_I),$$

and the parameter β in (3.2) chosen sufficiently large according to Theorem 1. Then the following bound holds for the discretization error:

$$\begin{aligned}\|\psi-\psi_h\|_E^2\leq C_{\mathrm{Th}2}\Bigg\{&h^{2\mu-2}\max_{t\in[0,T]}\sum_{\kappa\in\mathcal{T}_h}\left(|\dot{\psi}(t)|_{H^n(\kappa)}^2+|\psi(t)|_{H^n(\kappa)}^2\right)+h^{2\mu-2}\int_0^T\sum_{\kappa\in\mathcal{T}_h}\left(|\ddot{\psi}|_{H^n(\kappa)}^2+|\dot{\psi}|_{H^n(\kappa)}^2\right)\mathrm{d}s\\&+\int_0^T\|(\alpha-\alpha_h)\ddot{\psi}\|_{L^2}^2\,\mathrm{d}s\Bigg\},\end{aligned}\tag{5.11}$$

where $\mu=\min\{n,p+1\}$ and $h=\max_{\kappa\in\mathcal{T}_h}h_\kappa$, provided that $\gamma\in(0,1)$ in (5.5) is sufficiently small. The constant $C_{\mathrm{Th}2}>0$ depends on the polynomial degree, but not on the mesh size.

The proof of this auxiliary result is given in the appendix. Now we proceed directly with the analysis of the nonlinear model.

6. Analysis of the nonlinear model

Our next aim is to analyze the semi-discretization of the Westervelt equation given by (4.4). To this end, we will rely on our results for the linearized problem together with a fixed-point argument. We point out, however, that we have to restrict ourselves to the case $b > 0$. The reason for this is that we will need a uniform in h bound for $\|\ddot{\psi}_h\|_{L^2L^2}$. Such a bound follows from ψ_h being bounded in the energy norm, defined in (5.9), only if $b > 0$.

Theorem 3. *Let $c > 0$, $b > 0$, and $k \in \mathbb{R}$. Let the final time $T > 0$ be given and assume that the initial-boundary value problem (2.2) for the Westervelt equation has a solution*

$$\psi \in H^2(0,T; H_0^1(\Omega) \cap H^n(\Omega)), \text{ where } n > 1 + d/2,$$

for which it holds that

$$0 < \alpha_0 \leq 1 - 2k\dot{\psi} \leq \alpha_1 \qquad \text{in } \overline{\Omega} \times [0,T]$$

for some $\alpha_0, \alpha_1 > 0$. Assume that the polynomial degree $p \geq 2$ and that the approximate initial conditions are given by

$$(\psi_h(0), \dot{\psi}_h(0)) = ((\psi_0)_I, (\psi_1)_I). \tag{6.1}$$

Then for sufficiently small $h = \max_{\kappa \in \mathcal{T}_h} h_\kappa$ and

$$M(\psi) = \max_{t\in[0,T]} |\psi(t)|^2_{H^n} + \max_{t\in[0,T]} |\dot{\psi}(t)|^2_{H^n} + \max_{t\in[0,T]} \|\dot{\psi}(t)\|^2_{L^\infty} + \int_0^T (|\ddot{\psi}|^2_{H^n} + \|\ddot{\psi}\|^2_{L^\infty} + |\dot{\psi}|^2_{H^n})\,\mathrm{d}s,$$

the corresponding semi-discrete problem (4.4) for the Westervelt equation has a unique solution $\psi_h \in H^2(0,T;V_h)$ that satisfies the following error bound:

$$||\psi - \psi_h||^2_E \leq C_{\mathrm{Th}3}\, h^{2\mu-2} \sum_{\kappa\in\mathcal{T}_h} \left\{ \max_{t\in[0,T]} \left(|\dot{\psi}(t)|^2_{H^n(\kappa)} + |\psi(t)|^2_{H^n\kappa)} \right) + \int_0^T \left(|\ddot{\psi}|^2_{H^n(\kappa)} + |\dot{\psi}|^2_{H^n(\kappa)} \right) \mathrm{d}s \right\},$$

with $\mu = \min\{n, p+1\}$, provided that the parameter β in (3.2) is sufficiently large. The constant $C_{\mathrm{Th}3} > 0$ depends on $M(\psi)$ and on the polynomial degree, but not on the mesh size.

Proof. We conduct the proof by employing the Banach fixed-point theorem. Therefore, we first need to define a fixed-point map. We begin by introducing the ball

$$\mathcal{B}_h = \left\{ w_h \in H^2(0,T;V_h) : \quad ||\psi - w_h||^2_E \leq C_{\mathrm{Th}3}\, h^{2\mu-2} \sum_{\kappa\in\mathcal{T}_h} \max_{t\in[0,T]} \mathcal{E}_\kappa[\psi](t)\, (w_h(0), \dot{w}_h(0)) = (\psi_{0,h}, \psi_{1,h}) \right\},$$

where we have used the notation

$$\mathcal{E}_\kappa[\psi](t) = |\dot{\psi}(t)|^2_{H^n(\kappa)} + |\psi(t)|^2_{H^n(\kappa)} + \int_0^t \left(|\ddot{\psi}|^2_{H^n(\kappa)} + |\dot{\psi}|^2_{H^n(\kappa)} \right) \mathrm{d}s.$$

The constant $C_{\mathrm{Th}3} > 0$ will be made precise below.

Step 1: Defining the fixed-point map.
For $w_h \in \mathcal{B}_h$, we then define the operator $\mathcal{J} : w_h \mapsto \psi_h$, where ψ_h solves

$$\begin{cases} ((1 - 2k\dot{w}_h)\ddot{\psi}_h,\ v_h)_{L^2} + a_h(\tilde{\psi}_h, v_h) = 0 \qquad \text{for all } v_h \in V_h,\ t \in (0,T), \\ (\psi_h(0), \dot{\psi}_h(0)) = (\psi_{0,h}, \psi_{1,h}). \end{cases} \tag{6.2}$$

The operator $\mathcal{J}$ is well-defined thanks to the well-posedness result of Theorem 1, whose assumptions we verify below. We note that the set $\mathcal{B}_h$ is non-empty when $C_{\mathrm{Th}3} \geq C_{\mathrm{Th}2}$ because the solution of the linear problem (5.2) with $\alpha_h = \alpha$ belongs to it. Moreover, $\mathcal{B}_h$ is closed with respect to topology induced by $\|\cdot\|_E$.

Step 2: The self-mapping property.
We next want to verify that $\mathcal{J}(\mathcal{B}_h) \subset \mathcal{B}_h$. Let $w_h \in \mathcal{B}_h$. To show that $\psi_h = \mathcal{J}(w_h) \in \mathcal{B}_h$, we rely on Theorems 1 and 2, which guarantee stability and convergence for the linearized problem. We choose the variable coefficient in the linear model to be $\alpha_h = 1 - 2k\dot{w}_h$ and check that all the assumptions of these theorems are satisfied. In particular, we have to justify the non-degeneracy assumption (5.3) and the smallness of $\dot{\alpha}_h/\alpha_h$ in (5.5).

We already know that $\alpha_h = 1 - 2k\dot{w}_h \in H^1(0,T;V_h)$. We next rely on the inverse estimate given in Lemma 1 and properties of the interpolant stated in Lemma 3 to verify the non-degeneracy assumption (5.3) on α_h.

The coefficient α_h does not degenerate. Fix $t \in [0,T]$. We can pick an element $\hat{\kappa} \in \mathcal{T}_h$, such that

$$\max_{x\in\overline{\Omega}} |\dot{w}_h(x,t)| = \max_{x\in\hat{\kappa}} |\dot{w}_h(x,t)|. \tag{6.3}$$

By involving the local interpolant and then relying on the inverse estimate, we find that

$$\begin{aligned}
\max_{x\in\overline{\Omega}} |\dot{w}_h(x,t)|^2 &= \max_{x\in\hat{\kappa}} |\dot{w}_h(x,t)|^2 \\
&\overset{\text{triangle ineq.}}{\lesssim} \|\dot{\psi}_{I,\hat{\kappa}}(t) - \dot{w}_h(t)\|^2_{L^\infty(\hat{\kappa})} + \|\dot{\psi}_{I,\hat{\kappa}}(t)\|^2_{L^\infty(\hat{\kappa})} \\
&\overset{\text{inverse est.}}{\lesssim} h_{\hat{\kappa}}^{-d} \|\dot{\psi}_{I,\hat{\kappa}}(t) - \dot{w}_h(t)\|^2_{L^2(\hat{\kappa})} + \|\dot{\psi}_{I,\hat{\kappa}}(t)\|^2_{L^\infty(\hat{\kappa})} \\
&\overset{\text{triangle ineq.}}{\lesssim} h_{\hat{\kappa}}^{-d} \left(\|\dot{\psi}_{I,\hat{\kappa}}(t) - \dot{\psi}(t)\|^2_{L^2(\hat{\kappa})} + \|\dot{\psi}(t) - \dot{w}_h(t)\|^2_{L^2(\hat{\kappa})} \right) + \|\dot{\psi}_{I,\hat{\kappa}}(t)\|^2_{L^\infty(\hat{\kappa})}.
\end{aligned} \tag{6.4}$$

We can estimate the last three terms on the right-hand side of (6.4) by employing the stability and approximation properties of the interpolant, and the fact that $w_h \in \mathcal{B}_h$. By doing so, we obtain

$$\begin{aligned}
\max_{x\in\overline{\Omega}} |\dot{w}_h(x,t)|^2 &\lesssim h_{\hat{\kappa}}^{2\mu-d} |\dot{\psi}(t)|^2_{H^s(\hat{\kappa})} + h_{\hat{\kappa}}^{-d} h^{2\mu-d}\, C_{\mathrm{Th}3} \sum_{\kappa\in\mathcal{T}_h} \max_{t\in[0,T]} \mathcal{E}_\kappa[\psi](t) + \|\dot{\psi}_{I,\hat{\kappa}}(t)\|^2_{L^\infty(\hat{\kappa})} \\
&\lesssim h^{2\mu-d} |\dot{\psi}(t)|^2_{H^s(\Omega)} + C_{\mathrm{Th}3} \left(\frac{h}{h_{\hat{\kappa}}}\right)^d h^{2\mu-2-d} \sum_{\kappa\in\mathcal{T}_h} \max_{t\in[0,T]} \mathcal{E}_\kappa[\psi](t) + \|\dot{\psi}_{I,\hat{\kappa}}(t)\|^2_{L^\infty(\hat{\kappa})},
\end{aligned}$$

recalling that due to our assumptions, we have $\mu = \min\{n, p+1\} > 1 + d/2$. By using the L^∞ stability of the interpolant and the assumption on quasi-uniformity of the mesh, we infer

$$\max_{x\in\overline{\Omega}} |\dot{w}_h(x,t)|^2 \le C_1 M(\psi) \left(h^{2\mu-d} + C_{\mathrm{Th}3}(M(\psi))\, h^{2\mu-2-d} + 1 \right) := m \tag{6.5}$$

for every $t \in [0,T]$, where the constant $C_1 > 0$ above does not depend on the mesh size. We refer to (6.8) below for the exact form of $C_{\mathrm{Th}3}(M(\psi))$. By taking the maximum over $t \in [0,T]$ in (6.5), we further have

$$\|\dot{w}_h\|_{C(\overline{\Omega}\times[0,T])} \le \sqrt{m}.$$

We then choose $M(\psi)$ and h sufficiently small so that

$$0 < \alpha_0 \le 1 - 2|k|\sqrt{m} \le \alpha_h = 1 - 2k\dot{w}_h \le 1 + 2|k|\sqrt{m} \le \alpha_1$$

in $\overline{\Omega} \times [0,T]$.

The quotient $\dot{\alpha}_h/\alpha_h$ is sufficiently small. The assumption on $\dot{\alpha}_h/\alpha_h$ in Theorems 1 and 2 can be verified as follows:

$$\begin{aligned}
\left\| \frac{\dot{\alpha}_h}{\alpha_h} \right\|_{L^1L^\infty} = \left\| \frac{-2k\ddot{w}_h}{1-2k\dot{w}_h} \right\|_{L^1L^\infty} &\le \frac{2|k|}{1-2|k|\sqrt{m}} \|\ddot{w}_h\|_{L^1L^\infty} \\
&\le \frac{2|k|}{1-2|k|\sqrt{m}} \sqrt{T} \|\ddot{w}_h\|_{L^2L^\infty}.
\end{aligned}$$

We can bound $\|\ddot{w}_h\|_{L^2L^\infty}$ in a similar fashion as (6.3)–(6.5) by relying on the interpolant and inverse estimates. Note, however that this bound would degenerate if $b \to 0$ because by the definition of the energy norm (5.9) we have

$$\|\ddot{w}_h\|_{L^2L^2} \le \frac{c^2}{b} \|w_h\|_E. \tag{6.6}$$

Therefore, we find

$$\int_0^T \max_{x\in\overline{\Omega}} |\ddot{w}_h(s)|^2 \,\mathrm{d}s \lesssim h^{2\mu-d} \int_0^T |\ddot{\psi}(s)|^2_{H^s(\Omega)} \,\mathrm{d}s + \frac{c^4}{b^2} C_{\mathrm{Th}3} h^{2\mu-2-d} \sum_{\kappa\in\mathcal{T}_h} \max_{t\in[0,T]} \mathcal{E}_\kappa[\psi](t) + \int_0^T \|\ddot{\psi}_{I,\hat{\kappa}}(s)\|^2_{L^\infty(\hat{\kappa})} \,\mathrm{d}s,$$

from which it follows that

$$\int_0^T \max_{x\in\overline{\Omega}} |\ddot{w}_h(s)|^2 \,\mathrm{d}s \leq C_2 m, \tag{6.7}$$

where the constant $C_2 > 0$ does not depend on the mesh size, but it degenerates if b tends to zero. Therefore, for Theorem 2 to hold, we need that

$$\gamma := \frac{2|k|}{1-2|k|\sqrt{m}}\sqrt{TC_2 m}$$

is sufficiently small, which we can achieve by decreasing $M(\psi)$ and h.

Choosing the constant $C_{\mathrm{Th}3}$ so that $\mathcal{J}$ is a self-mapping. We have therefore verified all the assumptions of Theorems 1 and 2. On account of Theorem 2 and the resulting error estimate (5.11), we conclude that problem (6.2) has a unique solution $\psi_h \in C^2([0,T]; V_h)$ that satisfies

$$||\psi - \psi_h||_E^2 \leq C_{\mathrm{Th}2}\left(h^{2\mu-2}\sum_{\kappa\in\mathcal{T}_h}\max_{t\in[0,T]}\mathcal{E}_\kappa[\psi](t) + \max_{t\in[0,T]}\|\alpha(t)-\alpha_h(t)\|_{L^2}^2\int_0^T \|\ddot{\psi}\|_{L^\infty(\Omega)}^2\,\mathrm{d}s\right).$$

Noting that the error in α can be estimated according to

$$\begin{aligned}\max_{t\in[0,T]}\|\alpha(t)-\alpha_h(t)\|_{L^2}^2 &= \max_{t\in[0,T]}\|2k\dot{\psi}(t) - 2k\dot{w}_h(t)\|_{L^2}^2\\ &\leq 4k^2 C_{\mathrm{Th}3}\,h^{2\mu-2}\sum_{\kappa\in\mathcal{T}_h}\max_{t\in[0,T]}\mathcal{E}_\kappa[\psi](t),\end{aligned}$$

since $w_h \in \mathcal{B}_h$, we obtain

$$||\psi - \psi_h||_E^2 \leq C_{\mathrm{Th}2}\,(1 + 4k^2 C_{\mathrm{Th}3} M(\psi))h^{2\mu-2}\sum_{\kappa\in\mathcal{T}_h}\max_{t\in[0,T]}\mathcal{E}_\kappa[\psi](t).$$

For sufficiently small $M(\psi)$ such that $1 - 4k^2 C_{\mathrm{Th}2} M(\psi) > 0$, we can choose $C_{\mathrm{Th}3}$ as

$$C_{\mathrm{Th}3} := \frac{C_{\mathrm{Th}2}}{1 - 4k^2 C_{\mathrm{Th}2} M(\psi)}. \tag{6.8}$$

This choice of the constant $C_{\mathrm{Th}3}$ implies that

$$||\psi - \psi_h||_E^2 \leq C_{\mathrm{Th}3} h^{2\mu-2}\sum_{\kappa\in\mathcal{T}_h}\max_{t\in[0,T]}\mathcal{E}_\kappa[\psi](t);$$

in other words, $\psi_h \in \mathcal{B}_h$.

Step 3: Contractivity.
To prove that the operator $\mathcal{J}$ is strictly contractive, take $w_h^{(1)}$, $w_h^{(2)} \in \mathcal{B}_h$ and set $\psi_h^{(1)} = \mathcal{J}(w_h^{(1)})$, $\psi_h^{(2)} = \mathcal{J}(w_h^{(2)}) \in \mathcal{B}_h$. Denote $W_h = w_h^{(1)} - w_h^{(2)}$. Then the difference $\Psi_h = \psi_h^{(1)} - \psi_h^{(2)}$ satisfies the problem

$$((1 - 2k\dot{w}_h^{(1)})\ddot{\Psi}_h, v_h)_{L^2} + a_h(\tilde{\Psi}_h, v_h) = (2k\,\dot{W}_h\,\ddot{\psi}_h^{(2)}, v_h)_{L^2}, \qquad v_h \in V_h \tag{6.9}$$

for all time, with zero initial data. This equation corresponds to equation (A.4) satisfied by the approximation error in the proof of Theorem 2. Therefore, testing (6.9) with $\dot{\tilde{\Psi}}_h$ and proceeding analogously to the proof of Theorem 2 results in the estimate

$$||\Psi_h||_E^2 \lesssim 4k^2(1 + \tfrac{b}{c^2})\alpha_0^{-1}\left\{\int_0^T \|\ddot{\psi}_h^{(2)}\|_{L^\infty(\Omega)}^2\,\mathrm{d}s\right\}\max_{t\in[0,T]}|\dot{W}_h(t)|_{L^2}^2.$$

This inequality then corresponds to estimate (A.9) in the proof of Theorem 2 if we formally set the interpolant error to zero. We further have

$$||\Psi_h||_E^2 \lesssim 4k^2(1 + \tfrac{b}{c^2})\alpha_0^{-1}\left\{\int_0^T \|\ddot{\psi}_h^{(2)}\|_{L^\infty(\Omega)}^2\,\mathrm{d}s\right\}||W_h||_E^2. \tag{6.10}$$

We can bound $\|\ddot{\psi}_h^{(2)}\|^2_{L^2L^\infty}$ by proceeding in the same way as in (6.6)–(6.7). This term can thus be made sufficiently small by reducing $M(\psi)$ and h. From estimate (6.10), we then conclude that $\mathcal{J}$ is contractive for sufficiently small $M(\psi)$ and h.

On account of Banach's contraction principle, the mapping $\mathcal{J}$ has a unique fixed-point $\psi_h = \mathcal{J}(\psi_h) \in \mathcal{B}_h$, which is, in turn, the unique solution of the nonlinear semi-discrete problem (4.4) with approximate initial data (6.1). □

7. Computational DG approach for nonlinear sound waves

Starting from the semi-discrete equation (4.4), this section describes the numerical treatment and solution process involving the assembly of an equation in matrix-vector form and the time-integration scheme that is used. Discontinuous Galerkin approaches for nonlinear acoustic waves based on a first-order conservation system are investigated in, e.g., [38,56,57].

7.1. The matrix form of the semi-discrete problem

For the purpose of carrying out our numerical experiments, we consider here a more general case than before of having either a non-zero source term or inhomogeneous Dirichlet boundary conditions. We present the numerical treatment of the latter case; the simpler case of having a non-zero source term f can be treated in an analogous manner.

Let $\psi = g$ on $\Gamma_D = \partial\Omega$, where the function g is assumed to be sufficiently smooth on Γ_D, compatible with initial data. The Dirichlet conditions are imposed in a weak sense; see [19, Chapter 4, Section 4.2.2] for a detailed explanation. Therefore, in our semi-discrete weak form, the following terms arise additionally on the right-hand side:

$$\int_{\Gamma_D} -c^2\,\tilde{g}\,\left(\nabla v\cdot\underline{\mathbf{n}}\right)\,\mathrm{d}S + \int_{\Gamma_D}\chi\,\tilde{g}\,v\,\mathrm{d}S,$$

where, analogously to before, we have used the auxiliary notation $\tilde{g} = g + \frac{b}{c^2}\dot{g}$.

The semi-discrete form of (4.4) then reads as

$$\mathbf{M}\underline{\ddot{\psi}} + \left(\mathbf{K} - \mathbf{D} - \mathbf{D}^\top + \mathbf{P}\right)\left(\underline{\psi} + \tfrac{b}{c^2}\underline{\dot{\psi}}\right) - \mathcal{T}[\cdot, \underline{\dot{\psi}}, \underline{\ddot{\psi}}] = \underline{\mathbf{w}}, \tag{7.1}$$

where $\mathbf{M}$ denotes the standard mass matrix and $\mathbf{K}$ the stiffness matrix. In addition, we assemble the nonlinearity tensor $\mathcal{T}$, the DG penalty matrix $\mathbf{P}$, the DG jump matrix $\mathbf{D}$, and the Dirichlet data vector $\underline{\mathbf{w}}$. Furthermore, we introduce the shorthand notation $\mathbf{A} := \mathbf{K} - \mathbf{D} - \mathbf{D}^\top + \mathbf{P}$.

We therefore have a second-order system of ordinary differential equations with a nonlinear term on the right-hand side, which now remains to be solved by a suitable time-integration scheme. Herein the initial data approximations $(\psi_h(0), \dot{\psi}_h(0)) = (\psi_{0,h}, \psi_{1,h}) \in V_h \times V_h$ are represented in the finite element basis via the coefficient vectors $\underline{\psi}_0$ and $\underline{\psi}_1$ such that for the ODE-system we have $\underline{\psi}(0) = \underline{\psi}_0$ and $\underline{\dot{\psi}}(0) = \underline{\psi}_1$.

7.2. Time integration

In order to integrate the system of ordinary differential equations (7.1) in time, we employ either the Newmark scheme or the Newmark-type Generalized-α method; we refer to [31,36] for a similar strategy. The nonlinear term is resolved via a fixed-point iteration during the solving stage of the predictor-corrector scheme. The termination criterion that checks the relative change of the solution-vector between iteration steps is employed. In the experiments with realistic physical data, where we observe the nonlinear steepening of the wave front in our computational domain, we choose the Generalized-α scheme because it allows to add targeted numerical damping to the higher modes and subdue Gibbs oscillations.

The algorithm for conducting the timestep $n \mapsto n+1$ within the Generalized-α scheme is given in the following. It involves $\underline{\psi}^n$, $\underline{\dot{\psi}}^n$, and $\underline{\ddot{\psi}}^n$ as the approximations of ψ, $\dot{\psi}$, and $\ddot{\psi}$ at time level $t^n = n\Delta t$, where Δt is a suitable timestep. The so-called effective mass matrix

$$\mathbf{M}^* = (1-\alpha_m)\mathbf{M} + (1-\alpha_f)\gamma_{\mathrm{nm}}\Delta t\frac{b}{c^2}\mathbf{A} + (1-\alpha_f)\beta_{\mathrm{nm}}\Delta t^2\mathbf{A}$$

and the intermediate time $t_{n+1,\alpha} := (1-\alpha_f)t^{n+1} + \alpha_f t^n$ are also used within the time-stepping algorithm.

Predictor step:

$$\underline{\psi}_{\mathrm{pred}} = \underline{\psi}^n + \Delta t\underline{\dot{\psi}}^n + \frac{\Delta t^2}{2}(1-2\beta_{\mathrm{nm}})\underline{\ddot{\psi}}^n, \qquad \underline{\psi}_{\mathrm{pred},\alpha} = (1-\alpha_f)\underline{\psi}_{\mathrm{pred}} + \alpha_f\underline{\psi}^n$$
$$\underline{\dot{\psi}}_{\mathrm{pred}} = \underline{\dot{\psi}}^n + (1-\gamma_{\mathrm{nm}})\Delta t\underline{\ddot{\psi}}^n, \qquad \underline{\dot{\psi}}_{\mathrm{pred},\alpha} = (1-\alpha_f)\underline{\dot{\psi}}_{\mathrm{pred}} + \alpha_f\underline{\dot{\psi}}^n$$

Iteration over $\kappa = 1, 2, 3, \ldots, \kappa_{\max}$ with $\underline{\psi}_1 = \underline{\psi}^n$, $\underline{\dot{\psi}}_1 = \underline{\dot{\psi}}^n$, $\underline{\ddot{\psi}}_1 = \underline{\ddot{\psi}}^n$

Table 1
Numerical parameters used in the experiments.

	Test case 1	Test case 2	Test case 3	Test case 4
Newmark scheme	$\beta_{\text{nm}} = 0.25$ $\gamma_{\text{nm}} = 0.5$	$\beta_{\text{nm}} = 4/9$ $\gamma_{\text{nm}} = 5/6$	$\beta_{\text{nm}} = 4/9$ $\gamma_{\text{nm}} = 5/6$	$\beta_{\text{nm}} = 4/9$ $\gamma_{\text{nm}} = 5/6$
Generalized-α scheme	$\alpha_m = 0$ $\alpha_f = 0$	$\alpha_m = 0$ $\alpha_f = 1/3$		
DG penalty	$\beta = 10$	$\beta = 10$	$\beta = 250$	$\beta = 1750$

α-Combinations

$$\underline{\psi}_{\kappa,\alpha} = (1-\alpha_f)\underline{\psi}_{\kappa} + \alpha_f \underline{\psi}^n$$
$$\underline{\dot{\psi}}_{\kappa,\alpha} = (1-\alpha_f)\underline{\dot{\psi}}_{\kappa} + \alpha_f \underline{\dot{\psi}}^n$$
$$\underline{\ddot{\psi}}_{\kappa,\alpha} = (1-\alpha_m)\underline{\ddot{\psi}}_{\kappa} + \alpha_m \underline{\ddot{\psi}}^n$$

Solve algebraic system

$$\mathbf{M}^* \underline{\ddot{\psi}}_{\kappa+1} = \underline{\mathbf{w}}(t_{n+1,\alpha}) - \alpha_m \mathbf{M} \underline{\ddot{\psi}}^n - \frac{b}{c^2}\mathbf{A}\underline{\dot{\psi}}_{\text{pred},\alpha} - \mathbf{A}\underline{\psi}_{\text{pred},\alpha} + \mathcal{T}\left[\cdot, \underline{\dot{\psi}}_{\kappa,\alpha}, \underline{\ddot{\psi}}_{\kappa,\alpha}\right]$$

Corrector step:

$$\underline{\psi}_{\kappa+1} = \underline{\psi}_{\text{pred}} + \beta_{\text{nm}}\Delta t^2 \underline{\ddot{\psi}}_{\kappa+1}$$
$$\underline{\dot{\psi}}_{\kappa+1} = \underline{\dot{\psi}}_{\text{pred}} + \gamma_{\text{nm}}\Delta t \underline{\ddot{\psi}}_{\kappa+1}$$

Check termination criterion:

If $\dfrac{\|\underline{\ddot{\psi}}_{\kappa+1} - \underline{\ddot{\psi}}_{\kappa}\|}{\|\underline{\ddot{\psi}}_{\kappa+1}\|} < \text{TOL}$, **set** $\begin{cases} \underline{\psi}^{n+1} = \underline{\psi}_{\kappa+1} \\ \underline{\dot{\psi}}^{n+1} = \underline{\dot{\psi}}_{\kappa+1} \\ \underline{\ddot{\psi}}^{n+1} = \underline{\ddot{\psi}}_{\kappa+1} \end{cases}$

and **break iteration**

end iteration

The numerical parameters that are used in the forthcoming experiments can be found in Table 1. The physical and discretization parameters for each experiment are given below in their respective sections.

In Table 1, the values β_{nm} and γ_{nm} denote the parameters in the Newmark scheme given in the formulas above. The numbers α_m and α_f are the additional parameters in the Generalized-α scheme. TOL is the relative tolerance in the termination criterion of the fixed-point-iteration, $\kappa_{\max}$ stands for the maximum number of iterations after which the algorithm should abort. Those parameters were chosen to be $\text{TOL} = 10^{-5}$ and $\kappa_{\max} = 100$ throughout all experiments. Finally, β is the DG-penalty term introduced in (3.2).

8. Numerical results

In this section, we perform numerical experiments to illustrate our theoretical findings. The first two numerical tests are conducted in a two-dimensional computational setting based on a MATLAB implementation. The third and fourth, three-dimensional experiments were implemented in SPEED—a parallel, high-order spectral finite-element FORTRAN code [40].

8.1. Test case 1: exact solution known

In our first example, we simulate the Westervelt equation (2.1) with a given source term f on the right hand side, which we choose as

$$f = \left[16\pi^2(c^2-1)\sin(4\pi t) + 64\pi^3 b\cos(4\pi t)\right]\sin(4\pi x) + \left[64\pi^3 k \sin(4\pi t)\cos(4\pi t)\right]\sin(4\pi x)^2.$$

In this way, the exact solution is given by $\psi = \sin(4\pi x)\sin(4\pi t)$, which we use in the error analysis. In this numerical experiment, all the physical quantities involved are assumed to be dimensionless. Our computational domain is given by the rectangle $\Omega = (0,1) \times (0, \frac{2}{3}\sqrt{3})$. We tessellate it with N_{elem} polygonal elements in two ways: a regular hexagonal pattern and a random way using polygons with different number of edges each; see Fig. 1 for exemplary depictions of the resulting grids. The ratio of domain length and width is chosen such that the regular tessellation bears the same element shapes in the interior as well as (exactly halfed elements) on all four sides yielding control over the mesh quality. The initial conditions and Dirichlet boundary data are set to correspond to the values of ψ at time zero and on the boundary, respectively.

We choose the coefficients in the equation to be $c = 1$, $b = 10^{-5}$, $\beta_a = 10^{-4}$, and the mass density is $\rho = 1$. The time-discretization is conducted with final time $T = 0.8$ and the Newmark scheme, where the timestep size is always adapted in such a way, that the time-discretization error does not dominate in Fig. 2 and the convergence with respect to the number of elements can be observed.

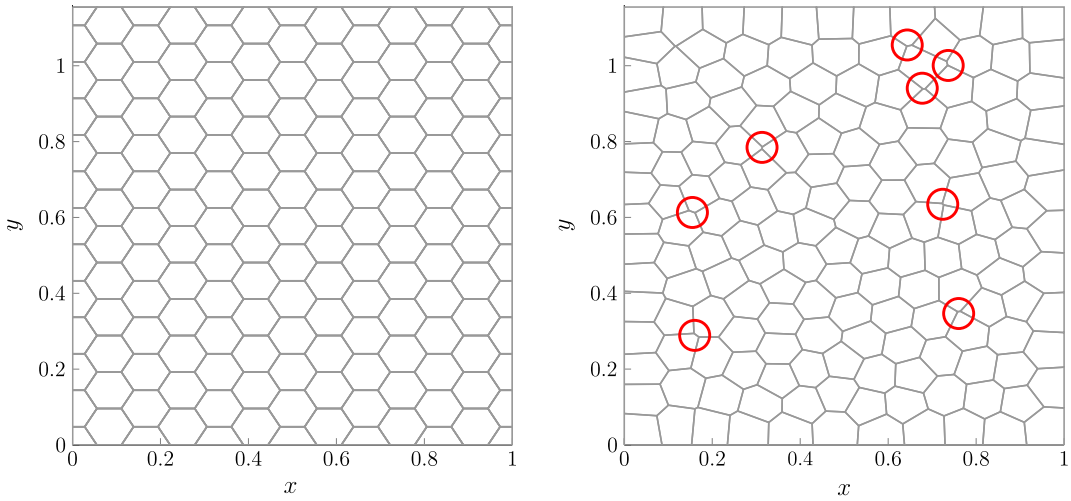

Fig. 1. Computational domain with exemplary polygonal grids. **(left)** regular hexagonal grid, **(right)** grid with arbitrary polygonal structure and highlighting of a few exemplary "small" edges, making the grid only suitable under the weaker assumptions discussed in Remark 1.

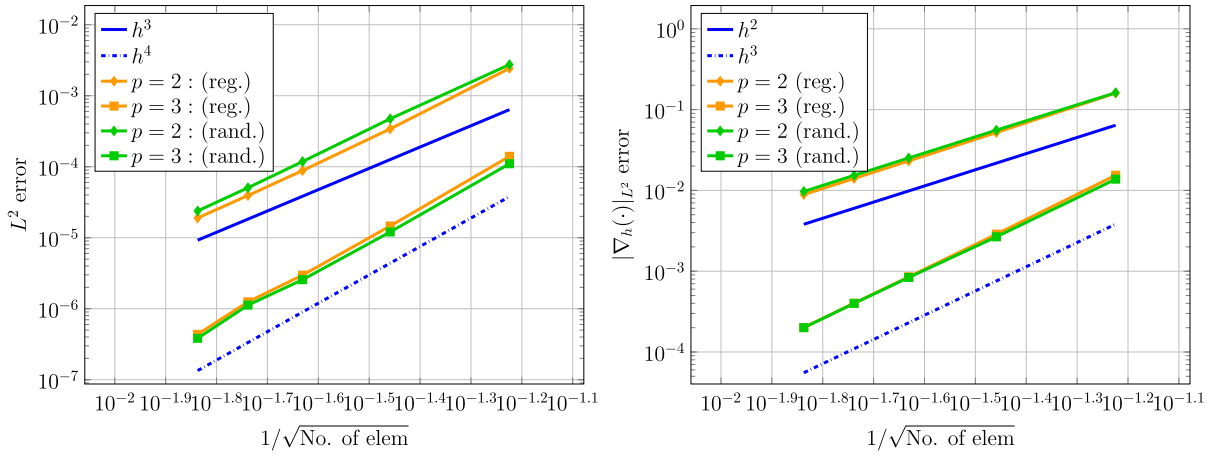

Fig. 2. L^2 and $|\nabla_h(\cdot)|_{L^2}$ errors of ψ_h at final time for four sequentially refined polygonal meshes and second- and third-order polynomials, comparing a sequence of regular polygonal grids (reg.) with a sequence of irregular ones (rand.).

We perform this experiment on a sequence of regular grids that satisfy our mesh assumptions and on an unstructured grid which might not; see Fig. 1. Such unstructured meshes satisfy the weaker assumptions discussed in Remark 1, which is why we want to test if we still observe the same order of convergence when using them.

Fig. 2 displays convergence results for five sequentially refined polygonal meshes, where we have employed polynomials of degree $p = 2$ and $p = 3$. As a reference, on the five levels the unstructured grid consists out of 281, 827, 1828, 2998, and 4727 elements, respectively. As expected in practice for DG methods, the L^2-error of the acoustic velocity potential converges with the order h^{p+1}; see, e.g., [28].

8.2. Test case 2: exact solution unknown

Our second example features a more realistic setting. The computational domain is chosen to be a rectangle with dimensions $H = 0.02$ m and $L = \frac{3}{\sqrt{3}} \cdot 0.02\,\text{m}$; see Fig. 3 left. The physical parameters are now set to

$$c = 1500\ \text{m/s},\ b = 6 \times 10^{-9}\ \text{m}^2/\text{s},\ \beta_a = 7,\ \text{and}\ \rho = 1000\ \text{kg/m}^3.$$

The time horizon is $T = 2.4 \times 10^{-5}$ s, resolved by a step size of $\text{dt} = 2 \times 10^{-9}$ s. Instead of a non-zero source term f, we employ inhomogeneous Dirichlet conditions. The excitation signal is given in the form $g(x, y, t) = g^{(s)}(x, y) \cdot g^{(t)}(t)$. Herein the temporal part responsible for the initialization of the wave oscillations is given by

$$g^{(t)}(t) = \begin{cases} \left(\frac{ft}{2}\right)^2 A \sin(\omega t), & t < \frac{2}{f}\,\text{s}, \\ A \sin(\omega t), & t \geq \frac{2}{f}\,\text{s}, \end{cases}$$

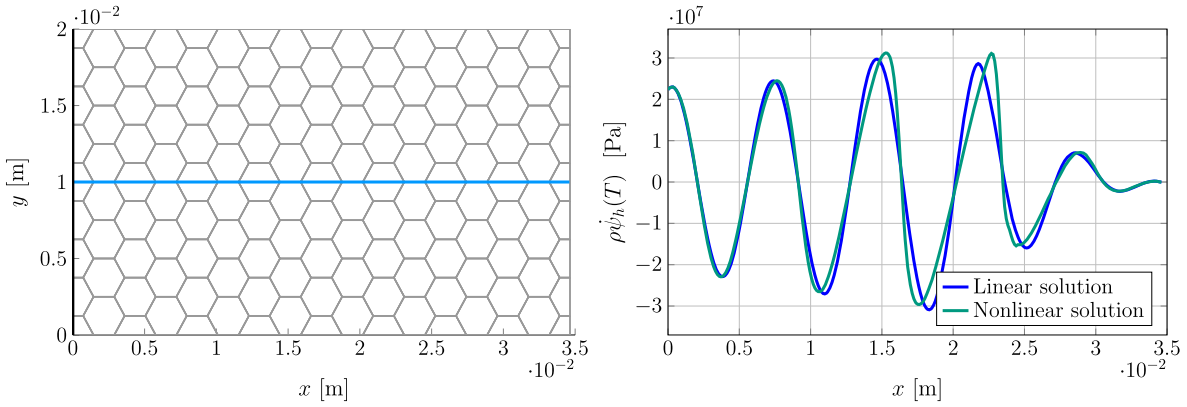

Fig. 3. (left) Computational domain with exemplary polygonal grid. The left boundary is the excitation part, where the Dirichlet data g is non-zero. At remaining boundary parts homogeneous Dirichlet data are imposed. The blue line is the axis of symmetry over which the solution is evaluated on the right. **(right)** Computed acoustic pressure field $u_h = \rho\dot{\psi}_h$ over the horizontal axis of symmetry of the channel at final time T of a simulation with increased amplitude $A = 0.0175\ \mathrm{m}^2/\mathrm{s}^2$, plotted together with the pressure wave obtain by solving the linear damped wave equation with same boundary and initial data. (For interpretation of the colors in the figure(s), the reader is referred to the web version of this article.)

while the spatial part is given by a mollifier-type function in order to get a spatially smooth transition between the inhomogeneous excitation and the homogeneous remaining boundary data. In particular, we have

$$g^{(s)}(x,y) = \begin{cases} 0, & x = 0\,\mathrm{m},\ y = 0\,\mathrm{m} \\ \exp\left(1 - \frac{1}{1-\left|\frac{1}{0.005}(y-0.005)\right|^2}\right), & x = 0\,\mathrm{m},\ 0\,\mathrm{m} < y < 0.005\,\mathrm{m} \\ 1, & x = 0\,\mathrm{m},\ 0.005\,\mathrm{m} \le y \le 0.015\,\mathrm{m} \\ \exp\left(1 - \frac{1}{1-\left|\frac{1}{0.005}(y-0.015)\right|^2}\right), & x = 0\,\mathrm{m},\ 0.015\,\mathrm{m} < y < 0.02\,\mathrm{m} \\ 0, & x = 0\,\mathrm{m},\ y = 0.02\,\mathrm{m} \\ 0, & 0\,\mathrm{m} < x \end{cases}$$

We therefore employ a spatially smooth, temporally modulated sinusoidal excitation with driving frequency $f = 210$ kHz and amplitude $A = 0.01\ \mathrm{m}^2/\mathrm{s}^2$, where ω denotes the angular frequency $\omega = 2\pi f$. Fig. 3 displays a plot of the acoustic pressure $u_h = \rho\dot{\psi}_h$ along the horizontal axis of symmetry of the channel at final time T. To better observe the nonlinear steepening, the figure also contains a pressure wave obtained by solving the linear damped wave equation (i.e., Westervelt's equation with $k = 0$).

We next want to analyze the behavior of the numerical solution with respect to h- and p-refinement. However, in this more realistic setting an exact solution is unknown. Therefore, instead of tracking the deviation from a given solution, we track a given quantity of interest. Here we choose to compute

$$Q(\psi_h) := \|\psi_h\|_{L^\infty(0,T;L^2(\Omega))}, \tag{8.1}$$

on different discretization levels. We note that

$$Q(\psi) - \|\psi_h - \psi\|_{L^\infty(0,T;L^2(\Omega))} \le Q(\psi_h) \le Q(\psi) + \|\psi_h - \psi\|_{L^\infty(0,T;L^2(\Omega))},$$

and so we expect that, for p fixed, $Q(\psi_h)$ behaves asymptotically as $q_1 + q_2 \cdot h^{p+1}$ for some constants q_1 and q_2.

h-refinement. We restrict ourselves to structured, quasi-uniform polygonal meshes consisting of $N_{\mathrm{elem}} \in \{220, 312, 420, 544, 684, 840, 1104, 1740, 2664\}$ elements. The polynomial degree is set to $p = 3$. Values $Q(\psi_h)$ for these levels of refinement are plotted in Fig. 4 on the left. In order to observe the convergence order, we perform a least-square fit of the $(h, Q(\psi_h))$ data pairs. We obtain a fitted curve

$$Q_f(h) = q_1 + q_2 \cdot h^4,$$

where q_1 and q_2 are subject to the least-square fit. The fitted curve Q_f with optimized parameters reads approximately as

$$Q_f(h) = 1.322735 \cdot 10^{-4} - 504.613929 \cdot h^4$$

and is plotted in Fig. 4 on the left as well. As expected, we observe $O(h^{p+1})$ convergence. The extrapolated value for the quantity of interest $Q_f(0)$ evaluates to $1.322735 \cdot 10^{-4}$.

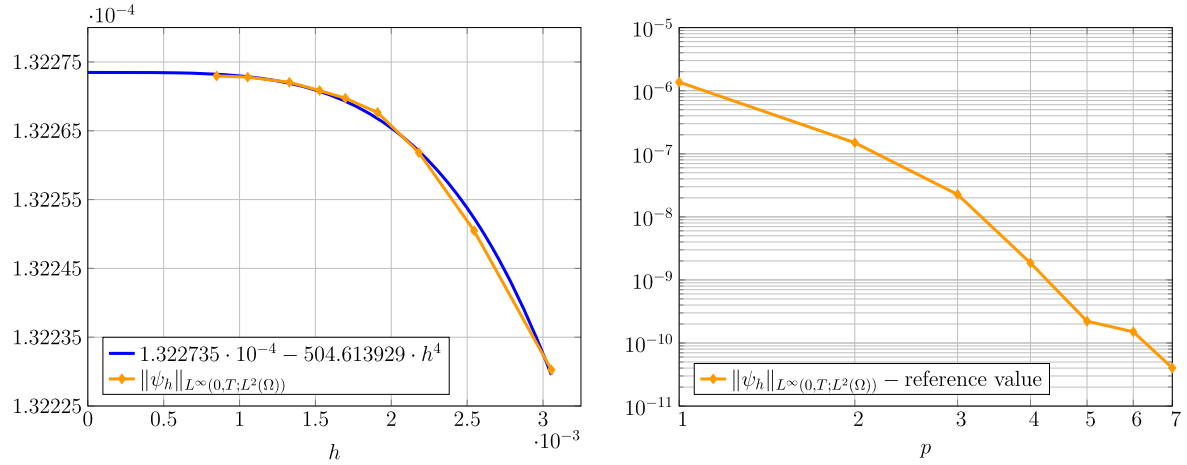

Fig. 4. (left) The quantity of interest $Q(\psi_h) = \|\psi_h\|_{L^\infty(0,T;L^2(\Omega))}$ computed on a sequence of polygonal meshes with third-order polynomials and a least-square fitted extrapolation-curve of order h^4. **(right)** Deviation of the computed quantity of interest $Q(\psi_h)$ from a reference value as a function of p on a fixed mesh.

p-refinement. We also perform a refinement analysis of the quantity of interest with respect to the polynomial degree. Here we choose a fixed mesh with $N_{\text{elem}} = 312$ elements and successively increase the polynomial degree $p \in \{1, 2, ..., 7\}$, where it should be mentioned that even though our theory holds for $p \geq 2$, the case $p = 1$ yields a similar result as well. The deviations of the resulting quantities from a reference value are plotted in Fig. 4 on the right. As the reference, we choose the extrapolated value of the h-refinement with degree $p = 4$. For $p = 7$, the quantity of interest evaluates to $1.322730 \cdot 10^{-4}$ with the deviation from the extrapolated reference value below $7.6 \cdot 10^{-5}$ %.

8.3. Test case 3: a three-dimensional example

Our third example is performed in a three dimensional setting, where we use the discontinuous Galerkin approach in a hybrid way. Fig. 5 shows an image of the computational geometry consisting of six different material blocks. The blocks differ in all relevant material parameters, given in Table 2. This example is motivated by nonlinear sound propagation in inhomogeneous media. These types of computational settings often arise in medical ultrasound when the sound waves propagate through human body with varying speed of sound and other medium parameters; see, for example, [46]. We, therefore, solve here Westervelt's equation

$$(1 - 2k(x)\dot{\psi})\ddot{\psi} - \operatorname{div}(c^2(x)\nabla\psi) - \operatorname{div}(b(x)\nabla\dot{\psi}) = 0$$

with coefficients in $L^\infty(\Omega)$. The pressure is then computed via $u = \varrho(x)\psi_t$, where the mass density is now as well in $L^\infty(\Omega)$. The stabilization function has the form

$$\chi_{|F} = \begin{cases} \beta \max\limits_{\kappa \in \{\kappa^+, \kappa^-\}} c_{|\kappa}^2 \dfrac{p^2}{h_\kappa} & \text{for all } F \in \mathcal{F}_h^i, \quad F \subset \partial\kappa^+ \cap \partial\kappa^-, \\ \beta c_{|\kappa}^2 \dfrac{p^2}{h_\kappa} & \text{for all } F \in \mathcal{F}_h^b, \quad F \subset \partial\kappa. \end{cases}$$

To save computational power, the blocks are meshed and discretized individually via conforming spectral elements within each block, while the discontinuous Galerkin approach deals with the non-matching grids on the interfaces.

Setup of the experiment. Block 1 has a width and length of 0.025 m and a height of 0.01 m; see Fig. 5. On its bottom surface, the wave excitation takes place. We use an excitation signal in the form of a Dirichlet condition similarly to Section 8.2. The four walls of the block are equipped with homogeneous Neumann/symmetry boundary conditions, its top surface with a homogeneous Dirichlet condition, except at the interfaces to the blocks 2 to 5. Those are truncated four-sided pyramids which are aligned in a regular way between blocks 1 and 6, each with a height of 0.01 m and homogeneous Dirichlet conditions on its four walls. Block 6, with a height of 0.04 m and the remaining measures as for Block 1, covers the upper part of the geometry, again equipped with homogeneous Neumann/symmetry conditions on its four sides and homogeneous Dirichlet conditions at top and bottom, except for the interfaces with the blocks 2 to 5.

The excitation signal is given by

$$g(t, x, y, z) = g^{(t)}(t) = \begin{cases} \left(\frac{ft}{2}\right)^2 A \sin(\omega t), & t < \frac{2}{f}\,\text{s} \\ 0, & t \geq \frac{2}{f}\,\text{s}; \end{cases}$$

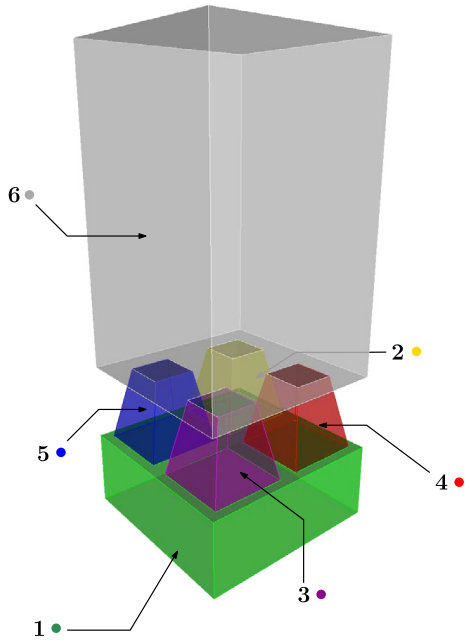

Fig. 5. Test case 3: Computational domain with six different material blocks. Each block has its own material parameters, mesh, and ansatz space. Interface coupling is done via the DG approach.

Table 2
Physical parameters of different material blocks.

Material block	1 ●	2 ●	3 ●	4 ●	5 ●	6 ●
c [m/s]	1500	1000	1000	3000	750	1500
b $[\mathrm{m}^2/\mathrm{s}]$	6×10^{-9}	4×10^{-9}	4×10^{-2}	4×10^{-9}	6×10^{-9}	6×10^{-9}
β_a	5	4	4	7	4	5
ρ $[\mathrm{kg}/\mathrm{m}^3]$	1000	1250	1250	2000	1500	1000

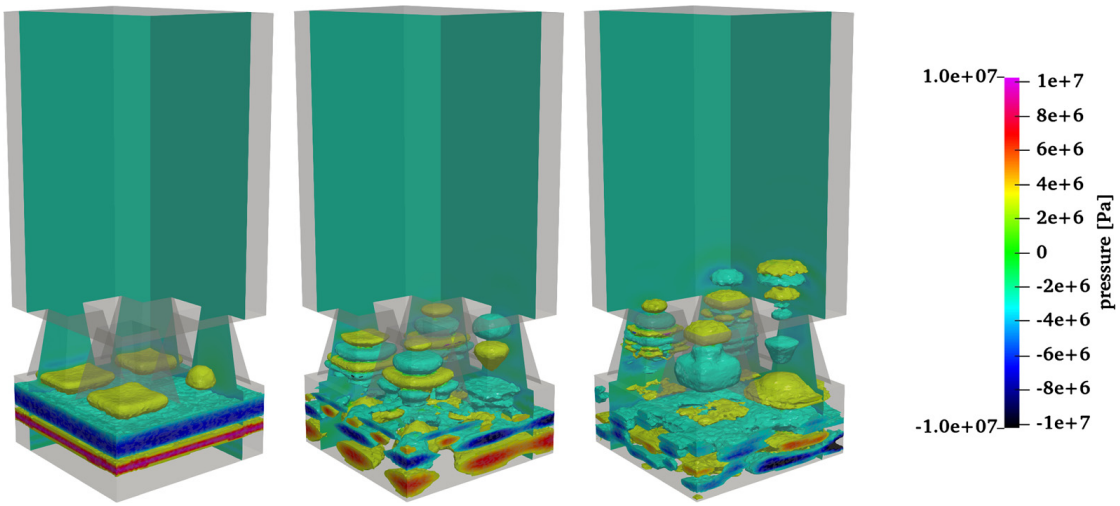

Fig. 6. Iso-volumina at time steps **(left)** 12000 **(middle)** 19000 **(right)** 24600 of the highest acoustic pressure amplitudes (in absolute value) $u_h = \rho \dot{\psi}_h$ during wave propagation through the four connecting channels of the computational domain. The orientation of the images is the same as in Fig. 5.

i.e., by a cut-off pulse-version of the continuous excitation signal used before. We use such a signal here in order to avoid interference within the block 1 originating from reflections off the walls between the interfaces to blocks 2 to 5. Amplitude and frequency are chosen as before. For the time discretization again the Generalized-α method is used with the final time $T = 2.217 \cdot 10^{-5}$ s, resolved with a step size of $\Delta t = 10^{-9}$ s.

Fig. 6 shows snapshots of the solution computed with $p = 2$ on 260730 elements. We observe iso-volumina of the highest acoustic pressure amplitudes at different time steps which show how the wave propagates through the four separate channels connecting the base block with the top block. Especially the deviations in the speed of sound are visible as the

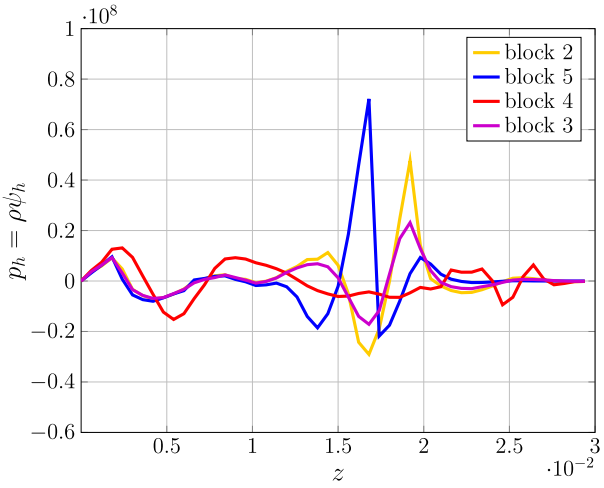

Fig. 7. Pressure signal within the four connecting "pillar"-like blocks 2, 3, 4, and 5 of the computational domain at time step 24400, showing the influence of different speeds of sound and damping parameters.

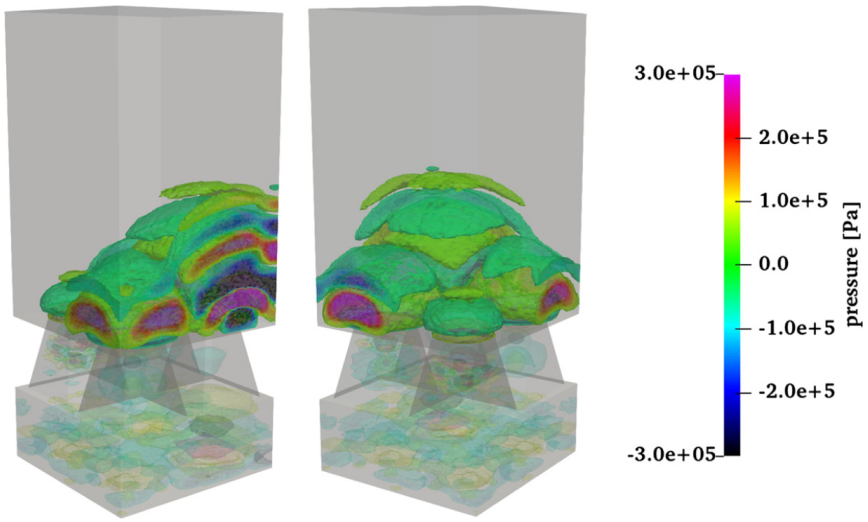

Fig. 8. Iso-volumina of the highest acoustic pressure amplitudes at time step 24600 within the upper part of the computational domain, where the individual waves coming from the connecting channels merge. **(left)** Same orientation of the domain as in Fig. 6 **(right)** View rotated by $\approx 90°$ at the same time step.

wave propagates much faster in block 4 (on the right) than, for example, in block 5 (on the left). This effect can also be seen in Fig. 7, where the pressure signal is plotted along the central axes of the four "pillars" at a given time step.

While the signals corresponding to blocks 2 and 3 in Fig. 7 are traveling with the same speed (cf. Table 2), the signal in block 3 is much more damped compared to block 2, due to the damping parameter b being much higher there. In contrast to that, the signal from block 5 is slower, while also higher in amplitude due to the changes in material properties and the signal in block 4 with the highest speed of sound has already passed through the "pillar"-like structure and decayed in amplitude afterwards due to spreading into the empty space of block 6.

Fig. 8 shows iso-volumina of the acoustic pressure field as well, this time focusing on the wave propagation in the upper part of the computational domain, i.e., block 6 where the four individual waves coming from the four connecting channels again merge together into a single acoustic wave field. We observe decrease in the amplitude compared to Fig. 6 due to the wave spreading.

As before, exact solution is not available. Therefore, we again track the quantity of interest given by (8.1). We evaluate it over an h-refinement with quadratic shape functions on meshes with mesh-sizes of $h_j = 0.001\sqrt[3]{2^{-j}}$, $j = 0, \ldots, 7$. The results are depicted in Fig. 9.

We observe a convergence of the quantity of interest towards a value of around $1.064 \cdot 10^{-5}$ as h approaches zero; see Fig. 9 on the right. We note, however, that allowing for the jumping material coefficients lies beyond the theory presented in this work. Therefore, we can conclude that the application of the spectral discontinuous Galerkin method on a problem with varying coefficients is feasible, while a rigorous convergence analysis is left for future work.

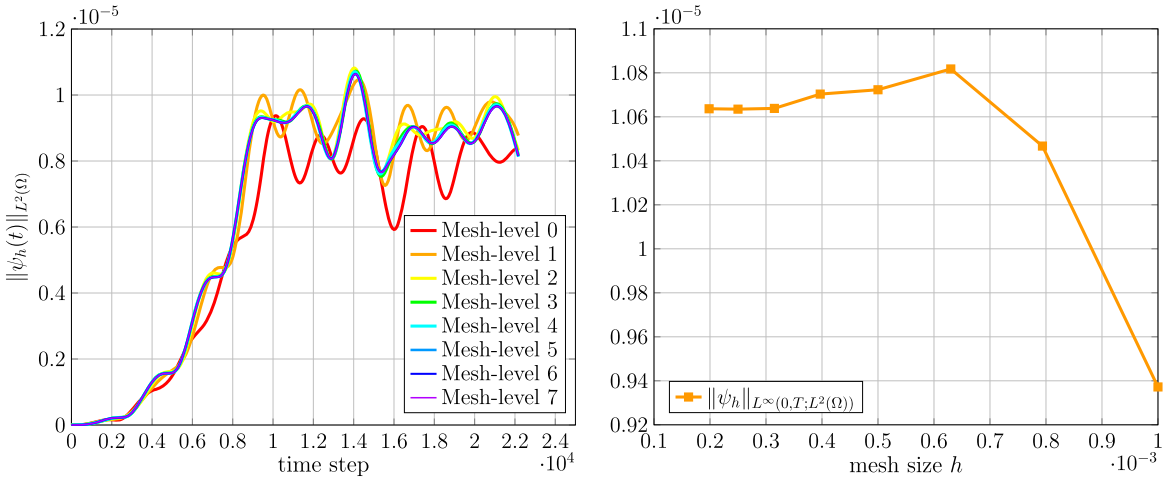

Fig. 9. Quantity of interest over an h-refinement with quadratic shape functions. **(left)** $L^2(\Omega)$ norm of the numerical solution over the course of time for all tested levels of refinement **(right)** Respective $L^\infty(0,T;L^2(\Omega))$-norm results on all 8 mesh levels in order to observe convergence.

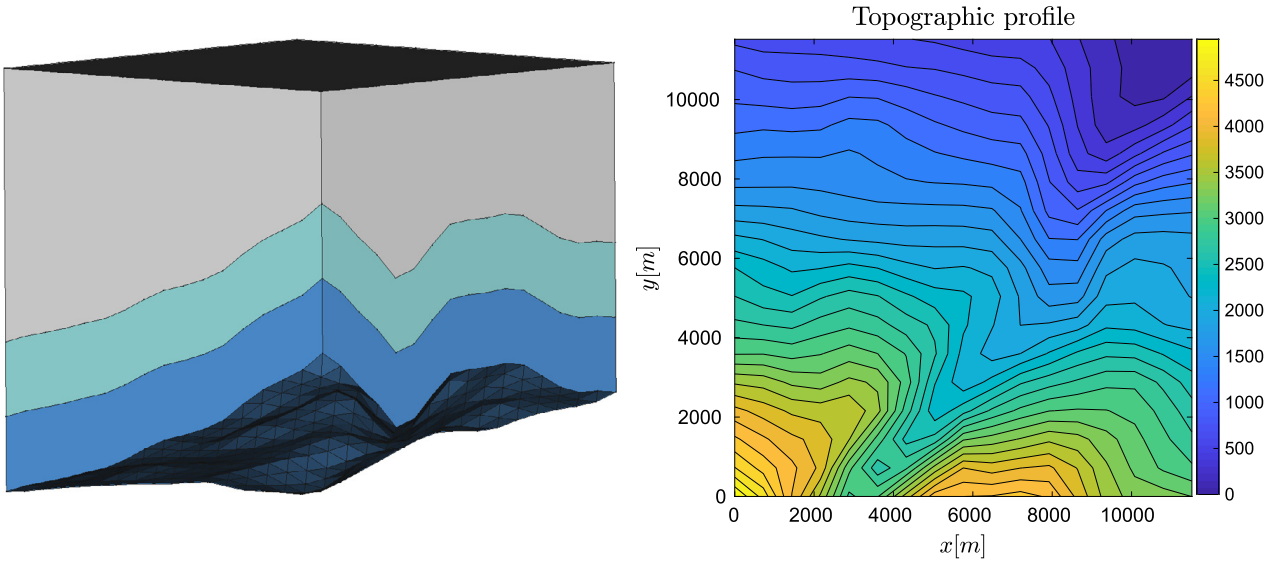

Fig. 10. **(left)** Acoustic domain consisting out of different layers of air with different material properties. **(right)** Topographic profile of the mountain range below the acoustic layers.

8.4. Test case 4: wave scattering

Our final example deals on a larger spatial scale, where seismic events take place. In particular, we are motivated by nonlinear effects that can be observed in seismic wave propagation [27,45]. In this experiment, the acoustic medium is a rectangularly cut-out block of air above a mountain-like range. On the top-surface of the acoustic domain, a wave is excited vertically and is traveling towards the mountain's surface where it gets reflected. On its way towards the mountain's surface, the wave travels through different layers of the acoustic medium bearing different material properties.

In the applicational context, these could be layers of air-currents of different temperature and hence varying density ρ and speed of sound c^2. The coupling between those layers is again performed by employing the discontinuous-Galerkin approach in a hybrid way to couple non-conforming meshes. This feature is especially useful in the context of locally refined grids. In the present case, this is done by resolving the layers with more complex dynamics closer to the reflecting mountain surface finer than the most upper air-layer, resulting in non-conforming mesh-interfaces between the layers.

Fig. 10 (left) shows an image of the computational domain highlighting the different layers in use. The bottom and middle layer have a height of 2000 m each. The top layer has a minimal thickness of 3000 m. Fig. 10 (right) shows the topographic profile of the mountain range below the air layers. The depicted area has a width and length of 11520 m and is located on the earth's surface with mid-point at 11.51855 °E, 48.07305 °N (Munich-area, Germany, with the Alps in the south). The elevation model was constructed from data in the *Digital Elevation Database* (http://srtm.csi.cgiar.org/). The altitudes have been smoothed and are exaggerated by a factor of 40 and normalized to a minimum of 0 m to create a more dynamic profile.

Table 3
Physical parameters of different air layers.

Material block	Top layer	Mid layer	Bottom layer
c [m/s]	351.88	331.30	315.77
ρ [kg/m^3]	1.1455	1.2922	1.4224

As for the material parameters, we use the following varying values, see Table 3.
The damping and nonlinearity parameters were chosen to be constant with values $b = 0.00005\,\frac{\mathrm{m}^2}{\mathrm{s}}$, $\beta_a = 1.2$. The upper surface of the top layer is equipped with a time-varying Dirichlet conditions:

$$g(t,x,y,z) = e^{-\frac{1}{2}\left[\left(\frac{x-\mu_x}{\sigma_x}\right)^2+\left(\frac{y-\mu_y}{\sigma_y}\right)^2\right]} \begin{cases} \left(\frac{ft}{2}\right)^2 A\,\sin(\omega t), & t < \frac{2}{f}\,\mathrm{s} \\ \left(1-\left(\frac{f\left(t-\frac{2}{f}\right)}{2}\right)^2\right) A\,\sin(\omega t), & \frac{2}{f}\,\mathrm{s} \le t < \frac{4}{f}\,\mathrm{s}; \\ 0, & \text{else}, \end{cases}$$

with parameters: $\mu_x = \mu_y = 5760\,\mathrm{m}, \sigma_x = \sigma_y = 1000\,\mathrm{m}$, $f = 0.1\,\mathrm{Hz}$, $A = 0.01\,\mathrm{m}^2/\mathrm{s}^2$. To the lower surface of the bottom block which constitutes the mountain's surface, we prescribe homogeneous Neumann conditions. On the remaining surfaces encasing the block of air, we employ the Engquist–Majda absorbing boundary conditions, i.e. $c\partial_n\psi = -\psi_t$ [24], to prevent unphysical reflections traveling back into the domain.

Due to the kilometer scale, the time-horizon of 90 s for this simulation is much larger than in the previous experiments on the centimeter scale. The simulation time is resolved once more by the Generalized-α-method with 30000 timesteps. For spatial discretization, 46516 elements for the top-layer, 82500 elements for the middle layer and 82264 elements for the bottom layer have been used, hence featuring a mesh that is refined more towards the reflection surface, where mesh-coupling between the non-conforming material layers is done via the discontinuous Galerkin method. In this example, the value of the penalty parameter in the DG approach is set to be larger than before. By this we allow for poorly shaped elements at the interfaces, and we do enforce the solution to have no significant jump at the interface between the layers. We note that this does not deteriorate the quality of the solution since the best approximation property of a constrained space having zero jump is in this special case of the same quality as of the unconstrained case. This is due to the fact that our mesh generator starts from a conforming surface mesh for the layers. The value $p = 2$ is chosen as degree of the basis functions.

Fig. 11 shows the snapshots of the acoustic potential at certain timesteps, such that the reflection of the wave on the mountain's surface can be observed.

9. Conclusion

We have considered the discretization of the Westervelt's nonlinear wave equation with strong damping to model sound propagation with losses through homogeneous media. For the space discretization, we proposed a high-order discontinuous Galerkin scheme that can support general polygonal/polyhedral meshes. The fully discrete formulation is then obtained based on employing either the Newmark scheme or the Newmark-type Generalized-α method. The nonlinear term is resolved via a fixed-point iteration during the solving stage of the predictor-corrector scheme.

For the semidiscrete formulation we proved existence, stability and *a priori* error estimates in a suitable (mesh-dependent) energy norm, under the assumption that the polynomial approximation order p is such that $p \ge 2$. To accomplish the theoretical analysis, preventing the equation from degenerating, and handling the nonlinearity in the model which involves the derivatives in time of the acoustic velocity potential, we made use of the Banach fixed-point theorem combined with a stability and convergence analysis of a linear wave equation with a variable coefficient in front of the second time derivative.

A wide set of two- and three-dimensional numerical experiments validate the theoretical convergence bounds and illustrate the practical performance of the proposed method on a practical test case stemming from medical ultra-sound applications and nonlinear seismic waves. Future developments include the extension of the proposed analysis to coupled non-linear elasto-acoustic wave propagation problems, by expanding on the recent results of [1,2] where discontinuous Galerkin and discontinuous Galerkin spectral element methods for the linear elasto-acoustic coupled problem have been proposed. Further research will also cover the extensive testing of the proposed method on a set of challenging test cases stemming from practical applications.

Declaration of competing interest

The authors declare that they have no known competing financial interests or personal relationships that could have appeared to influence the work reported in this paper.

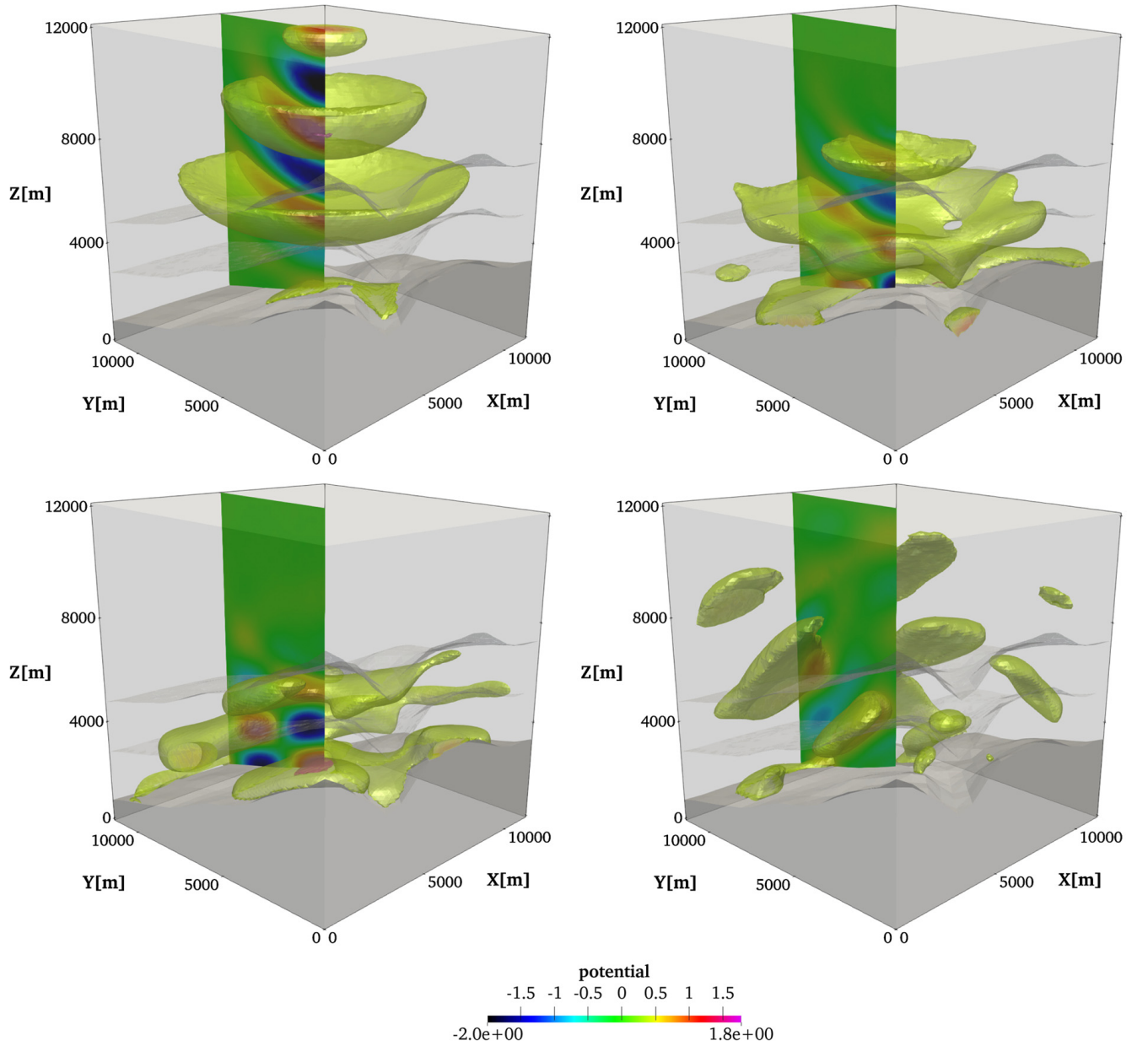

Fig. 11. Slicing half-plane (green) through the computational domain depicting values of the acoustic potential ψ together with iso-volumina $\{(x, y, z)^\top \in \Omega \mid \psi(t, x, y, z) \geq 0.4\}$ at time steps **(top left)** 13000, **(top right)** 17000, **(bottom left)** 19000, **(bottom right)** 24000. The gray base symbolizes the mountain range which is not simulated.

Acknowledgements

We would like to thank the reviewers for their insightful comments and remarks. Moreover, we are grateful to Bernhard Maier (Karlsruhe Institute of Technology) for pointing out an incorrect argument in a previous version of the manuscript.

P.F. Antonietti has been partially funded by PRIN grant n. 201744KLJL funded by the Ministry of Education, Universities and Research (MIUR). P.F. Antonietti and I. Mazzieri also acknowledge the financial support given by INdAm-GNCS.

M. Muhr, V. Nikolić, and B. Wohlmuth acknowledge the financial support provided by the Deutsche Forschungsgemeinschaft under the grant number WO 671/11-1.

Appendix A

We present here the proofs of Theorems 1 and 2.

Proof of Theorem 1. The linearized problem is non-degenerate and $\alpha_h \in H^1(0, T; V_h)$, and so local-in-time existence of a solution $\psi_h \in H^2(0, T_h; V_h)$ for some $T_h \leq T$ follows by relying on the standard theory of linear ordinary differential

equations; cf. [51, Theorem 1.44] and [43, Theorem 4.2]. The upcoming energy estimate will allow us to extend the existence interval to $[0, T]$.

We next focus on proving stability. In energy analysis of second-order wave equations, the first time derivative of the solution is a natural choice of test function. However, due to the presence of a varying coefficient α_h in our case, we would need to additionally test with a suitably scaled second time derivative. We combine these ideas and choose $v_h = \dot{\tilde{\psi}}_h = \dot{\psi}_h + \frac{b}{c^2}\ddot{\psi}_h$ as a test function.

Taking $v_h = \dot{\tilde{\psi}}_h$ in (5.2), integrating over $(0, t)$, where $t \leq T_h$, and performing integration by parts with respect to time leads to the identity

$$\begin{aligned} &\int_0^t (\alpha_h \ddot{\psi}_h, \dot{\tilde{\psi}}_h)_{L^2}\,\mathrm{d}s + \tfrac{1}{2}c^2\|\nabla_h\tilde{\psi}_h(s)\|_{L^2}^2\Big|_0^t + \tfrac{1}{2}\|\sqrt{\chi}\,[\![\tilde{\psi}_h(s)]\!]\|_{\mathcal{F}_h}^2\Big|_0^t \\ &= \langle \{\!\{c^2\nabla_h\tilde{\psi}_h(s)\}\!\}, [\![\tilde{\psi}_h(s)]\!]\rangle_{\mathcal{F}_h}\Big|_0^t. \end{aligned} \tag{A.1}$$

Above, we have made use of the fact that

$$\langle \{\!\{c^2\nabla_h\tilde{\psi}_h\}\!\}, [\![\dot{\tilde{\psi}}_h]\!]\rangle_{\mathcal{F}_h} + \langle [\![\tilde{\psi}_h]\!], \{\!\{c^2\nabla_h\dot{\tilde{\psi}}_h\}\!\}\rangle_{\mathcal{F}_h} = \frac{\mathrm{d}}{\mathrm{d}t}\langle \{\!\{c^2\nabla_h\tilde{\psi}_h\}\!\}, [\![\tilde{\psi}_h]\!]\rangle_{\mathcal{F}_h}.$$

We can employ Lemma 4 and inequality (5.4) to obtain

$$\begin{aligned} &\tfrac{1}{2}c^2\|\nabla_h\tilde{\psi}_h\|_{L^2}^2 + \tfrac{1}{2}\|\sqrt{\chi}\,[\![\tilde{\psi}_h]\!]\,\|_{\mathcal{F}_h}^2 - c^2\langle \{\!\{\nabla_h\tilde{\psi}_h\}\!\}, [\![\tilde{\psi}_h]\!]\rangle_{\mathcal{F}_h} \\ &\geq C_1(c^2\|\nabla_h\tilde{\psi}_h\|_{L^2}^2 + \|\sqrt{\chi}\,[\![\tilde{\psi}_h]\!]\,\|_{\mathcal{F}_h}^2) \end{aligned}$$

for all $t \in [0, T_h]$, provided that parameter β in (3.2) is sufficiently large. Similarly, we obtain

$$\begin{aligned} &\tfrac{1}{2}c^2\|\nabla_h\tilde{\psi}_h(0)\|_{L^2}^2 + \|\sqrt{\chi}\,[\![\tilde{\psi}_h(0)]\!]\,\|_{\mathcal{F}_h}^2 - \langle \{\!\{c^2\nabla_h\tilde{\psi}_h(0)\}\!\}, [\![\tilde{\psi}_h(0)]\!]\rangle_{\mathcal{F}_h} \\ &\leq C_2(c^2\|\nabla_h\tilde{\psi}_h(0)\|_{L^2}^2 + \|\sqrt{\chi}\,[\![\tilde{\psi}_h(0)]\!]\,\|_{\mathcal{F}_h}^2). \end{aligned}$$

The constants C_1, $C_2 > 0$ above are independent of c, b, or the mesh size, but depend on the polynomial degree p. It remains to estimate the α_h-term in (A.1). We recall how the auxiliary state $\tilde{\psi}_h$ is defined in (4.5) and employ integration by parts with respect to time, which results in

$$\begin{aligned} \int_0^t (\alpha_h \ddot{\psi}_h, \dot{\tilde{\psi}}_h)_{L^2}\,\mathrm{d}s &= \tfrac{b}{c^2}\int_0^t \|\sqrt{\alpha_h}\,\ddot{\psi}_h\|_{L^2}^2\,\mathrm{d}s + \int_0^t (\alpha_h\ddot{\psi}_h, \dot{\psi}_h)_{L^2}\,\mathrm{d}s \\ &= \int_0^t \left(\tfrac{b}{c^2}\|\sqrt{\alpha_h}\,\ddot{\psi}_h\|_{L^2}^2 - \tfrac{1}{2}\|\sqrt{\dot{\alpha}_h}\dot{\psi}_h\|_{L^2}^2\right)\mathrm{d}s \\ &\quad + \tfrac{1}{2}\|\sqrt{\alpha_h(s)}\dot{\psi}_h(s)\|_{L^2}^2\Big|_0^t. \end{aligned}$$

From here, we can further estimate the last term to obtain

$$\begin{aligned} \int_0^t (\alpha_h \ddot{\psi}_h, \dot{\tilde{\psi}}_h)_{L^2}\,\mathrm{d}s &\geq \tfrac{b}{c^2}\int_0^t \|\sqrt{\alpha_h}\,\ddot{\psi}_h\|_{L^2}^2\,\mathrm{d}s + \tfrac{1}{2}\|\sqrt{\alpha_h(s)}\dot{\psi}_h(s)\|_{L^2}^2\Big|_0^t \\ &\quad - \tfrac{1}{2}\int_0^t \sup_{x\in\Omega}\left|\frac{\dot{\alpha}_h(x)}{\alpha_h(x)}\right| \cdot \|\sqrt{\alpha_h}\dot{\psi}_h\|_{L^2}^2\,\mathrm{d}s \\ &\geq \tfrac{b}{c^2}\int_0^t \|\sqrt{\alpha_h}\,\ddot{\psi}_h\|_{L^2}^2\,\mathrm{d}s + \tfrac{1}{2}\|\sqrt{\alpha_h(s)}\dot{\psi}_h(s)\|_{L^2}^2\Big|_0^t \\ &\quad - \tfrac{1}{2}\max_{s\in[0,T_h]}\|\sqrt{\alpha_h(s)}\dot{\psi}_h(s)\|_{L^2}^2 \int_0^T \sup_{x\in\Omega}\left|\frac{\dot{\alpha}_h(x)}{\alpha_h(x)}\right|\mathrm{d}s, \end{aligned}$$

where we have additionally employed the fact that $t \leq T_h \leq T$ in the last step. By combining our previously derived estimates, we arrive at

$$
\begin{aligned}
&\tfrac{1}{2}\|\sqrt{\alpha_h(t)}\dot{\psi}_h(t)\|_{L^2}^2 + C_1c^2\|\nabla_h\tilde{\psi}_h(t)\|_{L^2}^2 \\
&+ \tfrac{b}{c^2}\int_0^t \|\sqrt{\alpha_h}\,\ddot{\psi}_h\|_{L^2}^2\,\mathrm{d}s + C_1\|\sqrt{\chi}\,[\![\tilde{\psi}_h(t)]\!]\|_{\mathcal{F}_h}^2 \\
&\leq \tfrac{1}{2}\|\sqrt{\alpha_h(0)}\dot{\psi}_h(0)\|_{L^2}^2 + C_2\left(c^2\|\nabla_h\tilde{\psi}_h(0)\|_{L^2}^2 + \|\sqrt{\chi}\,[\![\tilde{\psi}_h(0)]\!]\,\|_{\mathcal{F}_h}^2\right) \\
&+ \tfrac{1}{2}\max_{s\in[0,T_h]}\|\sqrt{\alpha_h}(s)\dot{\psi}_h(s)\|_{L^2}^2\int_0^T \sup_{x\in\Omega}\left|\frac{\dot{\alpha}_h(x)}{\alpha_h(x)}\right|\mathrm{d}s
\end{aligned}
\tag{A.2}
$$

for all $t\in[0,T_h]$. Taking the maximum of the above estimate over $[0,T_h]$ then yields

$$
\begin{aligned}
&(1-\gamma)\max_{t\in[0,T_h]}\|\sqrt{\alpha_h(t)}\dot{\psi}_h(t)\|_{L^2}^2 + c^2\max_{t\in[0,T_h]}\|\nabla_h\tilde{\psi}_h(t)\|_{L^2}^2 \\
&+ \tfrac{b}{c^2}\int_0^{T_h} \|\sqrt{\alpha_h}\,\ddot{\psi}_h\|_{L^2}^2\,\mathrm{d}s + \max_{s\in[0,T_h]}\|\sqrt{\chi}\,[\![\tilde{\psi}_h(t)]\!]\,\|_{\mathcal{F}_h}^2 \\
&\lesssim \|\sqrt{\alpha_h(0)}\dot{\psi}_h(0)\|_{L^2}^2 + c^2\|\nabla_h\tilde{\psi}_h(0)\|_{L^2}^2 + \|\sqrt{\chi}\,[\![\tilde{\psi}_h(0)]\!]\,\|_{\mathcal{F}_h}^2.
\end{aligned}
\tag{A.3}
$$

Since the right-hand side of (A.3) does not depend on T_h, we are allowed to extend the existence interval to $[0,T]$; i.e., we can set $T_h=T$. Uniqueness follows by linearity of the problem and the derived stability bound. □

Proof of Theorem 2. We begin the proof by observing that ψ satisfies the weak form (5.2) when $\alpha_h=\alpha$. Therefore, we can see the error $e=\psi-\psi_h$ as the solution of the following problem:

$$
(\alpha_h\ddot{e},v_h)_{L^2} + a_h(\tilde{e},v_h) = -((\alpha-\alpha_h)\ddot{\psi},v_h)_{L^2} \tag{A.4}
$$

for all $v_h\in V_h$ and all time $t\in(0,T]$, with

$$
(e(0),\dot{e}(0)) = (\psi_0-\psi_{0,h},\ \psi_1-\psi_{1,h}).
$$

By involving the interpolant, we can then rewrite equation (A.4) as

$$
(\alpha_h\ddot{e}_h,v_h)_{L^2} + a_h(\tilde{e}_h,v_h) = (\alpha_h\ddot{e}_I + (\alpha-\alpha_h)\ddot{\psi},v_h)_{L^2} + a_h(\tilde{e}_I,v_h) \tag{A.5}
$$

for $t\in(0,T]$ and all $v_h\in V_h$. We next test equation (A.5) with $v_h=\dot{\tilde{e}}_h\in V_h$ and estimate the resulting terms. By treating all the terms arising from the left-hand side of (A.5) as in the proof of Theorem 1, we arrive at the following counterpart of estimate (A.2) for the energy of e_h at time t:

$$
\begin{aligned}
&\|\sqrt{\alpha_h(t)}\,\dot{e}_h(t)\|_{L^2}^2 + \tfrac{b}{c^2}\int_0^t \|\sqrt{\alpha_h}\,\ddot{e}_h\|_{L^2}^2\,\mathrm{d}s + c^2\|\nabla_h\tilde{e}_h(t)\|_{L^2}^2 + \|\sqrt{\chi}\,[\![\tilde{e}_h(t)]\!]\,\|_{\mathcal{F}_h}^2 \\
&\lesssim \left|\int_0^t \left\{(\alpha_h\ddot{e}_I + (\alpha-\alpha_h)\ddot{\psi},\ \dot{\tilde{e}}_h)_{L^2} + a_h(\tilde{e}_I,\dot{\tilde{e}}_h)\right\}\mathrm{d}s\right| + \gamma\max_{s\in[0,t]}\|\sqrt{\alpha_h(s)}\dot{e}_h(s)\|_{L^2}^2,
\end{aligned}
\tag{A.6}
$$

where we have additionally used that $e_h(0)=\dot{e}_h(0)=0$ due to our choice of the approximate initial data. By employing Hölder's and then Young's inequality with $\varepsilon_1>0$, we obtain

$$
\begin{aligned}
&\int_0^t (\alpha_h \ddot{e}_I + (\alpha-\alpha_h)\ddot{\psi},\, \dot{e}_h + \tfrac{b}{c^2}\ddot{e}_h)_{L^2}\,\mathrm{d}s \\
&\le \int_0^t (\|\sqrt{\alpha_h}\ddot{e}_I\|_{L^2} + \left\|\tfrac{\alpha-\alpha_h}{\sqrt{\alpha_h}}\ddot{\psi}\right\|_{L^2})(\|\sqrt{\alpha_h}\dot{e}_h\|_{L^2} + \tfrac{b}{c^2}\|\sqrt{\alpha_h}\ddot{e}_h\|_{L^2})\,\mathrm{d}s \\
&\le \tfrac{1}{4\varepsilon_1}(1+\tfrac{b}{c^2})\int_0^t \left(\alpha_1\|\ddot{e}_I\|_{L^2}^2 + \alpha_0^{-1}\|(\alpha-\alpha_h)\ddot{\psi}\|_{L^2}^2\right)\mathrm{d}s \\
&\quad + 2\varepsilon_1\int_0^t \|\sqrt{\alpha_h}\dot{e}_h\|_{L^2}^2\,\mathrm{d}s + 2\varepsilon_1\tfrac{b}{c^2}\int_0^t \|\sqrt{\alpha_h}\ddot{e}_h\|_{L^2}^2\,\mathrm{d}s
\end{aligned}
$$

for all $t\in[0,T]$. We note that the following useful estimate holds for the bilinear form $a_h(\cdot,\cdot)$:

$$
\begin{aligned}
|a_h(\phi, v_h)| \lesssim\, & c^2\|\nabla_h\phi\|_{L^2}\|\nabla_h v\|_{L^2} + \|\chi^{-1/2}\{\!\{c^2\nabla_h\phi\}\!\}\|_{\mathcal{F}_h}\|\sqrt{\chi}[\![v_h]\!]\|_{\mathcal{F}_h} \\
& + c\tfrac{1}{\sqrt{\beta}}\|\nabla_h v_h\|_{L^2}\|\sqrt{\chi}[\![\phi]\!]\|_{\mathcal{F}_h} + \|\sqrt{\chi}[\![\phi]\!]\|_{\mathcal{F}_h}\|\sqrt{\chi}[\![v_h]\!]\|_{\mathcal{F}_h},
\end{aligned}
\tag{A.7}
$$

which we will use below with the choice of $\phi\in\{\tilde{e}_I, \dot{\tilde{e}}_I\}$. The term $\|\chi^{-1/2}\{\!\{c^2\nabla_h\phi\}\!\}\|_{\mathcal{F}_h}$ appearing in (A.7) is the reason why we need the bound (3.7) on the interpolant error. To estimate the $a_h(\tilde{e}_I, \dot{\tilde{e}}_h)$ term in (A.6), we employ integration by parts with respect to time and then twice inequality (A.7),

$$
\begin{aligned}
\int_0^t a_h(\tilde{e}_I, \dot{\tilde{e}}_h)\,\mathrm{d}s =\, & a_h(\tilde{e}_I(t), \tilde{e}_h(t)) - \int_0^t a_h(\dot{\tilde{e}}_I, \tilde{e}_h)\,\mathrm{d}s \\
\lesssim\, & c^2\|\nabla_h\tilde{e}_I(t)\|_{L^2}|\nabla_h\tilde{e}_h(t)|_{L^2} + \|\chi^{-1/2}\{\!\{c^2\nabla_h\tilde{e}_I(t)\}\!\}\|_{\mathcal{F}_h}\|\sqrt{\chi}[\![\tilde{e}_h(t)]\!]\|_{\mathcal{F}_h} \\
& + c\tfrac{1}{\sqrt{\beta}}\|\nabla_h\tilde{e}_h(t)\|_{L^2}\|\sqrt{\chi}[\![\tilde{e}_I(t)]\!]\|_{\mathcal{F}_h} + \|\chi^{1/2}[\![\tilde{e}_I(t)]\!]\|_{\mathcal{F}_h}\|\chi^{1/2}[\![\tilde{e}_h(t)]\!]\|_{\mathcal{F}_h} \\
& + \int_0^t \Big(c^2\|\nabla_h\dot{\tilde{e}}_I\|_{L^2}\|\nabla_h\tilde{e}_h\|_{L^2} + \|\chi^{-1/2}\{\!\{c^2\nabla_h\dot{\tilde{e}}_I\}\!\}\|_{\mathcal{F}_h}\|\sqrt{\chi}[\![\tilde{e}_h]\!]\|_{\mathcal{F}_h} \\
& + c\tfrac{1}{\sqrt{\beta}}\|\nabla_h\tilde{e}_h\|_{L^2}\|\sqrt{\chi}[\![\dot{\tilde{e}}_I]\!]\|_{\mathcal{F}_h} + \|\sqrt{\chi}[\![\dot{\tilde{e}}_I]\!]\|_{\mathcal{F}_h}\|\sqrt{\chi}[\![\tilde{e}_h]\!]\|_{\mathcal{F}_h}\Big)\,\mathrm{d}s.
\end{aligned}
$$

From here by Young's inequality with $\varepsilon_2\in(0,\varepsilon_1)$, we have

$$
\begin{aligned}
\int_0^t a_h(\tilde{e}_I, \dot{\tilde{e}}_h)\,\mathrm{d}s \lesssim\, & \varepsilon_1\left(c^2(1+\tfrac{1}{\beta})\|\nabla_h\tilde{e}_h(t)\|_{L^2}^2 + \|\sqrt{\chi}[\![\tilde{e}_h(t)]\!]\|_{\mathcal{F}_h}^2\right) \\
& + \varepsilon_2\int_0^t \left(c^2(1+\tfrac{1}{\beta})\|\nabla\tilde{e}_h\|_{L^2}^2 + \|\sqrt{\chi}[\![\tilde{e}_h]\!]\|_{\mathcal{F}_h}^2\right)\mathrm{d}s + \tfrac{1}{4\varepsilon_2}\,\bar{E}[e_I](t),
\end{aligned}
$$

where the modified energy of the interpolant error is given by

$$
\begin{aligned}
\bar{E}[e_I](t) :=\, & c^2\|\nabla_h\tilde{e}_I(t)\|_{L^2}^2 + \|\sqrt{\chi}[\![\tilde{e}_I(t)]\!]\|_{\mathcal{F}_h}^2 + \|\chi^{-1/2}\{\!\{c^2\nabla_h\tilde{e}_I(t)\}\!\}\|_{\mathcal{F}_h}^2 \\
& + \int_0^t \left(c^2\|\nabla_h\dot{\tilde{e}}_I\|_{L^2}^2 + \|\sqrt{\chi}[\![\dot{\tilde{e}}_I]\!]\|_{\mathcal{F}_h}^2 + \|\chi^{-1/2}\{\!\{c^2\nabla_h\dot{\tilde{e}}_I\}\!\}\|_{\mathcal{F}_h}^2\right)\mathrm{d}s.
\end{aligned}
$$

We fix $\varepsilon_1>0$ sufficiently small and include the derived bounds in estimate (A.6), from which we immediately have

$$
\begin{aligned}
E[e_h](t) \lesssim\, & \varepsilon_2 T \max_{t\in[0,T]} \Big(\|\sqrt{\alpha_h(t)}\dot{e}_h(t)\|_{L^2}^2 + c^2(1+\tfrac{1}{\beta})\|\nabla_h \tilde{e}_h(t)\|_{L^2}^2 \\
& + \|\sqrt{\chi}[\![\tilde{e}_h(t)]\!]\|_{\mathcal{F}_h}^2 \Big) + (1+\tfrac{b}{c^2})\,\alpha_0^{-1} \int_0^t \|(\alpha-\alpha_h)\ddot{\psi}\|_{L^2}^2 \,\mathrm{d}s \\
& + \frac{1}{4\varepsilon_2}\left(\bar{E}[e_I](t) + (1+\tfrac{b}{c^2})\alpha_1 \int_0^t \|\ddot{e}_I\|_{L^2}^2 \,\mathrm{d}s \right) \\
& + \gamma \max_{t\in[0,T]} \|\sqrt{\alpha_h(t)}\dot{e}_h(t)\|_{L^2}^2
\end{aligned}
\tag{A.8}
$$

for all $t \in [0,T]$. Above, we have also employed the inequality

$$
\int_0^t \|v\|_{L^2}^2 \,\mathrm{d}s \le T \max_{t\in[0,T]} \|v(t)\|_{L^2}^2,
$$

which holds for functions $v \in C([0,T];L^2(\Omega))$. By possibly decreasing ε_2 and γ, and then taking the maximum over $[0,T]$ of (A.8), we obtain

$$
\begin{aligned}
\max_{t\in[0,T]} E[e_h](t) \lesssim\, & (1+\tfrac{b}{c^2})\,\alpha_0^{-1} \int_0^T \|(\alpha-\alpha_h)\ddot{\psi}\|_{L^2}^2 \,\mathrm{d}s + \max_{t\in[0,T]} \bar{E}[e_I](t) \\
& + (1+\tfrac{b}{c^2})\alpha_1 \int_0^T \|\ddot{e}_I\|_{L^2}^2 \,\mathrm{d}s.
\end{aligned}
\tag{A.9}
$$

Recalling also the properties of the interpolant stated in Lemma 3 leads to

$$
\begin{aligned}
\|e_h\|_E^2 \lesssim\, & h^{2\mu-2} \max_{t\in[0,T]} \sum_{\kappa\in\mathcal{T}_h} \Big(c^2 |\psi(t)|_{H^n(\kappa)}^2 + \tfrac{b^2}{c^2} |\dot{\psi}(t)|_{H^n(\kappa)}^2 \Big) \\
& + h^{2\mu-2} \int_0^T \sum_{\kappa\in\mathcal{T}_h} \Big((\alpha_1 + \tfrac{b}{c^2}\alpha_1 + \tfrac{b^2}{c^2}) |\ddot{\psi}|_{H^n(\kappa)}^2 + c^2 |\dot{\psi}|_{H^n(\kappa)}^2 \Big) \,\mathrm{d}s \\
& + (1+\tfrac{b}{c^2})\,\alpha_0^{-1} \int_0^T \|(\alpha-\alpha_h)\ddot{\psi}\|_{L^2}^2 \,\mathrm{d}s.
\end{aligned}
$$

Together with estimate (5.10) for $\|e_I\|_E$, this yields the desired bound (5.11) for the discretization error. We note that the constant C_{Thm2} in the final estimate has the form

$$
C_{\mathrm{Thm2}} = O\left(c^2 + \tfrac{b^2}{c^2} + \tfrac{b}{c^2} + 1 \right). \quad \square
$$

References

[1] P.F. Antonietti, F. Bonaldi, I. Mazzieri, Simulation of three-dimensional elastoacoustic wave propagation based on a discontinuous Galerkin spectral element method, Int. J. Numer. Methods Eng. (2019).

[2] P.F. Antonietti, F. Bonaldi, I. Mazzieri, A high-order discontinuous Galerkin approach to the elasto-acoustic problem, Comput. Methods Appl. Mech. Eng. 358 (2020).

[3] P.F. Antonietti, A. Cangiani, J. Collis, Z. Dong, E.H. Georgoulis, S. Giani, P. Houston, Review of Discontinuous Galerkin Finite Element Methods for Partial Differential Equations on Complicated Domains, 1st edition, Lecture Notes in Computational Science and Engineering, vol. 114, Springer, 2016, pp. 281–310, Chapter 8.

[4] P.F. Antonietti, B.A. De Dios, I. Mazzieri, A. Quarteroni, Stability analysis of discontinuous Galerkin approximations to the elastodynamics problem, J. Sci. Comput. 68 (1) (2016) 143–170.

[5] P.F. Antonietti, I. Mazzieri, High-order discontinuous Galerkin methods for the elastodynamics equation on polygonal and polyhedral meshes, Comput. Methods Appl. Mech. Eng. 342 (2018) 414–437.

[6] D.N. Arnold, An interior penalty finite element method with discontinuous elements, SIAM J. Numer. Anal. 19 (4) (1982) 742–760.

[7] I. Babuška, M. Suri, The h-p version of the finite element method with quasi-uniform meshes, RAIRO Modél. Math. Anal. Numér. 21 (2) (1987) 199–238.

[8] F. Bassi, L. Botti, A. Colombo, Agglomeration-based physical frame dG discretizations: an attempt to be mesh free, Math. Models Methods Appl. Sci. 24 (8) (2014) 1495–1539.

[9] F. Bassi, L. Botti, A. Colombo, S. Rebay, Agglomeration based discontinuous Galerkin discretization of the Euler and Navier–Stokes equations, Comput. Fluids 61 (2012) 77–85.

[10] C.E. Baumann, J.T. Oden, A discontinuous *hp* finite element method for the Euler and Navier–Stokes equations, Int. J. Numer. Methods Fluids 31 (1) (1999) 79–95.
[11] S. Brenner, R. Scott, The Mathematical Theory of Finite Element Methods, vol. 15, Springer Science & Business Media, 2007.
[12] D.M. Campbell, Nonlinear dynamics of musical reed and brass wind instruments, Contemp. Phys. 40 (6) (1999) 415–431.
[13] A. Cangiani, Z. Dong, E.H. Georgoulis, *hp*-version space-time discontinuous Galerkin methods for parabolic problems on prismatic meshes, SIAM J. Sci. Comput. 39 (4) (2017) A1251–A1279.
[14] A. Cangiani, Z. Dong, E.H. Georgoulis, P. Houston, *hp*-version discontinuous Galerkin methods for advection-diffusion-reaction problems on polytopic meshes, ESAIM: Math. Model. Numer. Anal. 50 (3) (2016) 699–725.
[15] A. Cangiani, Z. Dong, E.H. Georgoulis, P. Houston, *hp*-Version Discontinuous Galerkin Methods on Polygonal and Polyhedral Meshes, SpringerBriefs in Mathematics, Springer International Publishing, 2017.
[16] A. Cangiani, E.H. Georgoulis, P. Houston, *hp*-version discontinuous Galerkin methods on polygonal and polyhedral meshes, Math. Models Methods Appl. Sci. 24 (10) (2014) 2009–2041.
[17] I. Christov, C. Christov, P. Jordan, Modeling weakly nonlinear acoustic wave propagation, Q. J. Mech. Appl. Math. 60 (4) (2007) 473–495.
[18] D.G. Crighton, Model equations of nonlinear acoustics, Annu. Rev. Fluid Mech. 11 (1) (1979) 11–33.
[19] D.A. Di Pietro, A. Ern, Mathematical Aspects of Discontinuous Galerkin Methods, vol. 69, Springer Science & Business Media, 2011.
[20] W. Dörfler, H. Gerner, R. Schnaubelt, Local well-posedness of a quasilinear wave equation, Appl. Anal. 95 (9) (2016) 2110–2123.
[21] J. Douglas Jr., T. Dupont, Interior penalty procedures for elliptic and parabolic Galerkin methods, in: Computing Methods in Applied Sciences, Second Internat. Sympos., Versailles, 1975, in: Lecture Notes in Phys., vol. 58, Springer, Berlin, 1976, pp. 207–216.
[22] F.A. Duck, Nonlinear acoustics in diagnostic ultrasound, Ultrasound Med. Biol. 28 (1) (2002) 1–18.
[23] B.O. Enflo, C.M. Hedberg, Theory of Nonlinear Acoustics in Fluids, vol. 67, Springer Science & Business Media, 2006.
[24] B. Engquist, A. Majda, Absorbing boundary conditions for numerical simulation of waves, Proc. Natl. Acad. Sci. 74 (5) (1977) 1765–1766.
[25] E.H. Georgoulis, Inverse-type estimates on *hp*-finite element spaces and applications, Math. Comput. 77 (261) (2008) 201–219.
[26] J. Gilbert, M. Campbell, A. Myers, B. Pyle, Differences between brass instruments arising from variations in brassiness due to nonlinear propagation, in: International Symposium on Musical Acoustics (ISMA), 2007.
[27] C. Godano, F. Oliveri, Nonlinear seismic waves: a model for site effects, Int. J. Non-Linear Mech. 34 (3) (1999) 457–468.
[28] M.J. Grote, A. Schneebeli, D. Schötzau, Discontinuous Galerkin finite element method for the wave equation, SIAM J. Numer. Anal. 44 (6) (2006) 2408–2431.
[29] M.F. Hamilton, D.T. Blackstock, Nonlinear Acoustics, Vol. 1, Academic Press, San Diego, 1998.
[30] J.S. Hesthaven, T. Warburton, Nodal Discontinuous Galerkin Methods: Algorithms, Analysis, and Applications, Springer Science & Business Media, 2007.
[31] J. Hoffelner, H. Landes, M. Kaltenbacher, R. Lerch, Finite element simulation of nonlinear wave propagation in thermoviscous fluids including dissipation, IEEE Trans. Ultrason. Ferroelectr. Freq. Control 48 (3) (2001) 779–786.
[32] T.J. Hughes, T. Kato, J.E. Marsden, Well-posed quasi-linear second-order hyperbolic systems with applications to nonlinear elastodynamics and general relativity, Arch. Ration. Mech. Anal. 63 (3) (1977) 273–294.
[33] B. Kaltenbacher, I. Lasiecka, Global existence and exponential decay rates for the Westervelt equation, Discrete Contin. Dyn. Syst., Ser. S 2 (3) (2009) 503.
[34] B. Kaltenbacher, I. Lasiecka, Well-posedness of the Westervelt and the Kuznetsov equation with nonhomogeneous Neumann boundary conditions, Conference Publications 2 (2011) 763–773.
[35] B. Kaltenbacher, V. Nikolić, M. Thalhammer, Efficient time integration methods based on operator splitting and application to the Westervelt equation, IMA J. Numer. Anal. 35 (3) (2014) 1092–1124.
[36] M. Kaltenbacher, Numerical Simulation of Mechatronic Sensors and Actuators, Vol. 2, Springer, 2007.
[37] S. Kawashima, Y. Shibata, Global existence and exponential stability of small solutions to nonlinear viscoelasticity, Commun. Math. Phys. 148 (1) (1992) 189–208.
[38] J.F. Kelly, S. Marras, X. Zhao, R.J. McGough, Linear and nonlinear ultrasound simulations using the discontinuous Galerkin method, J. Acoust. Soc. Am. 143 (4) (2018) 2438–2448.
[39] D. Maresca, A. Lakshmanan, A. Lee-Gosselin, J.M. Melis, Y.-L. Ni, R.W. Bourdeau, D.M. Kochmann, M.G. Shapiro, Nonlinear ultrasound imaging of nanoscale acoustic biomolecules, Appl. Phys. Lett. 110 (7) (2017) 073704.
[40] I. Mazzieri, M. Stupazzini, R. Guidotti, C. Smerzini, SPEED: spectral elements in elastodynamics with discontinuous Galerkin: a non-conforming approach for 3D multi-scale problems, Int. J. Numer. Methods Fluids 95 (12) (2013) 991–1010.
[41] S. Meyer, M. Wilke, Optimal regularity and long-time behavior of solutions for the Westervelt equation, Appl. Math. Optim. 64 (2) (2011) 257–271.
[42] A. Myers, R.W. Pyle Jr, J. Gilbert, D.M. Campbell, J.P. Chick, S. Logie, Effects of nonlinear sound propagation on the characteristic timbres of brass instruments, J. Acoust. Soc. Am. 131 (1) (2012) 678–688.
[43] V. Nikolić, B. Wohlmuth, A priori error estimates for the finite element approximation of Westervelt's quasi-linear acoustic wave equation, SIAM J. Numer. Anal. 57 (4) (2019) 1897–1918.
[44] C. Ortner, E. Süli, Discontinuous Galerkin finite element approximation of nonlinear second-order elliptic and hyperbolic systems, SIAM J. Numer. Anal. 45 (4) (2007) 1370–1397.
[45] O.V. Pavlenko, Nonlinear seismic effects in soils: numerical simulation and study, Bull. Seismol. Soc. Am. 91 (2) (2001) 381–396.
[46] M. Pérez-Liva, J. Herraiz, J. Udías, E. Miller, B. Cox, B. Treeby, Time domain reconstruction of sound speed and attenuation in ultrasound computed tomography using full wave inversion, J. Acoust. Soc. Am. 141 (3) (2017) 1595–1604.
[47] W. Reed, T. Hill, Triangular mesh methods for the neutron transport equation, Technical Report LA-UR-73-479, Los Alamos Scientific Laboratory, 1973.
[48] J. Resch, L. Krivodonova, J. Vanderkooy, A two-dimensional study of finite amplitude sound waves in a trumpet using the discontinuous Galerkin method, J. Comput. Acoust. 22 (03) (2014) 1450007.
[49] B. Rivière, Discontinuous Galerkin Methods for Solving Elliptic and Parabolic Equations, Frontiers in Applied Mathematics, vol. 35, Society for Industrial and Applied Mathematics (SIAM), Philadelphia, PA, 2008, Theory and implementation.
[50] P. Rosnitskiy, P. Yuldashev, V. Khokhlova, Effect of the angular aperture of medical ultrasound transducers on the parameters of nonlinear ultrasound field with shocks at the focus, Acoust. Phys. 61 (3) (2015) 301–307.
[51] T. Roubíček, Nonlinear Partial Differential Equations with Applications, vol. 153, Springer Science & Business Media, 2013.
[52] M. Ryles, F. Ngau, I. McDonald, W. Staszewski, Comparative study of nonlinear acoustic and lamb wave techniques for fatigue crack detection in metallic structures, Fatigue Fract. Eng. Mater. Struct. 31 (8) (2008) 674–683.
[53] C. Schwab, *p*- and *hp*-Finite Element Methods, Numerical Mathematics and Scientific Computation, The Clarendon Press, Oxford University Press, New York, 1998, Theory and applications in solid and fluid mechanics.
[54] I. Shevchenko, B. Kaltenbacher, Absorbing boundary conditions for nonlinear acoustics: the Westervelt equation, J. Comput. Phys. 302 (2015) 200–221.
[55] H. Sohn, H.J. Lim, M.P. DeSimio, K. Brown, M. Derriso, Nonlinear ultrasonic wave modulation for online fatigue crack detection, J. Sound Vib. 333 (5) (2014) 1473–1484.
[56] B. Tripathi, Discontinuous Galerkin method for propagation of acoustical shock waves in complex geometry, PhD thesis, 2015.

[57] B.B. Tripathi, A. Luca, S. Baskar, F. Coulouvrat, R. Marchiano, Element centered smooth artificial viscosity in discontinuous Galerkin method for propagation of acoustic shock waves on unstructured meshes, J. Comput. Phys. 366 (2018) 298–319.
[58] T. Tsuchiya, Y. Kagawa, A simulation study on nonlinear sound propagation by finite element approach, J. Accoust. Soc. Jpn. 13 (4) (1992) 223–230.
[59] P.J. Westervelt, Parametric acoustic array, J. Acoust. Soc. Am. 35 (4) (1963) 535–537.